GEOLOGY AND ORIGINS OF THE PEAK

GOLD-COPPER-SILVER SKARN DEPOSIT, TOK, ALASKA

By

Peter Edward Illig

Recommended:

Dr. Rainer Newberry, Advisory Committee Chair

Dr. Paul Layer, Advisory Committee Member

Dr. Jochen Mezger, Advisory Committee Member

Dr. Paul McCarthy, Chair,
Department of Geosciences

Approved:

Dr. Paul Layer, Dean,
College of Natural Science and Mathematics

Dr. John Eichelberger, Dean of the Graduate School

7 December 2015

Date

# GEOLOGY AND ORIGINS OF THE PEAK GOLD-COPPER-SILVER SKARN DEPOSIT, TOK, ALASKA

A

THESIS

Presented to the Faculty

of the University of Alaska Fairbanks

in Partial Fulfillment of the Requirements

for the Degree of

MASTER OF SCIENCE

By

Peter Edward Illig, B.S. Geology

Fairbanks, Alaska

December 2015

## Abstract

The distal Peak Au-Cu skarn deposit was discovered in 2012 on Tetlin native lands 15 miles southeast of Tok, Alaska. The deposit contains anomalous Au-Cu-Bi-Ag-Mo-Fe-Te-As-Pb-Co-W-Cd-Ni. At the time of drilling deposit style, mineralization and origin were not understood. Upper Paleozoic and older metamorphic rocks had been previously mapped in the area; however, no igneous or metasomatic rocks had been recognized. To better understand the deposit I created a 1:25,000 scale geologic map of the 25 $km^2$ exploration area; employed approximately 682,500 assays for metal ratios; described textures and minerals in 138 polished thin sections; employed approximately 3,000 meters of new core logging to produce a cross-section and long-section; acquired microprobe compositions of skarn amphibole, pyroxene and garnet; analyzed 122 rocks by X-ray fluorescence analysis; had Pb isotopic ratios determined for 3 galena samples; and had 5 rocks dated by $^{40}Ar/^{39}Ar$ and U-Pb techniques. Based upon this data, I define Peak as a distal amphibole-rich Cu-Au skarn. The skarn's plutonic source remains undiscovered, and is likely NE of, and well below the deposit. Based radiometric dating and trace element analyses of plutonic and volcanic rocks, the immediate area experienced intrusive and extrusive activity at 70-75 Ma in a volcanic arc setting.

## Table of Contents

## List of Figures

Page

## List of Tables

Page



## List of Appendices

**Acknowledgements**

In the spring of 2013 I began working for Avalon Development as a drill rig geologist and was provided the opportunity to work on the Peak deposit for my M.S. thesis. I would like to thank Curt Freeman and Chris VanTreeck for making this project available and their willingness for me to go in many different directions to further our collective understanding of mineralization at Tetlin. Secondly I thank Contango ORE Inc., and the village of Tetlin for allowing me full access to their lands, core and data. Without their support through employing me as a geologist and allowing the University of Alaska Fairbanks to work on their project this project would never have materialized. The generous financial support from Contango ORE Inc., the Society of Economic Geologists, SRK Inc. (US) and the University of Alaska Fairbanks Travel Grant allowed for the completion of analytical work and field work.

Ken Severin of the Advanced Instrument Laboratory provided valuable assistance using the new microprobe and assisted in tailoring EPMA and XRF routines specifically for geochemical and mineralogical questions. The analytical equipment at AIL were fundamental to my ability to investigate ore deposit geology at Tetlin.

I would like to thank my committee: Dr. Paul Layer, Dr. Jochen Mezger and Dr. Rainer Newberry for helping me develop my project goals at Tetlin. Rainer and Jochen served as incredible field partners even when we encountered 2 meter high piles of burned, fallen trees. Bryan Babb conducted extensive pyroxene analyses on Peak pyroxenes.

Lastly I would like to thank Dr. Rainer Newberry for being an incredible mentor during my time at UAF. His guidance has been pivotal in my training as a geologist. Rainer, thank you for your patience, counsel and introducing me to the wonders of skarn.

# Chapter 1 Introduction

## 1.1 Introduction to Tetlin

The Peak deposit is located on the Tetlin Indian lands located approximately 300 kilometers east-southeast of Fairbanks, Alaska (Figure 1.1). The 3,180 square kilometer Tetlin Reservation was established in 1930. No record of mining or mineral exploration exists for Tetlin lands previous to 2008 (Forbes and Carver, 1976; Richter, 1997; Cameron, 1999). Juneau Exploration secured a lease from the Tetlin Village for metals exploration and contracted Avalon Development Corporation to begin exploration in 2009. This lease is now controlled by Contango ORE, Inc.

Reconnaissance geological sampling, geochemical sampling and trenching were performed in the 2009 summer exploration season. Soil sampling, IP surveys and prospecting took place in 2010. By 2011, sufficient geological evidence for mineralization warranted geophysical surveys and the first drilling program. Eleven core holes for a total of 2,455 meters were drilled in summer 2011. In 2012, an additional 10,974 meters of core were drilled, accompanied by additional prospecting and soil sampling. It was during this drilling season that intervals containing significant concentrations of gold, silver and copper were intercepted as multiple meter intervals of massive pyrrhotite-chalcopyrite $\pm$ arsenopyrite. This mineralization was described as a chlorite-sulfide replacement of schist (VanTreeck et al., 2012; VanTreeck et al., 2013) and called the 'Peak' deposit.

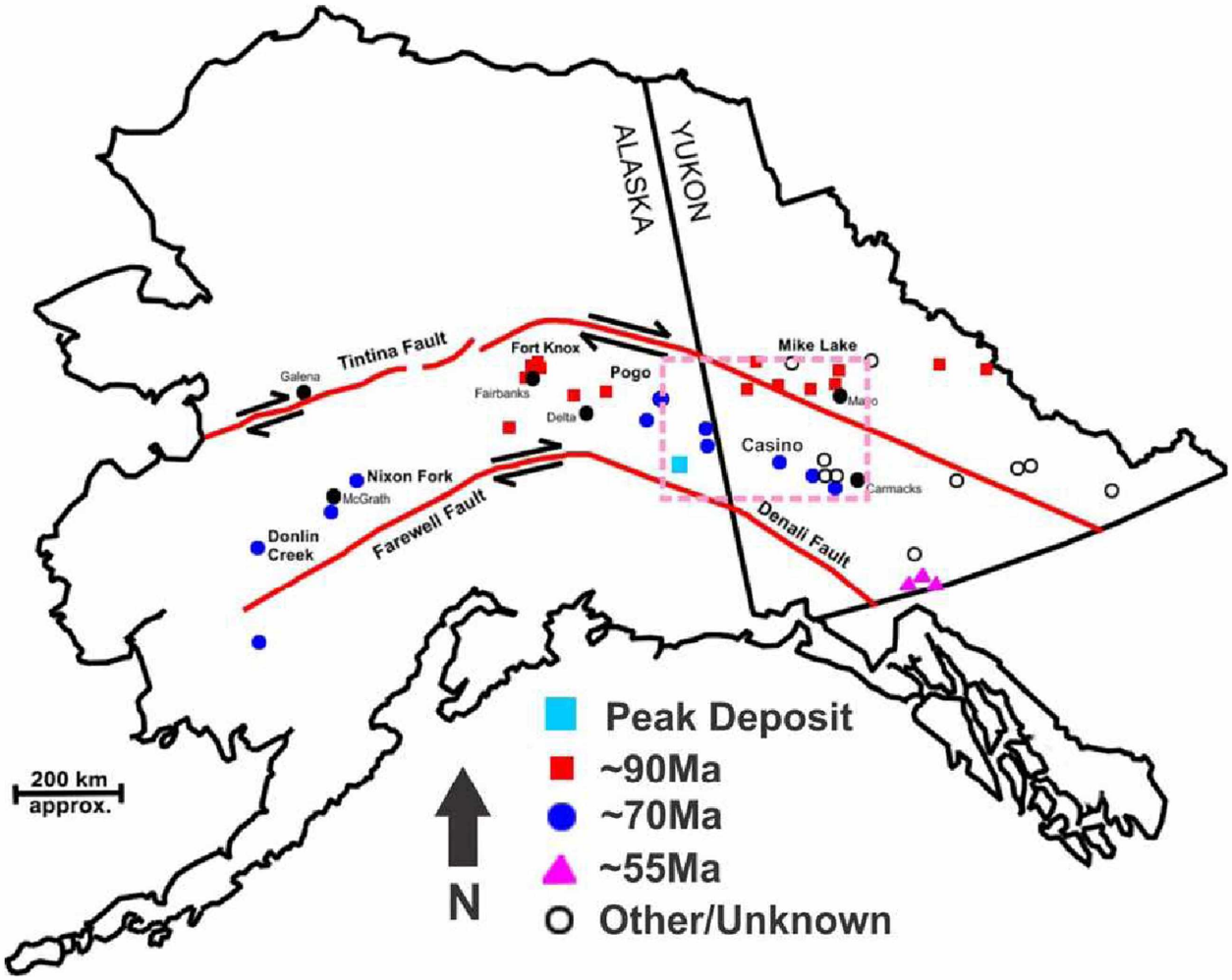


Figure 1.1. Location of major bounding faults, deposits and prospects of the Tintina Gold Province. Dashed pink box is location of figures 1.4 and 1.5. Adapted from Flanigan et al. (2000).

My involvement began in 2013 when I was hired by Avalon Development Corporation to work as a core logging geologist and begin my Masters studies at the University of Alaska Fairbanks on the Peak deposit. During the 2013 drilling season an additional 13,349 meters of core were drilled. Airborne geophysical surveys were conducted along with additional soil and rock sampling. The primary goal for the 2013 drilling season was to provide infill drilling of Peak so that an indicated gold-copper-silver resource could be calculated and released to the public. In January 2014, the indicated and

inferred gold equivalent resources were released and calculated at 783,115 and 332,969 ounces, respectively with a cut off of 0.5 grams per ton gold equivalent (Illig, 2014).

During the 2013 drilling season I used x-ray diffraction and petrographic analyses to show that the Peak deposit style is skarn related; randomly oriented, chlorine rich calcic amphibole is the predominant silicate phase in the Peak deposit. I also found rare hedenbergitic pyroxene undergoing retrograde reactions to hornblende, quartz and calcite. The lack of abundant skarn pyroxene and complete lack of skarn garnet contrasts to other known skarn deposits. Further, the essentially unexplored Tetlin lands are located outside of established mineral districts. This thesis is a summary of my findings concerning (1) deposit scale geology (particularly the unique nature of amphibole skarn mineralization at Peak); (2) exploration area geological mapping; and (3) regional setting for late Cretaceous plutonic related deposits in eastern interior Alaska.

## 1.2 Introduction to Skarns

Skarn deposits (e.g., Meinert et al., 2005) are typically moderate tonnage but high grade (which is key to their economic value) and have extremely variable ore metallogeny (Au, Cu, Zn, Pb, W and Fe among others). The gangue is usually calc-silicate minerals--typically grandite garnet, clinopyroxene, and (or) calcium -rich amphibole—but a variety of other minerals may be present. Skarns are hydrothermal in origin and usually caused by addition of elements from fluid into carbonate-rich rocks. Ore is deposited by a combination of pH changes associated with carbonate mineral destruction and change in temperature. The temperature range and thermal history of a skarn is related to depth of

formation (which can vary considerably); host rock variations also contribute to skarn variations.

Einaudi et al. (1981) described skarns as "coarse-grained Ca-Fe-Mg-Mn silicates formed by replacement of carbonate-bearing rocks accompanying regional or contact metamorphism or metasomatism". Evans (1987) described skarn as a "...metamorphic zone developed in the contact area around igneous intrusions when carbonate rocks are invaded and replaced with chemical elements that originate from the nearby igneous body." Meinert et al. (2005) describe skarn as "any calc-silicate rock". Although there is a lack of agreement to the definition of a skarn I apply the term to Ca-Fe-Mg-Mn silicates and sulfides that have likely replaced calcite-bearing rocks through metasomatic reactions. Calc-silicate rocks interpreted to have undergone isochemical reactions will be called calc-silicate hornfels (contact metamorphism) or calc-silicate schist (regional metamorphism). These distinctions can be difficult or impossible to determine in some cases because the divisions are based upon interactions that occurred in the past and cannot be directly seen. However, as noted by Deal (2012), determining these differences is important for understanding of the genesis of gold, silver and copper skarn ore.

Skarns are commonly divided into endoskarn (hosted within the intrusive or non-calcareous rocks) and exoskarn (calcareous protolith); the latter usually synonymous with 'skarn'. Skarns can be derived from either barren or mineralized intrusions (e.g. Einaudi et al., 1981). Exoskarn is mineralogically zoned: garnet-rich close to parent intrusion or fluid source and pyroxene-rich far from fluid source (Figure 1.2; Meinert et al., 2005). Amphibole is typically present as veins or a less abundant calc-silicate phase in skarn systems. Amphibole-rich skarns are not well documented. Clinopyroxene compositions

can exhibit spatial zoning patterns, with higher Fe/Mg pyroxene farther from source (Meinert et al., 2005). Spatial zoning of skarn amphibole compositions has not been investigated.

Skarns are commonly described as forming in three overlapping stages: 1. contact metamorphism by a pluton causes isochemical (non-metasomatic) metamorphism of nearby country rock; 2. 'prograde', 'high temperature' fluids from the intrusion cause formation of anhydrous Ca-Mg silicates (magnesium silicates almost exclusively in magnesian skarns); and 3. 'retrograde', 'lower temperature' breakdown of prograde minerals to hydrous silicates such as calcium rich amphiboles, epidote and chlorite (Meinert et al., 2005). This typically forms variations in anhydrous calc-silicate assemblages with zoning from garnet rich (proximal to intrusion) to pyroxene rich (distal). Amphibole is characteristically seen as replacements of pyroxene or garnet or in late fractures.

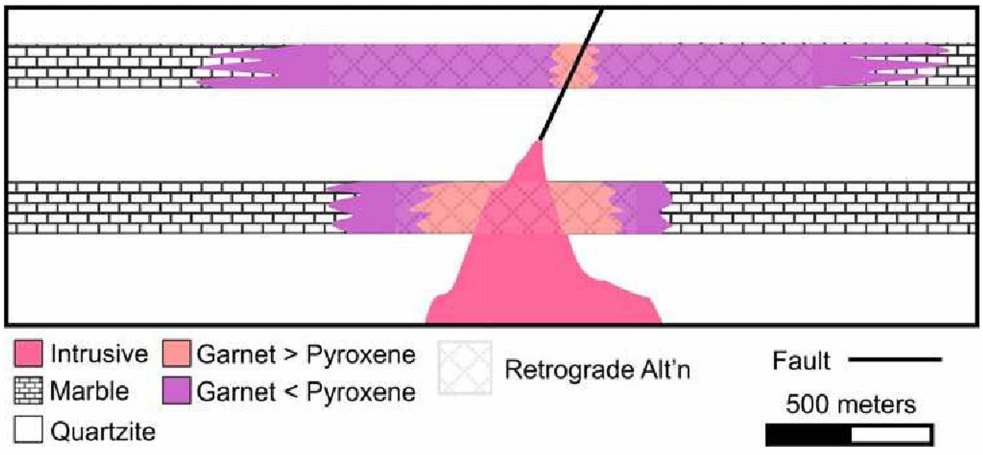


Figure 1.2: Cartoon cross section of zoning in a simple skarn system.

## 1.3 Location and Access

The Peak Zone skarn deposit is located approximately ~20 km SE of Tok, Alaska in the Tetlin Hills (Figure 1.3). The Tetlin exploration project is comprised of state mining claims adjoining lands leased from the Tetlin village. As of the end of 2013 there are 641 claims with a total of 3095.5 square kilometers (including the Tetlin reservation). The Peak deposit is located on the Tetlin reservation approximately 12 km south of the Alaska Highway. The drilling area is connected via a dirt road to the Tetlin village road. The 23 mile Tetlin village road remains open all winter long to serve the Tetlin village community.

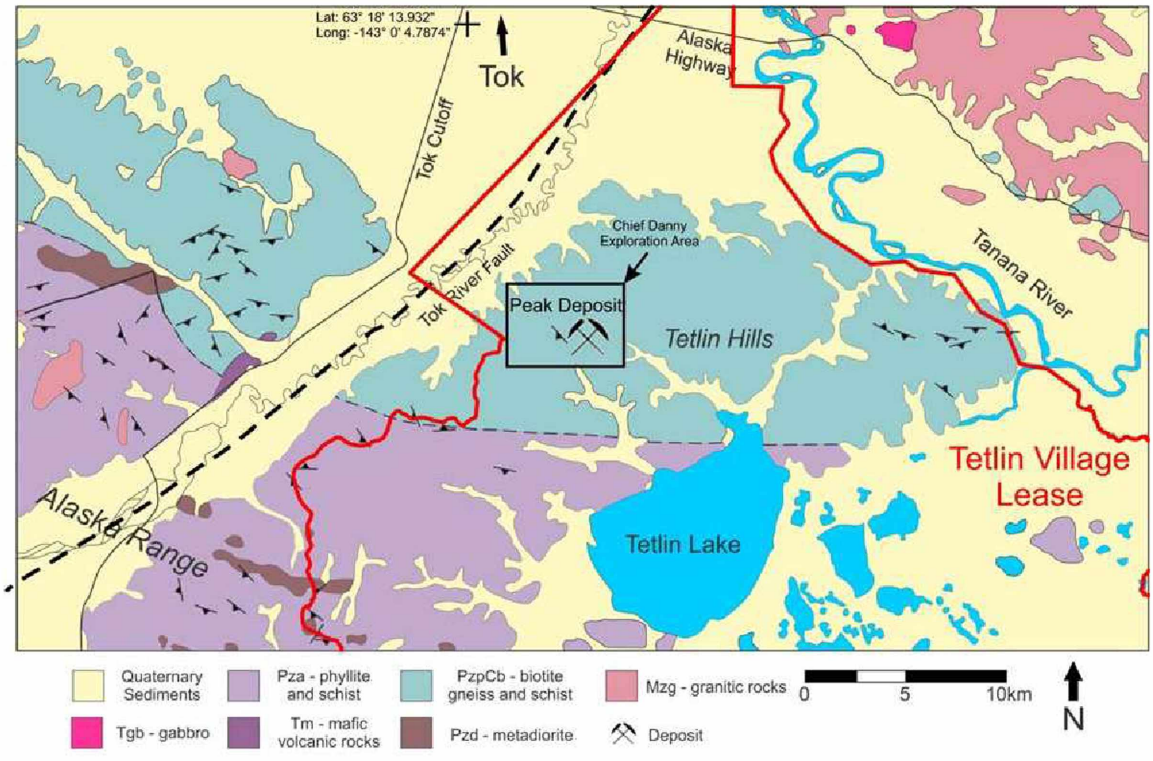


Figure 1.3—Geologic Map of Tetlin Village Lease and vicinity, modified from Foster (1970).

## 1.4 Regional Geology

Plutonic related gold, copper and molybdenum deposits of Cretaceous to early Tertiary ages (e.g. Fort Knox, Pogo, Casino) occur within the region bounded by the Denali and Tintina faults and together comprise the Tintina Gold Province (Figure 1.1). This metallogenic belt spans 2,000 km from Interior Alaska to northern British Columbia (Till et al., 2007). Two major gold mines operate in interior Alaska; Pogo approximately 60 km northeast of Delta Junction, Alaska and Fort Knox approximately 46 km north of Fairbanks, Alaska (Figure 1.1). The region is predominantly underlain by metamorphosed continental rocks that are interpreted as parautochtonous to ancestral North America (Dusel-Bacon et al., 2006; Nelson et al., 2006; Dusel-Bacon and Williams, 2009); regional metamorphism is of greenschist to epidote amphibolite facies and occurred before the mid-Cretaceous.

Numerous plutonic suites were emplaced in eastern Alaska and western Yukon in the Cretaceous to early Tertiary (ca. 115-50 Ma), including those associated with the Ft. Knox and Pogo deposits west of Peak (Figure 1.1). Steeply-dipping NE-trending faults have significant left-lateral and dip-slip motion, variably exposing plutonic and volcanic rocks of the same age (Figure 1.4). Mid-Cretaceous plutonic and volcanic rocks are the most common igneous rocks in the region (Figure 1.4). Late Cretaceous and early Tertiary plutons are generally small but widespread; late Cretaceous volcanic rocks are more common, especially in the western Yukon as the Carmacks Group and Donjek volcanics (Figure 1.4). Paleocene to Eocene (60-55 Ma) bimodal (although mostly felsic) intrusions and mafic volcanic rocks are widespread but tiny (Figure 1.4).

## 1.5 Regional Metallogeny

Several attempts have been made to classify and characterize metallogenic belts in eastern Alaska. Newberry et al. (1998) noted a NW-trending belt of late-Cretaceous porphyry deposits and postulated a NE-trending belt of early Tertiary intrusion-related deposits superimposed on mid-Cretaceous deposits (Figure 1.5). The Tetlin area mineralization was not known at the time, but plots in the '55 Ma porphyry belt'.

Based on new U-Pb ages and ignoring early Tertiary K-Ar ages, Allan et al. (2013) postulated a series of metalogenic belts in the western Yukon and eastern Alaska (Figure 1.6). In particular Allan et al. (2013) postulate two different, narrow 72-67 Ma mineralization belts in Eastern Interior Alaska, both claimed to be closely associated with steeply-dipping NE-striking faults (Figure 1.6). The Peak prospect lies outside of the proposed 'sixtymile belt' and many of the deposits and prospects are more than 10 km from a steeply-dipping fault, making a genetic connection implausible.

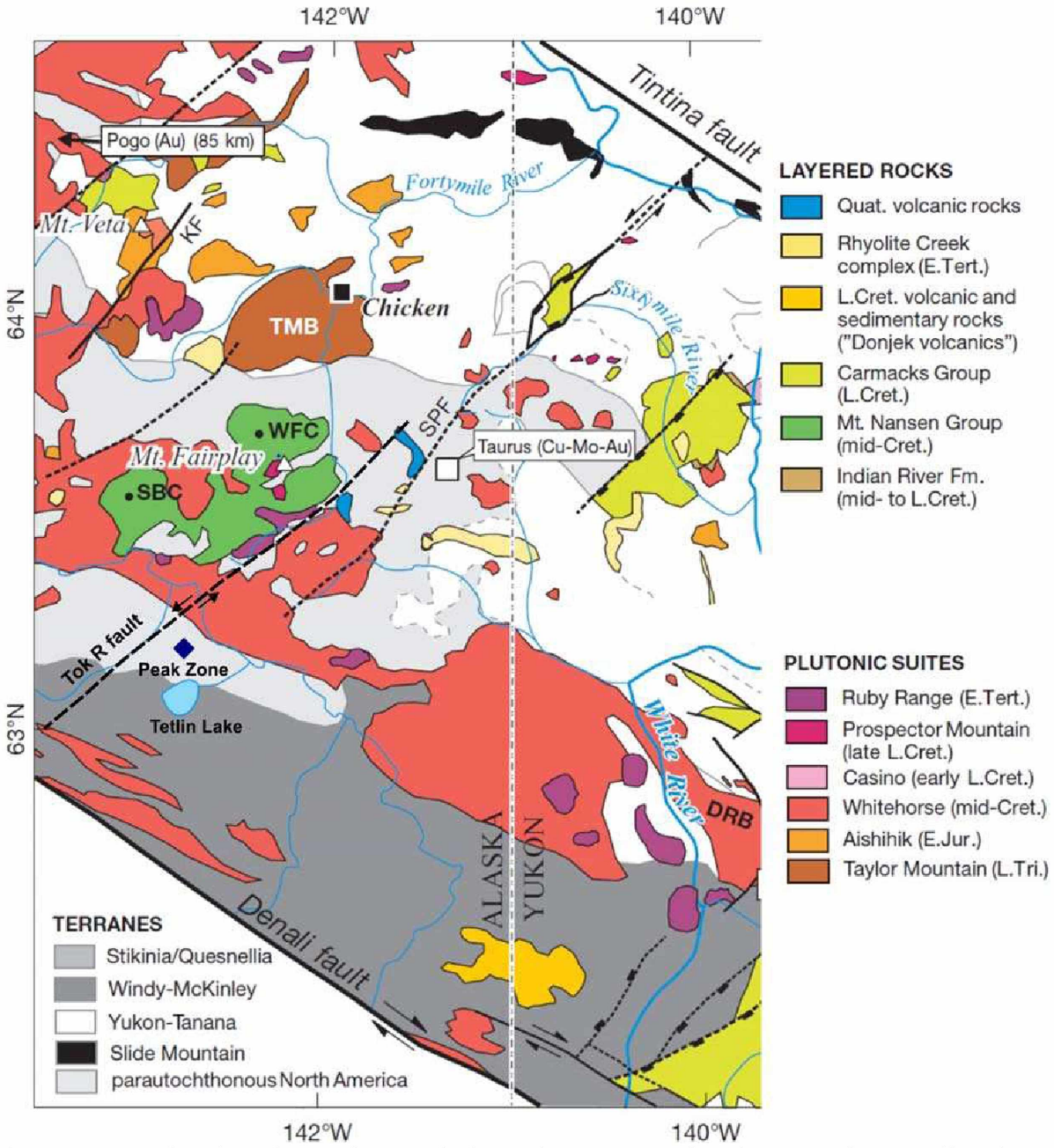


Figure 1.4: Regional geology of East Alaska and Western Yukon between the Denali and Tintina faults. Modified from Allan et al. (2013). SPF = Sixtymile-Pika Fault. Taurus is the closest prospect to Peak that contains a significant Cu resource.

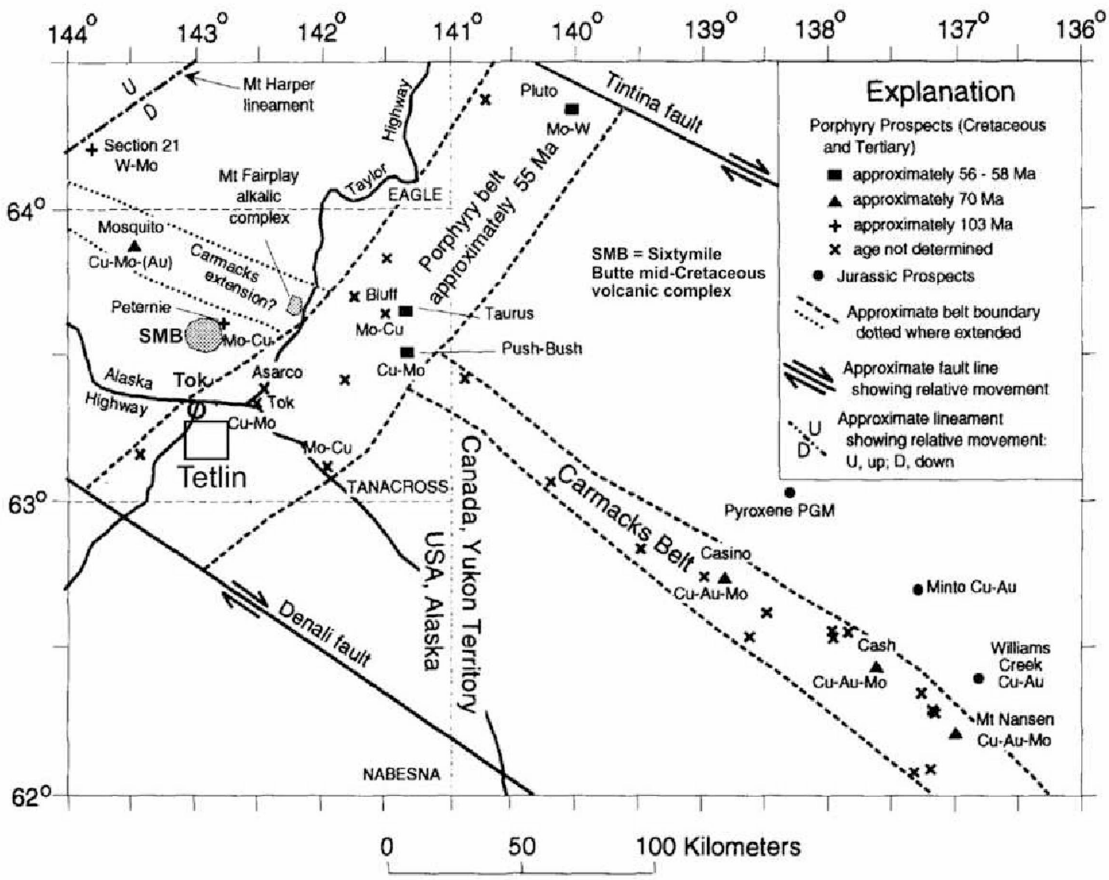


Figure 1.5: Hypothesized mineralization belts in Eastern Alaska and Western Yukon, modified from Newberry et al. (1998).

Many of the prospects in the general vicinity of the Tetlin lands are of broadly 'porphyry' affinity, that is, large tonnage, and low grade Cu-Mo-Au deposits in strongly altered felsic plutonic and associated volcanic rocks. An important exception is the Roadmetal prospect (Figure 1.6), which is both spatially closest to the Tetlin area and not a typical porphyry system. Mineralization at the Roadmetal prospect (Figure 1.7) consists of As-Au-Ag rich veins in granite. The prospect is described as a 3 km-long trend of Ag-Au-base metal mineralization. Diamond drilling (11,000 feet in 14 holes) intersected significant intercepts assaying 6 ppm Au and 200 ppm Ag with up to 0.8% Cu, 3% Pb, 0.9% Bi and 3% Sb (Doyon Ltd. Unpublished report).

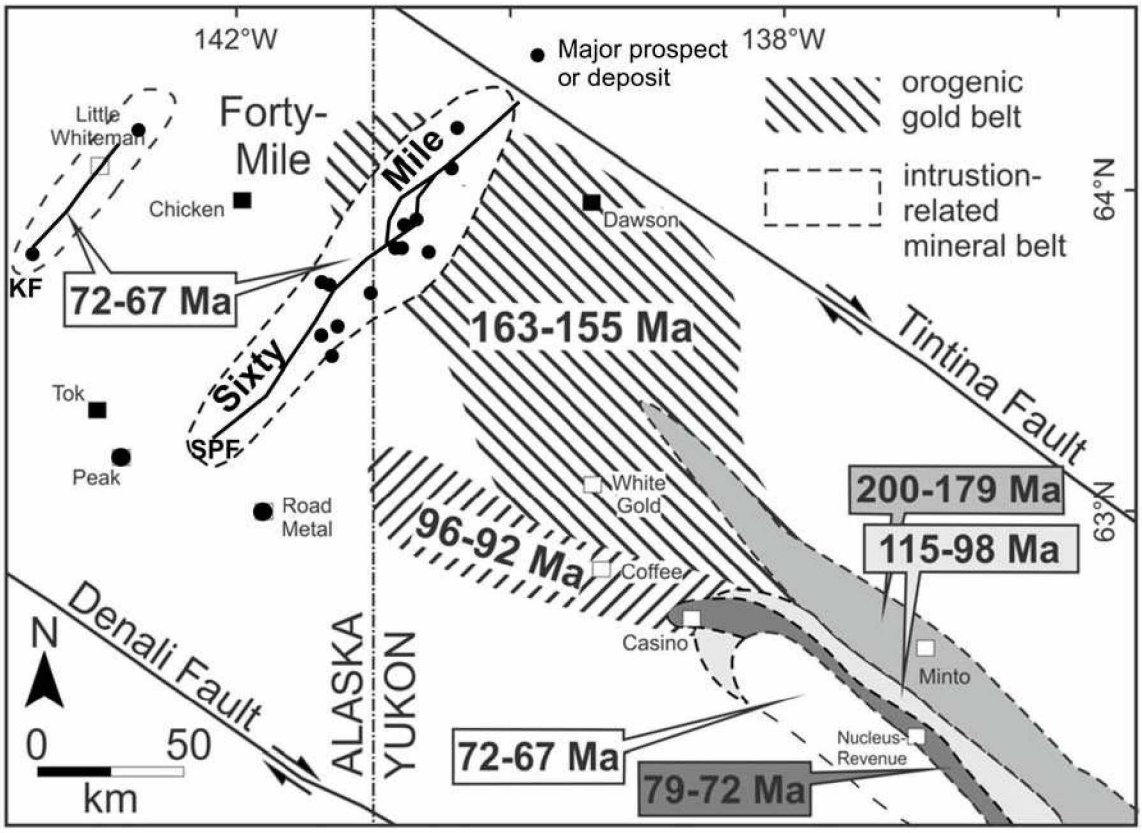


Figure 1.6 Postulated mineralization belts in Eastern Alaska and Western Yukon. Modified from Allan et al. (2013). SPF= Sixtymile-Pika fault; KF = Ketchumstuck fault.

Three $^{40}Ar/^{39}Ar$ radiometric determinations from rocks at the deposit (Table 1.1) yield ages of 91 Ma (regional granodiorite), 70 Ma (biotite from host quartz monzonite), and 67 Ma (fine-grained muscovite associated with mineralization) (Bundtzen et al., 2001).

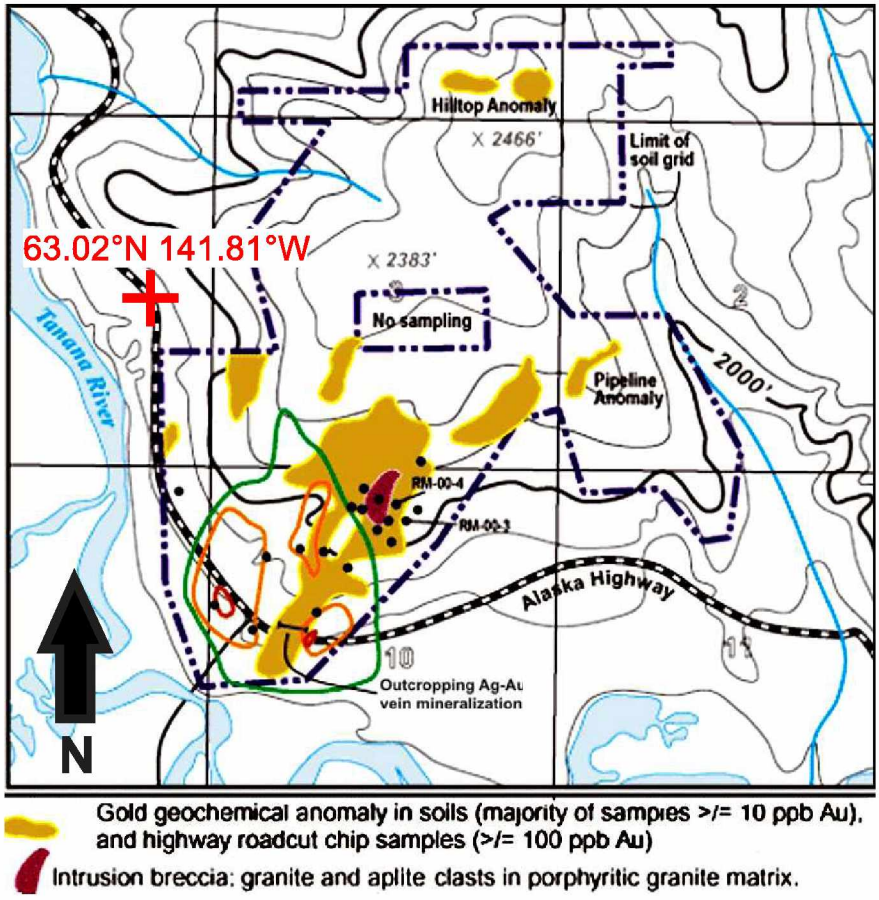


Figure 1.7: Map of Road Metal prospect and locations of elevated gold concentrations in soil and or intrusion matrix breccia. Many of the poorly exposed rocks in the area are mid-Cretaceous granite and granodiorite. Adapted from unpublished Doyon Ltd report. NS-EW grid spacing is 5000 feet.

Table 1.1: Radiometric age data for the Roadmetal prospect, Alaska. Data published with permission of Doyon Ltd.

| Sample | Min. | Integrated age (Ma) | Plateau age (Ma) | Plateau information | Isochron age (Ma) | Isochron information |
|---|---|---|---|---|---|---|
| **99BT582** | Bi | 69.8 ± 0.3 | **69.6 ± 0.3** | 6 fractions<br>72% release<br>MSWD = 0.1 | 69.9 ± 0.3 | $^{40}Ar/^{36}Ar_i$ = 324 ± 30<br>14 fractions<br>MSWD = 2.0 |
| **99BT32** | Bi | 91.7 ± 0.6 | **91.9 ± 0.7** | 9 fractions<br>99% release<br>MSWD = 0.9 | 91.3 ± 0.4 | $^{40}Ar/^{36}Ar_i$ = 189 ± 32<br>10 fractions<br>MSWD = 0.5 |
| **99BT11** | WM | 67.1 ± 0.3 | **67.1 ± 0.5** | 8 fractions<br>89% release<br>MSWD = 3.1 | 66.7 ± 0.4 | $^{40}Ar/^{36}Ar_i$ = 367 ± 40<br>11 fractions<br>MSWD = 1.9 |

## 1.6 Previous Work in the Immediate Study Area

Prior to 2014, the Tanacross Quadrangle 1:250,000 scale geologic map (Foster, 1970) was the most detailed map of the Tetlin lease area. Based on this map (Figure 1.3) the rocks are predominantly Upper Paleozoic and older polymetamorphosed metasedimentary, metavolcanic, and metaplutonic rocks. Marble is a notably sparse constituent. No significant deposits have been discovered in the immediate Tok area and no mineral prospects were known on the Tetlin lease lands prior to 2009.

In the summer of 2009, Avalon Development Corporation (contracted by lease owner Juneau Exploration, now controlled by Contango ORE, Inc.) conducted helicopter supported field reconnaissance, stream sampling and rock sampling. The Chief Danny prospect area, in which Peak is located, (Figure 1.3) was discovered during this time and was followed in the late summer by additional sampling and trenching at what is now known as the Discovery fault hosted Pb-Zn-Sb system.

At the end of the 2013 season a total of 1,687 rock samples, 3,916 soil samples, 847 pan concentrate samples, 1,084 stream sediment samples, 27,779 meters of core and 15,460 core samples had been collected and analyzed. Until mid-summer 2013 VanTreeck et al. (2012) modeled the Peak resource after the Salsigne Au-As-Bi-Ag-Cu chlorite replacement deposit of France (Reynolds, 1965; Demange et al., 2006). This deposit is apparently one in which quartzite was replaced by chlorite + sulfide. At that time the predominant silicate at Peak was believed to be chlorite, believed to replace quartz mica schist. My work in summer 2013 indicated that calcic amphibole was the predominant silicate and preliminary petrography indicated rare clinopyroxene. Chlorite, although present, is a minor mineral phase in ore. Based on this, some variety of skarn/replacement seemed more likely.

## 1.7 Thesis Goals and Methods

The fundamental questions I will be addressing in this thesis concern (1) what exactly is the Peak deposit and (2) how does the metallogeny and age of Peak tie into regional ages and metallogeny? My ultimate objective is to provide information that will assist exploration at both the deposit scale (where is there more?) and the regional scale (what other sorts of deposits should be expected?).

I employ compositional information from 130 drill holes and detailed geological relations and mineral compositions from approximately 3000 meters of re-logged core from Peak deposit and Chief Danny exploration area. I employ metal ratios and amphibole compositional zoning to infer fluid direction. Using these datasets I present a fluid vectoring model pointing to an undiscovered pluton at depth to the east. Combining $^{40}Ar/^{39}Ar$ and U-Pb geochronology, Pb isotopic analyses and trace element geochemistry of igneous rocks I propose a new model for tectonomagmatic controls on late Cretaceous mineralization south of the Fortymile and west of the Dawson Range mining districts.

## Chapter 2 Lithologies and Alteration

### 2.1 Introduction

Prior to this study, the 1:250,000 geologic map of the region (Figure 1.3; Foster, 1970) identified the entire Peak deposit area as 'biotite gneiss and schist'. Although this description generalizes the metamorphic units found on Tetlin lands it did not identify the variety of plutonic, volcanic and metamorphic rocks actually present (Figure 2.1). Field observations, core logging and major/trace element geochemistry were used to assist in their classification. The spatial distribution is based on limited foot traverses combined with drill hole lithology and detailed geophysical maps.

My mapping of the Chief Danny exploration area (Figure 2.1) identified three major types of igneous rocks: the Mohawk pluton, basaltic to rhyolitic composition volcanic rocks, and various dikes and sills. Intrusive rocks including igneous breccia intrude Upper Paleozoic and older polymetamorphosed metasedimentary, metavolcanic and metaplutonic rocks.

Metamorphic rocks are classified based upon texture, mineralogy and composition determined by XRF and fall within six broad groups: skarn, calc-silicate hornfels, semi-massive to massive sulfide, marble, amphibolite, hornblende gneiss, and schist. Skarn incorporates multiple affinities including garnet-pyroxene skarn, pyroxene-amphibole skarn and amphibole skarn. Schistose rocks are a diverse group of metasedimentary rocks which range in mineralogy from micaceous quartzite to calcareous schist with wide variations in quartz, mica, and calcite abundances.

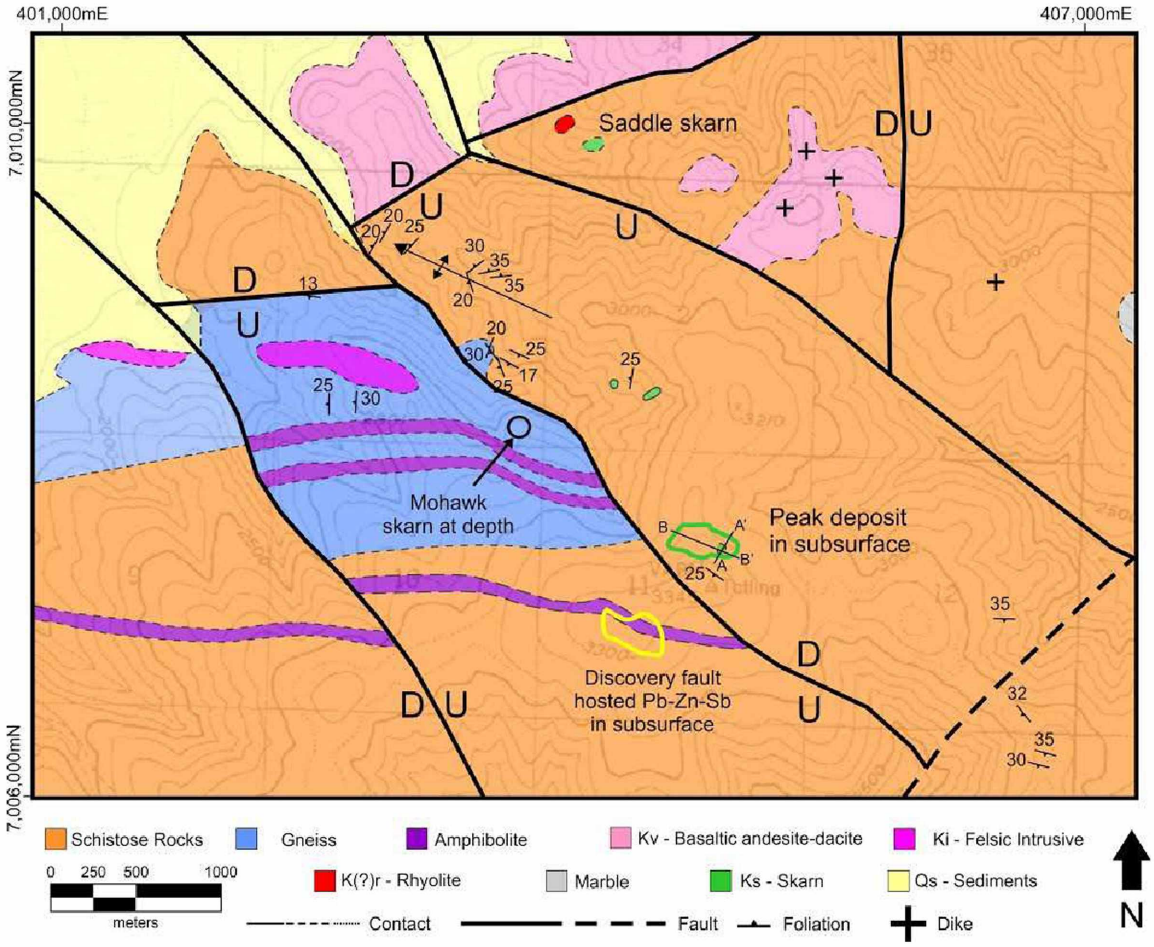


Figure 2.1 Simplified bedrock geologic map of the Chief Danny area. Grid is UTM, NAD83 Datum, Zone 7.

The metamorphic rocks have undergone multiple episodes of deformation. Skarn has not experienced post mineralization deformation, however due to folding of carbonate lithologies prior to metasomatism, deformational history plays a significant role in ore deposit morphology. An understanding of the rocks and alteration are critical to understanding the genesis of the Peak deposit.

## 2.2 Methods

Core at the Tetlin project was logged, sampled for assay by Avalon Development Corporation and stored at Young's Lumberyard, 8 kilometers east of Tok, Alaska. Quality control measures were emplaced at each step to ensure industry standard procedures were adhered to (VanTreeck et al., 2012; and VanTreeck et al., 2013). Core was sawn longitudinally and half was saved for archival purposes. Samples were crushed, pulverized and digested with a four acid (nitric, hydrofluoric, hydrochloric and perchloric acid) mix analyzed for 39 elements using standard ICP-MS techniques.

My analyses were conducted May 2013 to January 2015. This work included reflected and transmitted light petrography of 105 polished thin and thick sections, x-ray fluorescence (XRF) analysis of 93 polished rock 'pucks' and 3 rock pressed pellets, X-ray diffraction (XRD) of 40 powdered mounts, and electron probe microanalysis (EPMA) of major minerals from 24 slides.

Silicate (clinopyroxene, amphibole, garnet), sulfide, telluride and sulfosalt minerals were analyzed by EPMA using quantitative wavelength dispersive spectrometry (WDS) and semiquantitative energy dispersive spectrometry (EDS) methods. Gold and amphibole were analyzed by WDS using natural mineral standards. All EPMA analyses were completed on the JEOL JXA-8530F electron microprobe located in the Advanced Instrument Laboratory at the University of Alaska Fairbanks. Gold grains were analyzed with a 10 micron beam at 10 KeV and 15 nA. On peak count times were 60.0 seconds and high/low count times of 15.0 seconds. Amphibole grains were analyzed with a 5 micron beam at 15 KeV and 10 nA. On peak count times were 20.0 seconds and high/low count times were 10.0 seconds. Standard and crystal assignments can be found in Appendix 3.2.

Ninety-six (44 igneous and 52 metamorphic) samples were analyzed by XRF for major and trace elements. All XRF analyses were completed on the Panalytical Axios 4kW wavelength dispersive spectrometer located in the Advanced Instrument Laboratory at the University of Alaska Fairbanks. Three samples (13PI118, 13PI119 and 13PI120) were pulverized and made into pressed pellets, then analyzed. The remaining 96 samples were sawed (perpendicular to foliation for metamorphic rocks) and polished then analyzed. Comparison of slabs to pressed pellets shows excellent reproducibility between the two for medium- to fine-grained rocks. Each sample was analyzed by XRF between 20 and 30 minutes (depending on count statistics) with beam conditions ranging from 32-60 kV and 66-125 mA (depending on the element). XRF analyses can be found in Appendix 2.1.

Quantitative analyses were acquired on an electron microprobe (JEOL JXA-8530F) equipped with 4 tunable wavelength dispersive spectrometers. Operating conditions were 40 degrees takeoff angle, and a beam energy of 15 keV. The beam current was 2 nA, and the beam diameter was 2 microns. Peak counting times of 10-20 seconds and background counting times of 10 seconds were employed. Oxygen was calculated by cation stoichiometry and included in the matrix correction (phi-ro-z). The calculations and the mass absorption coefficients dataset from LINEMU Henke and CITZMU were used. Well-characterized minerals were employed as standards. Each point was analyzed twice and the results averaged.

The electron microprobe cannot distinguish between $Fe^{3+}$ and $Fe^{2+}$. For the raw analyses I assumed all iron was FeO. $Fe^{3+}$ was calculated for amphiboles with the assumption that cation Si+Al+Fe+Mg+Mn+Ti = 13.0 per 23 oxygens (perfect tetrahedral

+ octahedral site stoichiometry in calcic amphibole) and modifying $Fe^{2+}/Fe^{3+}$ until cations reached that total.

Potassium feldspar staining was used to assist mineral abundance estimates for felsic plutonic rocks, employing standard procedures (Lyons, 1971).

## 2.3 Igneous Rocks

### 2.3.1 Mohawk Pluton (Km)

A felsic intrusive body located 2-3 km NW of the Peak prospect (Figure 2.1) is locally known as the Mohawk pluton. Limited feldspar staining combined with XRF chemical analyses (Appendix 2) suggests that the pluton is composed predominantly of quartz monzonite with minor granite and granodiorite (Figure 2.2). These rocks are typically chlorite altered, hornblende-biotite quartz monzonite porphyry composed of approximately 10-15% quartz, 35-50% plagioclase feldspar, 20-45% alkali feldspar and 10-15% hornblende + biotite. Thin section examination shows that the matrix consists of 0.1-0.05 mm intergrown feldspar and quartz grains that are difficult to distinguish. Biotite occurs with chlorite altered rims; hornblende is typically unaltered.

The Mohawk pluton is not known to host significant concentrations of Cu or Au (VanTreeck et al., 2013). However, quartz + magnetite veinlets 1-2 mm thick are sporadic throughout drill hole intercepts and cause magnetic susceptibility up to 42 $x10^{-3}$ (SI). These magnetite bearing veins have only been observed in drill core and are not seen in outcrop. Non-veined plutonic samples yield magnetic susceptibility of 1-8 $x10^{-3}$ (SI), significantly higher than the typical surrounding metamorphic rocks (usually < 0.5 $x10^{-3}$ SI). Detailed

airborne geophysical maps outline a high magnetic body corresponding to outcrop of the Mohawk pluton.

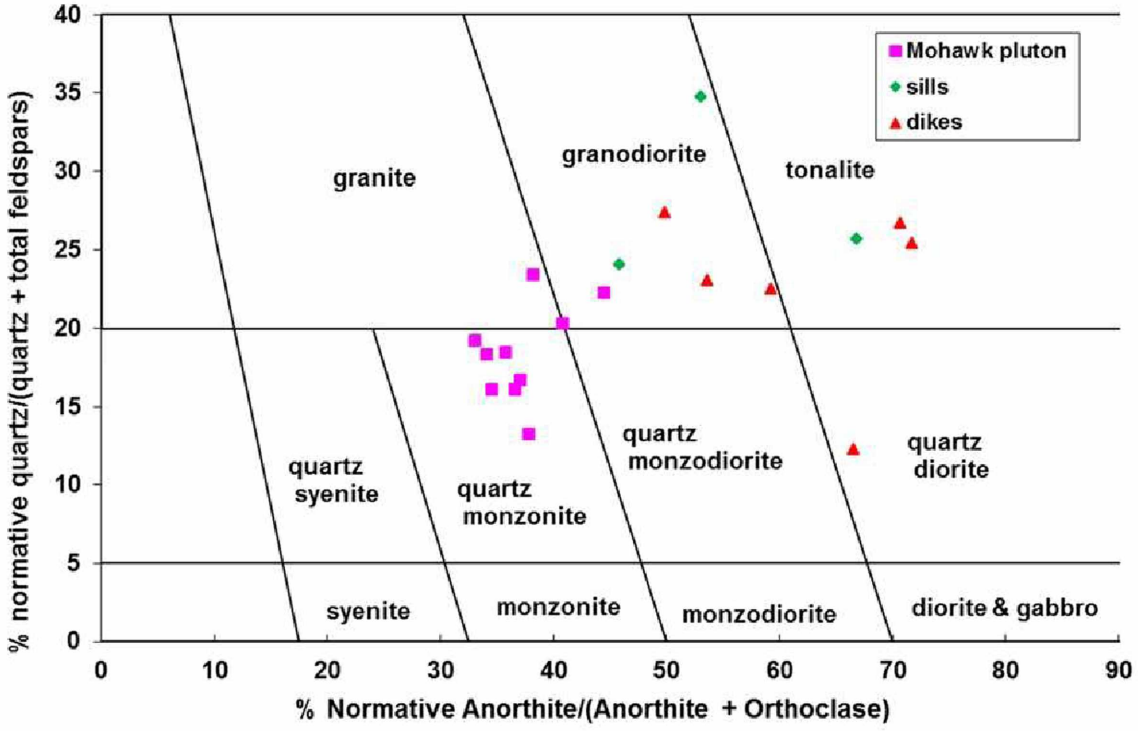


Figure 2.2: CIPW normative mineral compositions of felsic plutonic rocks from the Tetlin area on the plutonic rock classification diagram of Streckeisen and LeMaitre (1979). Normative mineralogy from XRF analyses (Appendix 2).

### 2.3.2 Felsic Sills (Ks) and Felsic to Mafic Dikes (Kd)

Tabular felsic bodies, largely sill-form, but also cutting across metamorphic foliation, are present in drill holes TET13128 (approximately half-way between the Mohawk pluton and the Peak deposit) and drill hole TET13116 (Figure 2.1). Based on drill core intercepts, these bodies are likely 15-70 cm thick. Mineralogically, the sills differ from the Mohawk pluton in that they contain larger (1-4 mm) and more abundant

quartz phenocrysts and generally less (5-10%) aphanitic groundmass. Based on their chemical compositions (Figure 2.2) their compositions are granodiorite to tonalite.

Float of fine-grained, sub-equigranular rocks occur sporadically in the northern part of the map area, largely in the 'Saddle skarn' fault block, but also in the southern part of the map area. Based on their textures and occurrences, they most likely represent igneous dikes. Dikes are clearly present in drill holes that intercept a rhyolite breccia body (Figure 2.1, Figure 2.3) in this same general area. Dikes as intercepted in drill core are typically 0.5-3 m wide and can be traced in drill core for more than 300 meters. Minerals in the dikes are rarely larger than 1 mm; aphanitic matrix comprises 0-20% of a dike. A single mafic dike was discovered in float in the northeastern part of the area (Figure 2.1.). This rock is primarily randomly-oriented phenocrysts of hornblende, plagioclase and other altered mafic minerals, set in a matrix of fine-grained calcite, epidote and chlorite. Based on their relative softness and ready effervescence when treated with HCl, most of the dikes are moderately to strongly altered.

Normative compositions of Chief Danny area dikes suggest compositions of granodiorite to tonalite are most common, but quartz diorite (and diorite?) are also present (Figure 2.2). Hydrothermal alteration precludes accurate rock name assignment based on chemical composition.

### 2.3.3 Igneous breccia

Approximately 200m northwest of the Saddle garnet + pyroxene skarn (Figure 2.1) a 50-70 meter wide breccia body of rhyolitic compositions was encountered in 2 drill holes

(Figure 2.3). This body has been referred to as a magmatic diatreme (VanTreeck et al., 2013). The pale colored rock consists of angular to sub-angular rhyolitic composition fragments 0.5 cm – 3 cm in diameter suspended in rhyolitic-composition matrix. Based on four acid digest geochemistry the rocks contain approximately 75% $SiO_2$ and are extremely depleted in Na2O (<0.1%) and slightly enriched in CaO (1-3%). This body does not contain abundant Au or Cu mineralization. It might represent a conduit for nearby felsic volcanic rocks.

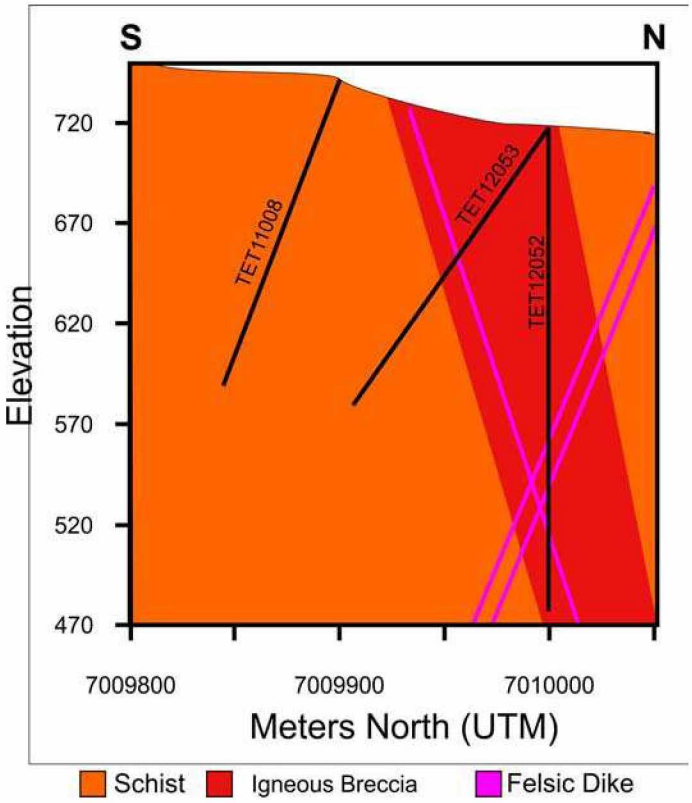


Figure 2.3: Cross section through felsic breccia body with cross-cutting, steeply-dipping dikes. See Figure 2.1 for location.

### 2.3.4 Volcanic Rocks (Kv)

Scattered exposures of late Cretaceous volcanic rocks occur on hilltops northwest of the Peak deposit; these appear to overly metamorphic rocks (Figure 2.1). The most northwesterly fault block in Figure 2.1 consists exclusively of volcanic rocks. Textures range from aphanitic to porphyritic with hornblende phenocrysts up to 1cm. Based on their compositions, these rocks range between basaltic andesite and rhyolite (Figure 2.4). Notably scarce are volcanic rocks of dacitic composition, a range which instead is occupied by many of the dikes and sills. Hornblende porphyry basaltic andesite has been dated as late Cretaceous (Chapter 5). Basaltic andesite is slightly weathered and commonly displays randomly oriented hornblende phenocrysts in an aphanitic groundmass (Figure 2.5). Where present in float, the volcanic rocks are distinguished by containing less than 50% phenocrysts and more than 50% aphanitic groundmass.

Rhyolitic volcanic rocks exposed on the surface are pervasively weathered and contain variably stretched-out clasts (Figure 2.6). I interpret these as higher in the volcanic stratigraphy because they are at higher elevation than the basaltic andesite outcrops in the same fault block. Contacts between rhyolite and the intermediate-mafic volcanic rocks were not identified in the field.

Tetlin felsic rocks (both plutonic and volcanic) have Rb, Nb and Y concentrations characteristic of arc related felsic igneous rocks (Figure 2.7). Tetlin mafic volcanic rocks (basaltic andesite) and the mafic dike have Nb, Ti, Zr and Y concentrations most like those of arc related basalts (Figure 2.8). Their sub-alkalic character (Figure 2.3) is also consistent with an arc-related origin. The spatial association of the more mafic and the felsic volcanic

rocks and the fact that both plot as 'arc-related' igneous rocks suggests that they are genetically related.

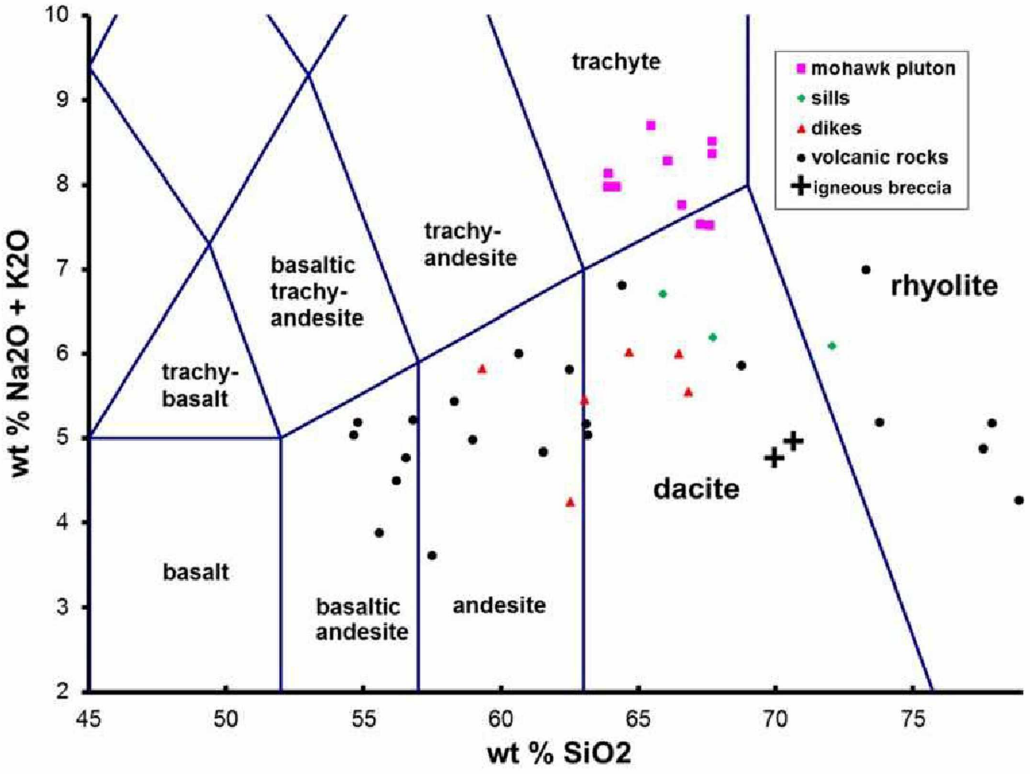


Figure 2.4: Total Alkali –Silica diagram with volcanic rock fields shown with XRF data for Tetlin area igneous rocks. Plutonic rock compositions are plotted for comparison. Data is in Appendix 2.1.

Figure 2.5: Typical hornblende pheric basaltic andesite.

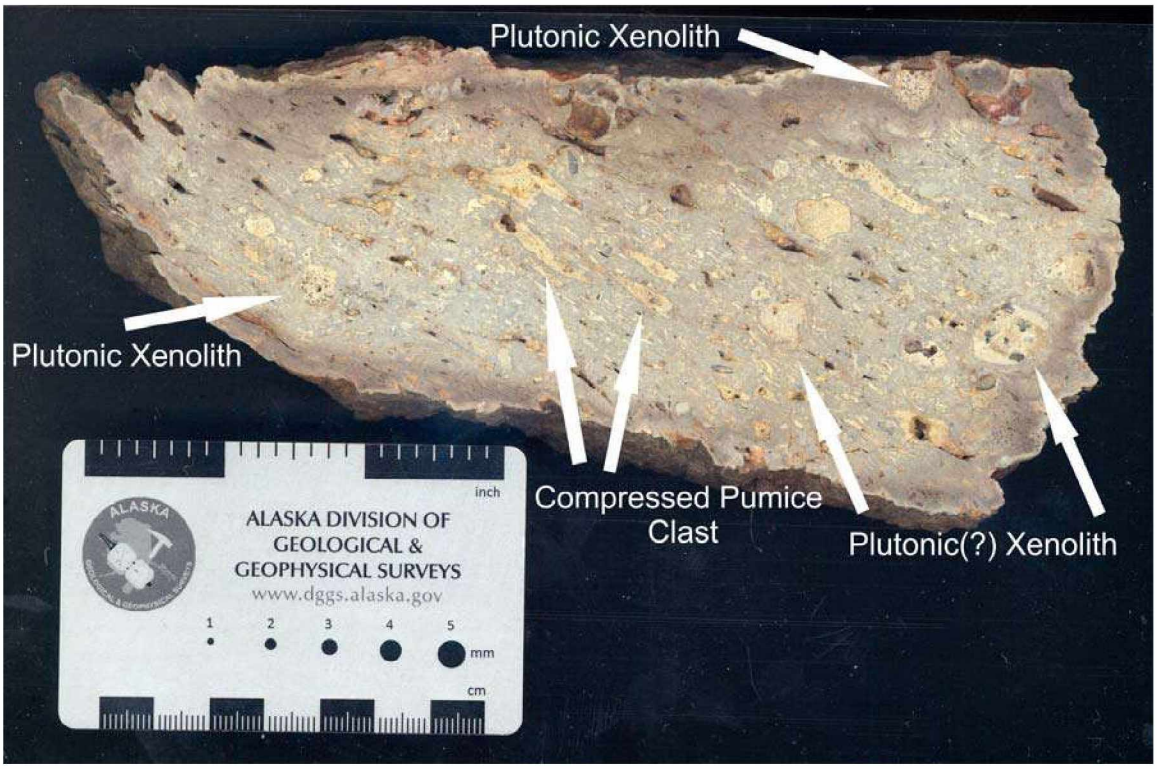


Figure 2.6: Polished sample of rhyolite with deformed pumice clasts.

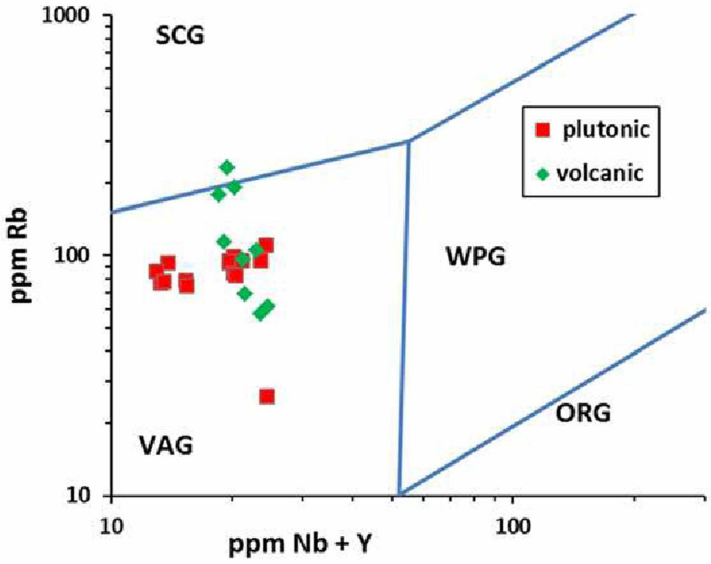


Figure 2.7: Tectonic discriminant diagram for felsic rocks (Pearce et al., 1984) with data from the Tetlin area (Appendix 2). VAG = Volcanic Arc granitoid; SCG = Syn-Collisional granitoid; WPG = Within-plate granitoid; ORG = Oceanic Ridge granitoid.

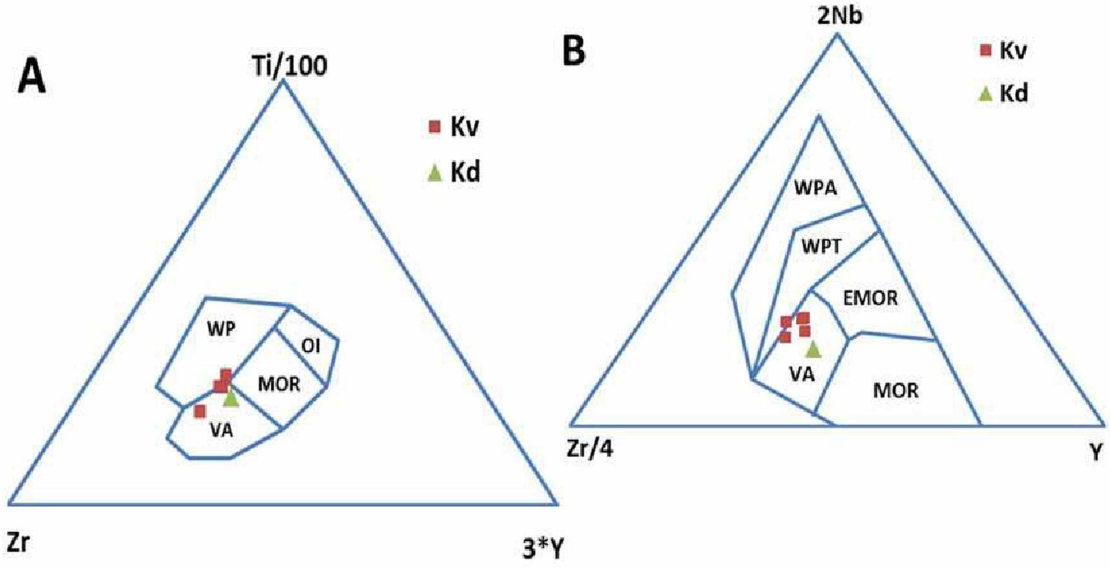


Figure 2.8: Tectonic discriminant diagrams for mafic rocks with data from Tetlin basaltic andesite (squares) and mafic dike (triangle). A: Ti-Zr-Y diagram (Pearce and Cann, 1973) B. Y-Zr-Nb diagram (Meschede, 1986). Abbreviations: WP = within-plate, WPA= within-plate alkali, WPT = within-plate tholeiite, VA = volcanic arc, MOR = mid-ocean ridge, OI = ocean island, EMOR = enriched mid-ocean ridge.

## 2.4 Metamorphic Rocks

### 2.4.1 Skarn (Ks)

Skarn is the most abundant Au-Cu-Ag bearing rock type at the Peak deposit and the Saddle skarn prospect. The Peak deposit skarn is dominated by randomly oriented, fine to coarse grained, high $Cl^-$, Fe rich amphibole (Figure 2.9 E,F, 2.12). It lacks garnet and contains at most traces of clinopyroxene (Figures 2.10, 2.11). The Saddle skarn contains abundant calcic pyroxene and garnet (Figure 2.9 A, B) with interstitial amphibole. The Mohawk skarn located SE of the Mohawk pluton (Figure 2.1) contains no garnet and is roughly half pyroxene and half amphibole.

Although the pyroxene $\pm$ garnet Saddle and Mohawk skarns resemble typical skarns, the virtual lack of calcic pyroxene and complete absence of garnet in the Peak deposit set it apart. Of 25 Peak calc-silicate-bearing thin sections, only five contained clinopyroxene. In both the Saddle and Mohawk skarns amphibole displays typical 'retrograde' textures; interstitial (Figure 2.9 A, B) and as psuedomorphs of pyroxene (Figure 2.9 C, D). The Peak deposit amphibole is fine (1 mm) to coarse (up to 1cm) grained. Pyroxene replacement textures occur (Figures 2.10, 2.11) but are uncommon. Unfortunately, because Fe-rich clinopyoxenes in calcic skarns are commonly elongate to acicular (unlike the 'normal' box shapes) it may be difficult to distinguish between an acicular primary skarn amphibole and an acicular secondary amphibole which has replaced an acicular pyroxene.

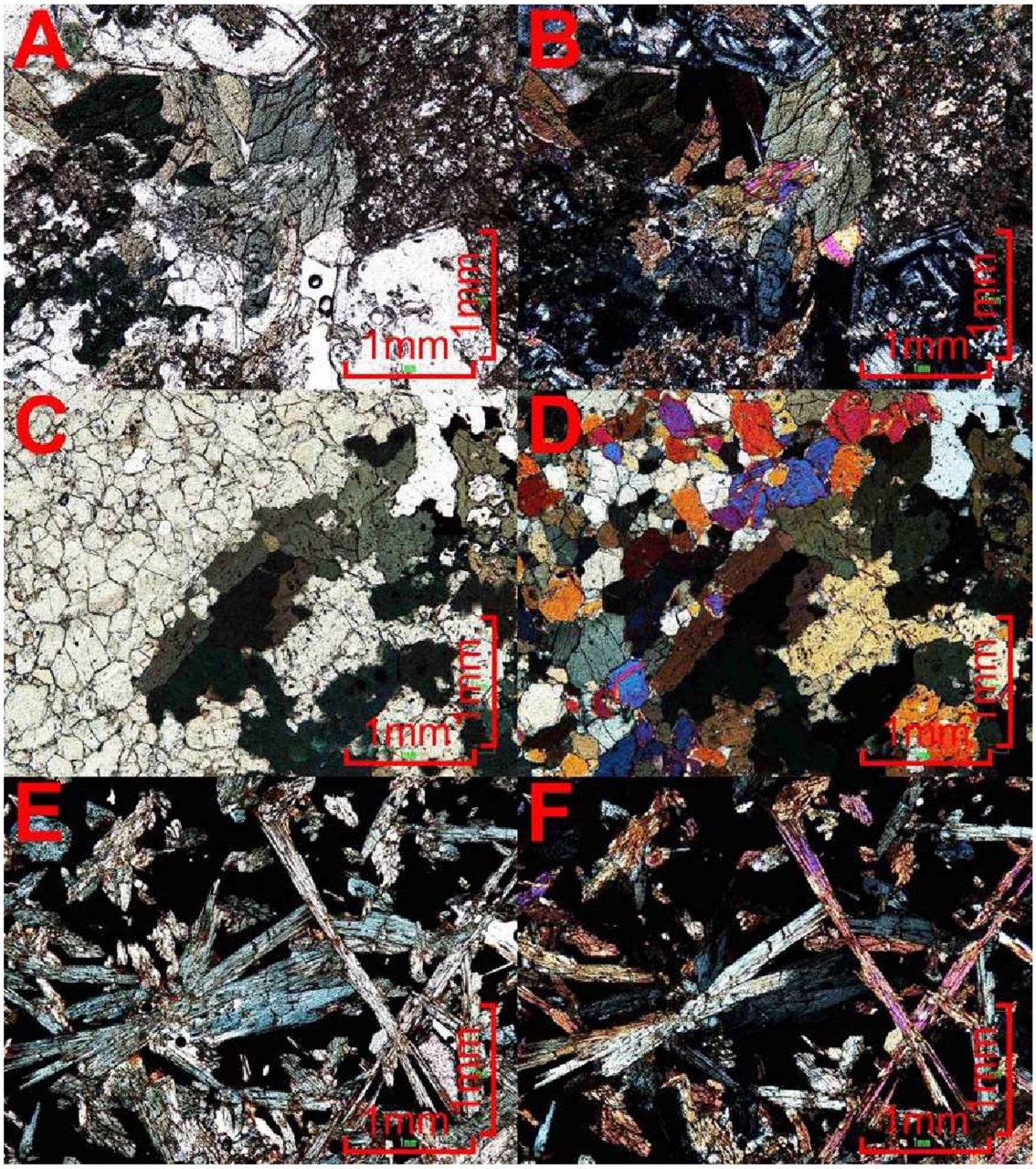


Figure 2.9: Photomicrographs of skarn samples from the Chief Danny exploration area. A) Pyroxene (altered) + garnet + amphibole skarn from Saddle skarn (plane polarized light). Amphibole and calcite are interstitial. B) same as A with crossed polars. C) Clinopyroxene + amphibole skarn from Mohawk skarn (plane polarized light). D) same as C with crossed polars. E) Amphibole skarn from Peak deposit (plane polarized light). Amphibole is coarse grained and randomly oriented, showing no evidence for replacement of previous calc-silicate minerals. F) Same as E with crossed polars.

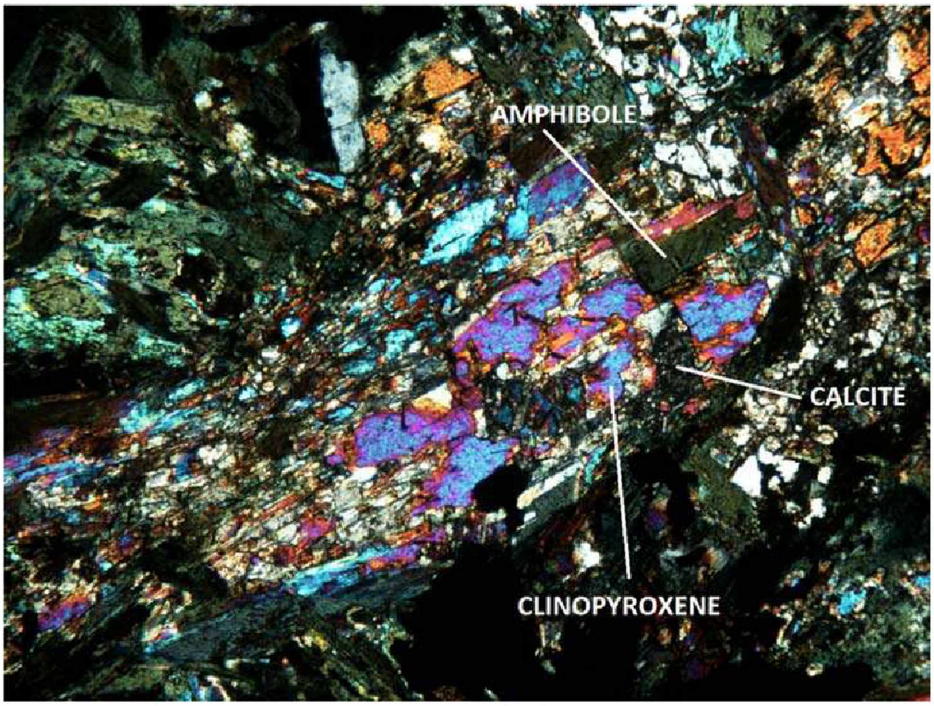

Figure 2.10: Crossed polars example of rare hedenbergitic clinopyroxene from Peak deposit undergoing retrograde replacement by amphibole + calcite + quartz. Field of view = 1.5 mm.

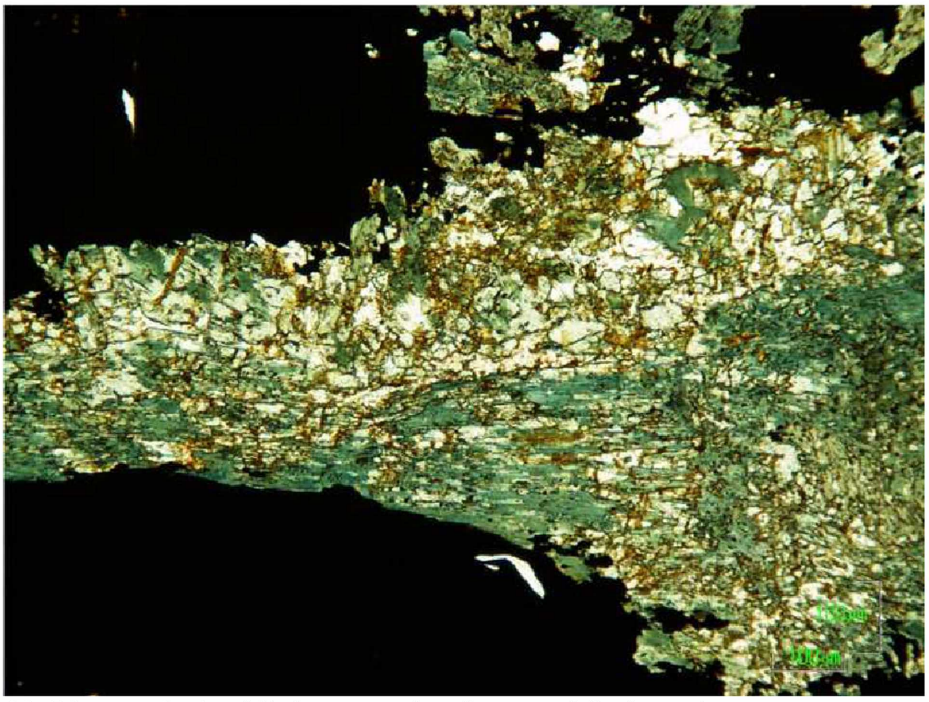
Figure 2.11: Plane polarized light example of an amphibole replacement texture of in Peak deposit skarn. The amphibole aggregate (green) present with intergrown pyroxene (colorless) and minor calcite + quartz displays an overall pyroxene (box) shape.

Figure 2.12: Typical core from Peak deposit Au-Cu skarn. On left coarse amphibole is randomly oriented, suggesting direct replacement of unknown, but likely layered, protolith. On right is finer grained amphibole skarn with chalcopyrite > pyrrhotite >arsenopyrite. Core width = 6cm.

Calcic amphiboles are complex solid solutions generally described by the formula $(Na,K)_{0-1}Ca_2(Mg,Fe,Al,Mn,Ti)_5(Si,Al)_8O_{22}(OH,Cl,F)_2$. Calcic amphiboles are broken into two major groups: those with Na+K < 0.5 (Figure 2.13A) and those with Na+K > 0.5 (Figure 2.13B). Both groups are then subdivided based on the relative amounts of Si and the ratio of $Mg/(Mg + Fe^{2+})$. Calcic amphiboles with Si < 7.5 atoms per formula unit are commonly referred to as 'hornblende' although hornblende s*ensu stricto* encompasses a restricted composition, including Na+K < 0.5 (Figure 2.13A).

Quantitative microprobe analyses of 16 amphibole-rich Peak samples show that the majority are classified as hastingsite with lesser ferro-edenite and minor hornblende (*sensu stricto*) and ferro-actinolite (Figure 2.13). This is consistent with a strong blue-brown pleochroism exhibited by the typical amphiboles. Semi-quantitative (Energy dispersive analysis) microprobe analyses of an additional 20 amphiboles from the Saddle and Mohawk skarns suggest these amphiboles are also hastingsite. For comparison, amphiboles from the gold skarn at Fortitude, Nevada (an amphibole rich distal gold skarn) are almost exclusively actinolite (Figure 2.13; Myers, 1994) whereas other Alaskan skarns possess amphibole compositions that overlap those from Tetlin. Tetlin skarn amphiboles also possess high Cl contents (Figure 2.14).

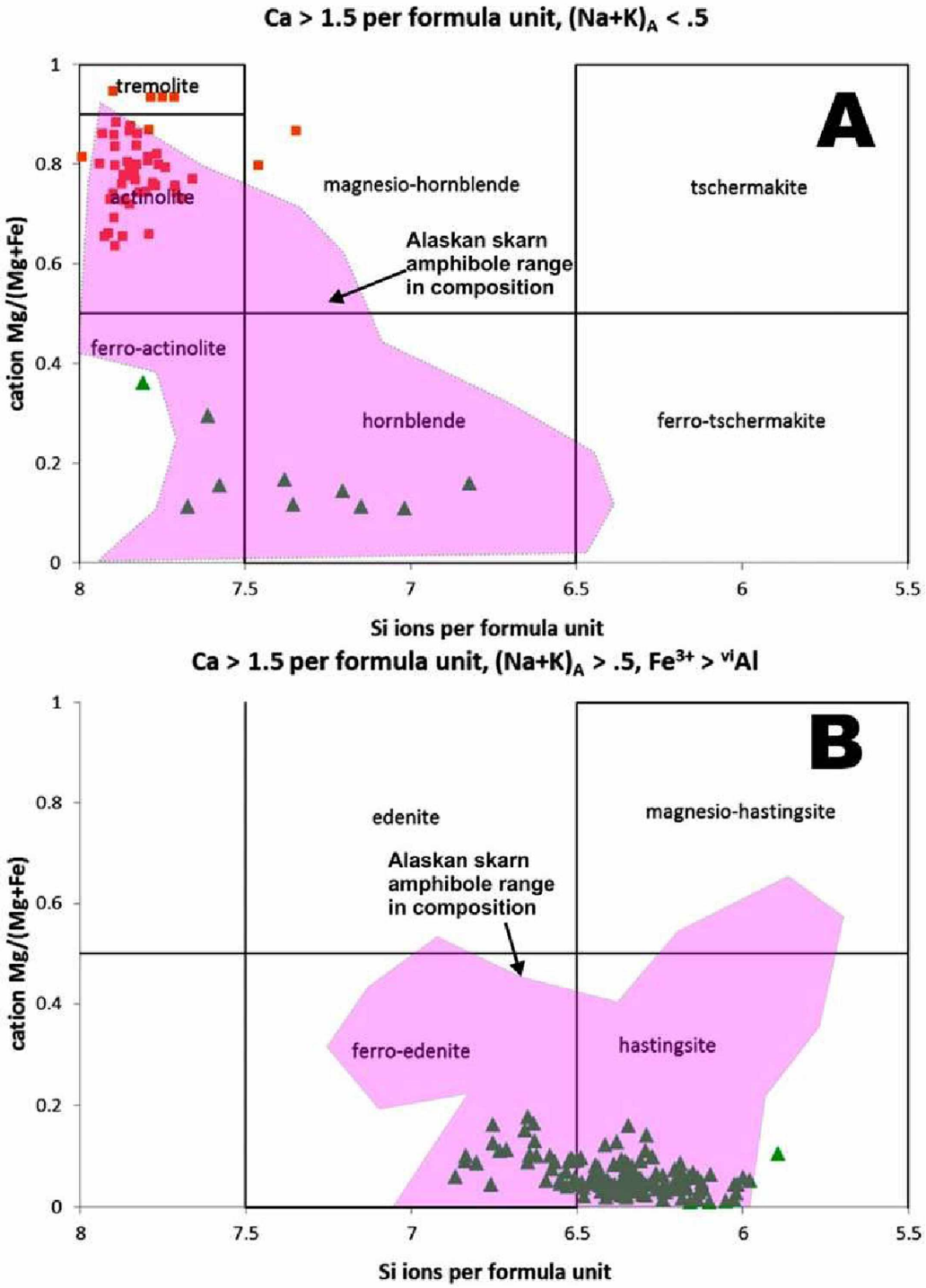


Figure 2.13: Classification diagrams for calcic amphiboles from the Peak skarn with data from the Fortitude skarn (Myers, 1994) and with range for other Alaskan skarns (Newberry, et al., 1997). Amphibole classification from Deer et al., 1997. Formula unit is based on 23 oxygens.

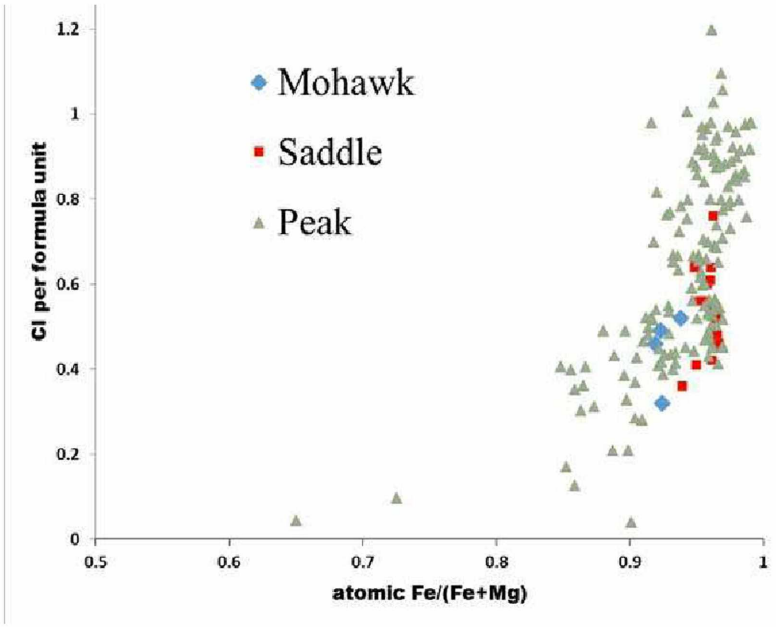


Figure 2.14: Atomic Cl per 23 oxygen formula unit vs. Fe/Fe+Mg for amphiboles from the Peak, Mohawk, and Saddle prospects. Data in Appendix 2

Skarn clinopyroxene at all three Tetlin skarns is fine-grained, usually 0.5-0.3 mm. Approximately 60 pyroxene grains from 9 different thin sections from Peak, Mohawk and Saddle were analyzed with the electron microprobe (EDS). Skarn clinopyroxene compositions are commonly expressed as mole percent of the $Fe^{2+}$ (hedenbergite =Hd) component. Based on 254 analyses (Table 2.1; Appendix 3.1) Peak pyroxenes have compositions of $Hd_{33-95}$ (average $Hd_{70}$); Mohawk pyroxenes have $Hd_{49-96}$ (average $Hd_{83}$); Saddle pyroxenes have $Hd_{26-70}$ (average $Hd_{48}$) (Figure 2.15). Histograms of clinopyroxene compositions show unimodal distributions for Peak and Mohawk. Pyroxene compositions at Saddle are bimodal, with modes at $Hd_{30-40}$ and $Hd_{60-70}$, making the 'average' misleading (Figure 2.16). The most common Peak pyroxene compositions are $Hd_{70-80}$; most common at Mohawk are $Hd_{88-96}$ (Figure 2.16). Pyroxene compositions approaching pure

hedenbergite are relatively common at Mohawk and the bulk of pyroxenes from Peak are hedenbergite-rich.

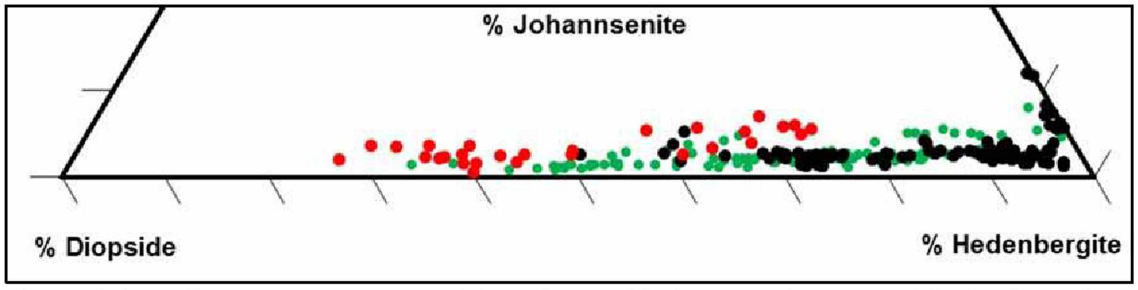


Figure 2.15: Clinopyroxene compositions from Chief Danny skarns: Saddle (red), Mohawk (black) and Peak (green) skarns based on EDS microprobe analyses plotted in terms of the major pyroxene endmembers. Each dot represents one analysis. Tick spacing is 10%. Data is in Appendix 2. Johannsenite = Jo = $CaMnSi_2O_6$, Diopside = Di = $CaMgSi_2O_6$, Hedenbergite = Hd = $CaFeSi_2O_6$

Table 2.1: Average pyroxene compositions from the Chief Danny area, presented as mole % of the major end-members

| Thin section | Location | % Jo | % Hd | %Di | N |
|---|---|---|---|---|---|
| 67 | Peak | $4 \pm 2$ | $75 + 14$ | $21 \pm 15$ | 25 |
| 72 | Peak | $2 \pm 1$ | $68 \pm 13$ | $30 \pm 14$ | 23 |
| 82 | Peak | $1 \pm 0.5$ | $53 \pm 6$ | $46 \pm 7$ | 23 |
| 56 | Peak | $1 \pm 1$ | $81 \pm 4$ | $17 \pm 4$ | 25 |
| 73 | Peak | $2 \pm 0.5$ | $71 \pm 3$ | $27 \pm 3$ | 20 |
| 65 | Mohawk | $3 \pm 1$ | $88 \pm 3$ | $9 \pm 3$ | 26 |
| 66 | Mohawk | $5 \pm 3$ | $89 \pm 7$ | $6 \pm 8$ | 30 |
| 64 | Mohawk | $2 \pm 1$ | $69 \pm 7$ | $28 \pm 7$ | 31 |
| 84 | Mohawk | $2 \pm 0.5$ | $87 \pm 8$ | $11 \pm 8$ | 25 |
| 205 | Saddle | $3 \pm 2$ | $48 \pm 14$ | $49 \pm 15$ | 28 |

Notes: uncertainty is one standard deviation; N = number of analyses; Jo = Johannsenite, Hd = Hedenbergite, Di = Diopside

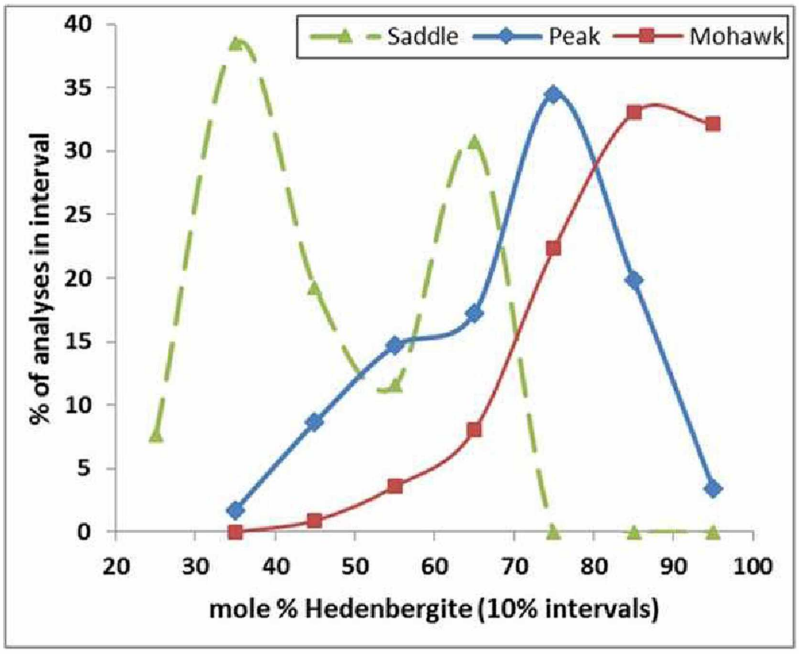


Figure 2.16: Histograms of pyroxene compositions for Peak, Mohawk and Saddle, showing differences in most abundant compositions for the three skarns.

Garnet is so far restricted to the Saddle skarn. Garnet is fine grained (75-200 μm) and exhibits anisotropism, as commonly seen in skarn garnet. Based on a small number of analyses from Saddle, garnet compositions vary tremendously (Figure 2.17) from essentially pure andradite ($Fe^{3+}$ end-member) to nearly pure grossularite (Al end-member). Mn contents are very low and Mg is below detection.

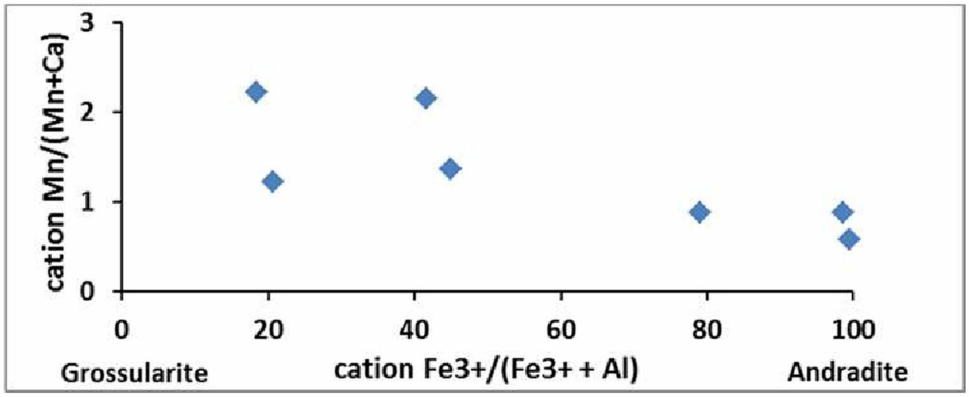


Figure 2.17: Compositions of garnet from the Saddle occurrence based on semi-quantitative microprobe analyses. Vertical axis is % Mn/(Mn+Ca).

Chlorite is a minor constituent of the silicate assemblage at the Peak deposit. It is typically seen as a retrograde alteration of amphibole. Chlorite probably constitutes less than 5% of Peak Deposit. It is typically associated with late quartz veins as radiating blooms which cut skarn and replace amphibole. Chlorite is fine grained (<50 μm).

### 2.4.2-Calc-silicate Hornfels

Laminated calc-silicate bearing rocks occur above the Peak deposit amphibole skarn. Thin (2mm- 1 cm thick) green layers containing randomly oriented, fine grained, amphibole, plagioclase, and clinozoisite are interlayered with micaceous quartzite (Figure 2.18). It is unclear to what extent these rocks represent isochemical contact metamorphism and to what extent they have experienced metasomatism. They appear to be relatively rare in the region, however.


Figure 2.18: Calc-silicate hornfels as exposed in drillcore. The yellow-green areas consist of fine-grained calc-silicate minerals.

### 2.4.3 Disseminated to Massive Sulfide

Massive to semi-massive sulfide and fracture hosted sulfide are common in the Peak deposit and the Discovery Pb-Zn-Sb system, respectively (Figure 2.1). In the Peak deposit massive sulfide occurs both with and without quartz (Figure 2.19). Quartz is randomly oriented, coarse and euhedral. Pyrrhotite is the predominant sulfide with lesser chalcopyrite and galena in both. No carbonate front has been identified to provide conclusive evidence that the sulfide has replaced carbonate. Fracture hosted sulfide is medium to very fine-grained pyrrhotite, galena, sphalerite and ambiguous black sulfide (Figure 2.20). Massive sulfide does not host significant Cu or Au grades. Coarse grained galena and marcasite is predominantly found in late sulfide veins which cut skarn, massive sulfide and host metamorphic rocks (Figure 2.20). Galena is also found as veins in coarse quartz + pyrrhotite rock updip of the Peak deposit.


Figure 2.19: Coarse grained, euhedral quartz + pyrrhotite (Po) ± chalcopyrite found up dip of the Peak deposit. Core diameter = 6cm.

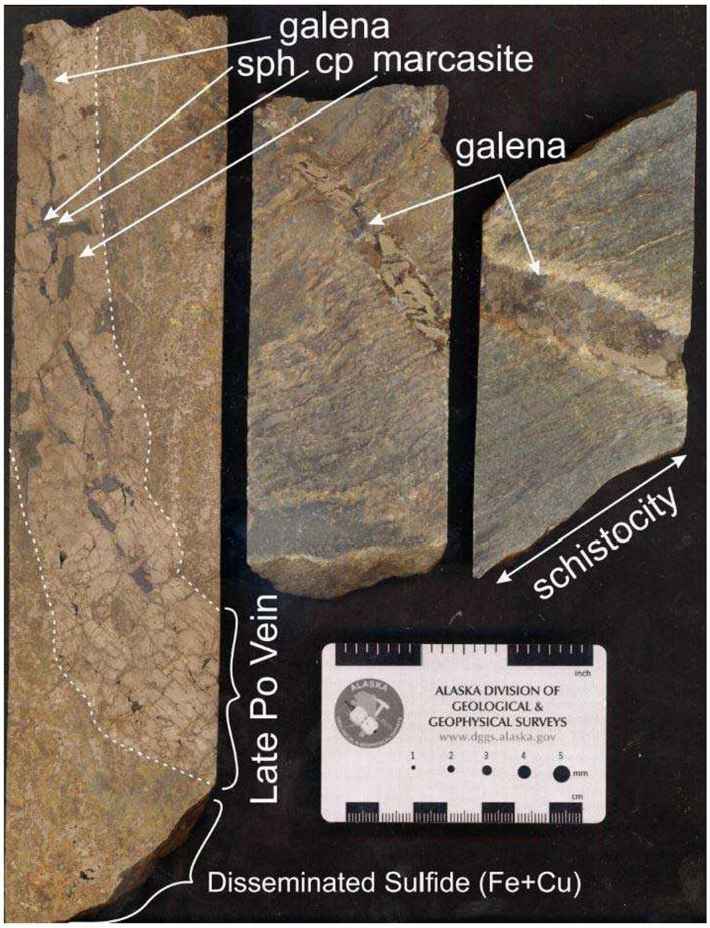


Figure 2.20: Variation in textures and mineralogy of fracture hosted sulfide veins which cut skarn, sulfide rock and schist.

### 2.4.4 Marble

Marble is rare in the Chief Danny exploration area. It is intercepted in core in the Peak deposit area and found on the surface on the eastern end of the Chief Danny exploration area (Figure 2.1). The unit is white to cream colored with variable amounts of interlayered muscovite. Drill core intercepts are up to 2 meters thick. Float boulders of nearly pure marble are more than a meter in diameter. Rare outcrops of marble show isoclinal recumbent folding. These recumbent marble folds are 0.5 to 1 meter in thickness

are cut by normal faults (e.g. Figure 2.21). Pure marble grades into calcareous schist for 10-30 cm and then into quartz schist (e.g. Figure 2.21).

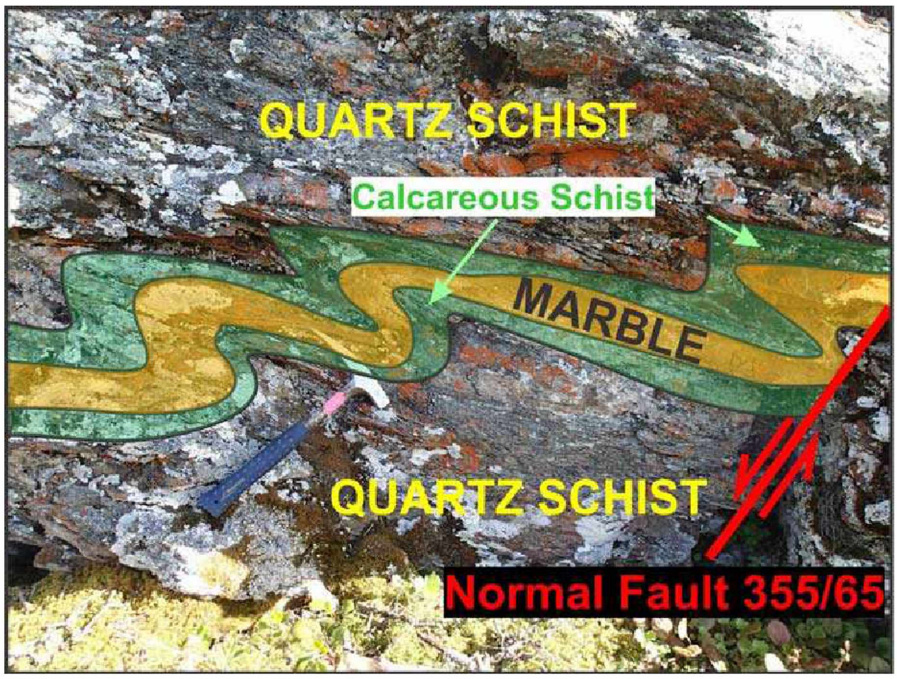


Figure 2.21: Photo of lightly folded marble grading into calcareous schist and surrounded by quartz schist. North striking normal fault cuts and displaces marble approximately 20cm.

### 2.4.5 Quartz-rich schistose rocks

Metamorphic rocks varying between schist and quartzite dominate the metamorphic package. This metasedimentary unit has fold limb amplitudes ranging from centimeters to hundreds of meters (e.g. Figure 2.1). Foliation is parallel to perpendicular to lithologic contacts. Schistose rocks are typically quartz rich with foliation defined by variable amounts of biotite and muscovite. This unit contains minor amounts of augen gneiss identified in outcrop, too small in extent to be mapped separately. Schist typically contains 0-5% garnet. The contacts between metasomatic rocks and host schistose rocks are sharp.

Quartzite and quartz schist, including rocks adjacent to amphibole skarn, exhibit no obvious hydrothermal alteration. However, such alteration is present in feldspathic schist, seen as chlorite 'blooms' interlayered within quartz rich schist. Garnet in these rocks is partially replaced by quartz + feldspar $\pm$ epidote $\pm$ pyrrhotite. Sulfide constitutes <1% of these rocks.

### 2.4.6 Amphibolite

Amphibolite occurs to the west of the Peak deposit near and within the Discovery fault hosted Pb-Zn-Sb system (Figure 2.1). This unit dips to the north and has been intersected in multiple drillholes in the Discovery zone area (Figure 2.23). Individual amphibolite layers are commonly 3-6 m thick (Figure 2.23) but zones containing abundant amphibolite are up to 50 meters thick (Figure 2.1). Amphibolite is weakly to moderately magnetic (0.1-1.2 x $10^{-3}$ SI) and is well foliated. The unit is fine grained, although foliation defined by hornblende is distinguishable in hand sample. Amphibolite is typically 70-80% hornblende, 20% plagioclase, 0-5% quartz, and 0-7% garnet. The protolith is inferred to be a mafic rock of some variety (flow, sill or dike) based upon basaltic chemical composition, e.g., low $SiO_2$ (48-58 wt%) and high $TiO_2$ (>1 wt %; Appendix 2.1). Amphibolite lacks the $Cl^-$ concentrations characteristic of metasomatic amphibole at the Peak deposit (Appendix 2.1).

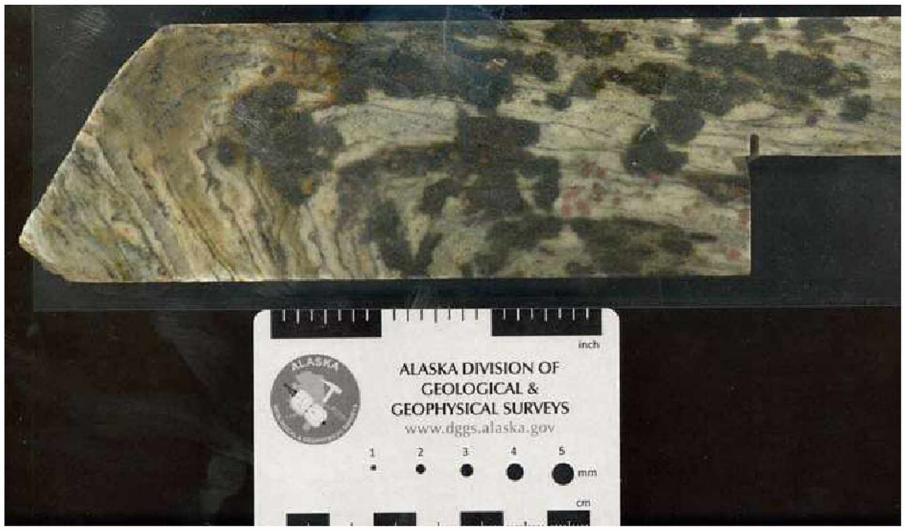


Figure 2.22: Drillcore showing alteration of feldspathic schist interlayered with micaceous quartz schist. Chlorite replaces feldspar and garnet is replaced by quartz + albite ± epidote.

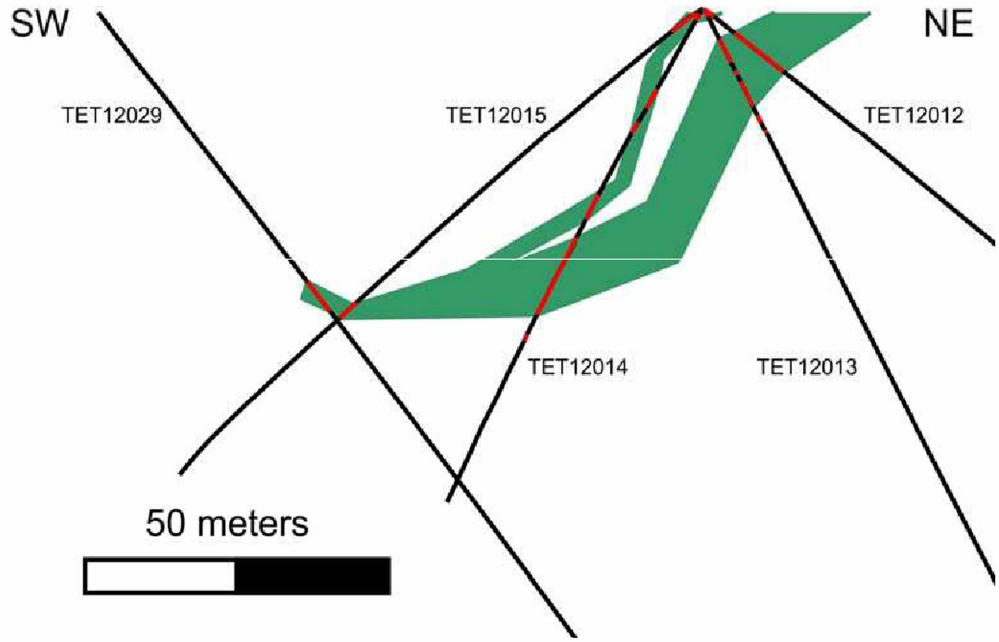


Figure 2.23: NNE-SSW cross section through Discovery zone (Figure 2.1) showing complex folding, bifurcation, and rapid changes in unit thickness. Red indicates amphibole intercepts in drill core; green is inferred amphibolite and white is undifferentiated schist and gneiss.

### 2.4.7 Hornblende Plagioclase Gneiss

Hornblende gneiss contains variable amounts of plagioclase, hornblende (primary and secondary), biotite and muscovite. Banding is defined by variation in modal abundance of hornblende versus quartz and feldspar. Foliation is defined by muscovite and biotite, which also form discrete mineralogical bands. These rocks are calcium rich (4-15 wt %; Appendix 2.1) but lack calcite. Plagioclase and hornblende are the predominant calcium-rich minerals. Primary hornblende is green and fine grained. Rare secondary hornblende is high in $Cl^-$, black and coarse grained.

Hornblende gneiss is only present northwest of the Discovery zone and surrounding the Mohawk pluton. Chemical compositions indicate it is relatively Ca-rich (5-12% CaO) but has intermediate silica (55-75 wt% SiO2) contents. Most likely it represents some variety of meta-igneous rock, as it is too mafic in composition for a sedimentary rock and in a few cases displays gradational contacts with amphibolite.

## 2.5 Discussion

I have called the host rock of the Peak deposit 'skarn' based on circumstantial evidence for the replacement of carbonate rocks by coarse grained calcic amphibole. In core logging and surface mapping no marble front or transition from skarn to unaltered protolith was encountered. Although marble, presumably the protolith of Peak, is in the exploration area, there is no obvious transition from amphibole $\pm$ sulfide rock to marble.

The virtual absence of pyroxene and garnet in the Peak deposit distinguishes it from other skarns in the Tetlin area. At Peak the dominant amphibole is aluminous, which complicates formation by replacement of carbonate rocks. Aluminum is generally

considered an 'immobile' component, but recent work indicates it becomes appreciably soluble in high-Cl fluids, probably due to formation of Na-Al-OH complexes (Tagirov and Schott, 2001). Further, Al-rich skarn amphiboles are relatively common (Figure 2.13B), so whatever conditions are required for their formation are not unusual. If, on the other hand, the aluminum is derived from the protolith, then micaceous marble, the typical type seen in the Tetlin area, is a logical host.

Clinopyroxene is present (albeit rare) in the Peak mineralization and it is unclear how much of the acicular amphibole at Peak is derived from acicular pyroxene. The garnet + pyroxene Saddle skarn and the pyroxene + amphibole Mohawk skarn both demonstrate that 'normal' skarns occur in the region. I propose that massive amphibole rock at Peak represents the most distal expression of skarn in the area. That is, I suggest that garnet-pyroxene skarn likely lies under Peak, perhaps at great depth.

An alternate hypothesis is that Peak was an amphibolite which has undergone extensive contact metamorphism. Amphibolite, however, typically contains 6-9% MgO, 0.2-0.7% K2O and 2% TiO2, whereas Peak amphibole typically contains 0.5-1.5% MgO, 1.8-2.5% K2O and 0.2-0.3% TiO2. Optically, amphibole in the amphibolite appears to most resemble hornblende *(sensu stricto)* a composition rarely seen at Peak (Figure. 2.13). Further, such an explanation does not account for the abundant massive to semi-massive sulfide interlayered with amphibole rock at Peak.

In sum, it is most likely that the amphibole-rich rock present with massive and semi-massive sulfide at Peak is some variety of carbonate replacement, i.e., 'skarn.'

Treating pyroxene at the Peak deposit as pure hedenbergite and garnet at the Saddle skarn as pure andradite (Figures 2.16, 2.17), I modeled skarn formation conditions in terms

of oxygen fugacity and temperature (Figure 2.24). I used ferroactinolite stability to model amphibole, because stability data is not available for the more complex amphibole compositions that characterize Peak (Figure 2.13). Ferroactinolite is only stable under low $fO_2$ and relatively low temperature conditions (Jenkins and Bozhilov, 2003) and it is unclear to what extent these conditions characterize Peak amphibole. The fact that (based on stoichiometric considerations) Peak amphiboles contain a significant amount of $Fe^{3+}$ implies stability of these amphiboles to conditions more oxidizing than ferroactinolite stability. Consequently, the yellow region of Figure 2.24 likely represents a minimum region for conditions present during formation of the Peak deposit.

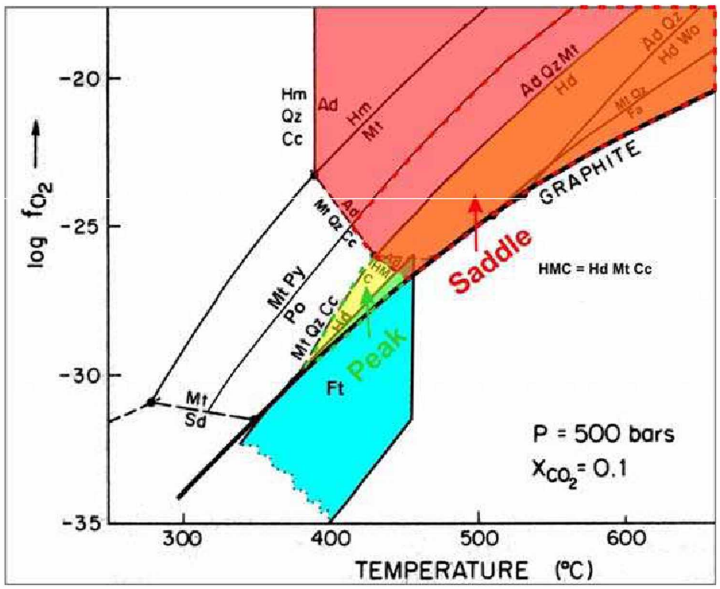


Figure 2.24: Temperature vs log oxygen fugacity diagram showing controls on skarn silicate, oxide and sulfide mineral assemblages. Hm = hematite; Qz = quartz; Cc = calcite; Ad = andradite; Mt = magnetite; Py = pyrite; Po = pyrrhotite; Hd = hedenbergite; Wo = wollastonite; Fa = fayalite; Sd = siderite; Ft = ferroactinolite. Adapted from Einaudi et al. (1981), Deer et al. (1997), and Jenkins and Bozhilov (2003).

The Saddle skarn, containing pure andradite (as well as garnet with significant grossular component), probably requires a higher temperature during formation (> 450°C) than does amphibole skarn. The presence of pyrrhotite in Saddle sulfide provides an upper

boundary of possible fO2, consistent with the presence of Fe-rich pyroxene (Figs. 2.16, 2.24). Andradite stability dictates the lower temperature stability while graphite provides the lowest fO2 boundary.

The formation of amphibole in skarns was traditionally thought to be due to convection of cooler meteoric water into the system (e.g. Einaudi et al., 1981). More recent studies suggest that it might be due to influx of relatively cool magmatic fluids (e.g., Meinert et al., 2005). Formation of amphibole at the Peak, Saddle and Mohawk skarns is compatible with both models. The high Cl contents of the amphiboles, however, strongly suggest that a magmatic fluid was a major component.

Almost certainly relatively low oxidation state was a controlling factor in silicate assemblages in the Chief Danny exploration area. Tetlin area skarns contain pyrrhotite, high-iron pyroxene, and high- to low-iron garnet, whereas typical Cu skarns contain pyrite, low-Fe pyroxene, and high-Fe garnet (Einaudi et al., 1981). The slightly more Fe-poor pyroxene at Saddle, combined with the presence of $Fe^{3+}$-rich garnet is compatible with the Saddle skarn representing a higher oxidation state system than either Peak or Mohawk. Alternatively, the different pyroxene compositions might reflect spatial zoning relative to source.

The systematic changes in pyroxene composition can be due to a variety of causes, but one pattern seen world-wide is increasing Fe/Mg with increasing distance from fluid source (e.g., Deal, 2012). If this is the case in the Tetlin area, and all Chief Danny area skarns formed from the same intrusion, then Saddle is the most proximal, Mohawk is most distal and Peak is in-between. Depending on the amount of movement on the faults between the Saddle, Peak, and Mohawk blocks (Figure 2.1), this could be accomplished by a single

unexposed body in the Peak structural block, but closer to Saddle than to Peak. Certainly the Mohawk pluton would not satisfy the apparent zoning requirements, as it is closest to Mohawk and farthest from Saddle. Furthermore, radiometric dating (Chapter 6) indicates that the Mohawk pluton and the Peak Deposit are not contemporaneous. Elemental zoning in the Peak Deposit (Chapter 3) also suggests a fluid source in a completely different direction from the Mohawk pluton. Consequently, garnet and pyroxene compositional data require at least one 'hidden' pluton in the Chief Danny area to be responsible for the 3 different skarns.

## Chapter 3 Mineralization and Zoning

### 3.1 Introduction

The Peak deposit is defined by lithologically controlled high concentrations of gold, silver, copper, bismuth ± tellurium, tungsten, cobalt, nickel, cadmium, lead, antimony and zinc. Ore is restricted to amphibole- and sulfide-rich rocks, but not all such rocks contain high metal values. These amphibole-and sulfide-rich rocks are interlayered with quartz rich metamorphic rocks (micaceous schist to quartzite), generally with sharp contacts. The purpose of this chapter is to describe the various styles of mineralization at Peak hosting Au-Cu ore and Pb-Zn-Sb veins and to describe the morphology and zoning of the ore body.

Although skarns can contain amphibole, 'skarn' consisting primarily of amphibole is rarely reported in the literature. Since Peak is distinctly different from most skarns, part of this chapter focuses on the nature of the calcic amphibole mineralization, its texture and chemistry. In addition I compare Peak to other skarns on the property as evidence for skarn formation on property and how Peak is different in texture and mineralogy from the Saddle and Mohawk skarns.

The most common sulfide and ore minerals which I identified at Peak (in decreasing order of abundance) are pyrrhotite, chalcopyrite, arsenopyrite, native bismuth, hedlyite [$Bi_7Te_3$], galena, sphalerite, gold-electrum, marcasite, pyrargyrite [$Ag_3SbS_3$], cassiterite, breithauptite [(Ni,Fe)Sb], ulmannite [(Ni,Co)SbS], greenockite [(Cd,Fe)S] and jonassonite [$AuBi_5S_4$].

Folding of metamorphic units plays a major role in the morphology of the Peak deposit. The morphology of the ore body has been described as dipping to the northeast

(VanTreeck et al., 2012; VanTreeck et al., 2013). Two major cross sections through the Peak deposit are presented to show an apparently folded body. Unfortunately, most drill hole logs 2011-2013 were not useful because many units (including skarn, calc-silicate hornfels, schist and gneiss) were logged as 'quartz mica schist'. I relogged 18 complete drill holes to construct lithologic cross sections. I combined drill hole descriptions, XRD analysis and petrography to assist in making lithologic identifications for fine grained green rocks.

This work relies heavily on mineralogic identifications made through a combination of petrographic analysis (reflected and transmitted light microscopy), electron microprobe analysis, and x-ray diffraction analysis.

## 3.2 Sulfide and Metal Mineral Textures and Occurrences

### 3.2.1 Pyrrhotite and Marcasite

Pyrrhotite ($Fe_{1-x}S$) is the predominant sulfide in the Peak skarn and sulfide replacement mineralization. Marcasite is present as a supergene phase replacing pyrrhotite (Figure 3.1A).

Pyrrhotite at Peak occurs as veins and disseminations, and as semi-massive and massive sulfide in skarn and calc-silicate hornfels. At the Saddle skarn it occurs as fine inclusions in pyrite (Figure 3.1B) and in altered feldspathic schist.

### 3.2.2 Pyrite

Pyrite ($FeS_2$) does not occur at Peak. However, it is the predominant sulfide (along with chalcopyrite) at the Saddle skarn and in igneous breccia. Pyrite also occurs in the Discovery fault-hosted Pb-Zn-Sb veins.

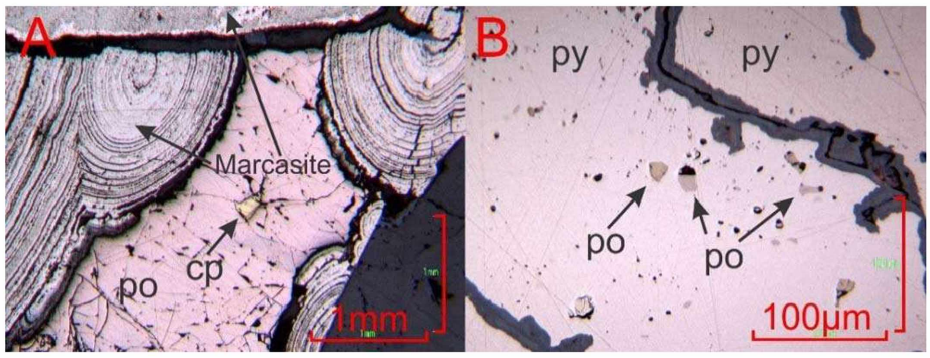


Figure 3.1: Photomicrographs illustrating pyrrhotite textures. A) marcasite replacing pyrrhotite (po) with inclusion of chalcopyrite (cp). B) inclusions of pyrrhotite and chalcopyrite in pyrite (py).

### 3.2.3 Copper Minerals

Chalcopyrite ($CuFeS_2$) is the predominant copper mineral in the Chief Danny area. In copper rich skarn it is nearly as abundant as pyrrhotite and occurs as disseminated or banded grains (< 0.1 mm to >1cm). Pyrrhotite- chalcopyrite rich bands commonly alternate with amphibole –rich rock at Peak (Figure 3.2). Native copper rarely occurs in the oxide cap of the Peak deposit.

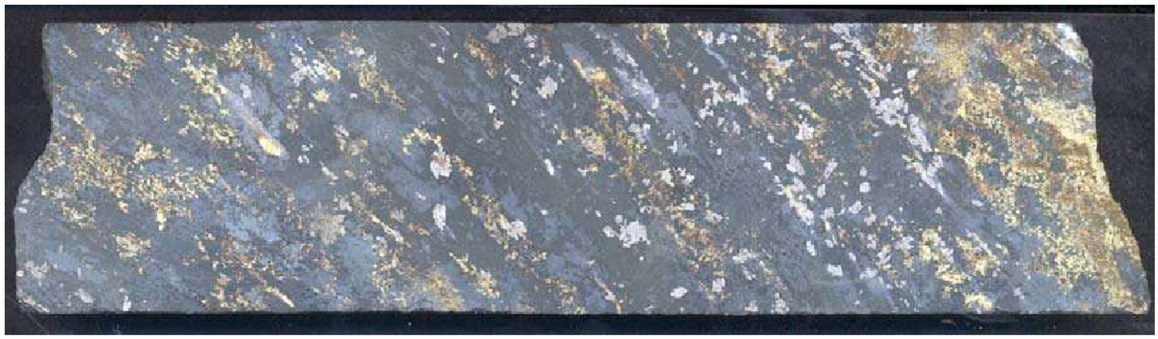

Figure 3.2: Core from copper rich amphibole skarn with alternating sulfide-amphibole layers.

### 3.2.4 Gold

Gold (gold-rich gold-silver solid solution) is responsible for the vast majority of Au grade in the Peak deposit. Gold grains are 10μm to 1mm in diameter (Figures 3.3-3.8). Throughout the deposit Au is generally associated with sulfide (Figures 3.3-3.8) however in the highest grade zones Au is also associated with hydrothermal amphibole. Au is coarsest (up to 1 mm) in the highest grade ore.

Gold fineness ((Au wt% /(Au wt% + Ag wt%)) * 1000) ranges considerably at Peak. Three different samples yielded distinctly different populations of gold fineness (580, 787 and 906). The highest fineness values were from the highest grade ore. The 580 and 787 fineness populations (Figures 3.7 and 3.3, respectively) might represent atypical assemblages and compositions.

### 3.2.5 Native Bismuth and Bi-bearing minerals

Native bismuth is pervasive throughout Au rich skarn. Bulk Bi concentrations are up to 0.35 wt%. Irregular contacts between Bi and Au are typical and suggest co-

precipitation. Most bismuth grains have irregular, rounded shapes (e.g., Figure 3.3). In rare cases, especially in the highest grade rocks, Bi, Au and tellurium-bearing minerals possess angular shapes. Native bismuth rarely occurs as veins with pyrrhotite and chalcopyrite.

Bismuth also occurs as complex assemblages that include sulfide and telluride minerals (Figures 3.7-3.9). The typical mineral assemblage seen with native bismuth is native Au + hedlyite ($Bi_7Te_3$). Both hedlyite and native bismuth are always anhedral and typically form rounded grain boundaries with one another and the surrounding sulfides and silicates. These assemblages are typically adjacent to euhedral arsenopyrite, chalcopyrite and rarely pyrrhotite. In one sample jonassonite ($AuBi_5S_4$), a rare Au bearing mineral, is in contact with Au and native bismuth (Figure 3.8). Hedlyite and arsenopyrite are also associated with jonassonite.

Rare hessite ($Ag_2Te$) was present in one sample, where it displays a complex intergrowth with galena and pyrrhotite in a hedylite host (Figure 3.9).

### 3.2.6 Arsenopyrite-Danaite

Arsenopyrite (Fe,Co,Ni)AsS is common in gold rich amphibole skarn at Peak. It is typically euhedral and easily recognized in core (Figure 3.2). Cobalt contents of analyzed arsenopyrite vary between 0 and 10 wt % (Figures 3.9, 3.10). Arsenopyrite that contains between 3 and 12% Co is 'danaite' and thus much of the 'arsenopyrite' at Peak is technically 'danaite'. Due to the high Co contents at Peak, arsenopyrite geothermometry was not attempted.

Wavelength dispersive (WDS) electron microprobe cobalt mapping of arsenopyrite-danaite shows both simple and complex Co zoning in the same thin section. Figure 3.9 shows simple zoning whereas Figure 3.10 shows complex zoning. Complex zoning presumably indicates a complex growth history.

### 3.2.7 Molybdenite

Molybdenite is rare; it occurs as visible grains up to 2mm and is restricted to amphibole skarn. Molybdenite variably is in contact with pyrrhotite or as single grains with amphibole. Concentrations above 1,000 ppm are in amphibole skarn in holes north of Peak and in a single hole in the western part of Peak.

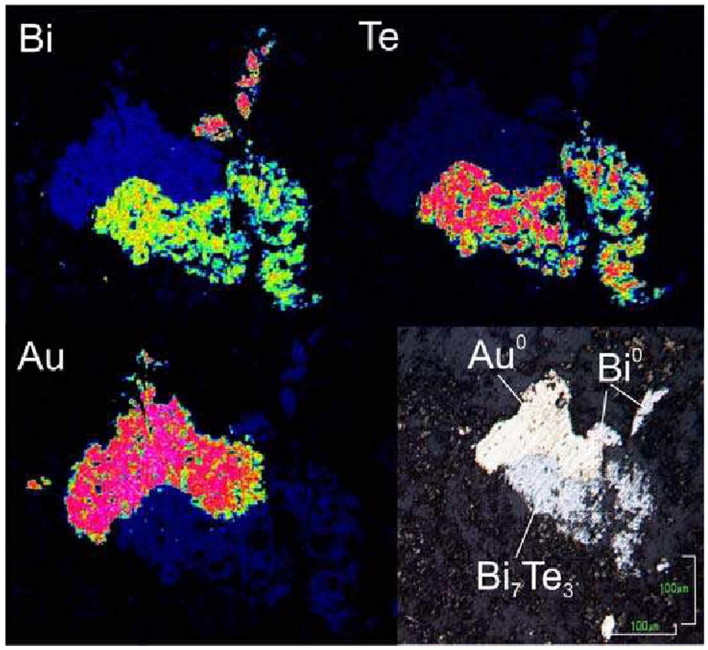


Figure 3.3: WDS EPMA maps of Au, Bi and Te in native Au, hedlyite ($Bi_7Te_3$) and native bismuth. All four images are of the same Au-B-Te assemblage.

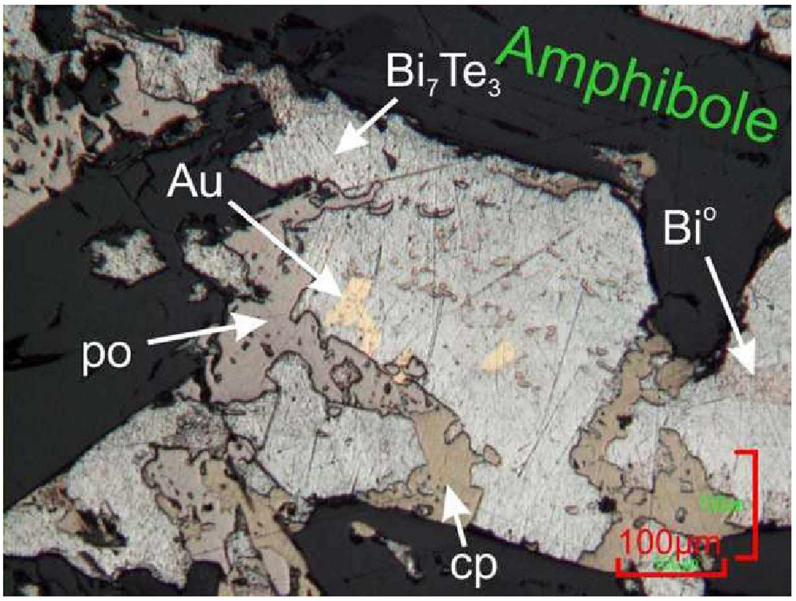


Figure 3.4: Reflected light photomicrograph of high grade Au amphibole skarn. Po = pyrrhotite; cp = chalcopyrite. Angular shapes of sulfide and metal are atypical for the Peak deposit.


Figure 3.5: Photo of high grade Au amphibole skarn. Multiple Au grains are visible without hand lens (up to 1mm in diameter). Sample width = 6cm.

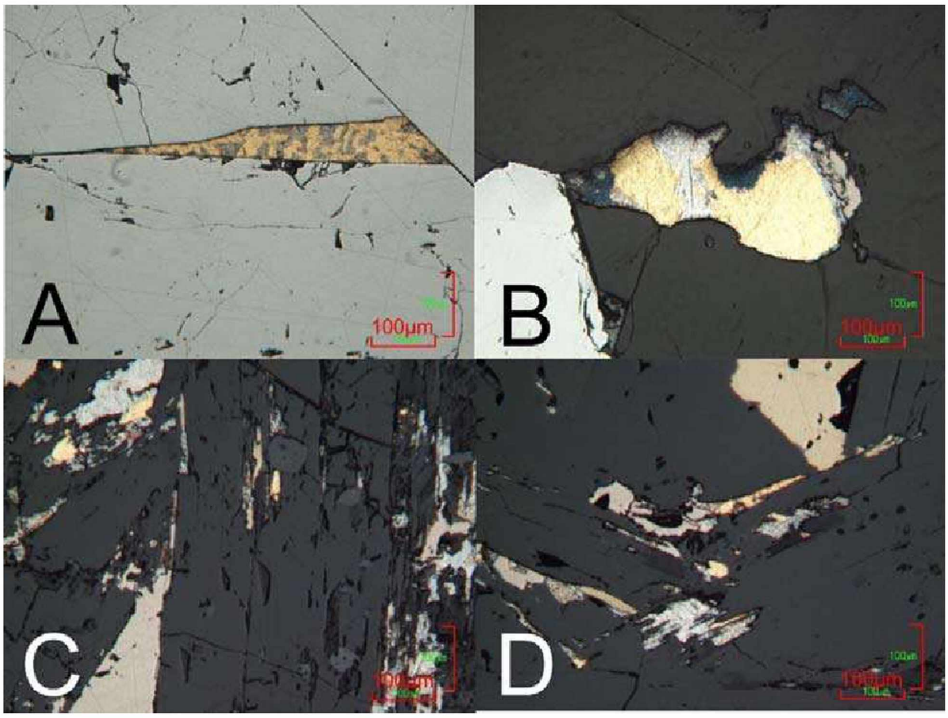


Figure 3.6: Reflected light photomicrographs of gold grains. A) Au + Bi$^{o}$ displaying exsolution texture (presumably from maldonite ($Au_2Bi$)). B) Au mineralization with hedlyite displaying typical irregular form. C) and D) high grade Au amphibole skarn with atypical angular shapes.

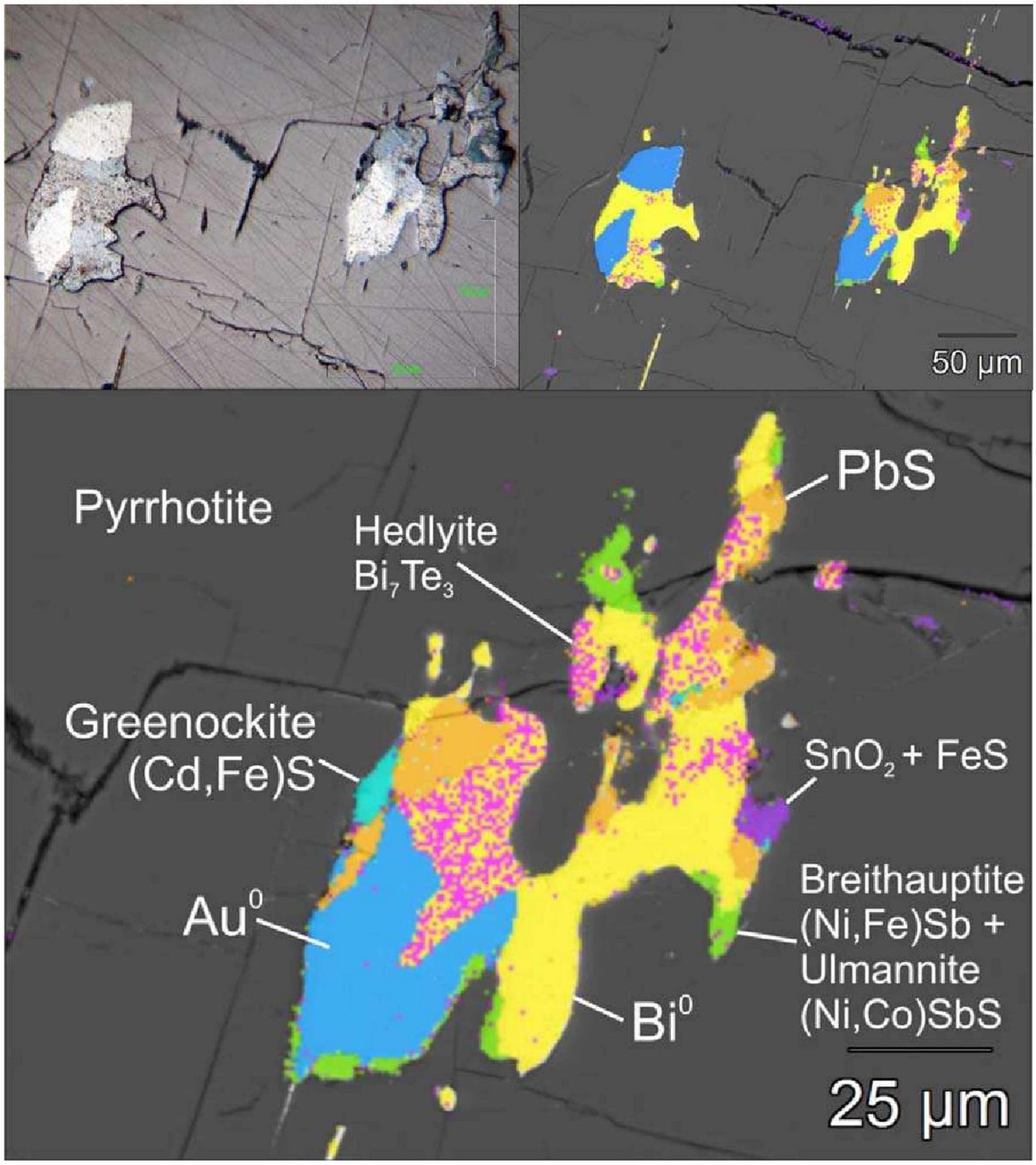


Figure 3.7: Images of a complex Au-Ag-Bi-Te-Pb-Ni-Co-Sb-Fe-Cd-Sn-S assemblage of mienrals. Top left = reflected light photomicrograph. Top right = energy-dispersive microprobe phase map at same scale as the optical image. Bottom = energy-dispersive microprobe phase map at an expanded scale (centered on right of center aggregate grain), showing the variety of different minerals intergrown in a small area.

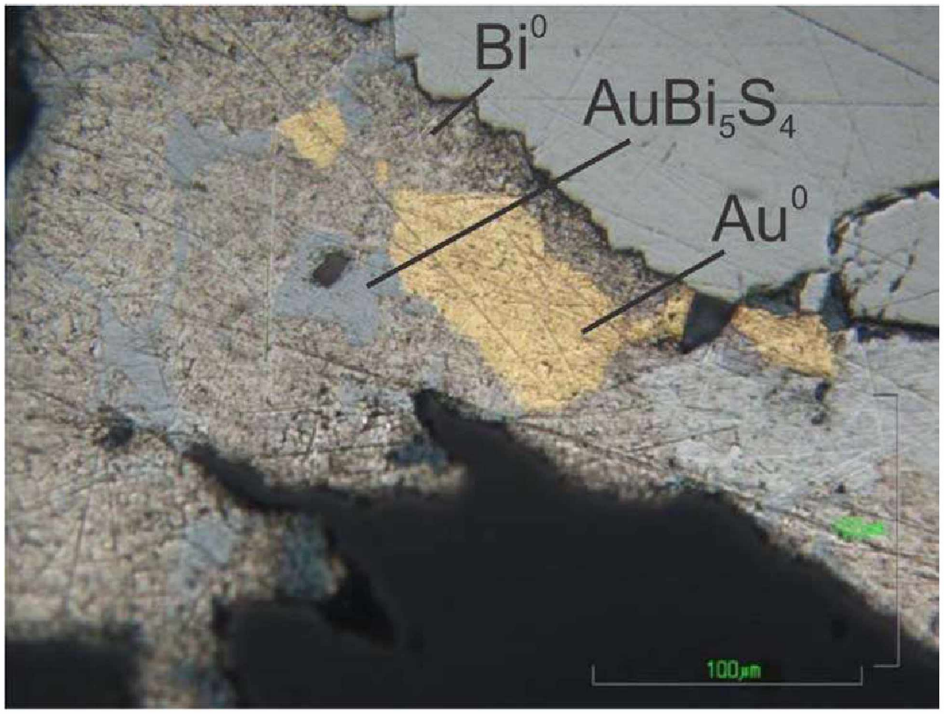


Figure 3.8: Reflected light photomicrograph of jonassonite ($AuBi_5S_4$) + Au + Bi + hedlyite ($Bi_7Te_3$) + arsenopyrite mineral assemblage.

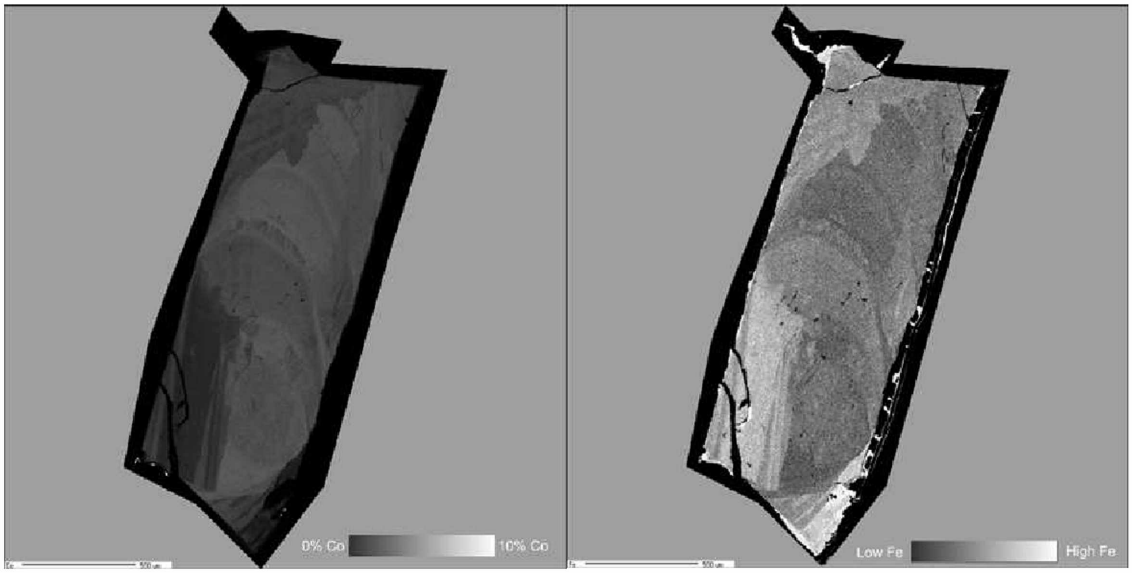


Figure 3.9: WDS electron microprobe map of Fe and Co in arsenopyrite-danaite solid solution. Scale bar is 0.5 mm. The Co zoning suggests relatively simple outward growth.

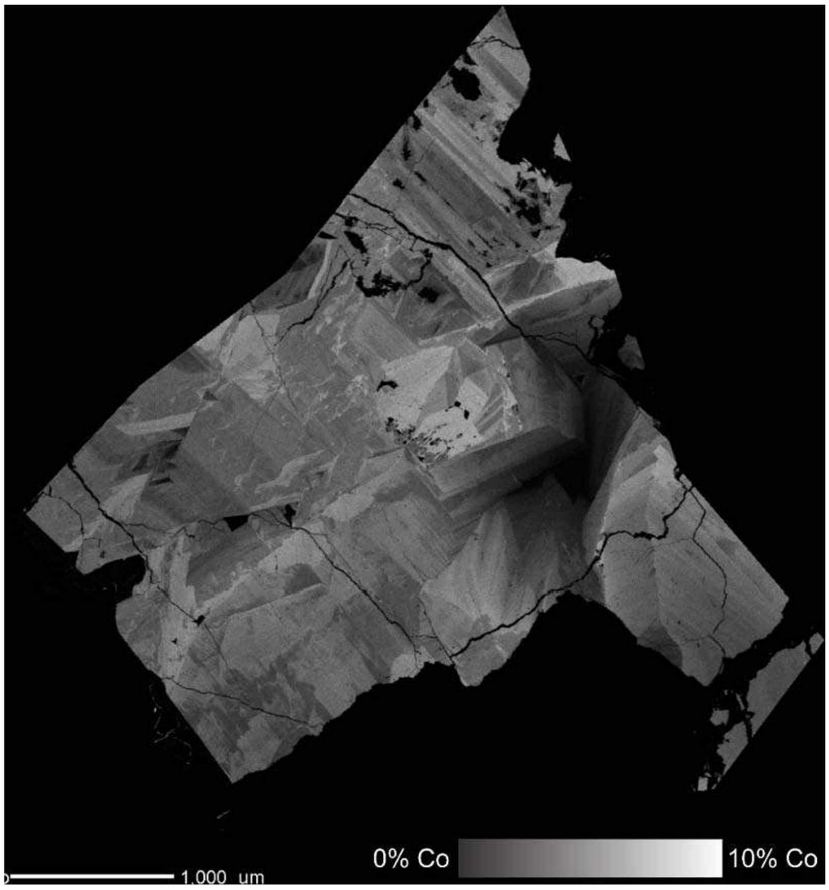


Figure 3.10: WDS microprobe map of Co in arsenopyrite-danaite. Chaotic Co zoning seen in this grain suggests a complex mineral-fluid interaction during growth. Scale bar is 1.0 mm.

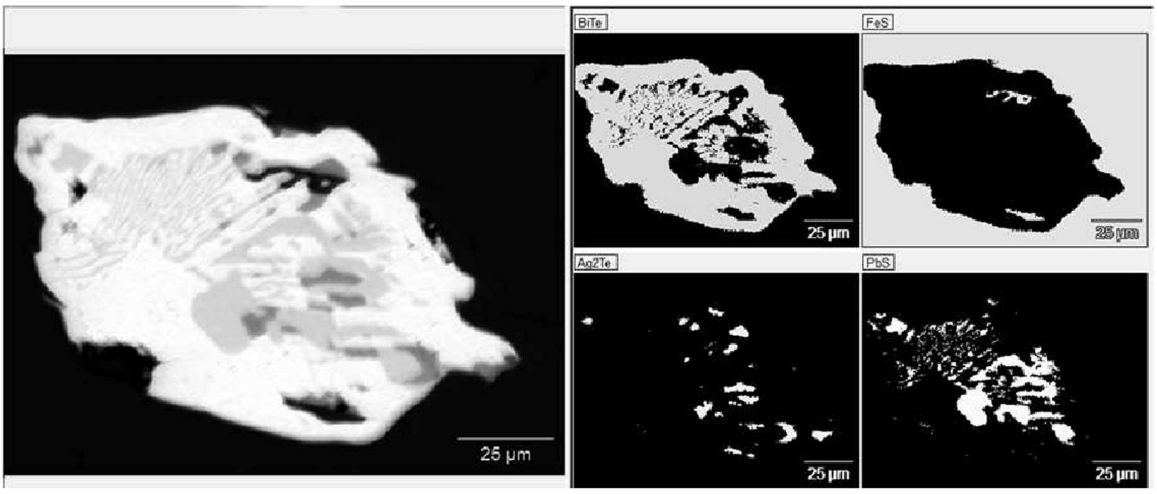


Figure 3.11: Images of complex hessite ($Ag_2Te$), galena and pyrrhotite intergrowths in hedlyite ($Bi_7Te_3$). Left = BSE image. Right = energy dispersive maps highlighting (bright areas) the various minerals.

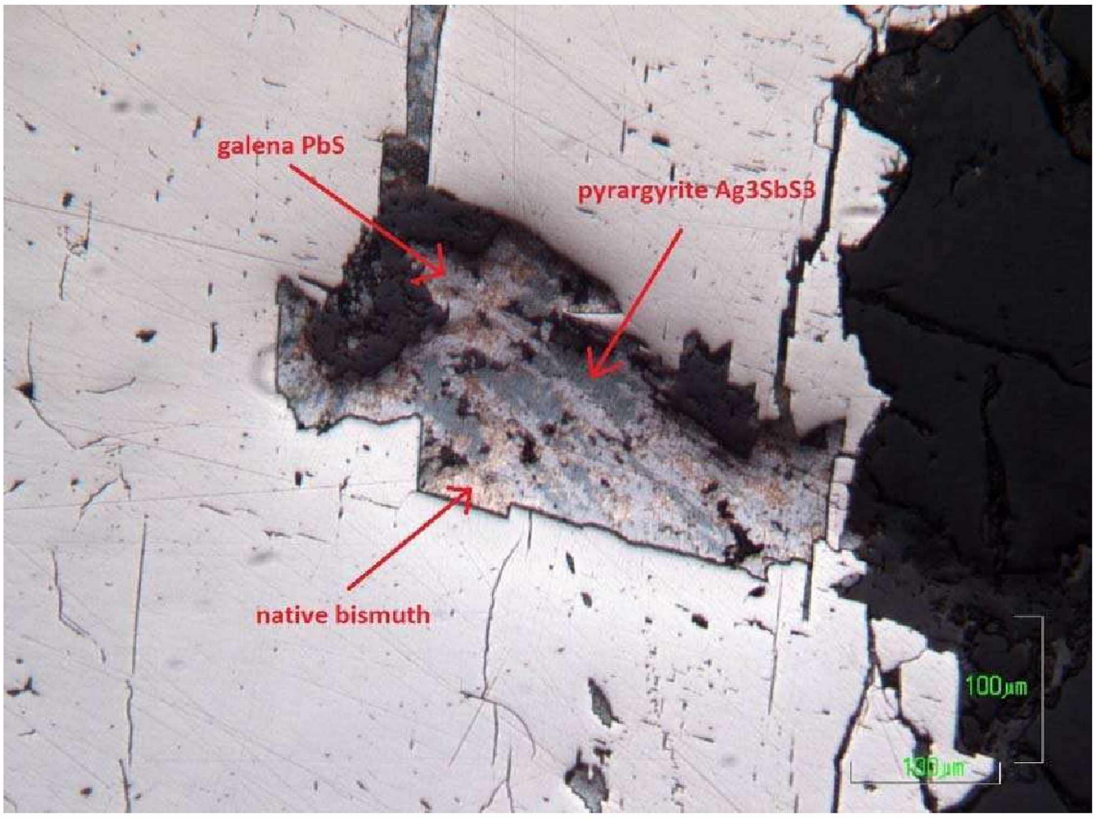


Figure 3.12: Reflected light photomicrograph of pyrargyrite, galena and native Bi filling fracture in arsenopyrite.

### 3.2.8 Galena, Sphalerite, Pyrargyrite and other silver phases

Galena (PbS) is relatively common in late veins which cut skarn, massive sulfide and surrounding schist (e.g., Figure 2.19). Galena occurs rarely in amphibole skarn with complex mineral assemblages (e.g., Figure 3.7). Galena is also associated with native bismuth and rare pyrargyrite ($Ag_3SbS_3$) in Cu-rich, Au-poor regions of the Peak resource (Figure 3.12). Typically it fills in cracks in arsenopyrite. I identified pyrargyrite in one silver-rich Peak sample. The lack of a strong Ag-Sb correlation (R=0.56; see section 3.3) suggests pyrargyrite is not the major silver phase. The presence of silver in electrum is one reason for the poor Ag-Sb correlation. However, especially in Ag-rich rocks, which also

possess Ag >> Au, additional Ag minerals must simply be present. Acanthite and argentopyrite have been reported in metallurgical reports prepared for Contango, Inc. I have not identified either mineral in polished thin section.

Coarse grained sphalerite variably accompanies galena in late veins (Figure 2.20). It is also present as fine grained 'stars' in chalcopyrite.

### 3.2.9 Ni-Sb-(S), Sn, W and Cd Minerals

Ulmannite (Ni,Co)SbS, breithauptite (Ni,Fe)Sb, cassiterite ($SnO_2$) and greenockite (CdS) are rare minerals occasionally associated with Au (Figure 3.7). Identifications of these minerals was possible by energy dispersive electron microprobe mapping as they are undistinguishable by reflect light microscopy. Grain sizes for all of these minerals do not exceed 20μm. Cassiterite is extremely fine grained and mixed with pyrrhotite. All of these phases occur in a single multi-mineral assemblage with electrum (fineness 580), native bismuth and hedlyite.

Scheelite is present in massive and very fine grained, crushed sulfide. Grain sizes are up to 0.5 mm as indicated by ultraviolet light examination. Based on drill hole assays, it is commonly present at concentrations of 0.01-.05%, rarely as high as 0.2%.

## 3.3 Metals and Metal Associations

Table 3.1 gives the maximum concentrations seen for a variety of metallic elements in drill core assays from the Peak Deposit. Clearly, the Peak zone contains elevated

concentrations of a wide variety of elements, notably Au, Ag, and Cu. I have identified the mineralogical sources of many of these elements but not others. For example, approximately 150 assays have Au:Ag ratios high enough for the Ag to be accounted for in electrum, but approximately 10 times as many have high Ag: Au ratios (up to 28,000) that require additional Ag minerals. I have identified only two (hessite and pyrargyrite) and both in only one sample. Acanthite and argentopyrite are also reported by internal metallurgical reports. Out of 75 assays with > 94 ppm Ag (and Ag>>Au), approximately 2/3 had Ag/Sb ratios low enough (<8) to permit a significant amount of pyrargarite; the other 1/3 had such high Ag/Sb (10-100) as to require additional Ag minerals beyond pyrargarite.

Table 3.1: Maximum concentrations of selected elements for Peak assays, values in ppm unless indicated otherwise

| % Fe | %As | %Bi | %Co | %Cu | %Mo | %Pb | %S | %Sb | %W | %Zn | Ag | Au | Ni |
|---|---|---|---|---|---|---|---|---|---|---|---|---|---|
| 58 | >1 | 0.36 | 1.3 | 8.3 | 0.28 | 6 | 38 | >1 | 0.8 | 4.8 | 828 | 208 | 763 |

I employed 17,572 drillcore assay values to determine correlation coefficients among Au, Ag, Al, As, Ba, Be, Bi, Ca, Cd, Co, Cr, Cu, Fe, K, La, Mg, Mn, Mo, Na, Nb, Ni, P, Pb, S, Sb, Sc, Sn, Sr, Ti, W, and Zn (Appendix 3). All data was log transformed for purposes of calculating correlation coefficients. No cutoffs were applied to any analyses: values below detection limit were changed to half the detection limit.

The combined data yield a Au:Bi correlation coefficient (R=0.49). Figure 3.13 shows log Bi vs. log Au; the majority of gold-rich data points are bound between the diagonal lines. These data show that Bi and Au correlate well in gold rich skarn, but many

samples contain abundant bismuth without gold. That is, all gold-rich samples also contain abundant Bi, but not vice-versa.

Table 3.2: R values for elements from drill core assays at the Peak Deposit.

| | Au | **Ag** | Bi | Cu | As | Ni | Co | **Pb** | Cd | Sn | Mo | Mn | Fe | Ca | K |
|---|---|---|---|---|---|---|---|---|---|---|---|---|---|---|---|
| Bi | **0.49** | 0.32 | | | | | | | | | | | | | |
| **Cu** | | **0.63** | 0.38 | | | | | | | | | | | | |
| As | 0.22 | 0.32 | 0.42 | 0.35 | | | | | | | | | | | |
| Ni | 0.34 | | | | | | | | | | | | | | |
| Co | 0.26 | 0.29 | 0.39 | 0.41 | **0.65** | 0.32 | | | | | | | | | |
| **Pb** | | **0.54** | | | | | | | | | | | | | |
| **Sb** | | **0.56** | 0.24 | 0.21 | 0.29 | | 0.22 | **0.68** | | | | | | | |
| Cd | | | | | | | | 0.29 | | | | | | | |
| Sn | | 0.37 | | 0.28 | 0.33 | | | 0.30 | | | | | | | |
| Zn | | | | | | | | 0.29 | **0.97** | | | | | | |
| Mo | 0.25 | | | | | 0.36 | | | | | | | | | |
| Mn | 0.22 | | | | | 0.37 | 0.25 | | | 0.24 | 0.23 | | | | |
| Fe | 0.31 | 0.29 | 0.33 | 0.40 | 0.39 | 0.29 | 0.37 | | | 0.40 | 0.27 | 0.34 | | | |
| Ca | 0.23 | | | | | 0.34 | 0.25 | | | | | **0.72** | 0.25 | | |
| K | -0.31 | -0.22 | | | -0.29 | -0.27 | -0.30 | | | -0.28 | -0.29 | -0.33 | **-0.61** | -0.34 | |
| Al | -0.34 | -0.28 | | -0.34 | -0.38 | | -0.34 | | | -0.28 | -0.30 | -0.25 | **-0.73** | -0.25 | **0.79** |

Notes: values of $|R|<.2$ are omitted for clarity. Bold values are > 0.48. Raw data from Avalon Development Corporation.

Other strong correlations include arsenic with cobalt (R=0.65) and cadmium with zinc (R=0.97). The former is due to the variable concentrations of Co in arsenopyrite (e.g., Figure. 3.10); the latter by consistent Cd in sphalerite. Rare CdS (e.g., Figure 3.7) and presumably variable Cd in sphalerite cause the less than perfect correlations. The upper limit for As of 10000 ppm (1%) also causes problems with defining a Co-As correlation, as actual As concentrations can exceed 10% in arsenopyrite-rich intervals.

Au and Cu moderately correlate with Fe, Bi and Ag. Lack of a significant Au-Ag correlation is due to the fact that the two elements mostly occur in different minerals; only

a small fraction of the Ag is present in electrum. Ag/Au ratios for samples with detectable Ag and Au range from greater than 28,000 to less than 0.05. The relatively high correlation of Ag with Cu suggests that some Ag may be present as solid solution in chalcopyrite. The absence of a strong correlation between Au and Cu indicates that gold is not particularly associated with chalcopyrite.

One of the strongest elemental associations is among Ag-Sb-Pb, with R values of 0.54-0.68 (Table 3.2). Such is compatible with appreciable fraction of the Ag present as the Ag-Sb sulfosalt pyrargaryite, and the associations with Pb suggest that galena is commonly associated with this sulfosalt, as I have locally observed. The poor (R = 0.29) correlation of Pb and Zn is consistent with the variable occurrence of sphalerite with galena.

No elements show significant correlation with W, consistent with the lack of spatial association between scheelite (the major W mineral present) and sulfides.

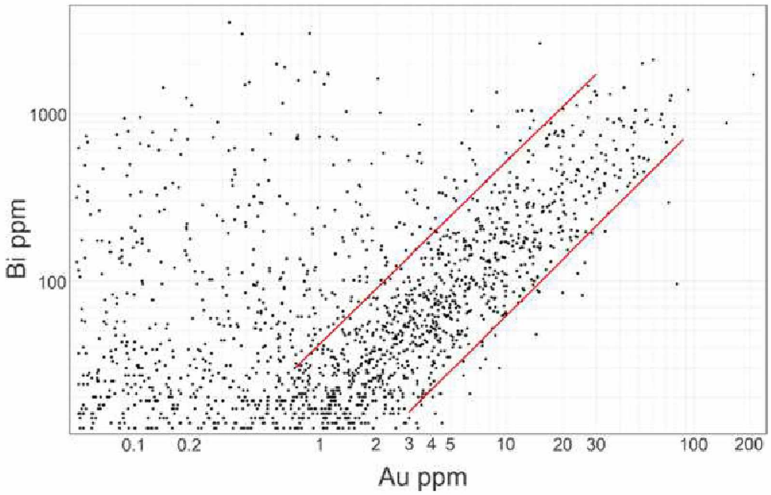


Figure 3.13: Au versus Bi for drillhole assay data from the Chief Danny Exploration Area. This includes Peak, Discovery and all holes drilled between 2011 and 2013. Red lines bound apparent grouping of majority of data points.

### 3.4 Spatial Distributions of Ore

The Peak deposit displays some Au:Cu zonation (Figure 3.14). Plotting copper intercepts above 0.5% and gold intercepts above 5 ppm show Au:Cu ratios increasing from east to west. Copper is pervasive throughout the Peak deposit except for the furthest west extent of the ore body. Copper-bearing skarn extends to the eastern extent of drilling. It is shown as a closed polygon as it represents the current ore body. Skarn with significant Ag begins approximately 25 meters west of the eastern extent of drilling and extends west approximately 100 meters from the current known extent of gold skarn. Skarn with appreciable Au begins approximately 100 meters west of the eastern extent of drilling (Figure 3.14).

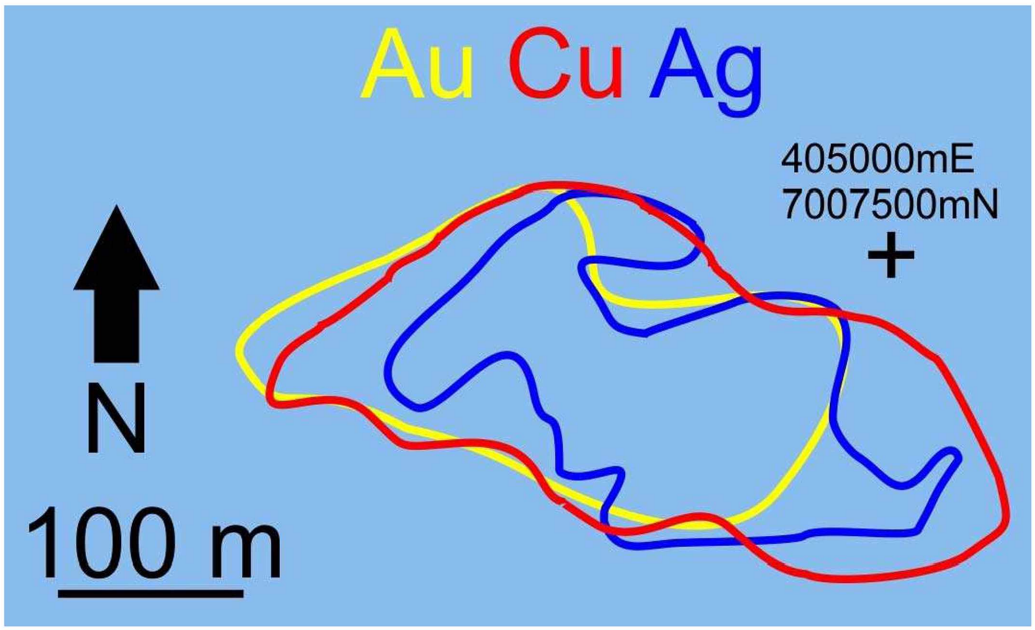


Figure 3.14: Plan map outlining significant concentrations of Au, Cu and Ag from drill core assays of the Peak deposit, projected vertically to a common plane. The cutoff grades for these outlines are 5 ppm for Au, 0.5% for Cu and 5 ppm for Ag. Modified from VanTreeck (2013).

Rock with significant gold concentration is restricted to the western two thirds of the Peak deposit (Figure 3.14). The region enclosing significant Ag partly overlaps both the Cu and Au zones. Partial overlap between Au and Ag reflects the wide variations in the Ag:Au ratio (>28,000 to <0.05) seen in the Peak assays. Pyrargyrite, acanthite, argentopyrite, and lesser hessite are likely in areas with high Ag:Au ratios. Gold and electrum also contain silver and represent major Ag phases in areas with Au>>Ag.

### 3.5 Ore Body Morphology

The Peak deposit is located entirely in the subsurface. It is defined by concentrations of Au > 5 ppm and (or) Cu > 0.5%. In a NE-SW cross-section looking northwest (Figure 3.15) the Peak deposit--including amphibole-rich rock, massive- and semi-massive sulfide as well as ore *per se*—can be modeled as a folded horizon. Skarn is 5-30 meters thick and is bounded by quartz-rich schistose rocks. In contrast, in long section B-B' (looking northeast; Figure 3.16) the deposit appears to be flat lying.

Calc-silicate hornfels up to 30 meters thick overlies and underlies much of the western skarn (Figures 3.15, 3.16). Such rock contains low concentrations of Au and Cu. Late Pb-Sb-(Zn) veins cut all other rock types. Based on oriented core measurements they dip to the northeast.

### 3.6 Silicate Mineral and Compositional Zoning

During logging I recognized no apparent silicate zoning. All skarn appeared to be dominated by amphibole, as corroborated by XRD analyses (Appendix 3). I only found pyroxene in the Peak deposit in 5 out of 25 calc silicate-bearing thin sections. I cannot say with confidence whether pyroxene was present in the sections that now contain amphibole without pyroxene.

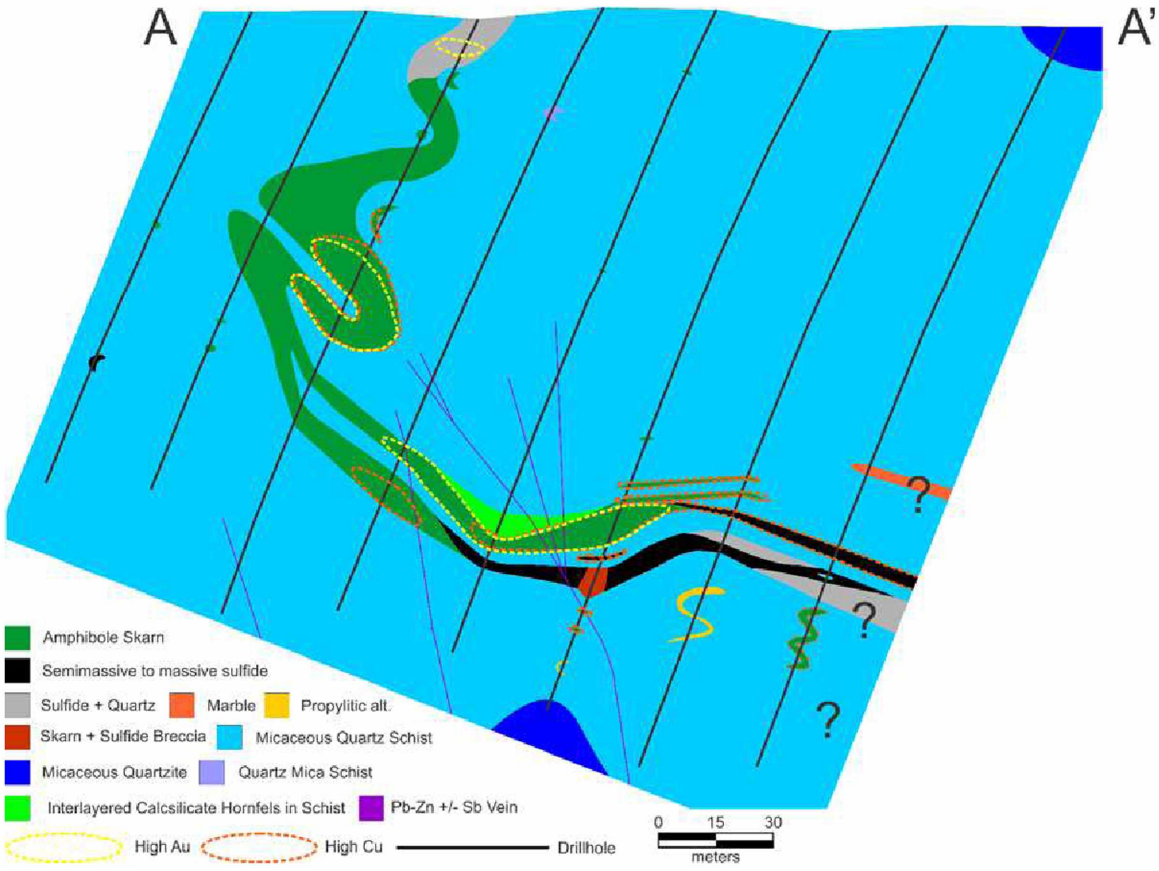


Figure 3.15: Interpretive cross section A-A' through Peak Deposit, looking west-northwest. Section location shown on Figure 2.1

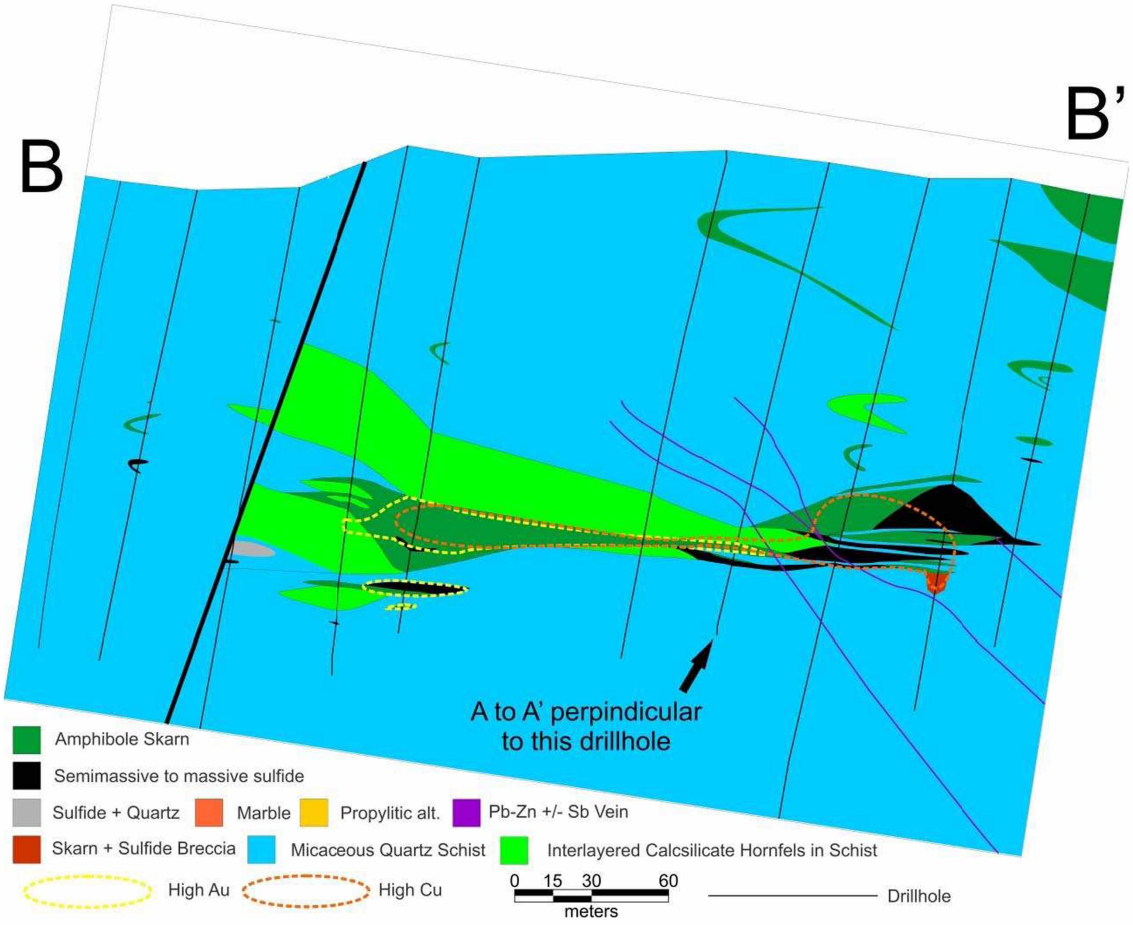


Figure 3.16: Interpretive long section B-B' through Peak Deposit looking north-northeast. Section is located on Figure 2.1

## 3.6 Discussion

### 3.6.1 Metallogeny and Metal zoning

Ore minerals at peak include native gold, electrum, chalcopyrite, pyrargyrite ($Ag_3SbS_3$), acanthite ($Ag_2S$), argentopyrite ($AgFe_2S_3$), and hessite ($Ag_2Te$). Additional metals present at Peak include Bi, Te, As, Sb, Zn, Cd, Ni, Co, and W (Table 3.1). This contrasts to the typical Au-Bi-Te (As) metallogeny of intrusive related deposits of interior Alaska (e.g. Fort Knox and Pogo; Flanigan et al., 2000). Copper rich skarn at Peak suggests instead an affinity with porphyry copper and associated deposits of easternmost Interior Alaska and western Yukon (e.g. Casino).

Elemental correlations at Peak are consistent with petrographic associations of various ore, sulfide, telluride and sulfosalt minerals. For example Au and Bi show a weak correlation (R=0.49) because although the two are associated, Cu skarn (lacking Au) also contains native bismuth. Exsolution textures between gold and native bismuth suggest that a small fraction of Au and Bi originally precipitated as maldonite (e.g. Figure 3.7A). The vast majority (>99%) of Au in thin section is (Au,Ag) suggesting a complex recrystallization history, possibly starting with a maldonite phase.

Many plutonic related gold systems possess strong Au:Bi correlation coefficients. Mid-Cretaceous deposits of Alaska yield correlation coefficients ($R^2$) between gold and bismuth of 0.71 to 0.89 for Fort Knox, Pogo and Dolphin (Flanigan et al., 2000). Late Cretaceous plutonic related gold deposits of Alaska yield lower correlation coefficients for gold and bismuth (0.24 to 0.74) for Nixon Fork, Shotgun, Golden Zone and Donlin Creek (Flanigan et al., 2000).

Bi:Au ratios for the Chief Danny exploration area range between approximately 9 to greater than 10,000. The majority of analyses from the Peak deposit yield Bi:Au ratios of 9-30, and the 450 highest Au samples yield an average Bi:Au of 21. These ratios are typical of plutonic related gold deposits (e.g. Fort Knox Bi:Au ~20; Pogo Bi:Au ~5; Nixon Fork Bi:Au 15; Flanigan et al., 2000). The maximum range in values is similar to other Au skarn deposits such as the Buckhorn (Bi:Au of 1 to >500; Deal, 2012).

Myers (1994) demonstrated Cu-Au (Pb-Zn-Ag) zoning (Figure 3.18) in the vicinity of the Fortitude skarn deposit, Nevada, with proximal Cu and distal Au (Ag-Zn-Pb). The Peak deposit is more complicated because all known outcrops and drill intercepts of intrusions are greater than 1 kilometer from the Peak deposit and are in separate fault blocks (Figure 2.1). These faults postdate mineralization and the original position of any intrusive body relative to the Peak deposit is poorly constrained. However, in comparison with Fortitude, high Cu:Au at Peak is present on the east side of the deposit (Figure 3.15), suggesting that the causative intrusion is east of Peak. This is the opposite direction from the current location of the Mohawk pluton (Figure 2.1). Although the Mohawk intrusion has a porphyritic texture and is in the general vicinity of the Mohawk skarn (Figure 2.1) it is implausible to make the fluid source for Peak simultaneously to the east and to the west of Peak. If the Fortitude model can be applied, the causative pluton lies below and east of the Peak deposit.

### 3.6.2 Ore Body Morphology

I interpret the Peak deposit as seen in cross-section (Figure 3.16) to consist of two bifurcating, sub-parallel horizons complexly deformed into 10 meter scale recumbent folds. Other interpretations are possible, but this is consistent with broader-scale folding present in the area. In particular meter-scale recumbent folding is present in marble layers near the SE edge of the map area (Figure 2.1) and 10 meter scale folding identified in amphibolite layers through a drill hole cross section of the Discovery zone (Figure 2.22) is likely recumbent. A bifurcation in amphibolite layer similar to the skarn bifurcation is also present (Figure 3.16). This folding occurred before metasomatism as the amphiboles in the skarn are randomly oriented and display no sign of alignment. That is, the original host rock (micaceous marble?) was complexly folded and then replaced during the hydrothermal skarn-forming event.

I have similarly interpreted the long section through the Peak deposit (Figure 3.17) as containing folded skarn horizons. The more-flat-lying aspect of the skarn in the long section seemingly indicates that this direction (WNW-ESE) is the strike of the layers. Folding in this section would imply two different stages of folding.

Mineralogical zoning as expressed in the long section and cross section is problematic. The long section shows a greater abundance of skarn horizons to the east and greater abundance of calc-silicate hornfels to the west. Such—in conjunction with the E to W zoning from Cu to Cu-Au to Au—suggests a fluid source to the east and thus, westward flowing fluids. The apparent interfingering between skarn and calc-silicate hornfels suggests that the amphibole-rich skarn may be a complex replacement of hornfels as well as marble. However, this same section shows that massive to semi-massive sulfides, which

are typically seen as marble replacements away from skarn--are restricted to the eastern part of the long section.

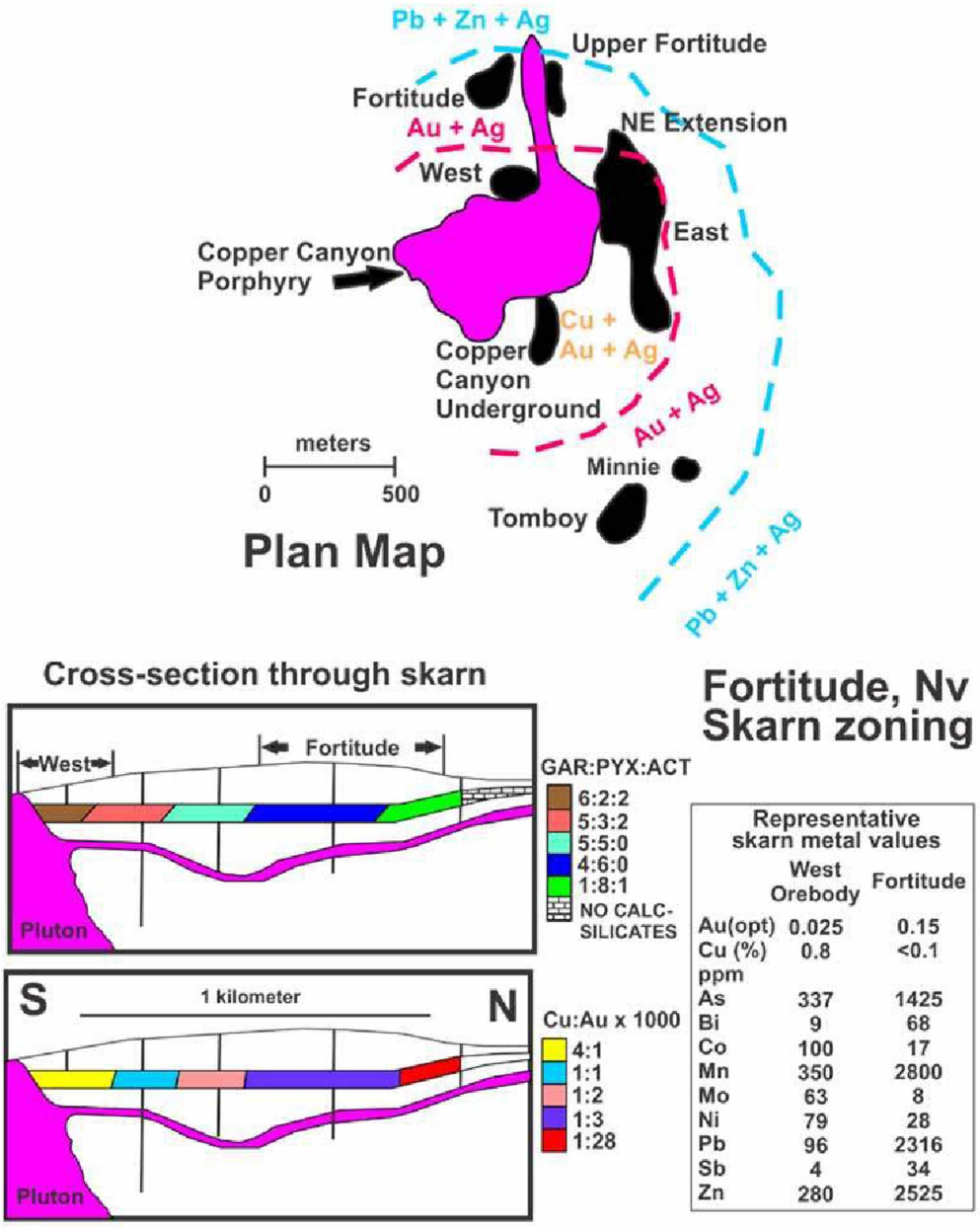


Figure 3.17: Mineral and metal zoning in and near the Fortitude skarn deposit, Nevada. Modified from Myers (1994).

The cross-section also poses difficulties with regards to metal zoning. A broad northeast to southwest zoning from Cu to Cu+Au suggests fluid flow from the north. Late Pb-Sb(Zn) bearing veins cross cut skarn, sulfide replacement and schist. Both the orientation of late Pb-rich veins and Cu:Au trends (high Cu:Au easterly and downdip) suggest an intrusive source easterly and at depth. However, the west to east change from skarn to massive- and semi-massive sulfide + quartz indicates lower temperature fluids to the east. Similarly, the only marble horizon encountered in either section is in the easternmost drill hole of the cross-section. One would expect to find unreplaced marble at the distal edge of mineralization. However, this isolated lens of marble is well above the skarn and may have simply escaped hydrothermal fluids.

I could not find a contact between skarn and marble in any drill hole or any surface exposure in the area. In two cases the skarn apparently terminates into coarse grained quartz + sulfide. In most cases it abruptly terminates against quartz schist. However, massive sulfide does contain variable amounts of calcite, which is compatible with direct sulfide replacement of marble.

One possible explanation for the mineralogical and metal zoning is that fluids did move upward from a source to the east of and below the Peak zone, outside of current drilling, but in a complex manner. As steeply dipping dip-slip faults are younger than—and offset—the volcanic rocks, it is likely that some post-ore tilting has occurred in the Peak zone. That is, the current geometry is likely tilted from the geometry at the time of ore formation. Skarn layers that are currently flat-lying or west-dipping in the eastern part of the cross-section could have been east-dipping at that time. In any event, it is not clear whether the amphibole-rich skarn represents a replacement of marble, of calc-silicate

hornfels, of a pyroxene-rich skarn, or of all three. Later, lower-temperature fluids using the same fluid conduits could have replaced amphibole skarn, but more likely replaced marble layers. These hypothetical marble layers were bypassed during the earlier amphibole skarn formation.

## Chapter 4 Structure

### 4.1 Introduction

Previous to this study a single foliation measurement had been published within the Chief Danny exploration area and no faults had been mapped. Although Foster (1970) mapped Chief Danny geology as metamorphic, she failed to detail the complex structural history. Locally the major northeast trending Caribou Creek and Dennison Fork lineaments in the Tok River basin are interpreted as Quaternary faults (Woodward-Clyde Consultants, 1979) although an alternative interpretation regards the NE trending valleys as remnants of Holocene glacial outburst flooding (Koehler and Carver, 2012).

Outcrops are rare in the study area, making it difficult to understand the structural setting. For this study field measurements, oriented drill core measurements and geologic mapping were used to document folding, faulting and other structural controls on mineralization in Chief Danny. Figure 4.1 shows the locations of drill holes with oriented core and major structural features in the region.

Oriented core measurements in the 2013 drill program contained errors which cannot be extracted due to incomplete records. Some strike direction measurements were taken 180 degrees from the true strike. Therefore the data may be skewed in a direction opposite to the true strike direction. However, no more than 20% of the data are suspect.

### 4.2 Foliation and Folds

Folded schist and the folded nature of Peak mineralization constitute two large scale folds that were identified in the field area from surface foliation measurements and

subsurface cross sections plotted from core logging. Northwest of Peak a northwest plunging antiformal fold with a wavelength of approximately 500 meters was identified by surface rock outcrop foliation measurements (Fig. 4.1). A cross section through the Peak deposit suggests Peak consists of a separate folded skarn horizon that can be traced for over 400 meters (Fig. 3.15). Based on the randomly oriented amphiboles in the skarn, the folding required for this convoluted shape occurred before skarn formation.

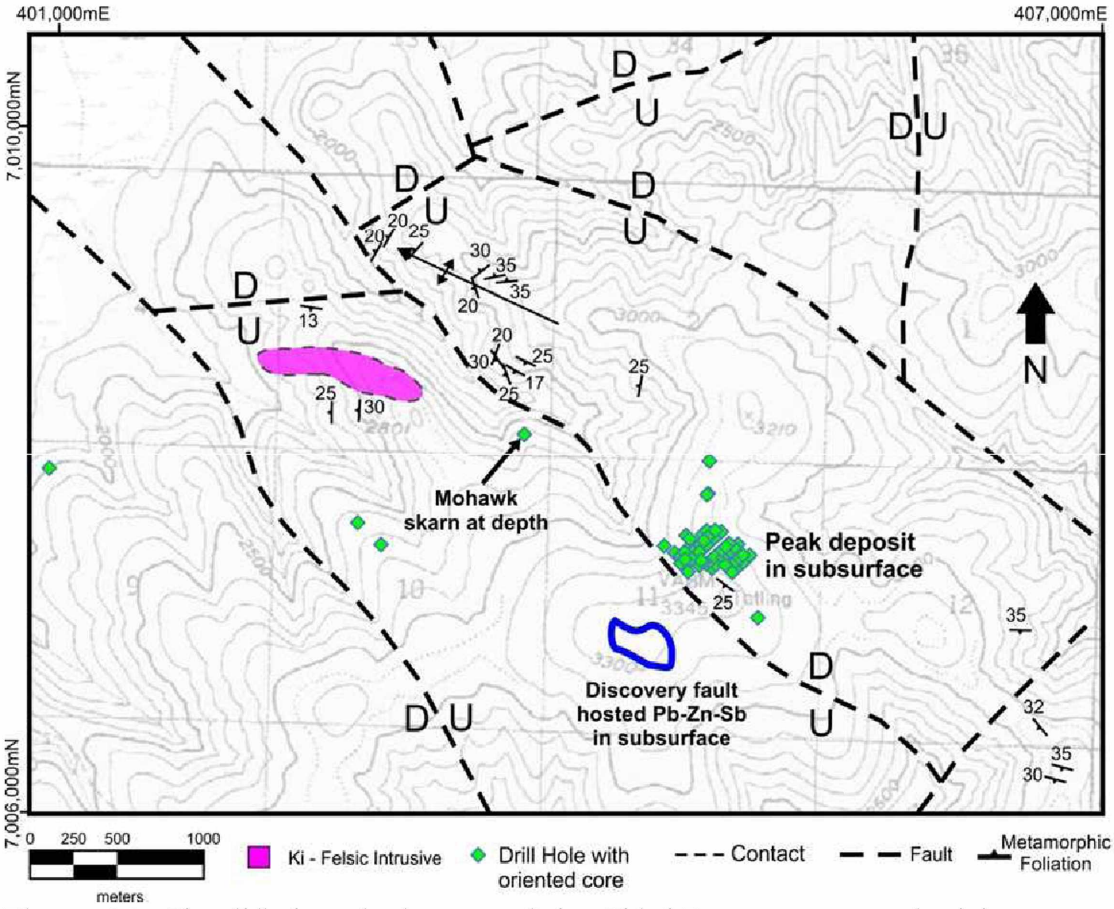


Figure 4.1: Simplified geologic map of the Chief Danny area, emphasizing structural features and locations of drill holes with oriented core. Foliation symbol includes dip angle. Modified from Figure 2.1.

Foliation in oriented core exhibits frequent changes in dip (0-90°) and in strike direction, but commonly strikes between 100° and 150°; 120-140° in the Peak area, where

it is mainly observed in oriented drill core and a single outcrop (Fig. 4.2). This is also in agreement with the long section through Peak (Fig. 3.16), oriented at 110°, which shows sub-horizontal contacts, i.e., suggesting that 110° is the approximate strike. For the four oriented drill holes outside of the Peak area a maximum in strike direction is also in the 120-140° range, but the distribution is much broader. If the major fold axis mapped in the Chief Danny area is representative, then foliation strikes are likely to be sub-parallel to the fold axis along the limbs and perpendicular to fold axis at the nose of the fold (as seen in Fig. 4.1).

Contacts between metamorphic units in drill core, are frequently, but not always, sub-parallel to nearby foliation. An analysis of nearly 100 examples of contact strike versus strike of nearby foliation shows that 57% of the pairs yield a difference of less than 26° (average is 11°) and 43% yield a difference of more than 30° (average is 116°). That is, in a majority of cases, contacts are sub-parallel to nearby foliation (Fig. 4.4), regardless of strike.

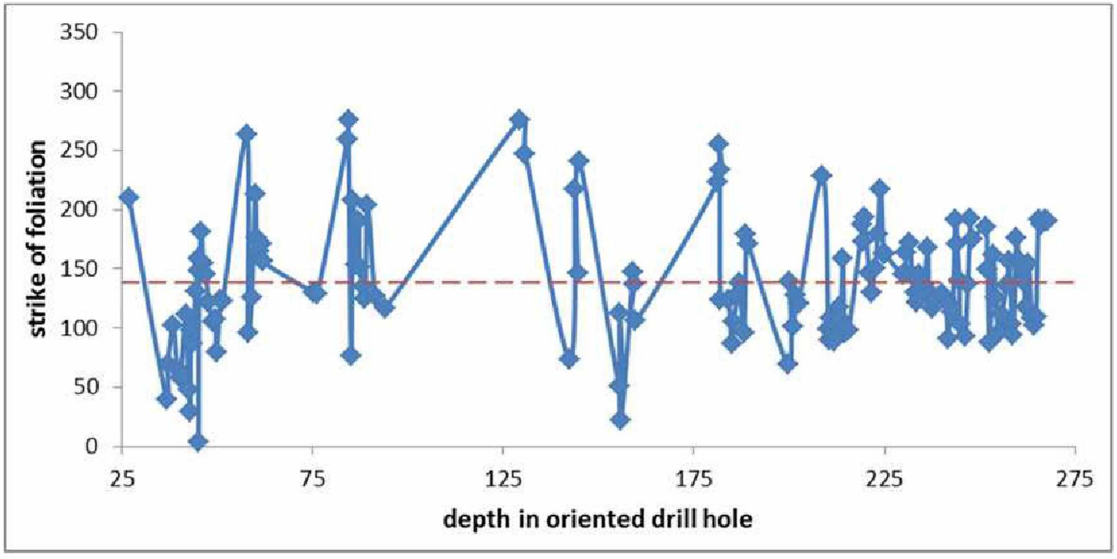


Figure 4.2: Strike of foliation vs. depth in drill hole for drill hole 118. Red dashed line is the average value.

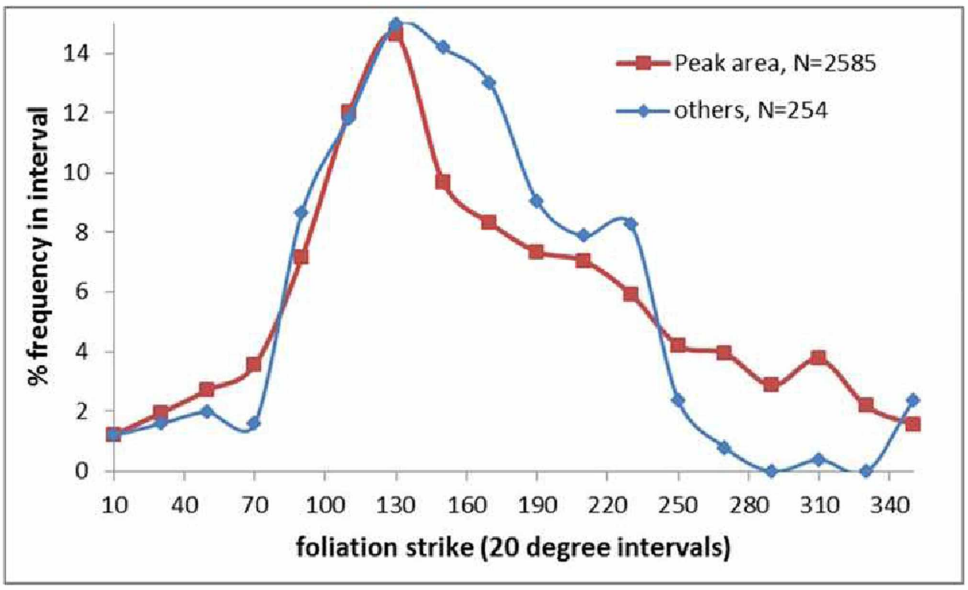


Figure 4.3: Distribution of foliation strike for oriented core, grouped into 20° intervals, from the immediate Peak area (red square) and for the 4 drill holes outside of Peak.

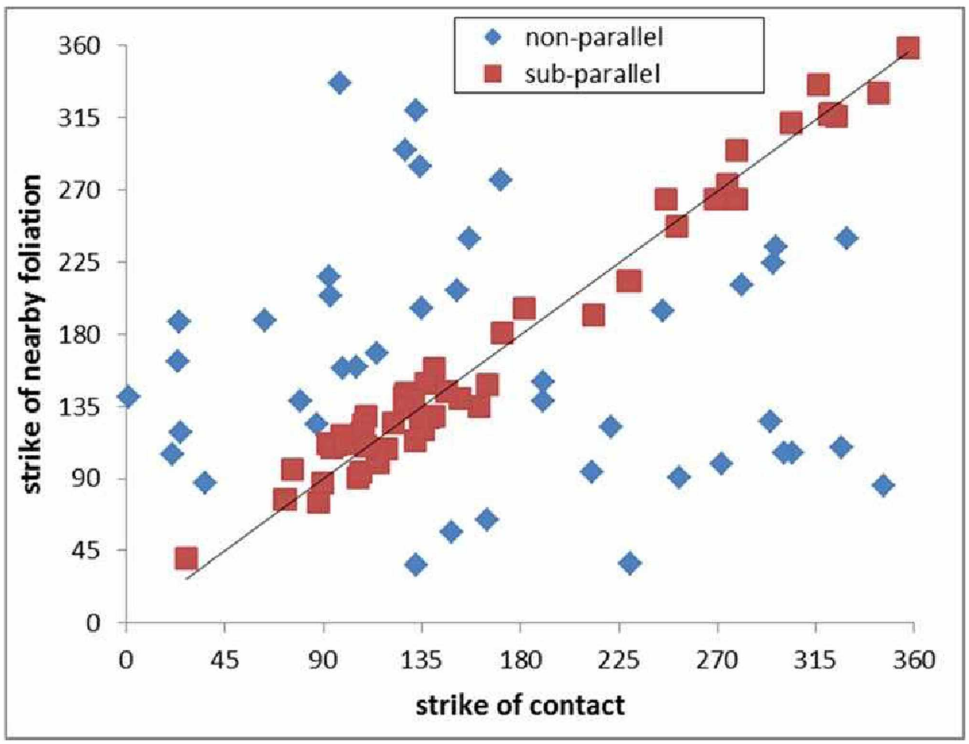


Figure 4.4: Strike of contact between metamorphic units and strike of nearby foliation for 97 pairs from oriented core in the Chief Danny area. Data from Avalon Dev. Corp. For more than half of the pairs, contact is sub-parallel to nearby foliation.

### 4.3 Veins and Fault Hosted Mineralization

Veins host Pb-Zn-Sb mineralization at both Peak and the Discovery zone. There are some differences: Discovery veins show a strong Pb-Zn-As-Sb-Ag association, whereas Peak veins only exhibit a strong Pb-Ag-Sb association. (That is, veins at Discovery invariably contain arsenopyrite and sphalerite; those two are commonly missing from veins at Peak). However, they are broadly similar in style and their sulfide-rich character.

Based on measurements from oriented Peak drill core (Fig. 4.5) veins at Peak predominantly strike 320-350°, that is, dip steeply ENE. Veins in the 3 oriented drill holes outside of both Peak and Mohawk, show a similar, but broader distribution centered on 310° (Fig. 4.5). In contrast, the bulk of veins in the oriented Mohawk drill hole strike at 80-100°, consistent with the only vein orientation (110°) known for Discovery (Fig. 4.6).

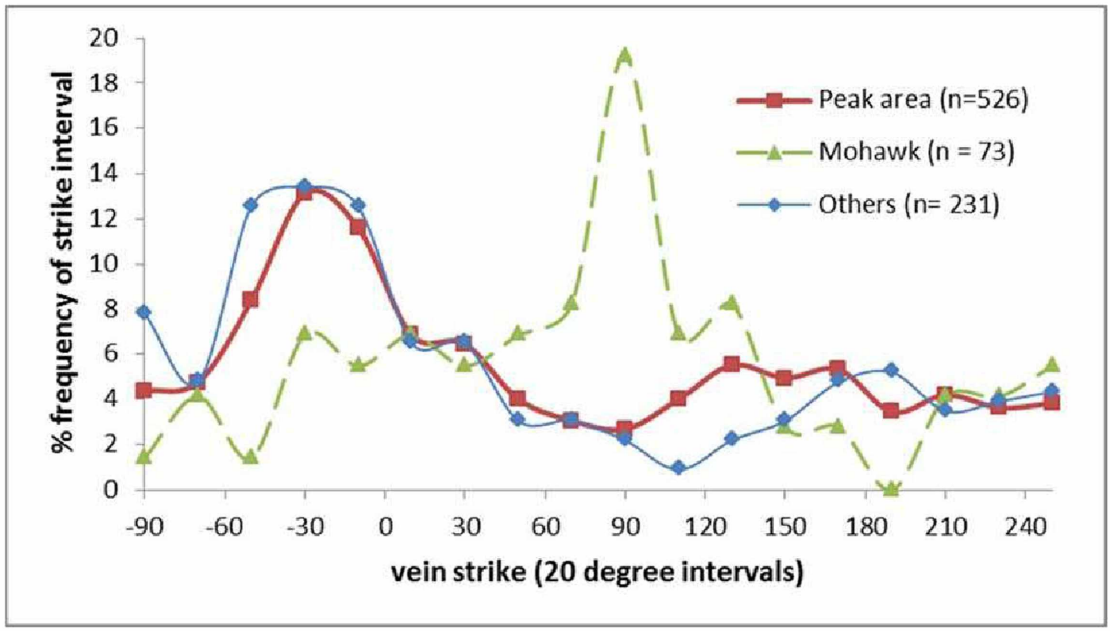


Figure 4.5: Vein strike direction histogram from oriented core measurements in the Chief Danny area. Data from Avalon Development Corporation.

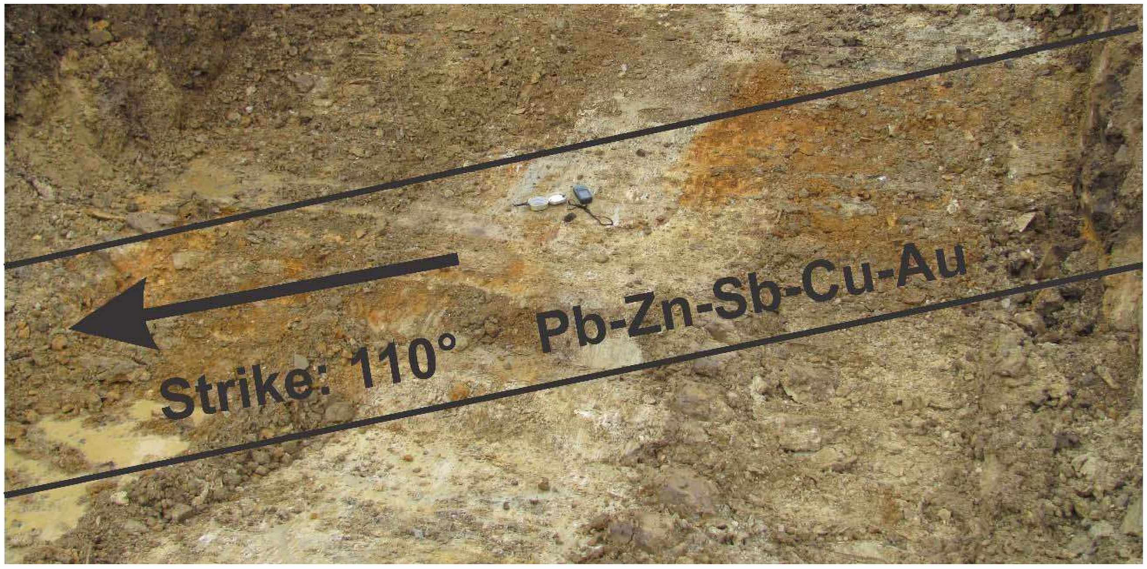


Figure 4.6: Vein hosted mineralization at the Discovery Zone. Compass and GPS for scale. Photo and data from Chris VanTreeck, Avalon Development Corporation.

### 4.4 Faults

Post-mineralization faulting has exposed metamorphic and plutonic rocks and preserved volcanic rocks. Based on surface mapping combined with airborne geophysics, three fault sets are observed at Chief Danny: northeast (typically 060-070), southeast (typically 130-140), and north-south striking (Figure 4.1). All three sets appear to be post-mineralization because all offset plutonic and volcanic rocks (Fig. 2.1). Of these, the northwest-striking set appear to be the largest and most clearly appear in the aero-resistivity map (as conductive zones). The dip direction of the major faults and their sense of displacement are unknown. No attempt has been made to reconstruct the pre-faulting position of the blocks in the study area.

Based on a tabulation of faults found in oriented drill core (Fig. 4.7) four major strike directions predominate: 320-340, 0-20, 120-140, and 180-200. Of these four, two (0-20 and 180-200) are clearly the same strike, but opposite dip and the other two are close to 180° apart, thus *probably* the same strike but opposite dip. That is, faults recorded in drill core are clearly post-mineralization and are sub-parallel to the kilometer-scale NNW-SSE and N-S striking faults mapped. Shears measured in the oriented core show an even more impressive maximum in the 120-140° group, that is, sub-parallel to the mapped NNW-SSE faults.

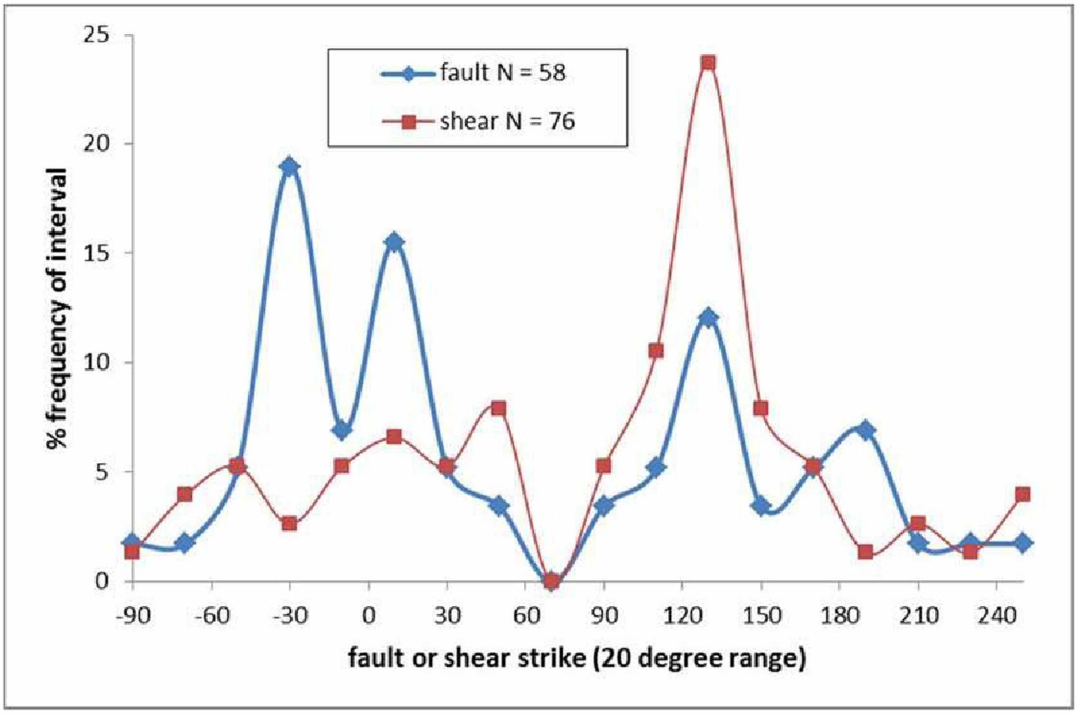


Figure 4.7: Distribution of fault and shear strike directions (in 20° intervals) from oriented core measurements from 2013 drill holes in the Chief Danny exploration area. Data from Avalon Development Corporation.

## 4.5 Discussion

The convoluted shape of the Peak skarn, as seen in cross-section (Fig. 3.15) is most likely caused by folding of marble-rich layers in the metamorphic package. Regionally, mid-Cretaceous and younger plutons cut metamorphic fabric and are not folded (Foster, 1970), so this folding took place pre-mid-Cretaceous.

Steeply dipping faults in the Chief Danny area cut the late-Cretaceous plutonic and volcanic rocks (Fig. 2.1) and may form some of the margins of the Peak ore body. WNW-striking faults are sub-parallel to the Denali fault and may be of related origins. Regionally, NE-striking faults are common in eastern Interior Alaska and may represent a conjugate fault system. Those in the Chief Danny area are sub-parallel to the regional Tok River fault. It is unclear where and how N-S striking faults fit into such regional patterns, however they occur both at the map scale (Fig. 4.1) and in drill core (Fig. 4.7).

In contrast to pre-plutonic folding and post-pluonic-faulting, veins and dikes record extensional directions at the time of igneous and hydrothermal activity. Dike orientations are not yet known, due to their apparent scarcity and the poor exposures present, but the Mohawk pluton has the shape of a large dike, elongated in WNW-ESE directions. Based on limited drill and trench data, veins in the Mohawk and Discovery areas (Fig. 4.1) also typically possess ESE strikes (90-110). It is tempting to consequently genetically relate these veins to the Mohawk pluton as they likely represent the same directions of extension.

Veins at the Peak deposit, however, rarely display strikes of 90-110 and instead most commonly strike 320-340 (Fig. 4.5). This direction is also consistent with the overall 310 orientation of the Peak deposit (Fig. 3.14). If skarn-forming fluids moved up-dip

along such structures, then the source of the Peak deposit is below and to the east, as suggested by metal zoning. That is, the contrasting vein orientations for Peak (in addition to other lines of evidence) suggest that Peak is related to a buried pluton, and not to the Mohawk pluton. Further, this buried pluton must not be the same age as the Mohawk, as the Peak veins strike is different from the Mohawk pluton.

Allan et al. (2013) claim that NE-striking faults control late Cretaceous Au-Cu deposits in the Forty mile mining district (Fig. 1.6), NE of Peak. In contrast, I see no evidence either that NE-striking faults were present in the late Cretaceous at Peak or that mineralizing fluids migrated along NE-striking zones. Indeed, the strike direction which is least commonly displayed by faults, shears, and veins in the Peak area is NE (Figs. 4.5, 4.6, 4.7).

## Chapter 5 Pb, C and O Isotopic Studies

### 5.1 Introduction

Pb isotopes were analyzed to provide constraints on age of mineralization. Tok is near the Devonian to Mississippian Delta VMS district and the Cretaceous Tintina Gold Province. Contrasting Pb isotopic signatures between the Devonian and the Cretaceous rocks allow for a low resolution measure of age.

Carbonate oxygen and carbon isotopes were analyzed to evaluate variation, and to assess the degree of isotopic exchange that the marble has undergone during formation of the Peak deposit.

Galena from Chief Danny core was sampled and submitted to the Geochronology Laboratory at the University of British Columbia. Analyses were completed by Janet Gabites with the Department of Earth and Ocean Sciences, using standard procedures. Sample locations and characteristics are in Table 5.1. Two of the samples (13PI014P and 13PI104P) were from veins which cut Peak skarn. 13PI013D was from a vein in the Discovery zone.

Table 5.1: Galena samples taken for Pb-isotopic studies

| number | Drillhole | Depth (m) | Deposit | Occurrence# |
|---|---|---|---|---|
| 13PI013D | TET11005 | 331.5 | Disovery | Ag-rich asp-gl-spl-cp-po vein |
| 13PI014P | TET12038 | 146.3 | Upper | Ag-Bi-rich spl-cp-gl-po vein |
| 13PI104P | TET13088 | 146.2 | Peak | Au-Ag-Bi-Mo rich cp-gl-po |

# asp = arsenopyrite, gl = galena, spl = sphalerite, cp = chalcopyrite, po = pyrrhotite

Calcite samples from marble, skarn, and veins of the Chief Danny area were collected (Table 5.2) and sent for isotopic analysis. One sample ('E Marble') is from the NE edge of the map area (Figure 2.1); the others are located in the Peak zone or within 800 meters of the Peak zone (Table 5.2). Oxygen and carbon isotopes were measured by Andreas Beinlich and Britta Neumann of the Mineral Deposit Research Unit at the University of British Columbia. Samples were analyzed on a Los Gatos Research off-axis integrated cavity output spectrometer (OA-ICOS), model CCIA-46. The methodology is described in Barker et al. (2011).

Table 5.2: Samples employed for C and O isotopic analysis

| Sample ID | location | rock description | location |
|---|---|---|---|
| E Marble | 407200 E, 708800 N | equigranular calcite marble | 2.5 km NE of Peak |
| C1 | DH 13-112, 503 m | calcite marble with muscovite layers | 0.5 km SE of Peak |
| C2 | DH 13-101, 152 m | calcite marble with minor muscovite | E edge of Peak |
| C3 | DH 13-103, 129 m | calcite marble | NE edge of Peak |
| C4 | DH 11-03, 46 m | calcite marble with schist interlayers | 0.6 km NE of Peak |
| C5 | DH 13-85, 144 m | sulfide-amph skarn with interstitial calcite | SE Peak |
| C6 | DH 13-89, 75 m | sulfide-rich skarn cut by calcite vein | central Peak |
| C7 | DH 13-85, 160 m | schist cut by calcite-cemented breccia | SE Peak |
| C8 | DH 13-103, 166 m | quartz-sulfide-calcite vein | NE edge of Peak |

## 5.2 Pb Isotopic Results

Lead isotopic results (Table 5.3) show little variation among the samples; oddly, one of the Peak galenas (13PI104P) is more similar to the Discovery galena than to the other galena. This is true for all the isotopic ratios, but especially for $^{207}Pb/^{204}Pb$, for which 13PI104P and 13PI013D yielded statistically indistinguishable values.

Figure 5.1 shows the data from Table 5.3 plotted with data from (a) Cretaceous plutons and plutonic related sulfides and (b) Devono-Mississippian stratabound massive

sulfides from the Yukon-Tanana Terrane. Samples from Chief Danny clearly plot in the Cretaceous field, with $^{204}Pb/^{206}Pb$ ratios that are much too high to represent Paleozoic Pb. Due to similarities in isotopic ratios, the Pb at Chief Danny is most likely derived from Cretaceous plutonic sources (i.e., plutonic-derived fluids). The fact that the Pb from a Discovery Zone vein is nearly indistinguishable from one of the Peak samples further emphasizes the close genetic link between the two. Whether the Discovery vein is part of the same hydrothermal event that caused the Peak Zone is unknown, but the Pb isotopic data is permissive of such.

Table 5.3: Lead isotopic results for galena from the Chief Danny area*

| **Sample Number** | **206Pb / 204Pb** | +/- | **207Pb / 204Pb** | +/- | **208Pb / 204Pb** | +/- | **207Pb / 206Pb** | +/- | **208Pb / 206Pb** | +/- |
|---|---|---|---|---|---|---|---|---|---|---|
| 13PI-104P | 19.168 | 0.004 | 15.674 | 0.002 | 38.953 | 0.008 | 0.8177 | 0.0001 | 2.0322 | 0.0002 |
| 13PI-014P | 19.149 | 0.005 | 15.637 | 0.003 | 38.841 | 0.010 | 0.8166 | 0.0001 | 2.0284 | 0.0003 |
| 13PI-013D | 19.178 | 0.003 | 15.679 | 0.003 | 38.990 | 0.007 | 0.8175 | 0.0000 | 2.0330 | 0.0001 |

*Results have been normalized using a fractionation factor of 0.12%, based on multiple analyses of NBS981 standard lead, and the values in Thirlwall, 2000. Errors are reported at the 2 sigma level.

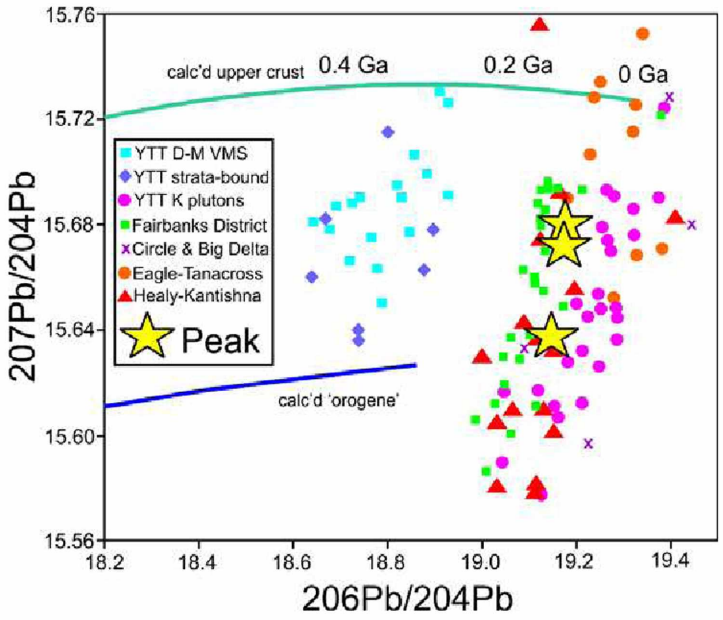


Figure 5.1: Peak lead isotopic data plotted with data from prospects and deposits of the Yukon-Tanana Terrane (YTT) of Interior Alaska and Yukon Territory. Blue symbols are for Devono-Mississippian stratabound deposits. All other symbols are for Cretaceous data: plutons (magenta circles) and plutonic-related deposits (others). Chief Danny data from Table 5.3. Non-Chief Danny data from: Aleinikoff et al. (1987), Godwin et al. (1988), and Gaccetta and Church, (1989).

### 5.3 Carbonate Carbon-Oxygen Isotopic Results

Carbon and oxygen isotopic measurements for the Chief Danny area (Table 5.3) show considerable variation. Most of the duplicate samples returned values that were within the quoted uncertainties of $\pm$ 0.6 permil, but the 'duplicate' sample C8 from DDH 13-103 is nothing like the original. The differences are disturbing.

Carbon and oxygen isotopic data are plotted along with reference fields and lines for studies involving contact metamorphism of carbonate rocks (Figure 5.2). In a general way much of the data follow the 'typical' change for increasing contact metamorphism as defined by Baumgartner and Valley (2001) and fields defined by data for Grenville marble (Kretz, 2001). The marble sample that is farthest from hydrothermal activity ('E Marble') has C/O isotopic ratios that plot in the field defined by Grenville marble (Kretz, 2001).

Marble samples from closer to Peak mineralization fall into two groups: (a) two (C3 and C4) have isotopic signatures near those of Grenville skarn (lower del $^{13}C$ with lower del $^{18}O$) and (b) two samples (C1 and C2) have values far from any for Grenville calcite (lower del $^{18}O$ but unchanged del $^{13}C$). Interstitial calcite sampled within skarn has an isotopic signature similar to the Grenville skarn and to two of the marble samples (Figure 5.2). Vein/breccia calcite samples again fall into two groups: (a) those with values similar to the skarn interstitial calcite (C6, C8) and those with isotopic values very much unlike all other values (C6 duplicate, C7). That two subsamples of the same vein calcite sample yield radically different results is problematic.

Table 5.4: Oxygen and carbon isotopic results from the Chief Danny area*

| Sample ID | location | Calcite type | del $^{13}C$ VPDB | del $^{18}O$ VSMOW |
|---|---|---|---|---|
| E Marble | 407222 E, 7088680N | marble | 3.30 | 18.50 |
| C1 | DH 13-112, 503 m | marble | 2.68 | 11.02 |
| C2 | DH 13-101, 152 m | marble | 3.14 | 9.47 |
| C2 dup | | | 2.41 | 10.06 |
| C3 | DH 13-103, 129 m | marble | -3.26 | 12.41 |
| C4 | DH 11-03, 46 m | marble | -2.85 | 9.91 |
| C5 | DH 13-85, 144 m | interstitial | -4.79 | 13.8 |
| C5 dup | | | -5.07 | 14.52 |
| C6 | DH 13-89, 75 m | vein | -4.74 | 10.29 |
| C6 dup | | | -4.36 | 10.26 |
| C7 | DH 13-85, 160 m | breccia | -10.12 | 13.28 |
| C8 | DH 13-103, 166 m | vein | -5.49 | 12.6 |
| C8 dup | | | -3.12 | 3.56 |

*standard deviation (1 sigma) is 0.63 for del $^{13C}$ and 0.64 for del $^{18}O$, based on repeated measurements of the BN13 calcite standard. Raw $\delta^{18}O$ values were converted to the V-SMOW scale using standard BN13; $\delta^{13}C$ was converted to the V-PDB scale using a two point calibration based on standards BN13 and Sigma Aldrich synthetic calcite. Dup = duplicate

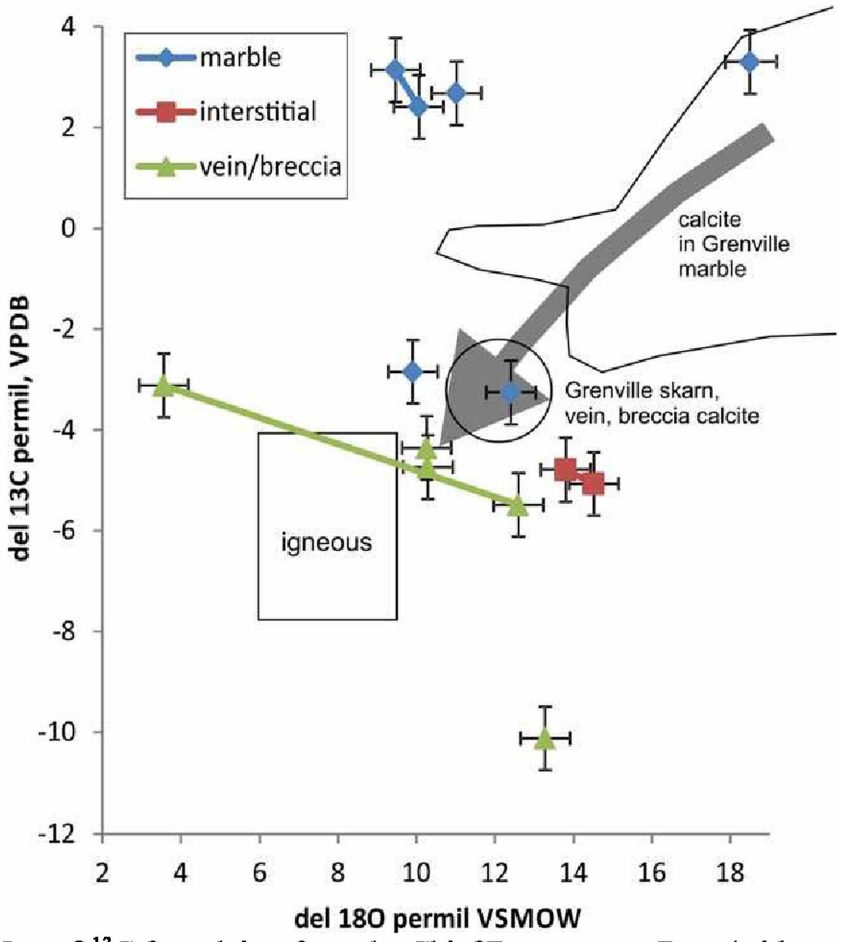


Fig 5.2: $\delta^{18}O$ vs. $\delta^{13}C$ for calcites from the Chief Danny area. Data (with quoted 1 sigma uncertainties) from this study. Fields for calcite from Grenville province marble and skarn, vein, and breccia are from Kretz, 2001. Box for igneous carbonate and generalized change with increasing contact metamorphism from Baumgartner and Valley (2001). Lines connect 'duplicate' analyses of the same sample.

## 5.4 Discussion

Galena isotopic analyses are particularly useful for distinguishing lead sampled from Paleozoic (older, less radiogenic lead) and Cretaceous (younger, more radiogenic lead) deposits. The data clearly indicate that although the Peak deposit is broadly stratiform, it cannot be a Paleozoic deposit which has recrystallized during contact metamorphism.

Carbonate isotopic results are more difficult to explain. Sample E Marble is located several kilometers from any manifestation of hydrothermal activity (Figure 2.1) and has an isotopic composition compatible with simple metamorphism of marine limestone. The other marble samples (located much closer to the Peak zone) although not visibly altered, display isotopic values requiring some degree of exchange with an external fluid, especially if E Marble is representative of local 'unaltered' marble. Half of these marble samples (with negative del $^{13}C$ values) are compatible with isotopic exchange between E Marble and a magmatic fluid (Figure 5.2). The other two marble samples (positive del $^{13}C$) require exchange with something else and (or) some different process or starting material. Nevertheless, the 4 marble samples closer to Peak Zone than E Marble uniformly yielded del $^{18}O$ values significantly lighter than that of 'E Marble'

Calcite in skarn yielded isotopic values not far from the isotopically light marble samples, suggesting that it represents 'residual' carbonate from the isotopically altered marble. Similarly, half of the vein/breccia samples yield 'reasonable' isotopic values similar to those of the interstitial skarn calcite (suggesting remobilization of calcite formed during contact metamorphism) the other half yield anomalous values with no ready explanation. Unfortunately, both ''reasonable' and 'anomalous' values were given by two aliquots of the same sample. This implies either analytical problems or gross isotopic variability within a single vein sample.

In sum, Pb isotopic data unambiguously indicate that Peak and Discovery Zone mineralization are Cretaceous and related to Cretaceous intrusions. If the marble sample spatially farthest from known mineralization is representative of 'original' marble, then O isotopes provide a means for assessing proximity to the hydrothermal footprint: Calcite

with del $^{18}O$ lighter than -12 per mil is located within 800 m of mineralization. Outside of this, the O/C isotopic data require either multiple source materials, multiple processes, and (or) multiple fluid types.

## Chapter 6 Radiometric Dating

### 6.1 Introduction

Radiometric dating was completed on plutonic, skarn and volcanic rocks to determine the chronology of Au-Cu mineralization and nearby magmatism. Typical skarn deposits (dominated by garnet + pyroxene) lack an abundance of potassium bearing minerals and are problematic to date. Normally cross cutting relationships and inferred igneous fluid sources are used to bracket the age of formation. In recent studies, garnet by U-Pb (Meinert et al., 2001), phlogopite by $^{40}Ar/^{39}Ar$ (Beuchat, 2003) and actinolite and hornblende by U-Pb (Mueller et al., 2004) have been used to directly date skarn formation. In this study I have directly dated skarn formation at the Peak deposit with ferroedenite-hastingsite by the $^{40}Ar/^{39}Ar$ method. Both U-Pb and $^{40}Ar/^{39}Ar$ methods were used to date igneous activity near the Peak deposit and to establish relative ages of plutonism, and volcanism and Peak skarn formation. Related igneous units are the porphyritic Mohawk pluton and basaltic andesite (Figure 2.1).

In typical skarn systems amphibole is not an abundant silicate phase and is difficult to separate from the rest of the calc-silicate assemblage. In addition it is commonly K-poor and Ca-rich, making it difficult to date by Ar radiometric techniques. At Peak, textural relationships between amphibole and sulfide suggest the two formed at or near the same time. The abundance of amphibole in the Peak deposit (>90% of silicates) allows for successful separation of the amphibole from other minerals which is necessary for accurate age analysis.

In addition to data from Tetlin lands, $^{40}Ar/^{39}Ar$ radiometric ages from the Road metal prospect (Figure 1.6, 1.7) near Northway are presented (Doyon Ltd. Unpubl. Report) with permission from Doyon Native Corporation. These ages are used to show coeval magmatism and Cu +/- Au mineralization also occurred near Northway, AK.

## 6.2 Methodology

### 6.2.1 Methods Overview

A total of 5 samples were dated in this study (Table 6.1). All samples for $^{40}Ar/^{39}Ar$ geochronology were prepared and dated by Jeff Benowitz at the Geochronology Laboratory at the University of Alaska Fairbanks. The single U-Pb analysis was completed by Paul O'Sullivan at Apatite to Zircon, Inc. Skarn and plutonic samples were cut from halved core at downhole depths ranging from approximately 52 meters to 185 meters (Table 6.2), that is, well below the zone of surface oxidation. Volcanic rock was sampled at the surface. Locations are given in North American Datum of 1983 (NAD83) Zone 7 for Universal Transverse Mercator (UTM). Locations for skarn and plutonic samples were calculated in LeapFrog™ using drill collar locations and downhole survey data. Collar locations were measured with differential GPS with an error of less than a tenth of a meter. Surface sample locations were measured from a handheld GPS unit and are accurate within 3 meters.

### 6.2.2 $^{40}Ar/^{39}Ar$ Dating Methodology

For $^{40}Ar/^{39}Ar$ analysis samples were submitted to the Geochronology laboratory at UAF where they were crushed, sieved, washed and hand-picked for hornblende mineral phases. The monitor mineral MMhb-1 (Samson and Alexander, 1987) with an age of 523.5 Ma (Renne et al., 1994) was used to monitor neutron flux (and calculate the irradiation parameter, J). The samples and standards were wrapped in aluminum foil and loaded into aluminum cans of 2.5 cm diameter and 6 cm height. The samples were irradiated in position 5c of the uranium enriched research reactor of McMaster University in Hamilton, Ontario, Canada for various megawatt-hours.

Table 6.1: Locations of samples for radiometric dating

| Sample Name | mineral | technique | UTM mE | UTM mN | Elevation (m) |
|---|---|---|---|---|---|
| TETPI024 | hornblende | $^{40}Ar/^{39}Ar$ | 404725 | 7007499 | 827 |
| TETPI034 | hornblende | $^{40}Ar/^{39}Ar$ | 404723 | 7007499 | 825 |
| TETPI035 | hornblende | $^{40}Ar/^{39}Ar$ | 402790 | 7008559 | 768 |
| TETPI100 | hornblende | $^{40}Ar/^{39}Ar$ | 404786 | 7009759 | surface |
| TETPI100 | zircon | U-Pb | 404786 | 7009759 | surface |

Upon the return from the reactor, the sample and monitors were loaded into 2 mm diameter holes in a copper tray that was then loaded in a ultra-high vacuum extraction line. The monitors were fused, and samples heated, using a 6-watt argon-ion laser following the technique described in York et al. (1981), Layer et al. (1987) and Benowitz et al. (2014).

### 6.2.3 Zircon U-Pb Dating Methodology

Thirty zircon grains were isolated and prepared for Laser Ablation ICP-MS (LA-ICP-MS) analysis using standard procedures combined with specific customized procedures described by Donelick et al. (2005). These 30 grains were analyzed by LA-ICP-MS at the Geoanalytical Laboratory, Washington State University, Pullman, Washington, U.S.A. Individual zircon grains were analyzed using a New Wave YP213 213 nm solid state laser ablation system using a 20 μm diameter laser spot size, 5 Hz laser firing rate, and ultra-high purity He as the carrier gas, as described in Solie et al. (2014). Of the 30 zircons, 28 were successfully analyzed and 24 yielded ages that were employed in determining the mean age.

### 6.2.4 Sample Descriptions

#### 13PI034 Ferroedenite-Hastingsite

Amphibole skarn was sampled at 184.7 meters down hole in drill hole TET12035, in the core of the Peak zone skarn. Electron probe microanalysis (Appendix 3) indicates these amphiboles typically contain 2-3 wt% Cl and 2-2.5 wt% $K_2O$ and are high-Al with compositions of ferroedenite-hastingsite (Figure 2.13). Amphiboles in the sample are typically coarse (0.5-2 mm), randomly oriented, intergrown with sulfide, and possess uniform optical properties (Figure 6.1B). The amphiboles show no sign of weathering or hydrothermal alteration.

**13PI024 Amphibole**

Amphibole skarn was sampled at 181.6 meters down hole in drill hole TET12035, within the core of the Peak skarn, approximately 3 meters above sample 13PI035. Amphibole in this sample occurs both as isolated grains and as clusters intergrown with clinopyroxene (Figure 6.1A). The amphiboles display variations in pleochroism within a single grain that indicate compositional zoning. The typical amphiboles are 100-200 microns long and 50-70 microns in diameter. The amphiboles display no evidence for weathering or secondary alteration.

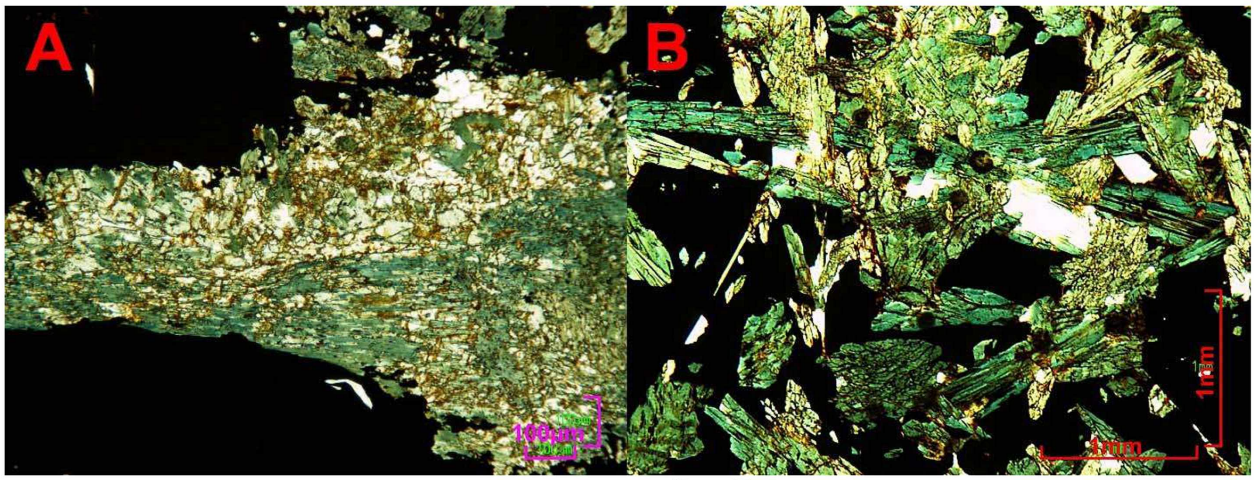


Figure 6.1: Photomicrographs of skarn sampled for $^{40}Ar/^{39}Ar$ radiometric age analysis. A) Sample 13PI24--fine grained amphibole cluster (green) intergrown with clinopyroxene (colorless) . B) Sample 13PI34--coarse grained, randomly oriented amphibole intergrown with sulfide.

**13PI035 Hornblende**

Hornblende was sampled at 68.5 meters down hole in drill hole TET11006, from the Mohawk pluton. The sample is 2.3 kilometers northwest of the Peak skarn (Figure 2.1; Table 6.1). Figure 6.2 is a photomicrograph taken from a thin section in the same interval

from which 13PI035 was sampled. Thin section examination indicated that although biotite has undergone partial alteration to chlorite, the hornblende shows no sign of alteration. 13PI035 was sampled in part of the core that showed the least amount of chloritization.

This same sample contained numerous euhedral zircon grains, most commonly visible as 50-80 micron inclusions in hornblende and biotite. Five kilograms of this interval of drill core was submitted for zircon separation and U-Pb dating.

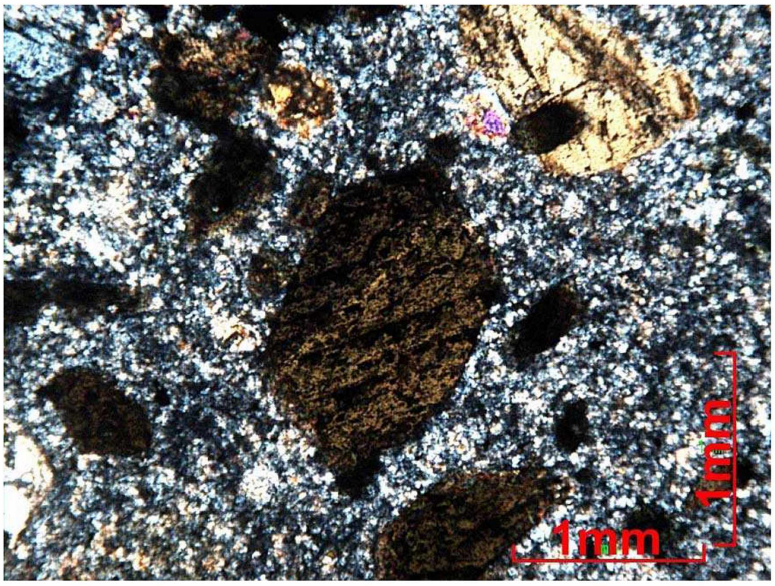


Figure 6.2: Crossed polars photomicrograph of hornblende in the Mohawk pluton.

**TETPI Hornblende**

Hornblende was sampled from a surface sample (14PI100) of basaltic andesite located approximately 500 meters north of the Peak deposit (Figure 2.1, Table 6.1). Hornblende is the predominant phenocryst in the basaltic andesite. There is a thin rim of oxidation around the surface of the sample and a single fracture with minimal oxidation

(Figure 2.5). This sample was chosen because of coarse grained hornblende (up to 1cm) and the lack of weathering or secondary alteration.

### 6.3 Results

A summary of all the radiometric results is given in Table 6.2, with all ages quoted to the ± 1 sigma level and calculated using the constants of Renne et al. (2010). The integrated age is the age given by the total gas measured and is analogous to a potassium-argon (K-Ar) age. The $^{40}Ar/^{39}Ar$ spectrum provides a plateau age if three or more consecutive gas fractions represent at least 50% of the total gas release and are within two standard deviations of each other (Mean Square Weighted Deviation less than ~2.5). The complete data set, including apparent ages, Ca/K ratios, and Cl/K ratios are given in Appendix 5.

All of the 28 zircons successfully analyzed yielded concordant ages (Figure 6.3); however, two of the zircons yielded anomalously old ages (late Paleozoic and mid-Cretaceous, Appendix 5). Two other zircons yielded ages of approximately 75 Ma, that is, 5 Ma older than the mean of the remaining 24 zircons (Figure 6.4). The mean age and one sigma uncertainty reported in Table 6.2 are based on the 24 remaining ages.

Table 6.2: Summary of radiometric age determinations with 1 sigma errors

| Sample | Rock | Mineral | Method | Plateau age | Integrated Age |
|---|---|---|---|---|---|
| TETPI024 | Skarn | hbl#1 | $^{40}Ar/^{39}Ar$ | 69.9±0.5 Ma | 70.1±0.5 Ma |
| | Skarn | hbl#2 | | 68.9±0.4 Ma | 68.9±0.4 Ma |
| TETPI034 | Skarn | hbl#1 | $^{40}Ar/^{39}Ar$ | 72.1±0.5 Ma | 72.1±0.5 Ma |
| | Skarn | hbl#2 | | 71.0±0.4 Ma | 70.9±0.4 Ma |
| TETPI035 | Qz-monz | hbl#1 | $^{40}Ar/^{39}Ar$ | 70.0 ±0.5 Ma | 71.2±0.7 Ma |
| | Qz-monz | hbl#2 | | 68.7±0.6 Ma | 68.0±0.7 Ma |
| TETPI | Andesite | hbl#1 | $^{40}Ar/^{39}Ar$ | 75.3 ±0.5 Ma | 73.7±0.5 Ma |
| | Andesite | hbl#2 | | 75.2+0.6 Ma | 76.6±0.9 Ma |
| TETPI035 | Qz-monz | Zircon | U-Pb | | 69.7 ±0.2 Ma |

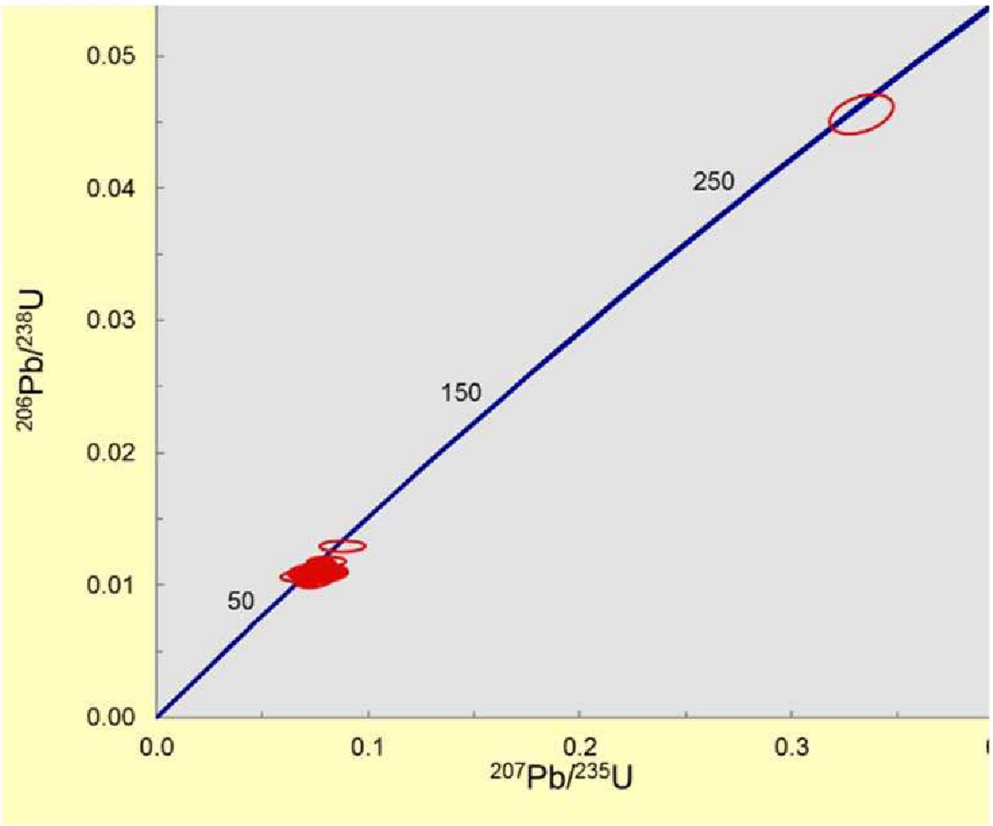


Figure 6.3: Concordia plot for analyzed zircons. The two zircons with anomalous old ages were not used in the mean age calculation. Error ellipses are two sigma.

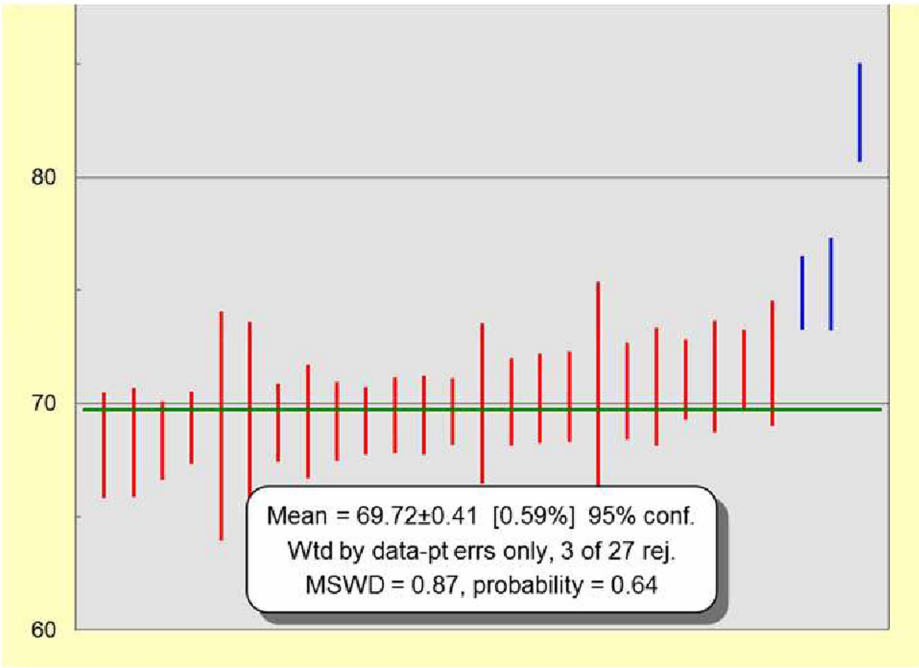


Figure 6.4: Plot showing zircon U-Pb ages and 2 sigma uncertainties (Ma) for 27 zircons from the Mohawk pluton. Data represented by the blue lines (3 oldest apparent ages) were not employed in the mean age calculated (green line).

**6.4 Discussion**

All the $^{40}Ar/^{39}Ar$ spectra display low temperature steps with high errors--but no systematic patterns--followed by relatively flat plateaus (Appendix 5). Such spectra are typical of minerals that have neither lost nor gained Ar after they cooled to their Ar retention temperatures (McDougall and Harrison, 1999). In contrast, most of the samples yielded either anomalously high or anomalously low Ca/K ratios for the first 1-3% of Ar released. Sample PI100—hornblende phenocryst from basaltic andesite—yielded anomalously high Ca/K for the first 10% of Ar released whereas sample PI035 (hornblende from the pluton) yielded anomalously low Ca/K for the 5-15% of Ar released (Appendix 5). These results almost certainly indicate that the hornblende samples contained small amounts of impurity minerals that degassed early in the heating sequence. Ar released from

these low-temperature fractions was not used in calculating the plateau ages. That these fractions are insignificant is indicated by the close agreement between plateau and integrated ages (Table 6.2).

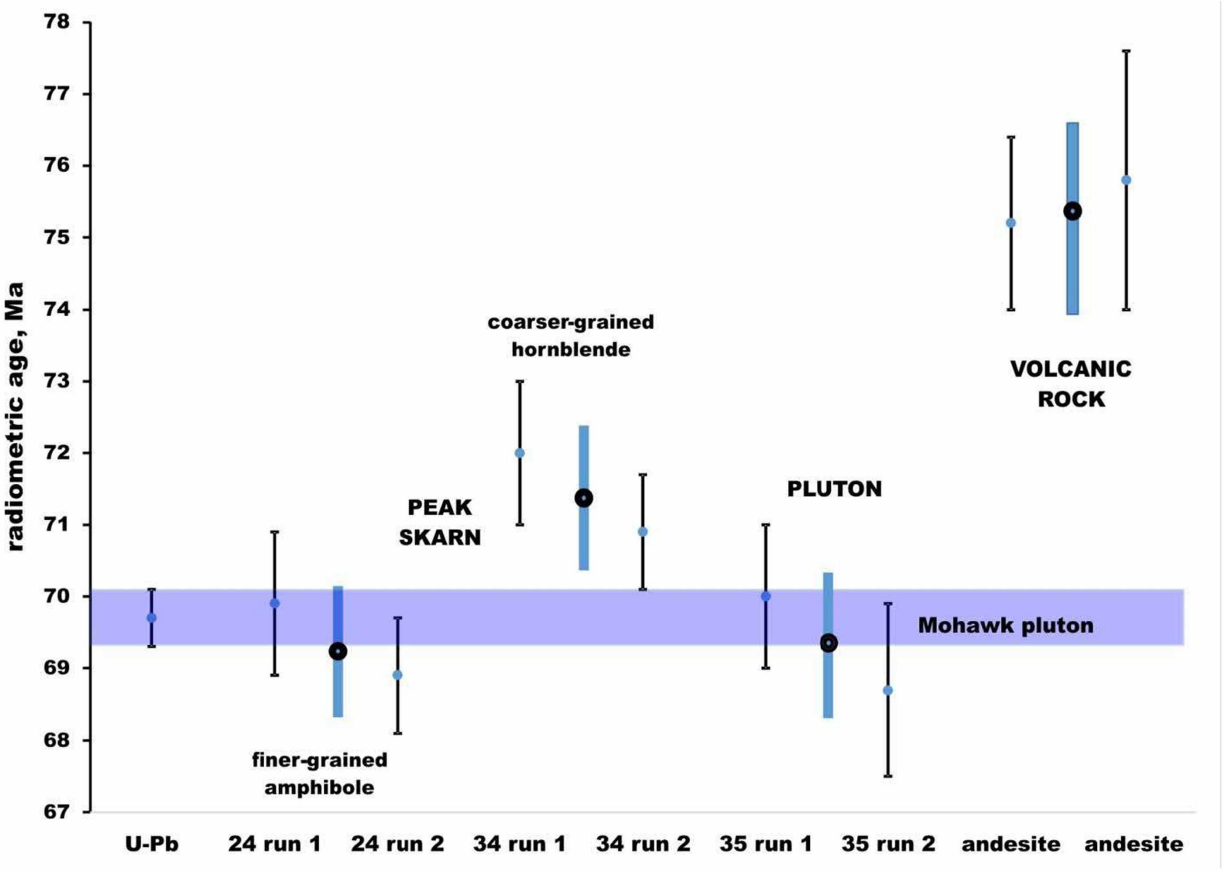


Figure 6.5: Radiometric ages for samples from the Tetlin area, with two sigma errors. Dark circles and thicker bands are average ages for the $^{40}Ar/^{39}Ar$ determinations. Data modified from Table 6.2.

Figure 6.5 shows the ages for the various samples plotted by sample number with two sigma analytical error bars. The duplicate $^{40}Ar/^{39}Ar$ age determinations are all statistically indistinguishable at the two sigma uncertainties and several ages are distinguishable based on this data. The most straightforward radiometric results are the U-Pb age (69.7$\pm$ 0.2 Ma, Table 6.2) and the $^{40}Ar/^{39}Ar$ ages for hornblende from volcanic rocks (75.5$\pm$0.7 Ma). Based on these results (Figure. 6.5; Table 6.2) the volcanic rocks

are approximately 5 Ma older than the pluton. This age difference is sufficiently great to require that they represent different batches of magma. In contrast, the mean age for hornblende (69.4 $\pm$ 0.5 Ma) and zircon (69.7$\pm$ 0.2 Ma) from the Mohawk pluton are statistically indistinguishable at the 1 sigma level and especially at the 2 sigma level (Figure 6.5). This lack of difference indicates that the pluton, and presumably the surrounding rocks, has not experienced a younger thermal event.

The skarn $^{40}Ar/^{39}Ar$ ages are problematic, however, because the two samples—3 meters apart in the drill core—yield statistically different ages (Figure 6.5, Table 6.2) even at the two sigma uncertainty. It is difficult to imagine that they truly represent different ages of formation, as any hydrothermal event of high enough temperature to create new amphibole would most likely cause the older amphibole—located 3 meters away—to experience some Ar loss or gain. Evidence of such is not obvious in the Ar spectra: all 4 of these exhibit flat plateaus that account for the bulk of Ar in the samples (Appendix 6).

The two easiest explanations for the age difference between the samples are (a) the 'older' hornblende contains 'excess' radiogenic argon and (b) the 'younger' hornblende continued loosing Ar by diffusion at temperatures below the Ar retention temperature of the 'older' hornblende. Neither explanation can be conclusively rejected, but the 'excess Ar' seems less likely.

Hornblende that has acquired Ar either during original formation or by diffusion after formation commonly either displays a so-called 'saddle' spectrum (youngest age at intermediate temperature fractions) or gives rise to an isochron with an initial $^{40}Ar/^{36}Ar$ ratio significantly greater than the present atmosphere (295.5). None of the spectra

exhibit 'saddle' behavior and none yield isochron diagrams with initial Ar ratios significantly different from atmospheric (Appendix 6). In sum, although 'excess radiogenic Ar' as the cause for the older skarn hornblende age cannot be ruled out, there is no evidence for such in the data.

In contrast, two different lines of evidence are consistent with the hypothesis that the 'younger' skarn hornblende age is due to greater diffusional loss of radiogenic Ar during initial cooling. These explanations involve grain size and compositional differences between hornblende in the two samples.

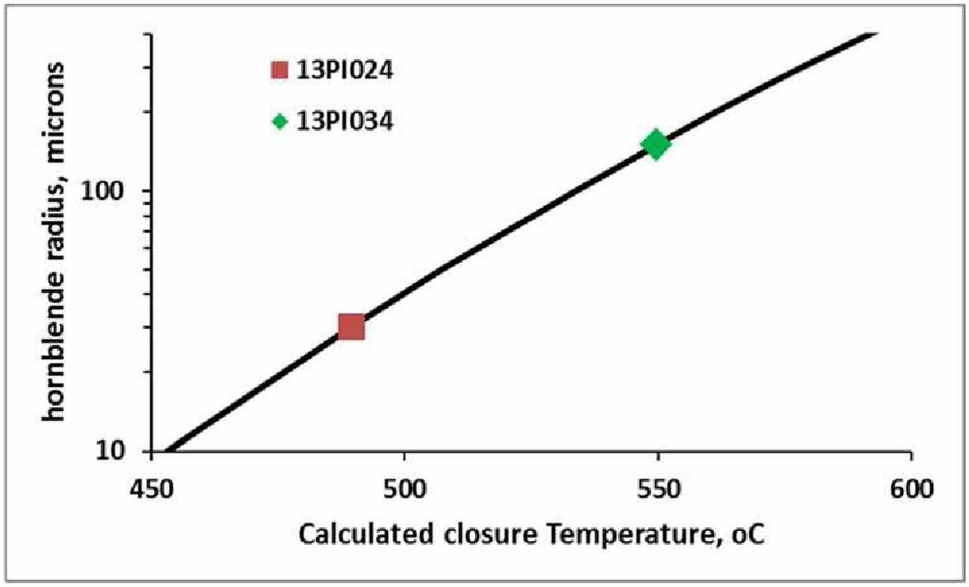


Figure 6.6: Calculated Ar closure temperature for hornblende modeled as a cylinder with variable radius, based on equations in McDougall and Harrison (1999). Model parameters are E = 64 kcal/mole, $D_o$ = 0.6 $cm^2$/sec, A =55, and cooling rate of 100°C/ Ma.

Diffusion theory requires that the smaller the grain size of a mineral, the lower the temperature at which it retains Ar. Using equations from McDougall and Harrison (1999) Figure 6.6 shows calculated Ar retention temperature versus hornblende radius for a diffusion model based on a uniform cylinder. These calculations are for a hornblende of 'typical' composition with 'typical' diffusional properties. The relative values of closure temperature are more important than the absolute values, as the latter depend on the actual composition of the amphibole (McDougall and Harrison, 1999). Based on the typical amphibole grain sizes estimated from thin section, the 'younger' amphibole should be open to Ar loss to a temperature approximately 60°C lower than that of the coarser grained amphibole. For a minimum cooling rate of 100°C per Ma, this amphibole should have reached its Ar retention temperature approximately 0.6 Ma later than the coarser amphibole. For a more realistic cooling rate of 200°C/Ma, the time gap drops to 0.3 Ma. Consequently, difference in grain size alone cannot explain the apparent 2 Ma difference in age (Table 6.2) between the two amphiboles.

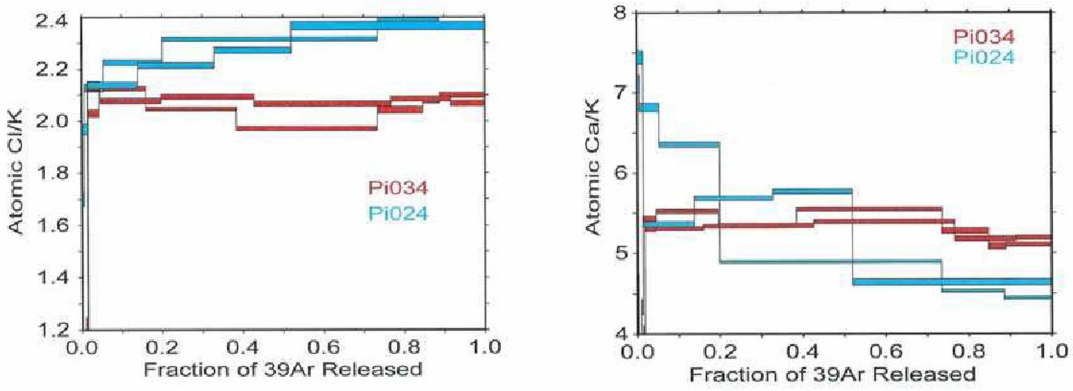


Figure 6.7: elemental ratios vs. fraction Ar released for two runs of the two different skarn amphiboles from the Peak deposit. A = atomic Ca/K. B = atomic Cl/K. Data from appendix 5.

A second explanation lies in the compositional differences between the two different amphibole samples, as indicated by differences in their Ca/K and Cl/K ratios (Figure 6.7). Sample PI034, the 'older' hornblende, is characterized by extremely uniform Ca/K and Cl/K ratios, consistent with the petrographic uniformity in optical characteristics. In contrast, sample PI024, the 'younger' amphibole, appears to contain a mix of two compositionally distinct amphiboles: one with high Ca/K and low Cl/K, which released Ar at lower temperatures and the other with lower Ca/K and higher Cl/K, apparent in the higher temperature fractions (Figure 6.7). These differences are consistent with petrographic observations of zoning between a darker and a paler amphibole within a single grain in the thin section.

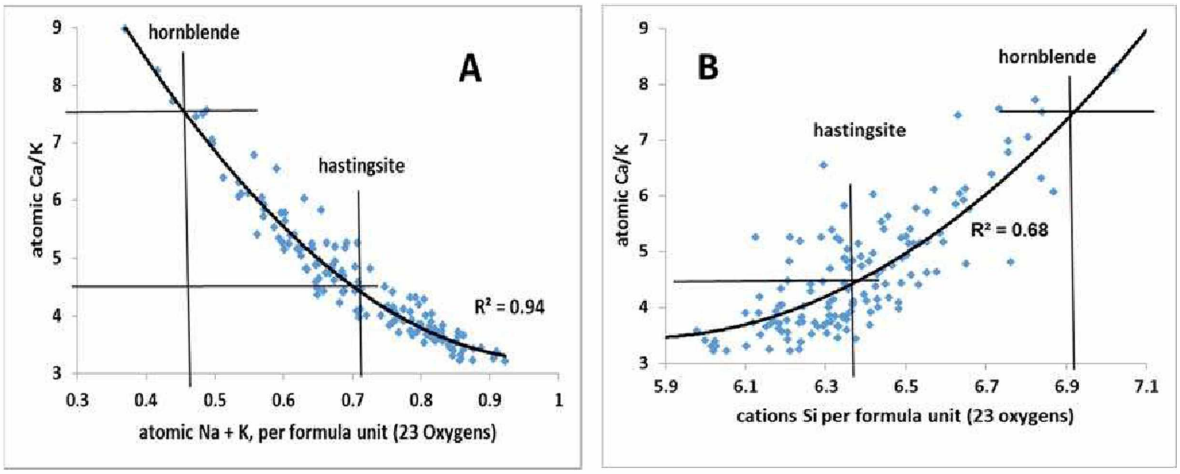


Figure 6.8: Relations between atomic Ca/K and other compositional characteristics of Peak amphiboles. Data in Appendix 3. Horizontal lines represent the approximate maximum and minimum values for Ca/K in sample PI024 based on Ar data (Appendix 6).

The compositional significance of the wide variations in Ca/K ratios for sample PI024 are ultimately related to the compositions of the amphiboles, as previously described. Individual analyses of Peak amphiboles show strong relations between atomic

Ca/K and other compositional variables. These are ultimately due to the fact that in calcic amphiboles, Na and K occur in a site that contains 0 to 1 Na+K (per formula unit) and filling this site requires coupled substitutions with other cations. In particular, Figure 6.8 shows a very strong relationship between atomic Ca/K and total Na+K and a strong relationship between Ca/K and Si per formula unit. Both of these parameters are critical to naming amphiboles (Fig 2.13) and the Ca/K data indicate that sample PI024 contains intergrown hornblende (higher Ca/K) and hastingsite (lower Ca/K).

The significance of the evidence for two different intergrown amphiboles is twofold. First, Ar retention temperature is a function of the amount of Si (Tschermak substitution) and the amount of Na+K. Lower Si (higher Al) and higher Na+K significantly raise the Ar retention temperature of amphibole (McDougall and Harrison, 1999). That is, these grains did not uniformly lose Ar by diffusion during cooling. Second, the presence of multiple compositional domains will cause the effective grain size of the mineral (with regards to diffusion) to decrease, as abrupt domain boundaries tend to be regions of relatively easy Ar loss (McDougall and Harrison, 1999).

In sum, the differences in apparent age between samples PI024 and PI034 are most readily explained as a combination of differences in grain size and differences in compositional uniformity. That is, the coarser, compositionally uniform amphibole (PI034) has yielded a reliably older 'true' age of formation whereas the finer grained and compositionally zoned amphibole (PI024) yielded an age significantly younger than the age of formation.

If the coarser-grained hornblende does yield the more reliable age of 71.5 $\pm$ 0.5 Ma (1 sigma) then the Peak skarn is significantly older than the Mohawk pluton (69.7 $\pm$ 0.2

Ma) and the Mohawk pluton cannot be responsible for the Peak mineralization. However, the $^{40}Ar/^{39}Ar$ age of volcanic rock near the Peak deposit suggests that either there was a relatively shallow magmatic system that lasted for a minimum of 5 Ma or that several 'batches' of magma were intruded and (or) extruded over a 5 Ma time period. This system includes the Mohawk pluton, the Peak skarn (and the presumed plutonic source below it), and volcanic rocks of basaltic-andesite composition. It is unknown whether the rhyolitic volcanic rocks, the Saddle garnet + pyroxene skarn and the Mohawk skarn are part of these magmatic events.

## Chapter 7 Discussion and Conclusions

### 7.1 Introduction

In my study of the Peak deposit I have presented a variety of geologic, compositional and mineralogical data in order to help create a genetic model for Au-Cu mineralization on Tetlin land. I will discuss this model and suggestions for further work from the deposit to regional scales. My goal is to increase our understanding of how the Peak deposit formed and the implications for mineral exploration in eastern interior Alaska.

The Peak skarn, defined exclusively by drilling, apparently consists of a single folded marble horizon replaced by randomly oriented, Cl-rich ferroedenite to hastingsite skarn ± chlorite; disseminated pyrrhotite, arsenopyrite, chalcopyrite; and semi-massive to massive pyrrhotite-arsenopyrite-chalcopyrite replacement of carbonate. Hedenbergitic pyroxene is rarely present as remnants retrograded to amphibole, quartz and calcite. Amphiboles are commonly coarse (mm) radial 'sprays' that do not exhibit pyroxene pseudomorph textures. The ferroedenite to hastingsite-rich skarn is, in turn, variably replaced by ferroactinolite ± chlorite ± calcite-quartz-sulfide. Euhedral quartz + Zn-Pb-Sb-rich coarse-grained sulfide mineralization is interpreted to be the lowest temperature assemblage and occurs as massive replacements and steeply dipping veins. Copper-bearing mineralization occurs throughout the Peak deposit, while gold-rich ore occurs in the updip and westerly portions.

Skarn is present in three different fault blocks, with uncertain temporal and spatial relations. Au-Cu skarn mineralization at the Peak deposit is not spatially associated with any known pluton or dike. Skarns at Mohawk (at depth) and Saddle (surface) contain

clinopyroxene + amphibole ± garnet and have received minimal exploration activity to date.

Based on a limited number of analyses, pyroxene compositions range from $Hd_{33-95}$ (Peak) through $Hd_{49-96}$ (Mohawk) to $Hd_{26-70}$ (Saddle). The Saddle prospect also contains garnet ranging from essentially pure andradite to 20% andradite and pyrite as the principal sulfide mineral. The high-Fe pyroxene at Peak, combined with pyrrhotite-dominated sulfide minerals and a lack of garnet, suggest a relatively low formation temperature and relatively low oxidation state. All of the skarns, which contain at least traces of pyrrhotite and high-iron pyroxenes, formed at relatively low oxidation states. Such low oxidation states are typical of gold-rich skarn deposits (Newberry et al., 1997).

I suspect that the three known skarns are only broadly related. Cl- and Fe-rich amphibole cuts and replaces earlier calc-silicates at all three. Amphiboles exhibit a general decrease in Cl with decreasing Fe/(Fe + Mg) and have the highest Cl contents of any known skarn amphiboles in Alaska. The generally higher Cl contents of amphiboles from Peak indicate that higher-Cl fluids were responsible for both silicates and associated ore deposition.

Pyrrhotite is the predominant sulfide mineral in skarn and massive sulfide at the Peak deposit. Native bismuth is abundant throughout the deposit and accounts for the bulk of Bi present. Bismuth and gold exhibit a weaker correlation than is typical of other Alaskan pluton-related deposits (e.g., Flanigan et al., 2000) as native bismuth occurs in gold absent, copper-rich ores but is also spatially associated with Au grains. Arsenopyrite (variably Co-enriched) is present throughout the deposit, typically with pyrrhotite and Au. Copper mineralization is chalcopyrite-rich. Gold mineralization is predominantly native

gold with trace jonassonite ($AuBi_5S_4$). Gold grains are most often inclusions in or adjacent to arsenopyrite and are up to one millimeter in diameter. Silver occurs in solid solution with gold, as pyrargyrite ($Ag_3SbS_3$), and as Hessite ($Ag_2Te$) in high Ag:Au ores. Minerals associated with native gold in trace amounts include hedlyite (Bi7Te3), breithauptite (Ni,Fe)Sb, ulmannite (Ni,Co)SbS, and Joseite-A (Bi4TeS2). Molybdenite is rarely present.

Late Cretaceous magmatism, responsible for Au, Cu and Mo deposition at Peak, began by 75 Ma and continued until at least 70 Ma. Hornblende from basaltic andesite records an age of eruption at 75.1 Ma; skarn amphibole formation at 71 Ma and crystallization of the Mohawk quartz monzonite pluton at 69.7 Ma. This record suggests intrusive rocks, extrusive rocks, and skarn were broadly comagmatic over a five million year period. In particular, a combination of $^{40}Ar/^{39}Ar$ and U-Pb dating indicates that the Peak deposit formed approximately 1 million years before intrusion of the Mohawk pluton (Figure 6.5). The Saddle skarn is spatially associated with an igneous-matrix breccia body similar in composition to nearby rhyolitic volcanic rocks, and different in composition from the Mohawk pluton (Figure 2.3).

All outcrops and intercepts of intrusions are greater than 1 km from the Peak deposit and are in separate fault blocks (Figure 2.1). The displacement along these faults postdates mineralization and the original position of this intrusive body relative to the Peak deposit is poorly constrained. Although the intrusion has a porphyry texture and it is in the vicinity of the Mohawk skarn, the radiometric ages indicate that the Mohawk pluton did not cause the Peak deposit. Lacking outcrop of a responsible pluton with an appropriate age, one must postulate that the pluton responsible for Peak is below and to the east of Peak, in an area not currently drilled (Figure 7.1). Based upon gold and copper endowment, amphibole

composition zoning, and late Pb-Zn-Sb vein orientations, fluids came from a pluton at depth. Post mineralization alteration is recorded in the alteration of primary skarn amphibole from hastingsite/ferroedenite to hornblende/ferro-actinolite, brecciation of skarn, semi-massive sulfide with calcite infilling and Pb-Zn-Sb veining which cuts all metamorphic rocks. No other major igneous activity has been recorded. Steeply-dipping faults with probably normal displacement postdate igneous activity at Tetlin and preserved volcanic rocks in the down-dropped blocks.

In summary the Peak Au-Cu deposit formed from a chain of geologic events between the Paleozoic and the late Cretaceous. A combination of receptive calcareous units, fluid conduits and the emplacement of magmas that generated metal-bearing hydrothermal fluids led to Au-Cu rich amphibole mineralization observed at the Peak deposit.

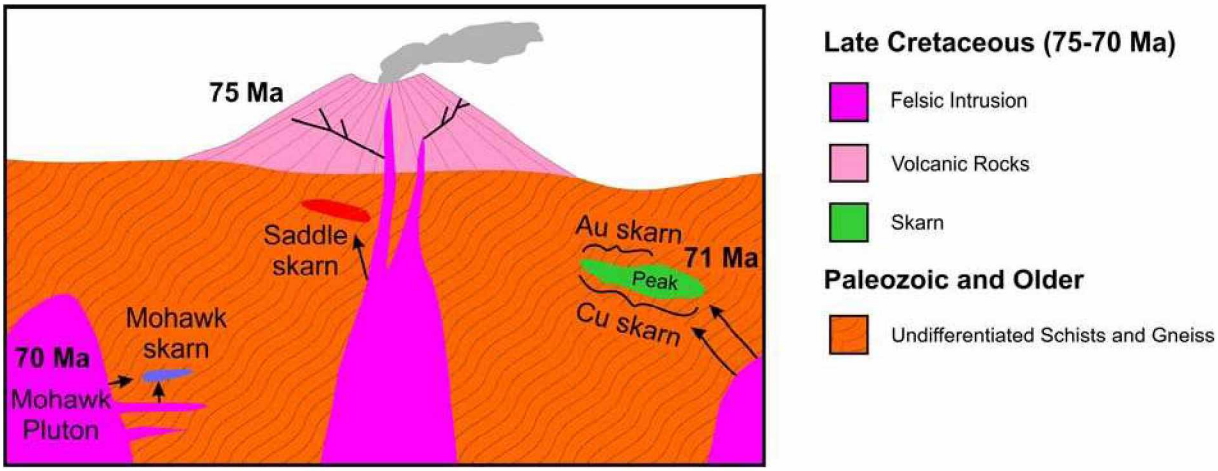


Figure 7.1: Cartoon cross section showing extrusive rocks, intrusive rocks, and skarn in the context of several independent hydrothermal systems suggested by radiometric dating. Although the 3 different igneous bodies are broadly related, they likely represent independently-derived magmatic bodies.

Pre-Cretaceous regional deformation formed complexly folded metamorphic rocks including amphibolite and micaceous marble. Contrasting compositions of metamorphic units control the distribution of Au-Cu ore. Marble is a sparse constituent of the metamorphic package and is the inferred protolith for skarn on Tetlin property, therefore controlling the distribution and morphology of skarn and carbonate replacement mineralization.

The age and geochemistry of igneous rocks and metallogeny of skarn on Tetlin lands suggest that it is part of the same magmatic event which formed the late Cretaceous porphyry deposits in Canada's Yukon. The Road Metal prospect has a broadly similar metallogeny (but with less Cu and more Ag) and age (69 Ma); limited compositional data suggests the Late Cretaceous magmas were broadly arc-related. Although Peak is near a major NE trending fault (Tok River fault, Figure 7.2) which lines up with other ~70 Ma prospects of the region, NE striking structures do not control mineralization and a single narrow NE-trending belt cannot explain the spatial distribution of 70 Ma prospects in the region. One possible explanation calls for several different NE-trending belts (one including Road Metal, another including Peak, and a third including Mosquito), another is a broad WNW trending belt of intrusion- related prospects including Road Metal and Mosquito (Figure 7.2).

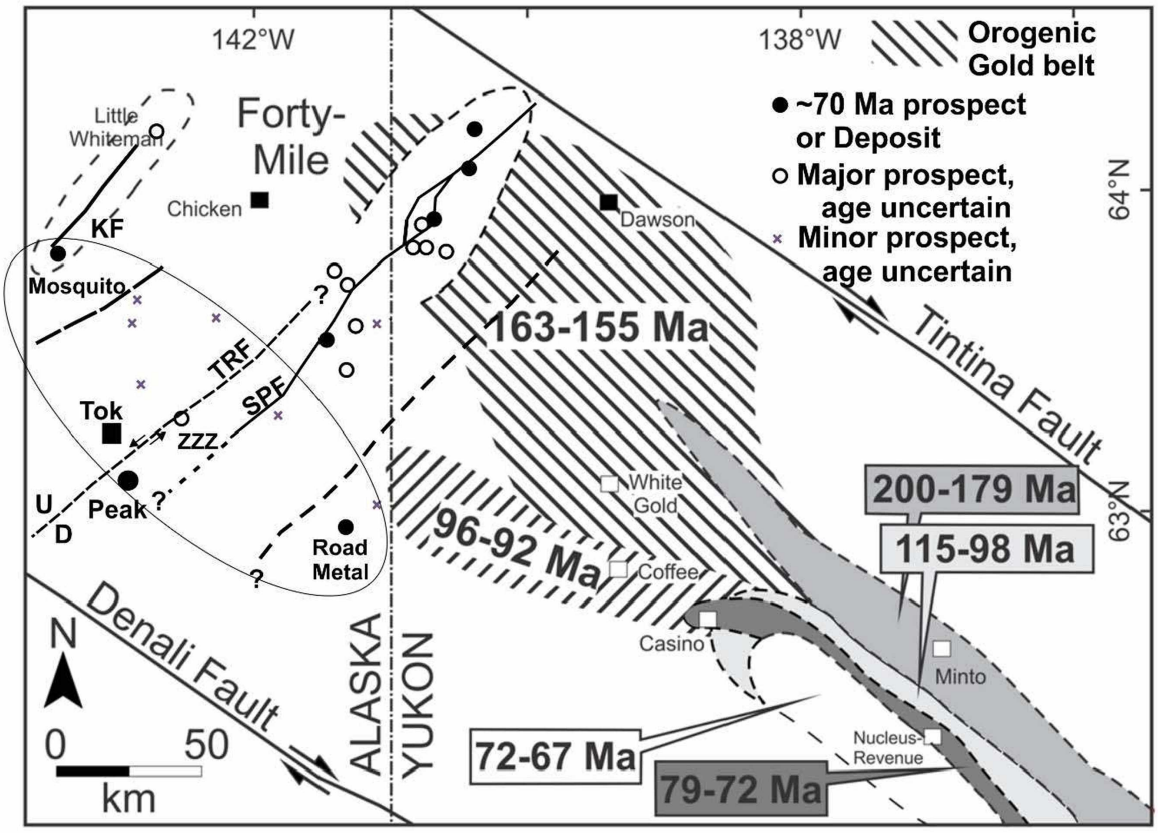


Figure 7.2: Postulated mineralization belts in Eastern Alaska and Western Yukon with several known steeply-dipping, NE-trending faults. Modified from Allan et al. (2013). SPF = Sixtymile-Pika fault; KF=Ketchumupstuck fault. TRF = Tok River fault. NW-trending oval is a postulated locus of ~ 70 Ma intrusion-related mineralization in eastern Interior Alaska.

The problem of assigning mineralization belts is seen at still broader scales than Figure 7.2. Graham et al. (2013) proposed that ~ 70 Ma intrusion-related mineralization west of the Denali fault links up with ~ 70 Ma intrusion-related mineralization east of the Denali fault (Figure 7.3). They also proposed a continuous belt of 70 Ma (arc?) magmatism, shown as the cross-hatched pattern on Figure 7.3. Addition of the various ~70 Ma prospects and deposits from Figure 7.2 onto the map of Graham et al. (2013), however, shows that the locus of magmatism is much wider than proposed and that some sort of NE-trending belt is superimposed on the overall NW-SE magmatic belt.

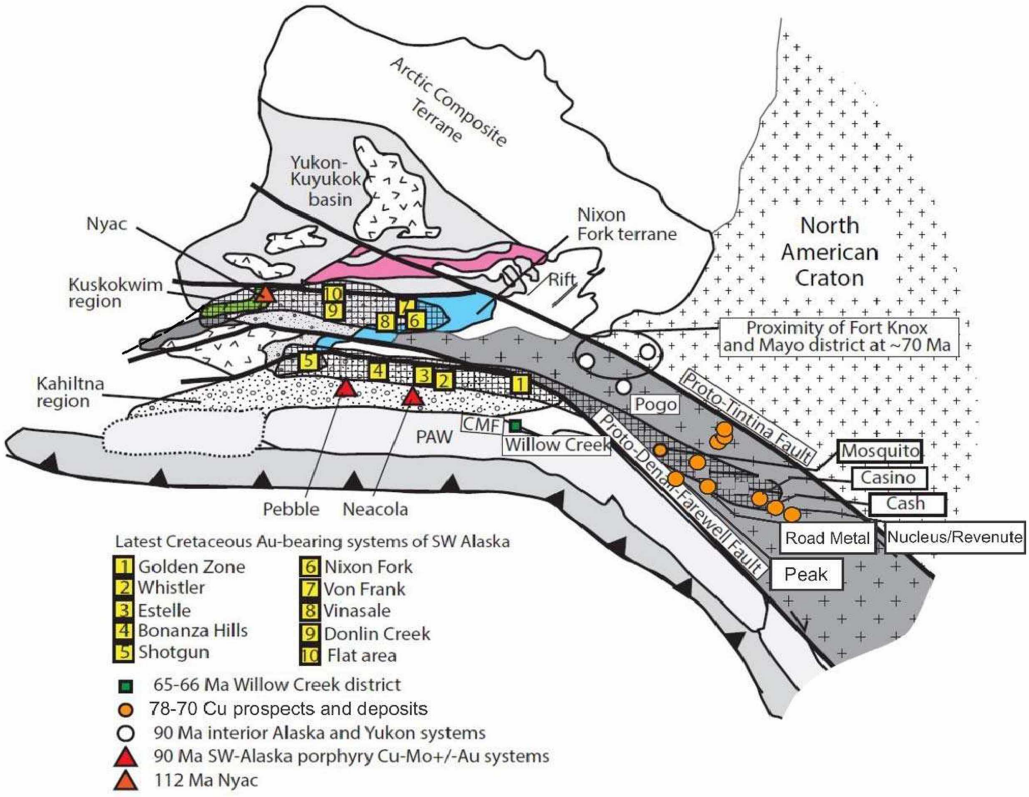


Figure 7.3: Estimated locations of intrusion-related deposits and prospects at ~70 Ma in Alaska. Dextral displacement along the Kaltag, Iditarod-Nixon Fork, Tintina, and Denali faults are restored assuming movement has occurred after 70 Ma. PAW = Peninsular-Wrangellia-Alexander superterrane, CMF = Castle Mountain fault. Cross-hatched area represents locus of ~ 70 magmatism. Modified from Graham et al. (2013) by addition of the Peak and Road Metal prospects and approximately 70 Ma intrusion-related prospects shown on Figure 7.2.

If, as suggested by Figure 7.3, the major magmatic belt is oriented approximately NW-SE then why should NE-trending belts also occur? More practically, should additional mineral exploration in the region be confined to narrow NE-trending belts? Additional radiometric dating of prospects and associated igneous rocks would presumably clarify the situation.

## 7.2 Problems Concerning the Origin and Zoning of the Peak Deposit

The genesis of the Peak deposit is not yet entirely clear. At Peak no silicate zoning (e.g., garnet to pyroxene to amphibole) has been identified. Amphibole skarn intergrown with coarse grained calcite with wollastonite have been identified, providing evidence for carbonate reactions, however no clear marble front has been delineated. No direct evidence for replacement of marble by amphibole + sulfide has been found. Sporadic evidence for replacement of pyroxene by amphibole is present in about 20% of the calc-silicate bearing Peak thin sections examined. Replacement of pyroxene does not prove that the rock was originally marble, but it at least indicates that it was unlikely to have been either schist or amphibolite. Although amphibole compositions at Peak resemble those of other Alaskan skarns (Figure 2.13) such is not conclusive evidence for replacement of carbonate.

The replacement of marble lenses is entirely possible; folded marble lenses have been encountered in drillcore near the Peak deposit and outside the zone of metasomatism in surface outcrop and float. Additionally oxygen and carbon isotopic values from calcite in marble far from and within the Peak deposit show a wide range (Table 5.3). Some of the isotopic values for marble and residual calcite in Peak are nearly magmatic (Figure 5.2), which suggests that metamorphic calcite interacted with magmatic fluids.

## 7.3 Suggestions for Future Work

One of the major remaining questions concerning the origin of the Peak deposit is the causative intrusion. Is it barren? Is it an economic porphyry Cu-Au deposit? Where is it? Magmatism at Peak is broadly coeval with the Casino porphyry belt, fluids that formed

the initial skarn at Peak were likely Cl-rich, and late Cretaceous rocks at Tetlin have compositional characteristics indicating an arc affinity (Figures 2.7, 2.8). Since the Peak represents a distal skarn system, it is likely more than a kilometer from the intrusive source. Pyroxene compositional zoning has been employed to vector towards the intrusive source, but due to the scarcity of pyroxene in the Peak deposit this is probably not realistic. Au:Cu endowment in conjunction with amphibole compositions might help to vector towards the responsible pluton. Currently a mineralogical fluid vectoring tool for amphibole has not been fully developed so a novel approach must be employed to make use of trends in amphibole compositions.

Drilling grids at Peak will outline economic distal Au skarn mineralization but alone will not lead to the causative intrusion. Cu rich skarn, barren skarn or barren metamorphic rocks will likely be present between Peak and the causative intrusion. Airborne geophysics have been used to target magnetic pyrrhotite at Peak deposit. The distribution of magnetic and pyrrhotite (the lower temperature polymorph) is unknown. Porphyry Cu deposits rarely contain pyrrhotite, and it is unclear what the sulfide and oxide assemblage would be in the hypothetical deep plutonic source to Peak. This combined with the likely depth to the hypothetical mineralized pluton makes airborne magnetic surveys of dubious value in the search for the pluton. Silicate mineral and metal endowment zoning remain the best tools for directing exploration if the goal is to determine the nature of the Peak causative intrusion.

Regional mapping, dating of plutons and compositional investigations of late Cretaceous intrusions between the Yukon border and the Eastern Alaska Range should be a focus to further understand the regional significance of the Peak deposit. The question

remains as to whether this region of Eastern Interior Alaska south of the Alaska-Canada Highway has been overlooked as a potential mining district.

To conclude, the Peak skarn is a high grade Au-Cu furthest distal skarn deposit. The lack of anhydrous calc-silicates sets it apart from a typical skarn. Importantly it was apparently not derived by retrograde alteration of pre-existing pyroxene (garnet) skarn but at least some represents direct replacement of a calcite-rich rock by metasomatic, Cl- Al- and Fe-rich amphibole. Further: (1) significant Au-Cu mineralization occurs in a region of Alaska far beyond currently documented mining districts, (2) the source of Peak is probably in an northeasterly direction at depth and innovative mineralogical tools will be needed to aid in its discovery, and (3) late Cretaceous arc magmatism extends into Alaska from Yukon, consequently (4) eastern interior Alaska remains prospective for undiscovered Cu-Au intrusion related resources.

References

Allan, M.M., Mortensen, J.K., Hart, C.R, Bailey, L.A., Sánchez, M.G., Ciolkiewicz, W, McKenzie, G.G., and Creaser, R.A., 2013. Magmatic and metallogenic framework of west-central Yukon and eastern Alaska, in Tectonics, Metallogeny, and Discovery: The North American Cordillera and Similar Accretionary Settings (eds: M Colpron, T Bissig, B Rusk and J Thompson), Soc. Econ. Geol., special publication 17, p 111–168.

Aleinikoff, J.N., Dusel-Bacon, C., Foster, H.L., and Nokleberg, W.J., 1987, Lead isotopic fingerprinting of tectono-stratigraphic terranes, east-central Alaska: Canadian Journal of Earth Sciences, v. 24, p. 2089-2098.

Barker, S.L., Dipple, G.M., Dong, F., and Baer, D.S., 2011. Use of laser spectroscopy to measure the $^{13}C/^{12}C$ and $^{18}O/^{16}O$ compositions of carbonate minerals. Analytical Chemistry, v. 83,- p. 2220-2226.

Baumgartner, L.P., and Valley, J.W., 2001, Stable isotope transport and contact metamorphic fluid flow, Rev. Min. Geochem., v. 43, p. 415-467.

Benowitz, J. A., Layer, P. W., and Vanlaningham, S., 2014, Persistent long-term (c. 24 Ma) exhumation in the Eastern Alaska Range constrained by stacked thermochronology. Geological Society, London, Special Publications, 378(1), 225-243.

Beuchat, S., 2003, Geochronological, structural, isotopes and fluid inclusion constraints of the polymetallic Domo de Yauli district, Peru, Genève, Terre and Environment, v. 41, 130 pp.

Bundtzen, T., Schaefer, C., Dashevsky, S., 2001, Road Metal – A New Silver-Gold-Polymetallic Lode Discovery at Northway Junction, Eastern-Interior Alaska, Alaska Geological Society Geology Symposium, p. 4-5.

Cameron, C., 1999, Alaska Resource Data File for the Tanacross Quadrangle, Alaska: U.S. Geol. Surv. Open File Rept. 99-358, 69 pp.

Deal, M.L., 2012, Origins and Zoning of the Buckhorn Gold Skarn, NE Washington: Unpublished M.S. thesis, Fairbanks, University of Alaska, 164 pp.

Deer, W. A., Howie, R. A., Zussman, J., 1997, Rock-forming Minerals: Double-Chain Silicates, Volume 2B. Geological Society of London, 764 pp.

Demange, M., Pascal, M.L., Raimbault, L., Armand, J., Forette, M.C., Serment, R., and Touil, A., 2006, The Salsigne Au-As-Bi-Ag-Cu deposit, France: Econ. Geol., v. 101, p. 199-234.

Donelick, R.A, O'Sullivan, P.B., and Ketcham, R.A., 2005. Apatite fission-track analysis. Reviews in Mineralogy and Geochemistry, Mineralogical Society of America, v. 58, p. 49-94.

Dusel-Bacon, C., Hopkins, M.J., Mortensen, J.K., Dashevsky, S.S., Bressler, J.R., and Day, W.C., 2006, Paleozoic tectonic and metallogenic evolution of the pericratonic rocks of east-central Alaska and adjacent Yukon: Geological Association of Canada, Special Paper no. 45, p. 25–74.

Dusel-Bacon, C., and Williams, I.S., 2009, Evidence for prolonged mid- Paleozoic plutonism and ages of crustal sources in east-central Alaska from SHRIMP U-Pb dating of syn-magmatic, inherited, and detrital zircon: Canadian Journal of Earth Sciences, v. 46, p. 21–39.

Einaudi, M.T., Meinert, L.D., and Newberry, R.J., 1981, Skarn Deposits: Economic Geology, 75th Anniversary Volume, p. 317-391.

Evans, A.M., 1987, An Introduction to Ore Geology, Blackwell Science Ltd., 2nd Ed, 368 pp.

Flanigan, B., Freeman, C., Newberry, R., McCoy, D., Hart, C., 2000, Exploration models for mid and late cretaceous Intrusion-related gold deposits in Alaska and the Yukon Territory, Canada, in Geology and Ore Deposits 2000: The Great Basin and Beyond, Geological Society of Nevada, p. 138-157.

Forbes, R.B. and Carver, C.L., 1976, A preliminary assessment of the mineral resource potential of the Tetlin Reserve, Alaska: U.S. Bureau of Indian Affairs, Contract E00C14201203, 23 pp., 4 plates.

Foster, H.L., 1970, Reconnaissance geologic map of the Tanacross quadrangle, Alaska: U.S. Geological Survey, Miscellaneous Geologic Investigations Series Map I-593, scale 1:250,000.

Gaccetta, J.D. and Church, S.E., 1989, Lead isotope data base for sulfide occurrences from Alaska: U.S. Geological Survey, Open-File Report, 89-688, 63 pp.

Godwin, C.I., Gabites, J.E., and Andrew, A., 1988, Leadtable: A galena lead isotope data base for the Canadian Cordillera: British Columbia Geological Survey, Paper 1988-4, 188 pp.

Graham, G. E., Goldfarb, R. J., Gibler, M. L., and Roberts, M., 2013, Tectonic evolution and Cretaceous gold metallogenesis of southwestern Alaska. Society of Economic Geologists Special Publication 17, p. 169-200.

Illig, P.E., 2014, Alaska's Newest Gold Deposit: Mineralization and Geochemistry of the Peak Zone Distal Gold Skarn, Tetlin Project, Tok, Alaska. Alaska Miners Association 24th Fairbanks biennial Mining conference, Abstracts with Program, p. 14. (www.contangoore.com/presentation.html accessed January 2, 2014).

Jenkins, D.M. and Bozhilov, K.N., 2003, Stability and thermodynamic properties of ferro-actinolite: A re-investigation, American Journal of Science, v. 33, p. 723-752.

Koehler, R.D., and Carver, G.A., 2012, Active and potentially active faults along the Alaska Highway corridor, Tetlin Junction to the Canada border: Alaska Division of Geological and Geophysical Surveys Preliminary Interpretive Report 2012-2, 23 pp.

Kretz, R., 2001, Oxygen and carbon isotopic composition of grenville marble, and an appraisal of equilibrium in the distribution of isotopes between calcite and associated minerals, Otter Lake, Quebec, Canada, Canadian Mineralogist, v. 39, pp. 1455-1472.

Layer, P.W., Hall, C.M. and York, D., 1987, The derivation of 40Ar/39Ar age spectra of single grains of hornblende and biotite by laser step heating, Geophys. Res. Lett., v. 14, 757-760.

Lyons, P.C., 1971, Staining of feldspars on rock slab surfaces for modal analysis: Short Communications, Mineralogical Magazine, v. 38, p. 519.

McDougall, I. and Harrison, T.M., 1999, Geochronology and Thermochronology by the 40Ar/39Ar method-2nd ed, Oxford University Press, New York, 269 pp.

Meinert, L.D., Nicolescu, S., Mortensen, J.K., and Cornell, D.H., 2001, U-Pb dating of hydrothermal garnet from skarn deposits; implications for petrogenesis and ore deposits: Geological Society of America, Abstracts with Programs, v. 33, p. 130.

Meinert, L.D., Dipple, G.M., Nicolescu, S.N., 2005, World Skarn Deposits in Economic Geology 100th Anniversary Volume, p. 299-336.

Meschede, M., 1986, A method of discriminating between different types of mid-ocean ridge basalts and continental tholeiites with the Nb–Zr–Y diagram. Chemical Geology, v. 56, p. 207– 218.

Mueller, A.G., Nemchin, A.A., and Frei, R., 2004, The Nevoria Gold Skarn Deposit, Southern Cross Greenstone Belt, Western Australia: II. Pressure-Temperature-Time Path and Relationship to Postorogenic Granites: Economic Geology, v. 99, p. 453-478.

Myers, G.L., 1994, Geology of the Copper Canyon-Fortitude skarn system, Battle Mountain, Nevada: Unpublished Ph.D. thesis, Pullman, Washington, Washington State University, 356 pp.

Nelson, J.L., Colpron, M., Piercey, S.J., Dusel-Bacon, C., Murphy, D.C., and Roots, C.F., 2006, Paleozoic tectonic and metallogenic evolution of the pericratonic terranes in Yukon, northern British Columbia and eastern Alaska: Geological Association of Canada, Special Paper no. 45, p. 323–360.

Newberry, R.J., Layer, P.W., Solie, D.N., and Burleigh, R.E, 1998, New 40Ar/39Ar Dates for Intrusions and Mineral Prospects in the Eastern Yukon-Tanana Terrane, Alaska--Regional Patterns and Significance, in Gray, J.E., and Riehle, J.R., eds., Geologic studies in Alaska by the U.S. Geological Survey, 1996: U.S. Geological Survey Professional Paper 1595, p. 131-159.

Newberry, R.J., Allegro, G.L., Cutler, S.E., Hagen-Levelle, J.H., Adams, D.D., Nicholson, L.C., Weglarz, T.B.,Bakke, A.A.,Clautice, K.H.,Coulter, G.A., Ford, M.J., Myers, G.L., and Szumigala, D.J., 1997, Skarn Deposits of Alaska: in, R.J. Goldfarb and L.D. Miller, eds., Mineral Deposits of Alaska: Economic Geology, Monograph 9, p. 355-395.

Pearce, J A, Harrius, N B W and Tindle, A G, 1984, Trace element discrimination diagrams for the tectonic interpretation of granitic rocks, Journal of Petrology, v. 25(4), p. 956–983.

Pearce, J.A., and Cann, J.R., 1973, Tectonic setting of basic volcanic rocks determined using trace element analyses. Earth and Planetary Science Letters, v. 19.2, p. 290-300.

Renne, P. R., Mundil, R., Balco, G., Min, K., and Ludwig, K. R., 2010, Joint determination of 40K decay constants and 40Ar*/40K for the Fish Canyon sanidine standard, and improved accuracy for $^{40}Ar/^{39}Ar$ geochronology. Geochimica et Cosmochimica Acta, v. 74, p. 5349.

Renne, P. R., Deino, A. L., Walter, R. C., Turrin, B. D., Swisher, C. C., Becker, T. A., Curtis, G.H., Sharp. W.D., and Jaouni, A. R., 1994, Intercalibration of astronomical and radioisotopic time. Geology, v. 22, p. 783-786.

Richter, D. H., 1997, Alaska Resource Data File for the Nabesna Quadrangle, Alaska: U.S. Geol. Surv. Open File Rept. 97-749, 94 pp.

Reynolds, D.G., 1965, Geology and mineralization of the Salsigne gold mine, France: Economic Geology, v. 60, p. 772–791.

Samson, S. D., and Alexander E. C., 1987, Calibration of the interlaboratory 40Ar/39Ar dating standard, MMhb1. Chemical Geology, v. 66, p. 27-34.

Siron, C.R., Hitzman, M.W., and McLeod, R., 2010, Geology of the Little Whiteman carbonate hosted replacement Zn-Pb-Ag-(Cu) prospect, western Fortymile district, Alaska: Society of Economic Geologists, Special Publication 15, p. 421–436.

Solie, D.N., O'Sullivan, P., Werdon, M., Freeman, L., Newberry, R., Szumigala, D., and Hubbard, T., 2014, Zircon U-Pb Age Data, Alaska Highway Corridor, Tanacross and Nabesna quadrangles, Alaska RAW-DATA FILE 2014-16, 29 pp.

Streckeisen, A.L., and LeMaitre, R.W., 1979, Chemical approximation to modal QAPF classification of the igneous rocks: Neus Jahrbuch fur Mineralogie, v. 136, p. 169-206.

Tagirov, B. and Schott, J., 2001, Aluminum speciation in crustal fluids revisited, Geochimica et Cosmochimica Acta, v. 65, p. 3965–3992

Thirlwall, M.F., 2000, Inter-laboratory and other errors in Pb isotope analyses investigated using a 207Pb—204Pb double spike: Chemical Geology, v. 163, p. 299–322.

Till, A.B., Roeske, S.M., Bradley, D.C., Friedman, R., and Layer, P.W., 2007, Early Tertiary transtension-related deformation and magmatism along the Tintina fault system, Alaska *in* Till, A.B., Roeske, S.M., Sample, J.C., and Foster, D.A., eds., Exhumation Associated with Continental Strike-Slip Fault Systems: Geological Society of America, Special Paper 434, p. 233-264.

VanTreeck, C., Freeman, C.J., Wolf, K., Raymond, L., 2012, Geology and Mineralization of the Tetlin project, Tanacross and Nabesna Quadrangles, Eastern Interior Alaska: Internal Report by Avalon Development Corp. for Anglo Alaska Gold Corp., 119 pp.

VanTreeck, C., Freeman, C.J., Wolf, K., Raymond, L., 2013, Final Report for the Tetlin Project, Eastern Interior Alaska: Internal Report by Avalon Development Corp. for Anglo Alaska Gold Corp., 119 pp.

VanTreeck, C., 2013, Geology and Mineralization of the Chief Danny Prospect Contango Ore Inc. Tetlin Project, Tok, AK. Alaska Miners Association Anchorage biennial Mining Conference, p. 4-5.

Woodward–Clyde Consultants, 1979, Identification of candidate significant faults in the Delta Junction–Yukon Territory border section of the Alaska Natural Gas Transportation System Corridor, Final Report prepared for Fluor Engineers and Constructors, Inc.

York, D., Hall, C.M., Yanase, Y., Hanes, J.A. and Kenyon, W.J., 1981, 40Ar/39Ar dating of terrestrial minerals with a continuous laser, Geophys. Res. Lett., v. 8, p. 1136-1138.

## Appendix 1: Metallogeny of Western Yukon and Eastern Interior Alaska

The large Fortymile mining district has produced an estimated 500,000 troy ounces of gold since discovery in 1886 (Yeend, 1996). The district is primarily placer gold. The Purdy quartz-calcite-gold vein, which produced about a ton of ore (Saunders, 1960), is the only lode from which there is recorded production. Lode sources of placer gold in the Fortymile district are poorly constrained however gold-quartz veins associated with shear zones and faults have been proposed as local sources (Yeend, 1996). Silver-lead carbonate replacement and skarn prospects (e.g. Little Whiteman, Fish, Oscar, Drumstick, Eva, and Mitchell) have been attributed to the N-E trending Kechumstuk fault, Early Jurassic and Late Cretaceous intrusions (Werdon et al., 2004; Dusel-Bacon and Williams, 2009; Siron et al., 2010, Day et al., 2014) with possible fault conduits.

The Taurus and Bluff porphyry prospects are the most significant late Cretaceous prospects of the Forty Mile district. The Taurus Cu-Au-Mo porphyry prospect (Late Cretaceous?) has an inferred resource 75.2 Mt with a grade of 0.275% Cu, 0.116 g/t Au and 0.032% Mo (Harrington, 2011). Although this resource has been dated at 57 +/- 2 Ma (K-Ar, biotite; Nokleberg et al., 1995), the adjacent Bluff Cu-Mo porphyry prospect has yielded an older age (72-71 Ma, U-Pb zircon).

The Mosquito Cu-Mo porphyry prospect is also on trend with the Kechumstuk fault (Allan et al., 2013), however its structural relation to the Fortymile district mineralization is unknown. Cu-(Mo-Au) porphyry, Mo-(Cu-W) porphyry, Ag-rich polymetallic veins and Ag-rich carbonate replacement mineralization of the forty mile district have been attributed to transtensional fault systems (Allan et al., 2013).

The Dawson Range district has a lower historic placer gold production, but contains significant lode resources. Mineralization styles include porphyry, skarn, epithermal and polymetallic veins in breccias and fractures. Porphyry and epithermal mineralization occur as a 120-km long belt that extends from the Casino deposit in the NW to the Mt. Nansen camp in the SE (Allan et al., 2013).

Significant placer gold production has occurred at Moosehorn (>68,000 oz), Mount Nansen camp (>33,000 oz), Casino and Mt. Cockfield (>22,000 oz) and the Freegold camp (>17,000 oz). The only active mine in the Dawson Range is the Minto Cu-Au deposit (Figure 1.6). It has a resource of 60 Mt with average grades of 1% Cu and 0.4 g/t Au (Mercer and Sagman, 2012). This resource is characterized by disseminated chalcopyrite and bornite in deformed granitic rocks and is atypical of porphyry resources in this region (Allan et al., 2013).

Porphyry systems of the Dawson Range are Casino, Nucleus-Revenue, Sonora Gulch, Mt. Cockfield, Cash, Antoniuk and Cyprus (Allan et al., 2013). The largest, Casino (75-74 Ma, U-Pb zircon, $^{187}Re/^{187}Os$ molybdenite), has a measured and indicated resource of 1,056 Mt at .2% Cu, 0.23 g/t Au and 0.022% Mo (Selby and Creaser, 2001; Huss et al., 2013; Allan et al., 2013). The Nucleus prospect (~76 Ma, U-Pb zircon, 40Ar/39Ar musc, , $^{187}Re/^{187}Os$ molybdenite) has an indicated and inferred resource of 90 Mt with grades of 0.65% Cu, 0.60 g/t Au and 0.94 g/t Ag (Armitage et al., 2012; Bineli Betsi, 2012; Allan et al., 2013). Revenue (78-75 Ma, U-Pb zircon, $^{187}Re/^{187}Os$ molybdenite) has an inferred resource of 101 Mt with grades of 0.13% Cu (Armitage and Campbell, 2011; Bineli Betsi, 2012; Allan et al., 2013). Nucleus and Revenue are now recognized as part of the same porphyry system with additional exploration potential (Armitage and Campbell, 2011;

Armitage et al., 2012). Additional resources include the Cash Cu-Mo porphyry (77-76 Ma, $^{187}Re/^{187}Os$ molybdenite) with an inferred resource of 36 Mt with grades of 0.170% Cu, 0.2 g/t Au, 0.4 g/t Ag and 0.018% Mo (Sinclair et al., 1981; Selby and Creaser, 2001) and the Antoniuk Au porphyry-breccia system (107.5 +/- 1.0 Ma, U-Pb zircon) with an inferred resource of 3.9 Mt with grades of 1.16 g/t Au (Allan et al., 2013).

# References


Armitage, A., and Campbell, J., 2011, Technical report on the revised resource estimate on the Nucleus Au-Cu-Ag deposit, Freegold Mountain project: Northern Freegold Resources Ltd., 48 p. (http://www.northernfreegold.com/i/pdf/Nucleus_2011_43101_report.pdf, accessed January 2, 2015).

Armitage, A., Campbell, J., and Sexton, A., 2012, Technical report on the resource estimate for the Revenue Au-Cu-Mo porphyry deposit, Freegold Mountain project: Northern Freegold Resources Ltd., 74 pp.

Bineli Betsi, T., 2012, Petrogenesis of Au-Bi-As-Cu, Cu-Mo ± W, and basemetal- Au-Ag mineral occurrences, in the Mount Freegold region (Dawson Range), Yukon, Canada: Unpublished Ph.D. thesis, Fredericton, Canada, University of New Brunswick, 515 pp.

Day, W.C., O'Neill, J.M., Dusel-Bacon, C., Aleinikoff, J.N., Siron, C.R., 2014, Geologic map of the Kechumstuk fault zone in the Mount Veta area, Fortymile mining district, east-central Alaska. U.S. Geological Survey Scientific Investigations Map 3291, scale 1:63,360.

Harrington, E., 2011, Technical report on the Taurus property: Senator Minerals Inc., 136 pp.

Huss, C., Drielick, T., Austin, J., Giroux, G., Casselman, S., Greenaway, G., Hester, M., and Duke, J., 2013, Casino project Form 43-101F1 technical report feasibility study: Western Copper and Gold Corp., 203pp. (http://www.westerncopperandgold.com/_resources/reports/CasinoNI43-101-Jan2013.pdf, accessed January 2, 2015).

Mercer, B., and Sagman, J., 2012, Phase VI preliminary feasibility study technical report, Minto mine: Minto Explorations Ltd., 368 p. (http://capstonemining.com/i/pdf/PFS.pdf, accessed December 9, 2012).

Saunders, R.H., 1960, Report on the Purdy gold-quartz prospect, Eagle quadrangle: Alaska Division of Geological and Geophysical Surveys Prospect Evaluation 60-9, 2 pp.

Selby, D., and Creaser, R.A., 2001, Late and mid-Cretaceous mineralization in the northern Canadian Cordillera: Constraints from Re-Os molybdenite dates: Economic Geology, v. 96, p.1461–1467.

Sinclair, W.D., Cathro, R.J., and Jensen, E.M., 1981, The Cash porphyry copper-molybdenum deposit, Dawson Range, Yukon Territory: Canadian Inst. Mining and Metallurgy Bulletin, v. 74, p. 67–75.

Werdon, M.B., Flynn, R.L., and Szumigala, D.J., 2004, Alaska resource data file, Eagle quadrangle: U.S. Geological Survey, Open File Report 2004- 1056, 418 pp.

Yeend, W.E., 1996, Gold placers of the historical Fortymile River region, Alaska: U.S. Geological Survey, Bulletin 2125, 75 pp.

# APPENDIX 2: X-ray Fluorescence Analyses

## Table A2.1: X-ray Fluorescence analyses of Tetlin metamorphic rocks

**Analyses by X-ray Fluorescence**

| Sample Name | 14PI060 | 14PI76B | 14PI46 | TET1105-15 | ET13101-10 | TET1226-33 | TET1103-15' | 14PI001 | 14PI92 | T13-116 12 | 14PI-135 | 14PI62 | 14PI43 | 14PI21 | 14PI-74 | 14PI51 | 14PI142 | 14PI96B | 14PI151 | 14RN108 | 14RN86 | 14RN116 |
|---|---|---|---|---|---|---|---|---|---|---|---|---|---|---|---|---|---|---|---|---|---|---|
| Rock Type | gn | gn | alt'd amph | alt'd amph | alt'd amph | alt'd Q sch | fld calc qzite | fs-qz sch | gneiss | gneiss | gneiss? | hb gneiss | hbl pl gneiss | hbl rock | hbl rock | hb-pl gn | orthogn | orthogn | paragn | paragn | pl amph | pl-hb gn |
| Major Elements (wt. %) | | | | | | | | | | | | | | | | | | | | | | |
| SiO2 | 69.95 | 53.87 | 48.76 | 48.88 | 57.58 | 89.14 | 66.69 | 84.94 | 73.12 | 67.22 | 71.13 | 77.43 | 54.67 | 78.01 | 81.41 | 57.76 | 74.09 | 71.75 | 74.21 | 62.12 | 51.64 | 55.27 |
| Al2O3 | 5.34 | 17.96 | 14.72 | 12.85 | 8.61 | 5.73 | 4.29 | 7.43 | 12.02 | 15.33 | 13.61 | 9.61 | 18.38 | 7.66 | 7.48 | 14.91 | 11.71 | 12.81 | 13.12 | 18.64 | 15.51 | 15.59 |
| FeO | 11.12 | 10.03 | 7.75 | 17.73 | 14.77 | 1.52 | 0.99 | 1.57 | 3.05 | 4.15 | 3.92 | 3.51 | 5.67 | 4.85 | 3.29 | 8.40 | 3.46 | 4.26 | 3.42 | 6.96 | 8.92 | 7.82 |
| MgO | 2.01 | 1.42 | 6.52 | 6.14 | 8.92 | 0.44 | 0.30 | 0.54 | 0.88 | 1.63 | 1.71 | 0.72 | 5.36 | 0.50 | 0.46 | 1.62 | 1.74 | 1.79 | 0.91 | 1.68 | 5.84 | 2.30 |
| CaO | 8.89 | 11.34 | 17.43 | 7.19 | 4.62 | 0.13 | 25.04 | 0.45 | 6.15 | 4.57 | 3.79 | 3.33 | 10.11 | 5.39 | 4.17 | 11.30 | 3.78 | 3.87 | 0.84 | 0.78 | 12.28 | 15.28 |
| Na2O | 1.10 | 3.26 | 2.25 | 1.70 | 0.12 | 1.24 | 1.57 | 3.83 | 3.71 | 4.02 | 3.09 | 1.53 | 3.79 | 2.66 | 2.14 | 3.88 | 2.58 | 2.56 | 3.08 | 3.46 | 2.81 | 2.56 |
| K2O | 0.91 | 1.34 | 0.15 | 2.61 | 0.90 | 1.49 | 0.62 | 0.86 | 0.50 | 1.94 | 2.08 | 3.12 | 0.92 | 0.51 | 0.44 | 1.02 | 2.06 | 2.31 | 3.68 | 5.03 | 0.39 | 0.22 |
| MnO | 0.23 | 0.12 | 0.15 | 0.20 | 0.17 | 0.01 | 0.04 | 0.02 | 0.07 | 0.06 | 0.06 | 0.06 | 0.08 | 0.07 | 0.05 | 0.30 | 0.07 | 0.10 | 0.05 | 0.13 | 0.20 | 0.28 |
| TiO2 | 0.26 | 0.55 | 1.91 | 2.10 | 2.50 | 0.20 | 0.35 | 0.27 | 0.35 | 0.77 | 0.34 | 0.36 | 0.72 | 0.24 | 0.23 | 0.58 | 0.37 | 0.38 | 0.53 | 0.94 | 1.99 | 0.47 |
| P2O5 | 0.11 | 0.08 | 0.22 | 0.19 | 1.37 | 0.04 | 0.08 | 0.04 | 0.12 | 0.27 | 0.15 | 0.13 | 0.18 | 0.09 | 0.31 | 0.11 | 0.12 | 0.08 | 0.05 | 0.12 | 0.26 | 0.09 |
| BaO | 0.02 | 0.03 | 0.01 | 0.17 | 0.03 | 0.06 | 0.03 | 0.04 | 0.03 | 0.04 | 0.11 | 0.10 | 0.01 | 0.02 | 0.03 | 0.02 | BDL | 0.07 | 0.11 | 0.14 | 0.03 | 0.02 |
| Total | 93.0 | 99.7 | 99.6 | 83.4 | 88.8 | 99.8 | 99.9 | 100.0 | 99.8 | 99.8 | 100.0 | 96.5 | 90.5 | 99.6 | 99.7 | 94.3 | 99.9 | 99.9 | 99.8 | 99.8 | 95.0 | 96.4 |
| Minor Elements (ppm) | | | | | | | | | | | | | | | | | | | | | | |
| Cr | 24 | 61 | 202 | 213 | 340 | 44 | BDL | 49 | 33 | 84 | 59 | 20 | 67 | 64 | 44 | 50 | BDL | 77 | 74 | 114 | 62 | 56 |
| Cu | 84 | 241 | 12 | 285 | 22 | BDL | BDL | BDL | 60 | 47 | BDL | 75 | 9 | BDL | 0 | 14 | BDL | BDL | BDL | BDL | 56 | 12 |
| Ni | 45 | BDL | 62 | 126 | 183 | BDL | BDL | BDL | 45 | BDL | 9 | 6 | 34 | BDL | BDL | 28 | BDL | BDL | BDL | 13 | 28 | 21 |
| Rb | 29 | BDL | 7 | 128 | 46 | 56 | 26 | 35 | 37 | 81 | 69 | 87 | 58 | 19 | 22 | 44 | 76 | 8 | 106 | 183 | 17 | 12 |
| Sr | 127 | 447 | 311 | 136 | 143 | 36 | 258 | 77 | 285 | 213 | 246 | 177 | 395 | 22 | 176 | 324 | 123 | 189 | 178 | 156 | 355 | 360 |
| V | 39 | 147 | 347 | 373 | 194 | 51 | BDL | BDL | BDL | 226 | BDL | 34 | 121 | BDL | BDL | 51 | BDL | 129 | 103 | 127 | 366 | 61 |
| Zn | 90 | 65 | 93 | 183 | 1851 | 123 | BDL | 19 | 42 | 61 | BDL | 32 | 63 | 44 | 31 | 84 | 43 | 46 | 51 | 87 | 83 | 97 |
| Zr | 93 | 66 | 135 | 145 | 407 | 138 | 118 | 267 | 182 | 167 | 118 | 279 | 277 | 153 | 147 | 198 | 111 | 90 | 170 | 115 | 157 | 167 |
| Y | 19 | 12 | 36 | 50 | 21 | 12 | 12 | 7 | 15 | 18 | 20 | 19 | 43 | 12 | 18 | 24 | 15 | 39 | 12 | 26 | 63 | 31 |
| Nb | 6 | 14 | 9 | 11 | 73 | BDL | 25 | BDL | 13 | 11 | BDL | 11 | 21 | BDL | 6 | 26 | 685 | 8 | 8 | 16 | 9 | 13 |
| Pb | 6 | 55 | 13 | 55 | 170 | 28 | 25 | 18 | 23 | 22 | BDL | 8 | 2 | 32 | 32 | 5 | BDL | 29 | 30 | 50 | 14 | 9 |

**Analyses by X-ray Fluorescence**

| Sample Name | 14PI006 | 14PI-163 | 14RN135 | TET1104-38 | T13101-25. | 14PI002 | 14PI07B | TET1105 21 | 14PI152 | 14PI003 | 14PI145 | 14PI154 | 14PI71 | ET1105-4 | ET12026-1 | T13-111-.' | 14PI144 | 14PI150 | 14PI155 | 14PI007A | 14PI45 | 14PI50 |
|---|---|---|---|---|---|---|---|---|---|---|---|---|---|---|---|---|---|---|---|---|---|---|
| Rock Type | qz musc sch | qz musc sch | qz sch | qz sch | qz sch | qzite | qzite | qz sch | qz musc sch | qz sch | qz sch | qz sch | qz sch | qz sch | qz sch | qz sch | | | | amphib | amphib | amphib |
| Major Elements (wt. %) | | | | | | | | | | | | | | | | | | | | | | |
| SiO2 | 69.46 | 69.31 | 87.28 | 80.11 | 75.74 | 96.48 | 90.09 | 84.68 | 64.33 | 82.58 | 86.79 | 80.64 | 85.14 | 83.84 | 84.82 | 81.18 | 67.18 | 73.60 | 82.07 | 48.27 | 48.63 | 50.15 |
| Al2O3 | 15.41 | 11.61 | 6.32 | 11.72 | 9.97 | 2.03 | 4.89 | 7.70 | 20.34 | 9.87 | 6.80 | 9.71 | 7.80 | 8.48 | 8.37 | 9.77 | 18.02 | 12.52 | 9.53 | 14.10 | 14.08 | 14.70 |
| FeO | 5.79 | 11.83 | 1.56 | 3.35 | 4.67 | 0.34 | 0.69 | 2.03 | 4.63 | 2.66 | 0.86 | 2.72 | 1.22 | 1.94 | 1.92 | 1.28 | 3.11 | 2.68 | 3.91 | 13.55 | 13.12 | 12.71 |
| MgO | 2.16 | 0.84 | 0.44 | 0.81 | 1.96 | 0.23 | 0.34 | 0.78 | 1.79 | 0.68 | 0.42 | 0.74 | 0.57 | 0.53 | 0.82 | 0.50 | 1.00 | 0.44 | 0.59 | 7.33 | 7.07 | 6.59 |
| CaO | 0.10 | 1.08 | 0.57 | 0.15 | 2.56 | 0.05 | 0.25 | 0.32 | 0.31 | 0.25 | 0.44 | 0.99 | 0.53 | 0.16 | 0.59 | 1.58 | 3.79 | 4.67 | 0.18 | 10.99 | 11.15 | 10.44 |
| Na2O | 0.18 | 2.81 | 1.90 | 0.25 | 0.87 | 0.07 | 2.85 | 2.41 | 1.37 | 1.35 | 1.95 | 2.18 | 1.02 | 2.32 | 0.36 | 2.84 | 2.17 | 1.52 | 0.94 | 2.27 | 2.69 | 2.55 |
| K2O | 5.71 | 2.06 | 1.37 | 3.02 | 2.46 | 0.58 | 0.71 | 1.49 | 6.06 | 2.11 | 2.31 | 2.33 | 3.25 | 2.23 | 2.72 | 2.46 | 3.77 | 3.81 | 2.31 | 0.68 | 0.59 | 0.26 |
| MnO | 0.02 | 0.02 | 0.03 | 0.05 | 0.05 | 0.00 | 0.01 | 0.03 | 0.05 | 0.05 | 0.01 | 0.04 | 0.02 | 0.01 | 0.02 | 0.02 | 0.03 | 0.03 | 0.04 | 0.22 | 0.19 | 0.21 |
| TiO2 | 0.83 | 0.22 | 0.38 | 0.41 | 0.98 | 0.15 | 0.12 | 0.34 | 0.84 | 0.35 | 0.28 | 0.46 | 0.30 | 0.28 | 0.27 | 0.24 | 0.65 | 0.44 | 0.35 | 2.17 | 2.08 | 2.01 |
| P2O5 | 0.09 | 0.05 | 0.10 | 0.03 | 0.59 | 0.02 | 0.02 | 0.03 | 0.05 | 0.02 | 0.04 | 0.08 | 0.03 | 0.04 | 0.03 | 0.05 | 0.17 | 0.17 | 0.03 | 0.26 | 0.26 | 0.23 |
| BaO | 0.12 | 0.16 | 0.05 | 0.09 | 0.14 | 0.03 | 0.03 | 0.19 | 0.22 | 0.08 | 0.09 | 0.09 | 0.11 | 0.16 | 0.07 | 0.07 | 0.10 | 0.13 | 0.05 | 0.01 | 0.01 | BDL |
| Total | 81.9 | 91.3 | 99.9 | 99.9 | 99.8 | 99.9 | 99.9 | 99.9 | 99.8 | 99.9 | 99.9 | 99.9 | 100.0 | 100.0 | 99.9 | 99.9 | 99.9 | 99.9 | 99.9 | 96.8 | 97.7 | 97.3 |
| Minor Elements (ppm) | | | | | | | | | | | | | | | | | | | | | | |
| Cr | 74 | BDL | BDL | 80 | 112 | 36 | BDL | BDL | 122 | 69 | 50 | 64 | 50 | 58 | 53 | 60 | 102 | 69 | 87 | 227 | 206 | 199 |
| Cu | 46 | BDL | BDL | BDL | BDL | BDL | BDL | BDL | 49 | BDL | 48 | 27 | BDL | 70 | 64 | BDL | 34 | 211 | 49 | 93 | 108 | 291 |
| Ni | 19 | BDL | BDL | BDL | 43 | BDL | BDL | 42 | 116 | BDL | BDL | BDL | BDL | 82 | BDL | BDL | 37 | 19 | 107 | 104 | 104 | 98 |
| Rb | 204 | 100 | 54 | 106 | 101 | 27 | 31 | 52 | 214 | 7 | 65 | 72 | 91 | 78 | 107 | 64 | 152 | 93 | 72 | 37 | 15 | 4 |
| Sr | 61 | 200 | 102 | 61 | 138 | 120 | 37 | 40 | 171 | 69 | 129 | 161 | 93 | 57 | 108 | 163 | 303 | 214 | 90 | 210 | 223 | 215 |
| V | 104 | BDL | 57 | 80 | 158 | BDL | BDL | BDL | 182 | 93 | BDL | 72 | 71 | BDL | 74 | BDL | 108 | 71 | 47 | 377 | 379 | 355 |
| Zn | 51 | 9 | 23 | 53 | 72 | 24 | BDL | 23 | 87 | 51 | 27 | 30 | 32 | 41 | 109 | 42 | 47 | 43 | 40 | 114 | 120 | 127 |
| Zr | 159 | 100 | 562 | 132 | 215 | 130 | 106 | 349 | 223 | 154 | 258 | 189 | 150 | 131 | 204 | 121 | 148 | 112 | 82 | 135 | 142 | 128 |
| Y | 21 | 10 | 24 | 48 | 10 | 4 | 6 | 7 | 12 | 8 | 10 | 14 | 16 | 8 | 15 | 8 | 31 | 23 | 11 | 39 | 39 | 37 |
| Nb | 16 | BDL | 12 | 26 | 26 | BDL | BDL | BDL | 17 | BDL | 8 | 11 | 5 | BDL | 8 | BDL | 18 | 16 | BDL | 9 | 10 | 7 |
| Pb | 126 | BDL | BDL | 21 | 29 | 30 | 18 | BDL | 33 | BDL | 21 | 21 | 18 | 23 | 33 | 22 | 21 | 30 | 17 | 18 | 9 | 15 |

Qz = quartz; gn = gneiss; gb = hornblende; pl = plagioclase; amphib = amphibolite; qzite = quartzite; musc = muscovite; alt'd = altered; fld = feldspar; sch = schist.

# Table A2.2: X-ray fluorescence analyses for igneous rocks from Tetlin and Northway.

**Analyses by X-ray Fluorescence**

| Sample Name | 14PI158 | 14PI160 | 14PI100 | 14PI100B | 14PI121 | 14PI149 | 14PI153 | 14PI157 | 14PI165 | 14PI167A | 14PI101 | 14PI100B | 14PI49 | 14PI94B | 14PI161 | 14PI162 |
|---|---|---|---|---|---|---|---|---|---|---|---|---|---|---|---|---|
| Rock Type | alt'd rhy | alt'd rhy | b. andes | b. andes | b. andes | b. andes | b. andes | b. andes | b. andes | b. andes | b. andes | b. andes | b. andes | b. andes | rhyolite | rhyolite |
| Major elements (wt. %) | | | | | | | | | | | | | | | | |
| SiO2 | 77.88 | 78.87 | 54.80 | 56.55 | 58.98 | 50.83 | 56.81 | 57.52 | 54.65 | 56.22 | 55.92 | 56.55 | 66.90 | 59.33 | 73.29 | 77.58 |
| Al2O3 | 14.30 | 13.23 | 16.96 | 16.11 | 14.99 | 14.48 | 17.64 | 15.13 | 14.79 | 14.96 | 14.71 | 16.11 | 13.79 | 17.14 | 14.45 | 14.68 |
| FeO | 1.22 | 2.52 | 7.68 | 7.49 | 7.36 | 11.43 | 5.03 | 8.42 | 7.42 | 8.83 | 8.19 | 7.49 | 7.95 | 6.33 | 2.17 | 1.74 |
| MgO | 0.78 | 0.56 | 6.01 | 5.34 | 4.34 | 6.21 | 5.12 | 5.06 | 1.12 | 5.22 | 3.44 | 5.34 | 2.01 | 4.61 | 0.63 | 0.65 |
| CaO | 0.09 | 0.10 | 7.73 | 8.21 | 7.86 | 10.76 | 8.86 | 8.45 | 15.60 | 8.30 | 11.65 | 8.21 | 5.00 | 5.15 | 1.65 | 0.05 |
| Na2O | 0.10 | 0.10 | 3.19 | 3.40 | 3.59 | 3.20 | 4.07 | 2.75 | 3.31 | 2.41 | 2.83 | 3.40 | 2.13 | 3.83 | 3.27 | 0.08 |
| K2O | 5.07 | 4.17 | 2.00 | 1.36 | 1.39 | 0.56 | 1.14 | 0.85 | 1.72 | 2.09 | 1.45 | 1.36 | 0.35 | 1.98 | 3.72 | 4.79 |
| MnO | 0.01 | 0.01 | 0.12 | 0.11 | 0.11 | 0.18 | 0.08 | 0.18 | 0.21 | 0.14 | 0.18 | 0.11 | 0.20 | 0.17 | 0.06 | 0.01 |
| TiO2 | 0.23 | 0.21 | 1.05 | 1.01 | 0.90 | 1.98 | 0.80 | 1.05 | 0.73 | 1.16 | 1.02 | 1.01 | 1.09 | 0.78 | 0.22 | 0.22 |
| P2O5 | 0.14 | 0.05 | 0.16 | 0.17 | 0.17 | 0.21 | 0.21 | 0.37 | 0.18 | 0.27 | 0.29 | 0.17 | 0.45 | 0.36 | 0.06 | 0.01 |
| BaO | 0.11 | 0.13 | 0.17 | 0.11 | 0.18 | 0.01 | 0.09 | 0.09 | 0.18 | 0.26 | 0.17 | 0.11 | 0.02 | 0.19 | 0.39 | 0.13 |
| Result | 90.5 | 94.0 | 98.2 | 97.8 | 95.1 | 97.1 | 98.3 | 95.1 | 91.3 | 93.8 | 92.5 | 97.82 | 97.2 | 89.4 | 99.1 | 85.8 |
| Minor elements (ppm) | | | | | | | | | | | | | | | | |
| Cr | BDL | 5 | 110 | 95 | 70 | 191 | 187 | 90 | 84 | 77 | 101 | 95 | 5 | 62 | BDL | 7 |
| Cu | 7 | 6 | 8 | 7 | 30 | 279 | 14 | 36 | 17 | 26 | 48 | 7 | 12 | 34 | 6 | 13 |
| Ni | BDL | 2 | 33 | 32 | 31 | 84 | 61 | 19 | 29 | 27 | 33 | 32 | 3 | 44 | 3 | BDL |
| Rb | 231 | 192 | 60 | 46 | 49 | 12 | 29 | 48 | 96 | 121 | 95 | 46 | 17 | 60 | 114 | 179 |
| Sr | 43 | 54 | 614 | 654 | 663 | 262 | 742 | 548 | 407 | 638 | 516 | 654 | 412 | 758 | 446 | 20 |
| V | 16 | 22 | 211 | 195 | 149 | 336 | 169 | 202 | 126 | 179 | 165 | 195 | 216 | 143 | 31 | 25 |
| Zn | 15 | 89 | 71 | 67 | 103 | 108 | 76 | 116 | 117 | 121 | 130 | 67 | 62 | 77 | 53 | 25 |
| Zr | 122 | 101 | 135 | 138 | 165 | 126 | 162 | 148 | 156 | 170 | 167 | 138 | 170 | 154 | 115 | 102 |
| Y | 8.7 | 8.8 | 15.7 | 13.9 | 14.2 | 33.2 | 15 | 15.1 | 16 | 20.5 | 19 | 13.9 | 25.5 | 18.4 | 10 | 7.6 |
| Nb | 10.8 | 11.5 | 6.3 | 5.4 | 6.1 | 7.7 | 6.4 | 7.3 | 8.8 | 9.4 | 9 | 5.4 | 8.8 | 5.5 | 9.1 | 11 |
| Pb | 57 | 47 | 19 | 16 | 11 | 18 | 11 | 48 | 19 | 13 | 24 | 16 | 10 | 16 | 35 | 47 |

**Analyses by X-ray Fluorescence**

| Sample Name | 99BT32 | 99BT582 | 14PI95a | 13PI118 | 13PI119 | 13PI120 | 1413116B226m | 14PI164 | 14PI168 | 14PI171 | 14PI173 | 14PI53a | 14PI603 | 14PI604 | 14RN110 | 14RN112 | 14RN114 | 14PI116 | 14PI116B |
|---|---|---|---|---|---|---|---|---|---|---|---|---|---|---|---|---|---|---|---|
| Rock Type | Ki | Ki | Ki | Ki | Ki | Ki | Ki | Ki | Ki | Ki | Ki | Ki | Ki | Ki | Ki | Ki | Ki | diabase | diabase |
| Major Elements (wt. %) | | | | | | | | | | | | | | | | | | | |
| SiO2 | 67.83 | 58.57 | 73.78 | 64.21 | 63.91 | 63.88 | 67.73 | 62.54 | 63.07 | 66.48 | 64.67 | 67.27 | 72.05 | 65.92 | 66.62 | 66.10 | 67.63 | 48.03 | 47.69 |
| Al2O3 | 16.22 | 15.21 | 15.10 | 16.20 | 16.11 | 16.21 | 16.36 | 15.56 | 14.49 | 14.27 | 14.44 | 15.41 | 14.10 | 15.55 | 16.12 | 16.52 | 16.19 | 16.95 | 16.79 |
| FeO | 2.90 | 5.89 | 3.49 | 4.98 | 4.98 | 4.96 | 3.38 | 5.73 | 5.97 | 4.62 | 5.04 | 3.37 | 2.95 | 3.68 | 3.25 | 3.16 | 2.80 | 11.72 | 11.65 |
| MgO | 1.28 | 4.71 | 1.03 | 1.63 | 1.92 | 1.91 | 1.10 | 2.66 | 3.01 | 2.12 | 2.35 | 1.14 | 1.02 | 1.18 | 1.03 | 0.79 | 0.84 | 6.65 | 7.24 |
| CaO | 4.52 | 6.64 | 0.31 | 3.79 | 3.74 | 3.86 | 4.19 | 7.80 | 6.73 | 5.29 | 6.20 | 4.00 | 2.95 | 5.83 | 4.11 | 4.16 | 4.03 | 8.78 | 9.48 |
| Na2O | 3.37 | 2.74 | 1.89 | 3.65 | 3.38 | 3.54 | 4.56 | 2.38 | 3.31 | 3.19 | 3.66 | 3.63 | 4.01 | 3.09 | 4.15 | 3.77 | 4.27 | 2.38 | 2.57 |
| K2O | 3.07 | 4.62 | 3.29 | 4.32 | 4.74 | 4.44 | 1.63 | 1.85 | 2.13 | 2.79 | 2.34 | 3.89 | 2.06 | 3.59 | 3.61 | 4.51 | 3.25 | 3.41 | 2.58 |
| MnO | 0.06 | 0.14 | 0.12 | 0.09 | 0.10 | 0.10 | 0.03 | 0.10 | 0.11 | 0.10 | 0.11 | 0.07 | 0.03 | 0.04 | 0.07 | 0.06 | 0.06 | 0.21 | 0.23 |
| TiO2 | 0.46 | 0.75 | 0.53 | 0.59 | 0.56 | 0.58 | 0.61 | 0.77 | 0.72 | 0.55 | 0.59 | 0.60 | 0.43 | 0.52 | 0.49 | 0.41 | 0.44 | 1.22 | 1.09 |
| P2O5 | 0.10 | 0.35 | 0.12 | 0.18 | 0.18 | 0.18 | 0.20 | 0.19 | 0.18 | 0.17 | 0.18 | 0.20 | 0.16 | 0.24 | 0.17 | 0.15 | 0.16 | 0.31 | 0.41 |
| BaO | 0.12 | 0.23 | 0.21 | 0.22 | 0.24 | 0.22 | 0.09 | 0.30 | 0.14 | 0.33 | 0.30 | 0.29 | 0.14 | 0.22 | 0.24 | 0.24 | 0.22 | 0.18 | 0.12 |
| Total | 96.315 | 97.49 | 81.66 | 95.337 | 92.787 | 93.858 | 96.553 | 93.589 | 91.919 | 94.255 | 93.891 | 90.009 | 95.403 | 92.086 | 93.925 | 92.773 | 96.043 | 89.858 | 93.157 |
| Minor Elements (ppm) | | | | | | | | | | | | | | | | | | | |
| Cr | 7 | 98 | 24 | 18 | 7 | 9 | 2 | 32 | 62 | 28 | 50 | BDL | BDL | 3 | BDL | BDL | BDL | 6 | 7 |
| Cu | 6 | 68 | 19 | 26 | 13 | 17 | 6 | 11 | 15 | 7 | 9 | 12 | 27 | 10 | 9 | 11 | 9 | 39 | 45 |
| Ni | 2 | 18 | 11 | 6 | 5 | 6 | 6 | 19 | 19 | 12 | 15 | 3 | 14 | 6 | 3 | 4 | 2 | 23 | 25 |
| Rb | 83 | 146 | 96 | 93 | 99 | 95 | 79 | 95 | 83 | 111 | 95 | 93 | 75 | 84 | 77 | 86 | 78 | 162 | 125 |
| Sr | 323 | 879 | 168 | 682 | 672 | 687 | 773 | 801 | 598 | 488 | 619 | 821 | 589 | 546 | 846 | 874 | 832 | 733 | 798 |
| V | 56 | 201 | 73 | 52 | 48 | 50 | 50 | 119 | 116 | 83 | 91 | 43 | 42 | 60 | 42 | 33 | 35 | 295 | 284 |
| Zn | 30 | 75 | 277 | 68 | 64 | 66 | 31 | 63 | 65 | 49 | 81 | 47 | 26 | 42 | 54 | 49 | 50 | 101 | 102 |
| Zr | 79 | 124 | 112 | 169 | 160 | 169 | 159 | 188 | 167 | 144 | 149 | 145 | 153 | 185 | 142 | 147 | 147 | 134 | 136 |
| Y | 8.4 | 15.3 | 11.5 | 10.1 | 10.4 | 9.5 | 7.9 | 13.3 | 12.9 | 15 | 13.8 | 6.7 | 8.7 | 10.1 | 7.8 | 6.7 | 6.8 | 26.9 | 28.9 |
| Nb | 6 | 6.6 | 9.8 | 9.6 | 9.8 | 10.2 | 7.4 | 7.9 | 7.5 | 9.2 | 9.7 | 7.2 | 6.7 | 10.1 | 5.5 | 6.3 | 6.7 | 7.4 | 7 |
| Pb | 16 | 15 | 80 | 51 | 17 | 14 | 8 | 7 | 15 | 10 | 8 | 13 | 12 | 15 | 13 | 21 | 15 | 8 | 8 |

Ki = Cretaceous intrusive. b. = basaltic.

# Appendix 3: Microprobe Mineral Compositions

## Table A3.1: Amphibole compositions by EPMA

| Sample ID | Depth | Cl | SiO2 | TiO2 | Al2O3 | FeO | MnO | CaO | MgO | K2O | Na2O | Total | Mineral name* |
|---|---|---|---|---|---|---|---|---|---|---|---|---|---|
| TET13085 | 157m | 1.45 | 38.69 | 0.23 | 8.79 | 33.77 | 0.22 | 10.42 | 1.38 | 2.15 | 0.82 | 97.9 | Ferro-edenite |
| TET13103 | 177.5m | 2.67 | 37.58 | 0.27 | 9.24 | 32.90 | 0.20 | 11.33 | 1.12 | 2.22 | 1.03 | 98.6 | Ferro-edenite |
| | | 0.37 | 48.77 | 0.09 | 2.24 | 27.49 | 0.21 | 11.43 | 5.84 | 0.34 | 0.23 | 97.0 | Hornblende |
| | | 0.17 | 50.79 | 0.06 | 1.04 | 25.05 | 0.27 | 11.91 | 7.57 | 0.22 | 0.19 | 97.3 | Hornblende |
| | | 2.66 | 34.86 | 0.25 | 9.40 | 33.93 | 0.24 | 10.71 | 1.48 | 1.99 | 0.97 | 96.5 | Ferro-edenite |
| TET13082 | | 1.87 | 38.40 | 0.37 | 8.83 | 33.18 | 0.24 | 11.12 | 0.74 | 1.90 | 0.77 | 97.4 | Ferro-edenite |
| 313-5 | | 1.17 | 45.94 | 0.08 | 4.61 | 32.52 | 0.32 | 11.34 | 2.64 | 0.59 | 0.48 | 99.7 | Ferro-actinolite |
| 313-10 | | 1.61 | 37.61 | 0.33 | 9.79 | 33.77 | 0.28 | 11.39 | 0.58 | 1.82 | 0.87 | 98.1 | Ferro-edenite |
| 313-3 | | 2.14 | 39.90 | 0.27 | 7.30 | 33.96 | 0.28 | 11.34 | 0.91 | 1.84 | 0.79 | 98.7 | Hastingsite |
| 313-4 | | 2.12 | 38.26 | 0.46 | 8.00 | 33.27 | 0.29 | 11.43 | 0.86 | 2.09 | 0.79 | 97.6 | Ferro-edenite |
| 313-6 | | 1.80 | 39.74 | 0.23 | 7.63 | 34.20 | 0.24 | 11.24 | 0.79 | 1.65 | 0.69 | 98.2 | Hastingsite |
| 313-7 | | 1.62 | 37.83 | 0.32 | 9.92 | 33.52 | 0.26 | 11.27 | 0.60 | 1.83 | 0.95 | 98.1 | Ferro-edenite |
| 313-8 | | 1.93 | 38.03 | 0.35 | 8.85 | 33.64 | 0.21 | 11.39 | 0.64 | 1.96 | 0.78 | 97.8 | Ferro-edenite |
| 313-9 | | 1.86 | 37.67 | 0.30 | 9.74 | 33.85 | 0.29 | 11.37 | 0.60 | 1.98 | 0.97 | 98.6 | Ferro-edenite |
| TET13083 | 126.4m | 2.34 | 39.53 | 0.27 | 8.32 | 34.03 | 0.28 | 11.11 | 0.68 | 2.35 | 0.68 | 99.6 | Ferro-edenite |
| | | 1.89 | 39.12 | 0.30 | 8.16 | 34.01 | 0.31 | 11.16 | 0.82 | 2.12 | 0.75 | 98.7 | Ferro-edenite |
| | | 2.46 | 38.92 | 0.25 | 8.43 | 33.97 | 0.25 | 11.25 | 0.73 | 2.36 | 0.69 | 99.3 | Ferro-edenite |
| | | 1.64 | 39.57 | 0.25 | 8.23 | 34.12 | 0.24 | 11.25 | 0.76 | 1.81 | 0.72 | 98.6 | Ferro-edenite |
| | | 2.02 | 39.65 | 0.25 | 8.03 | 34.07 | 0.25 | 11.20 | 0.80 | 2.06 | 0.67 | 99.0 | Hastingsite |
| | | 1.82 | 38.61 | 0.22 | 9.41 | 33.95 | 0.24 | 11.15 | 0.70 | 2.00 | 0.84 | 98.9 | Ferro-edenite |
| | | 2.03 | 38.94 | 0.41 | 8.22 | 34.55 | 0.29 | 11.27 | 0.74 | 2.24 | 0.67 | 99.3 | Ferro-edenite |
| | | 1.95 | 38.36 | 0.39 | 8.60 | 33.87 | 0.30 | 11.07 | 0.69 | 2.26 | 0.72 | 98.2 | Ferro-edenite |
| | | 2.00 | 38.30 | 0.29 | 9.03 | 34.32 | 0.26 | 11.13 | 0.72 | 2.09 | 0.86 | 99.0 | Ferro-edenite |

| | | | | | | | | | | | | | |
|---|---|---|---|---|---|---|---|---|---|---|---|---|---|
| | | 1.92 | 39.50 | 0.28 | 8.04 | 34.19 | 0.25 | 11.25 | 0.82 | 2.13 | 0.66 | 99.0 | Ferro-edenite |
| TET13082 | 29.3m | 2.84 | 37.69 | 0.33 | 9.92 | 33.65 | 0.22 | 11.22 | 0.48 | 2.53 | 0.87 | 99.8 | Ferro-edenite |
| | | 3.37 | 37.27 | 0.37 | 9.54 | 33.80 | 0.24 | 11.04 | 0.68 | 2.60 | 0.87 | 99.8 | Ferro-edenite |
| | | 2.41 | 38.65 | 0.33 | 9.58 | 33.21 | 0.32 | 11.26 | 0.95 | 2.36 | 0.79 | 99.9 | Ferro-edenite |
| | | 2.41 | 37.87 | 0.24 | 10.64 | 32.20 | 0.27 | 11.43 | 1.24 | 2.38 | 1.01 | 99.7 | Ferro-edenite |
| | | 3.09 | 36.12 | 0.39 | 10.67 | 33.12 | 0.25 | 10.87 | 0.68 | 2.77 | 0.79 | 98.8 | Ferro-edenite |
| | | 2.43 | 39.15 | 0.29 | 8.98 | 33.24 | 0.28 | 11.22 | 1.36 | 2.01 | 0.86 | 99.8 | Ferro-edenite |
| | | 2.86 | 37.40 | 0.39 | 10.56 | 32.30 | 0.27 | 11.21 | 1.09 | 2.58 | 0.98 | 99.6 | Ferro-edenite |
| | | 3.16 | 37.06 | 0.33 | 10.41 | 33.71 | 0.23 | 11.00 | 0.56 | 2.49 | 1.03 | 100.0 | Ferro-edenite |
| TET13082 | 34.1m | 1.89 | 41.96 | 0.10 | 5.97 | 33.26 | 0.29 | 11.24 | 1.80 | 1.50 | 0.71 | 98.7 | Hastingsite |
| | | 0.64 | 47.15 | 0.10 | 3.05 | 32.49 | 0.35 | 11.44 | 3.16 | 0.45 | 0.32 | 99.2 | Ferro-actinolite |
| | | 1.57 | 43.66 | 0.08 | 5.09 | 33.46 | 0.26 | 11.28 | 1.96 | 1.15 | 0.58 | 99.1 | Ferro-actinolite |
| | | 2.36 | 37.13 | 0.26 | 10.60 | 32.59 | 0.30 | 11.09 | 0.93 | 2.22 | 1.02 | 98.5 | Ferro-edenite |
| | | 2.27 | 39.97 | 0.22 | 7.86 | 32.84 | 0.30 | 10.81 | 1.25 | 1.96 | 0.75 | 98.2 | Hastingsite |
| | | 2.51 | 38.81 | 0.23 | 8.03 | 34.11 | 0.25 | 10.26 | 0.90 | 1.97 | 0.72 | 97.8 | Ferro-edenite |
| | | 1.81 | 40.87 | 0.33 | 7.54 | 32.76 | 0.30 | 11.32 | 1.73 | 1.63 | 0.75 | 99.1 | Hastingsite |
| | | 2.62 | 37.26 | 0.48 | 10.89 | 33.03 | 0.31 | 11.18 | 0.47 | 2.41 | 0.79 | 99.4 | Ferro-edenite |
| | | 2.83 | 37.01 | 0.40 | 9.74 | 33.59 | 0.26 | 11.15 | 0.62 | 2.48 | 0.88 | 99.0 | Ferro-edenite |
| TET13082 | 46.5m | 2.37 | 36.47 | 0.21 | 11.95 | 32.56 | 0.26 | 11.21 | 0.82 | 2.64 | 0.84 | 99.3 | Ferro-edenite |
| | | 0.15 | 48.27 | 0.02 | 1.11 | 34.01 | 0.70 | 10.74 | 2.09 | 0.30 | 0.13 | 97.5 | Hornblende |
| | | 0.77 | 45.41 | 0.15 | 2.85 | 33.30 | 0.52 | 10.96 | 2.11 | 0.61 | 0.26 | 96.9 | Ferro-actinolite |
| | | 2.78 | 37.96 | 0.48 | 9.65 | 33.79 | 0.22 | 11.27 | 0.60 | 2.36 | 0.97 | 100.1 | Ferro-edenite |
| | | 2.56 | 38.26 | 0.43 | 9.73 | 33.81 | 0.28 | 11.23 | 0.60 | 2.14 | 0.98 | 100.0 | Ferro-edenite |
| | | 3.52 | 38.10 | 0.04 | 9.77 | 31.95 | 0.14 | 11.36 | 1.64 | 2.56 | 0.80 | 99.9 | Ferro-edenite |
| | | 2.27 | 37.82 | 0.25 | 10.51 | 33.02 | 0.21 | 11.25 | 0.91 | 2.35 | 0.86 | 99.5 | Ferro-edenite |

| | | | | | | | | | | | | | |
|---|---|---|---|---|---|---|---|---|---|---|---|---|---|
| | | 2.02 | 37.85 | 0.30 | 9.05 | 34.43 | 0.25 | 10.47 | 1.09 | 1.96 | 0.75 | 98.2 | Ferro-edenite |
| | | 2.40 | 37.64 | 0.21 | 10.67 | 32.82 | 0.21 | 10.86 | 0.92 | 2.46 | 0.79 | 99.0 | Ferro-edenite |
| | | 2.35 | 36.52 | 0.26 | 11.80 | 32.22 | 0.25 | 11.44 | 0.93 | 2.82 | 0.84 | 99.4 | Ferro-edenite |
| TET13082 | 71.7m | 3.45 | 36.88 | 0.23 | 9.45 | 34.97 | 0.26 | 10.97 | 0.27 | 2.63 | 0.87 | 100.0 | Ferro-edenite |
| | | 2.62 | 39.32 | 0.16 | 7.83 | 33.95 | 0.23 | 11.26 | 0.69 | 2.15 | 0.72 | 98.9 | Hastingsite |
| | | 3.43 | 36.53 | 0.14 | 9.65 | 34.22 | 0.23 | 11.05 | 0.19 | 2.86 | 0.74 | 99.0 | Ferro-edenite |
| | | 3.44 | 36.29 | 0.14 | 9.86 | 34.48 | 0.22 | 10.91 | 0.18 | 2.77 | 0.80 | 99.1 | Ferro-edenite |
| | | 2.80 | 38.14 | 0.15 | 8.74 | 34.54 | 0.23 | 11.22 | 0.53 | 2.45 | 0.73 | 99.5 | Ferro-edenite |
| | | 3.38 | 37.63 | 0.11 | 8.63 | 34.59 | 0.24 | 11.05 | 0.41 | 2.63 | 0.74 | 99.4 | Ferro-edenite |
| | | 1.63 | 37.54 | 0.26 | 10.42 | 33.91 | 0.29 | 11.29 | 0.76 | 1.80 | 1.00 | 98.9 | Ferro-edenite |
| | | 3.27 | 36.50 | 0.14 | 10.20 | 35.02 | 0.24 | 11.07 | 0.20 | 2.89 | 0.76 | 100.3 | Ferro-edenite |
| | | 3.19 | 37.76 | 0.12 | 8.92 | 34.45 | 0.23 | 11.14 | 0.40 | 2.56 | 0.75 | 99.5 | Ferro-edenite |
| | | 2.44 | 38.03 | 0.42 | 8.99 | 33.61 | 0.27 | 11.02 | 0.69 | 2.23 | 0.85 | 98.5 | Ferro-edenite |
| TET13082 | 86.0m | 2.81 | 38.72 | 0.22 | 7.78 | 34.49 | 0.21 | 11.08 | 0.37 | 2.28 | 0.82 | 98.8 | Ferro-edenite |
| | | 1.86 | 39.43 | 0.36 | 7.48 | 34.03 | 0.30 | 11.27 | 0.99 | 1.84 | 0.73 | 98.3 | Hastingsite |
| | | 3.05 | 37.23 | 0.58 | 9.16 | 34.04 | 0.27 | 11.24 | 0.28 | 2.47 | 0.83 | 99.1 | Ferro-edenite |
| | | 2.84 | 40.69 | 0.12 | 6.37 | 34.07 | 0.27 | 11.27 | 0.79 | 1.97 | 0.67 | 99.1 | Hastingsite |
| | | 3.02 | 37.89 | 0.20 | 8.51 | 34.20 | 0.37 | 11.19 | 0.40 | 2.49 | 0.86 | 99.1 | Ferro-edenite |
| | | 2.69 | 36.26 | 0.50 | 11.46 | 32.99 | 0.27 | 11.28 | 0.23 | 2.80 | 0.78 | 99.3 | Ferro-edenite |
| | | 3.04 | 38.25 | 0.42 | 8.35 | 34.91 | 0.27 | 11.15 | 0.33 | 2.43 | 0.87 | 100.0 | Ferro-edenite |
| | | 3.04 | 38.75 | 0.22 | 9.12 | 34.11 | 0.27 | 11.20 | 0.44 | 2.31 | 0.94 | 100.4 | Ferro-edenite |
| | | 2.99 | 36.69 | 0.49 | 9.18 | 34.17 | 0.33 | 11.00 | 0.28 | 2.49 | 0.89 | 98.5 | Ferro-edenite |
| TET13082 | 104.2m | 1.50 | 39.49 | 0.40 | 8.69 | 33.05 | 0.23 | 11.38 | 1.30 | 1.73 | 0.72 | 98.5 | Ferro-edenite |
| | | 1.61 | 39.84 | 0.26 | 8.40 | 32.26 | 0.25 | 11.24 | 1.54 | 1.64 | 0.80 | 97.8 | Hastingsite |
| | | 1.41 | 40.38 | 0.38 | 7.86 | 32.93 | 0.29 | 11.30 | 1.50 | 1.55 | 0.68 | 98.3 | Hastingsite |
| | | 1.65 | 40.30 | 0.39 | 8.02 | 33.61 | 0.29 | 11.32 | 1.17 | 1.85 | 0.69 | 99.3 | Hastingsite |

| | | | | | | | | | | | | | |
|---|---|---|---|---|---|---|---|---|---|---|---|---|---|
| | | 1.97 | 38.95 | 0.15 | 8.92 | 32.82 | 0.21 | 11.38 | 1.40 | 2.02 | 0.76 | 98.6 | Ferro-edenite |
| | | 1.76 | 39.08 | 0.36 | 9.37 | 32.62 | 0.25 | 11.33 | 1.39 | 1.97 | 0.83 | 98.9 | Ferro-edenite |
| | | 1.96 | 39.96 | 0.21 | 8.54 | 32.45 | 0.33 | 11.29 | 1.59 | 1.92 | 0.87 | 99.1 | Ferro-edenite |
| | | 1.58 | 39.60 | 0.38 | 8.90 | 32.61 | 0.22 | 11.29 | 1.37 | 1.76 | 0.79 | 98.5 | Ferro-edenite |
| | | 1.88 | 40.14 | 0.26 | 8.70 | 32.15 | 0.27 | 11.40 | 1.62 | 1.86 | 0.76 | 99.0 | Hastingsite |
| | | 1.69 | 40.90 | 0.22 | 7.70 | 32.29 | 0.28 | 11.41 | 1.80 | 1.62 | 0.75 | 98.7 | Hastingsite |
| TET13082 | 116.5m | 1.50 | 41.59 | 0.38 | 7.44 | 30.96 | 0.26 | 11.35 | 3.10 | 1.56 | 0.74 | 98.9 | Hastingsite |
| | | 1.88 | 39.66 | 0.42 | 8.35 | 32.23 | 0.28 | 11.36 | 1.66 | 1.96 | 0.75 | 98.5 | Ferro-edenite |
| | | 1.30 | 42.15 | 0.39 | 7.13 | 30.89 | 0.27 | 11.40 | 2.84 | 1.37 | 0.69 | 98.4 | Hastingsite |
| | | 1.39 | 39.21 | 0.29 | 9.04 | 31.30 | 0.21 | 11.45 | 2.04 | 1.60 | 0.93 | 97.5 | Ferro-edenite |
| | | 1.02 | 38.82 | 0.24 | 10.04 | 31.70 | 0.29 | 11.38 | 1.77 | 1.46 | 0.91 | 97.6 | Ferro-edenite |
| | | 1.80 | 39.14 | 0.37 | 10.32 | 30.70 | 0.21 | 11.47 | 2.35 | 1.83 | 1.06 | 99.2 | Ferro-edenite |
| | | 1.49 | 41.29 | 0.39 | 7.91 | 30.54 | 0.21 | 11.46 | 2.63 | 1.67 | 0.83 | 98.4 | Hastingsite |
| | | 1.46 | 41.10 | 0.39 | 7.48 | 30.93 | 0.24 | 11.54 | 2.92 | 1.60 | 0.76 | 98.4 | Hastingsite |
| | | 1.33 | 39.44 | 0.26 | 9.61 | 30.72 | 0.26 | 11.58 | 2.69 | 1.67 | 1.00 | 98.5 | Ferro-edenite |
| | | 0.77 | 41.39 | 0.31 | 8.24 | 31.33 | 0.36 | 11.64 | 2.24 | 1.31 | 0.65 | 98.2 | Hastingsite |
| TET13092 | 74.9m | 2.33 | 38.34 | 0.17 | 8.76 | 32.86 | 0.24 | 11.03 | 1.34 | 2.09 | 0.81 | 98.0 | Ferro-edenite |
| | | 3.10 | 37.30 | 0.28 | 8.84 | 33.56 | 0.19 | 10.97 | 1.00 | 2.47 | 0.79 | 98.5 | Ferro-edenite |
| | | 1.93 | 38.82 | 0.19 | 8.83 | 33.14 | 0.25 | 11.04 | 1.41 | 1.84 | 0.76 | 98.2 | Ferro-edenite |
| | | 1.35 | 41.57 | 0.08 | 7.05 | 32.75 | 0.30 | 11.41 | 1.95 | 1.50 | 0.65 | 98.6 | Hastingsite |
| | | 1.59 | 38.93 | 0.33 | 9.34 | 32.97 | 0.27 | 11.32 | 1.31 | 1.83 | 0.93 | 98.8 | Ferro-edenite |
| | | 1.49 | 42.15 | 0.15 | 6.09 | 33.57 | 0.27 | 11.34 | 1.61 | 1.27 | 0.69 | 98.6 | Hastingsite |
| | | 1.58 | 40.23 | 0.28 | 8.08 | 33.42 | 0.24 | 11.07 | 1.50 | 1.72 | 0.65 | 98.8 | Hastingsite |
| | | 1.73 | 40.11 | 0.37 | 7.49 | 32.49 | 0.32 | 11.18 | 1.72 | 1.76 | 0.70 | 97.9 | Hastingsite |
| TET13085 | 161.2m | 1.79 | 39.49 | 0.34 | 8.87 | 32.30 | 0.18 | 11.27 | 2.10 | 1.84 | 0.83 | 99.0 | Ferro-edenite |
| | | 1.11 | 42.43 | 0.21 | 6.30 | 31.76 | 0.25 | 11.29 | 2.82 | 1.23 | 0.60 | 98.0 | Ferro-actinolite |
| | | 3.02 | 38.50 | 0.15 | 7.70 | 33.58 | 0.30 | 11.19 | 0.98 | 2.26 | 0.82 | 98.5 | Ferroedenite |
| | | 2.51 | 37.46 | 0.23 | 9.48 | 34.16 | 0.29 | 10.35 | 0.83 | 2.21 | 0.93 | 98.5 | Ferro-edenite |

| | | | | | | | | | | | | | |
|---|---|---|---|---|---|---|---|---|---|---|---|---|---|
| TET13094 | 131.2m | 2.99 | 37.94 | 0.25 | 8.93 | 33.37 | 0.32 | 11.16 | 0.87 | 2.44 | 0.88 | 99.1 | Ferro-edenite |
| | | 3.42 | 37.31 | 0.12 | 9.65 | 33.42 | 0.35 | 11.20 | 0.51 | 2.79 | 0.96 | 99.7 | Ferro-edenite |
| | | 3.74 | 37.26 | 0.10 | 9.31 | 34.14 | 0.28 | 11.16 | 0.61 | 2.91 | 0.78 | 100.3 | Ferro-edenite |
| | | 3.11 | 37.25 | 0.14 | 9.74 | 33.46 | 0.27 | 11.28 | 0.69 | 2.67 | 0.88 | 99.5 | Ferro-edenite |
| | | 3.13 | 37.08 | 0.14 | 9.61 | 33.83 | 0.29 | 11.11 | 0.66 | 2.58 | 0.87 | 99.3 | Ferro-edenite |
| | | 3.85 | 37.99 | 0.09 | 9.00 | 33.04 | 0.24 | 11.30 | 0.61 | 2.76 | 0.91 | 99.8 | Ferro-edenite |
| | | 2.57 | 38.30 | 0.35 | 8.45 | 33.08 | 0.32 | 11.32 | 1.25 | 2.20 | 0.99 | 98.8 | Ferro-edenite |
| | | 2.78 | 38.08 | 0.32 | 8.53 | 32.98 | 0.26 | 11.38 | 1.22 | 2.51 | 0.86 | 98.9 | Ferro-edenite |
| | | 1.58 | 41.77 | 0.32 | 7.00 | 31.74 | 0.26 | 11.45 | 2.24 | 1.42 | 0.84 | 98.6 | Hastingsite |
| | | 3.31 | 37.95 | 0.11 | 9.06 | 33.27 | 0.27 | 11.33 | 0.69 | 2.48 | 0.93 | 99.4 | Ferro-edenite |
| TET13094 | 135.0m | 3.24 | 35.92 | 0.30 | 10.65 | 33.43 | 0.36 | 11.36 | 0.44 | 2.97 | 0.88 | 99.6 | Ferro-edenite |
| | | 2.93 | 38.62 | 0.15 | 8.87 | 32.47 | 0.23 | 11.36 | 1.58 | 2.36 | 0.83 | 99.4 | Ferro-edenite |
| | | 4.19 | 36.89 | 0.13 | 9.16 | 33.32 | 0.24 | 11.43 | 0.75 | 2.96 | 0.81 | 99.9 | Ferro-edenite |
| | | 3.39 | 37.50 | 0.18 | 8.70 | 33.47 | 0.26 | 11.35 | 0.84 | 2.56 | 0.82 | 99.1 | Ferro-edenite |
| | | 3.21 | 37.38 | 0.20 | 8.85 | 32.80 | 0.28 | 11.33 | 0.94 | 2.55 | 0.85 | 98.4 | Ferro-edenite |
| | | 3.16 | 35.53 | 0.32 | 10.33 | 32.85 | 0.35 | 11.20 | 0.72 | 2.85 | 0.89 | 98.2 | Ferro-edenite |
| | | 3.43 | 37.19 | 0.31 | 9.02 | 32.91 | 0.28 | 11.43 | 0.76 | 2.63 | 0.80 | 98.8 | Ferro-edenite |
| | | 2.98 | 34.74 | 0.26 | 9.25 | 31.73 | 0.22 | 11.04 | 1.00 | 2.38 | 0.82 | 94.4 | Ferro-edenite |
| | | 3.52 | 37.60 | 0.09 | 8.23 | 33.29 | 0.32 | 11.28 | 1.13 | 2.60 | 0.78 | 98.8 | Ferro-edenite |
| | | 2.74 | 37.28 | 0.26 | 9.32 | 33.01 | 0.21 | 11.40 | 1.40 | 2.21 | 1.00 | 98.8 | Ferro-edenite |
| TET13083 | 131.0m | 3.58 | 37.03 | 0.15 | 8.87 | 33.44 | 0.20 | 10.93 | 0.74 | 2.60 | 0.87 | 98.4 | Ferro-edenite |
| | | 3.28 | 38.92 | 0.22 | 9.79 | 33.28 | 0.23 | 11.01 | 0.86 | 2.68 | 0.90 | 101.2 | Ferro-edenite |
| | | 3.17 | 37.38 | 0.12 | 9.34 | 34.16 | 0.22 | 11.17 | 0.74 | 2.49 | 0.91 | 99.7 | Ferro-edenite |
| | | 1.97 | 38.62 | 0.34 | 9.04 | 33.29 | 0.23 | 11.39 | 0.87 | 1.97 | 0.90 | 98.6 | Ferro-edenite |
| | | 2.12 | 41.83 | 0.11 | 5.96 | 33.92 | 0.31 | 11.19 | 1.09 | 1.55 | 0.66 | 98.7 | Hastingsite |

| | | | | | | | | | | | | | |
|---|---|---|---|---|---|---|---|---|---|---|---|---|---|
| | | 2.20 | 39.55 | 0.23 | 7.73 | 33.67 | 0.20 | 11.21 | 0.93 | 2.04 | 0.75 | 98.5 | Hastingsite |
| | | 3.13 | 38.25 | 0.27 | 9.59 | 33.13 | 0.24 | 10.95 | 0.62 | 2.51 | 1.03 | 99.7 | Ferro-edenite |
| | | 3.23 | 38.12 | 0.12 | 7.93 | 33.80 | 0.21 | 11.11 | 0.88 | 2.54 | 0.80 | 98.8 | Ferro-edenite |
| | | 1.71 | 39.90 | 0.38 | 8.86 | 33.73 | 0.24 | 11.28 | 0.84 | 2.00 | 0.79 | 99.7 | Ferro-edenite |
| | | 1.77 | 40.23 | 0.29 | 8.37 | 33.61 | 0.28 | 11.29 | 0.81 | 1.83 | 0.75 | 99.2 | Hastingsite |
| TET13083 | 143.4m | 1.49 | 38.53 | 0.33 | 9.63 | 33.50 | 0.27 | 11.32 | 0.66 | 1.77 | 0.76 | 98.3 | Ferro-edenite |
| | | 2.37 | 38.81 | 0.16 | 8.04 | 33.57 | 0.33 | 11.45 | 1.05 | 2.06 | 0.76 | 98.6 | Ferro-edenite |
| | | 1.93 | 38.86 | 0.30 | 8.96 | 33.20 | 0.29 | 11.37 | 0.73 | 1.92 | 0.76 | 98.3 | Ferro-edenite |
| | | 1.59 | 38.46 | 0.11 | 9.43 | 32.96 | 0.29 | 11.56 | 1.02 | 1.85 | 0.79 | 98.1 | Ferro-edenite |
| | | 1.55 | 39.70 | 0.32 | 8.33 | 33.80 | 0.18 | 11.46 | 0.81 | 1.83 | 0.68 | 98.7 | Ferro-edenite |
| | | 1.69 | 38.97 | 0.13 | 8.74 | 33.13 | 0.34 | 11.37 | 0.80 | 1.69 | 0.76 | 97.6 | Ferro-edenite |
| | | 1.67 | 38.70 | 0.37 | 8.31 | 33.76 | 0.23 | 11.40 | 0.87 | 1.99 | 0.66 | 98.0 | Ferro-edenite |
| | | 3.42 | 37.15 | 0.16 | 9.85 | 32.90 | 0.22 | 11.48 | 0.90 | 2.82 | 0.85 | 99.7 | Ferro-edenite |
| | | 2.48 | 39.89 | 0.14 | 7.29 | 32.07 | 0.18 | 11.61 | 1.61 | 2.04 | 0.77 | 98.1 | Hastingsite |
| | | 3.42 | 38.59 | 0.16 | 9.21 | 33.39 | 0.25 | 11.27 | 0.90 | 2.63 | 0.85 | 100.7 | Hastingsite |
| TET13084 | 152.7m | 3.14 | 38.36 | 0.03 | 8.33 | 34.38 | 0.27 | 11.21 | 0.48 | 2.29 | 0.89 | 99.4 | Ferro-edenite |
| | | 1.20 | 44.32 | 0.08 | 4.51 | 32.95 | 0.28 | 11.38 | 2.11 | 1.07 | 0.48 | 98.4 | Ferro-actinolite |
| | | 0.47 | 47.72 | 0.04 | 1.62 | 32.68 | 0.38 | 11.62 | 3.01 | 0.30 | 0.19 | 98.1 | Hornblende |
| | | 2.91 | 38.15 | 0.02 | 8.00 | 34.19 | 0.26 | 10.94 | 0.52 | 2.22 | 0.86 | 98.1 | Ferro-edenite |
| | | 3.26 | 38.70 | 0.00 | 8.24 | 35.05 | 0.18 | 11.21 | 0.35 | 2.41 | 0.82 | 100.2 | Ferro-edenite |
| | | 2.99 | 38.23 | 0.00 | 8.81 | 34.34 | 0.17 | 11.20 | 0.40 | 2.40 | 0.86 | 99.4 | Ferro-edenite |
| | | 1.04 | 41.80 | 0.30 | 7.19 | 32.32 | 0.27 | 11.51 | 1.92 | 1.28 | 0.72 | 98.4 | Hastingsite |
| | | 1.50 | 41.39 | 0.21 | 6.44 | 32.81 | 0.29 | 11.21 | 1.52 | 1.34 | 0.67 | 97.4 | Hastingsite |

Table A3.2: Garnet Compositions by EPMA

| Sample ID | Depth | MgO | Al2O3 | SiO2 | CaO | MnO | FeO | %Ad | %Gr |
|---|---|---|---|---|---|---|---|---|---|
| Saddle | Surface | 0 | 17.9 | 38.3 | 37 | 1.1 | 5.7 | 24 | 76 |
| | | 0.2 | 20.1 | 37.7 | 17.1 | 3 | 21.9 | 52 | 48 |
| | | 0 | 17.4 | 37.5 | 38.1 | 0.6 | 6.4 | 27 | 73 |
| | | 0 | 0.1 | 36.4 | 35.6 | 0.3 | 27.5 | 100 | 0 |
| | | 0 | 0 | 36.4 | 35.6 | 0.4 | 27.6 | 100 | 0 |
| | | 0 | 4.2 | 36.6 | 36.4 | 0.5 | 22.3 | 84 | 16 |
| | | 0 | 12.4 | 37.6 | 36.5 | 1 | 12.5 | 50 | 50 |

Table A3.3: Pyroxene Compositions by EPMA

| T/S # | MgO wt% | SiO2 wt% | CaO wt% | MnO wt% | FeO wt% | %Di | %Jo | %Hd |
|---|---|---|---|---|---|---|---|---|
| 67 | 7.0 | 52.2 | 24.7 | 0.8 | 15.2 | 1 | 6 | 93 |
| | 0.3 | 48.9 | 22.9 | 1.4 | 25.4 | 12 | 6 | 83 |
| | 1.0 | 49.5 | 23.0 | 1.3 | 24.8 | 1 | 5 | 95 |
| | 1.5 | 49.7 | 23.1 | 1.4 | 23.9 | 33 | 1 | 66 |
| | 5.6 | 51.6 | 24.3 | 1.0 | 17.3 | 19 | 4 | 77 |
| | 7.6 | 52.2 | 24.8 | 0.4 | 14.4 | 6 | 4 | 89 |
| | 1.7 | 49.8 | 23.3 | 1.4 | 23.4 | 15 | 5 | 80 |
| | 1.3 | 49.5 | 23.4 | 1.3 | 23.8 | 46 | 2 | 52 |
| | 2.4 | 50.6 | 23.8 | 1.4 | 21.9 | 32 | 5 | 63 |
| | 5.1 | 51.5 | 24.1 | 0.6 | 18.5 | 34 | 4 | 62 |
| | 6.4 | 52.1 | 24.3 | 0.9 | 16.2 | 37 | 4 | 59 |
| | 0.2 | 49.2 | 23.0 | 2.2 | 25.0 | 25 | 3 | 72 |
| | 2.2 | 49.8 | 23.3 | 1.4 | 23.0 | 14 | 5 | 81 |
| | 3.9 | 50.9 | 23.8 | 0.8 | 20.6 | 2 | 8 | 90 |
| | 5.9 | 51.9 | 24.4 | 1.0 | 16.6 | 40 | 3 | 57 |
| | 5.3 | 51.7 | 24.3 | 1.2 | 17.5 | 32 | 2 | 66 |
| | 5.1 | 51.5 | 24.2 | 1.3 | 17.8 | 16 | 5 | 79 |
| | 7.2 | 52.7 | 24.7 | 0.7 | 14.7 | 9 | 5 | 87 |
| | 2.3 | 50.2 | 23.8 | 1.4 | 22.1 | 11 | 5 | 84 |
| | 1.0 | 49.2 | 23.1 | 1.1 | 25.1 | 48 | 1 | 51 |
| | 3.0 | 50.4 | 24.0 | 1.1 | 21.2 | 35 | 3 | 61 |
| | 5.2 | 51.6 | 24.4 | 0.3 | 18.6 | 9 | 5 | 86 |
| | 0.1 | 48.6 | 23.0 | 1.3 | 26.1 | 7 | 5 | 89 |
| | 1.8 | 49.7 | 23.6 | 1.5 | 23.0 | 3 | 5 | 92 |
| | 0.1 | 48.7 | 23.2 | 1.6 | 25.6 | 44 | 3 | 53 |
| 72 | 3.8 | 51.0 | 23.4 | 0.9 | 21.0 | 24 | 3 | 73 |
| | 5.5 | 51.8 | 24.1 | 0.5 | 17.8 | 35 | 2 | 63 |
| | 1.7 | 49.9 | 23.3 | 0.8 | 24.2 | 11 | 3 | 87 |
| | 5.3 | 51.7 | 23.9 | 0.6 | 18.4 | 15 | 2 | 82 |
| | 2.4 | 50.2 | 23.5 | 0.6 | 23.3 | 43 | 1 | 55 |

| | | | | | | | | |
|---|---|---|---|---|---|---|---|---|
| | 7.1 | 52.3 | 24.2 | 0.4 | 16.0 | 23 | 2 | 75 |
| | 3.6 | 50.4 | 23.6 | 0.4 | 21.0 | 28 | 2 | 70 |
| | 4.4 | 50.9 | 23.8 | 0.5 | 19.6 | 36 | 2 | 62 |
| | 5.7 | 51.7 | 24.1 | 0.6 | 17.7 | 20 | 2 | 78 |
| | 3.2 | 50.5 | 23.6 | 0.5 | 21.8 | 18 | 2 | 80 |
| | 2.8 | 50.2 | 23.4 | 0.6 | 22.7 | 14 | 3 | 83 |
| | 2.2 | 50.2 | 23.2 | 0.7 | 23.4 | 28 | 2 | 69 |
| | 4.5 | 51.1 | 24.0 | 0.6 | 19.7 | 45 | 2 | 53 |
| | 7.3 | 52.7 | 24.4 | 0.4 | 15.2 | 36 | 1 | 63 |
| | 5.6 | 51.8 | 23.9 | 0.3 | 17.7 | 65 | 1 | 33 |
| | 10.9 | 53.7 | 25.2 | 0.4 | 9.9 | 61 | 1 | 37 |
| | 10.1 | 53.3 | 25.1 | 0.4 | 11.0 | 26 | 1 | 72 |
| | 4.1 | 50.9 | 23.4 | 0.4 | 20.1 | 30 | 2 | 68 |
| | 4.7 | 51.4 | 23.4 | 0.5 | 19.2 | 21 | 3 | 77 |
| | 3.3 | 50.9 | 23.1 | 0.7 | 21.9 | 33 | 2 | 66 |
| | 5.3 | 51.4 | 23.7 | 0.6 | 18.9 | 28 | 2 | 71 |
| | 4.5 | 51.3 | 23.5 | 0.5 | 20.3 | 25 | 2 | 73 |
| | 3.9 | 50.9 | 23.7 | 0.6 | 20.9 | 33 | 2 | 65 |
| 82 | 7.8 | 52.4 | 24.6 | 0.4 | 14.7 | 48 | 1 | 51 |
| | 6.3 | 51.6 | 24.3 | 0.5 | 16.6 | 40 | 2 | 59 |
| | 7.2 | 52.0 | 24.3 | 0.4 | 15.0 | 46 | 2 | 53 |
| | 8.5 | 52.6 | 24.8 | 0.3 | 13.0 | 53 | 1 | 46 |
| | 8.2 | 51.9 | 24.9 | 0.2 | 13.3 | 52 | 1 | 47 |
| | 7.8 | 52.2 | 25.0 | 0.3 | 14.2 | 49 | 1 | 50 |
| | 7.8 | 52.4 | 24.8 | 0.4 | 14.7 | 48 | 1 | 51 |
| | 8.1 | 52.4 | 24.8 | 0.2 | 13.6 | 51 | 1 | 48 |
| | 7.9 | 52.7 | 24.8 | 0.3 | 13.4 | 51 | 1 | 48 |
| | 6.0 | 51.8 | 24.5 | 0.8 | 17.0 | 38 | 3 | 60 |
| | 6.5 | 51.2 | 23.7 | 0.3 | 17.1 | 40 | 1 | 59 |
| | 7.5 | 52.2 | 24.6 | 0.4 | 14.8 | 47 | 1 | 52 |
| | 8.3 | 52.8 | 24.7 | 0.4 | 13.5 | 52 | 1 | 47 |
| | 9.1 | 53.3 | 25.0 | 0.2 | 12.4 | 56 | 1 | 43 |
| | 7.3 | 52.4 | 24.4 | 0.4 | 15.4 | 45 | 1 | 53 |
| | 5.9 | 51.6 | 24.2 | 0.3 | 17.9 | 37 | 1 | 62 |
| | 8.1 | 52.3 | 24.8 | 0.3 | 13.4 | 51 | 1 | 48 |
| | 6.4 | 51.8 | 24.5 | 0.4 | 16.9 | 40 | 1 | 59 |
| | 7.9 | 52.2 | 25.1 | 0.4 | 13.8 | 50 | 1 | 49 |
| | 5.3 | 51.3 | 24.5 | 0.6 | 18.1 | 34 | 2 | 64 |
| | 5.4 | 50.9 | 24.0 | 0.4 | 18.3 | 34 | 2 | 65 |
| | 8.0 | 52.6 | 24.7 | 0.4 | 13.8 | 50 | 1 | 49 |
| | 6.7 | 51.8 | 24.8 | 0.4 | 16.2 | 42 | 1 | 57 |
| 84 | 0.4 | 48.5 | 22.3 | 0.4 | 27.5 | 2 | 1 | 96 |
| | 1.1 | 49.4 | 22.9 | 0.7 | 25.4 | 7 | 3 | 90 |

| | | | | | | | | |
|---|---|---|---|---|---|---|---|---|
| | 1.0 | 49.0 | 22.6 | 0.4 | 26.5 | 6 | 2 | 92 |
| | 0.7 | 48.9 | 22.4 | 0.5 | 27.0 | 4 | 2 | 94 |
| | 0.6 | 49.0 | 22.3 | 0.4 | 26.9 | 4 | 2 | 95 |
| | 0.7 | 49.2 | 23.1 | 0.9 | 25.9 | 4 | 3 | 92 |
| | 0.9 | 48.7 | 22.2 | 0.5 | 26.9 | 5 | 2 | 93 |
| | 3.8 | 50.5 | 23.2 | 0.7 | 21.5 | 23 | 2 | 74 |
| | 1.1 | 48.8 | 22.2 | 0.6 | 26.4 | 7 | 2 | 91 |
| | 1.4 | 49.4 | 23.4 | 0.8 | 24.8 | 9 | 3 | 89 |
| | 3.7 | 50.6 | 23.4 | 0.8 | 21.1 | 23 | 3 | 74 |
| | 1.0 | 48.6 | 22.2 | 0.6 | 26.6 | 6 | 2 | 92 |
| | 2.4 | 49.8 | 23.0 | 0.9 | 23.7 | 15 | 3 | 82 |
| | 3.0 | 50.3 | 23.3 | 0.7 | 22.3 | 19 | 3 | 79 |
| | 4.0 | 50.8 | 23.4 | 0.8 | 20.8 | 25 | 3 | 73 |
| | 0.9 | 48.5 | 22.6 | 0.5 | 26.5 | 6 | 2 | 93 |
| | 1.0 | 49.1 | 22.5 | 0.6 | 26.2 | 6 | 2 | 92 |
| | 3.9 | 50.5 | 23.3 | 0.8 | 21.3 | 24 | 3 | 73 |
| | 0.4 | 48.4 | 22.0 | 0.5 | 27.9 | 2 | 2 | 96 |
| | 4.1 | 50.9 | 23.2 | 0.6 | 20.7 | 25 | 2 | 72 |
| | 1.9 | 50.2 | 23.3 | 0.7 | 23.8 | 12 | 2 | 85 |
| | 1.4 | 49.3 | 22.9 | 0.6 | 25.5 | 9 | 2 | 89 |
| | 0.4 | 48.2 | 22.6 | 0.5 | 27.5 | 2 | 2 | 96 |
| | 0.9 | 48.7 | 22.3 | 0.7 | 26.5 | 6 | 2 | 92 |
| | 1.4 | 49.5 | 22.9 | 0.6 | 25.3 | 9 | 2 | 89 |
| 65 | 1.6 | 49.4 | 23.1 | 0.8 | 24.7 | 10 | 3 | 87 |
| | 1.1 | 48.9 | 23.1 | 0.9 | 25.2 | 7 | 3 | 90 |
| | 0.2 | 48.8 | 22.9 | 1.7 | 26.2 | 1 | 6 | 93 |
| | 2.1 | 50.0 | 23.5 | 0.9 | 23.5 | 13 | 3 | 84 |
| | 1.5 | 49.6 | 22.9 | 0.7 | 24.9 | 9 | 3 | 88 |
| | 1.5 | 49.3 | 23.2 | 0.7 | 24.7 | 10 | 3 | 88 |
| | 1.3 | 49.1 | 22.3 | 0.7 | 25.7 | 8 | 2 | 89 |
| | 1.3 | 49.1 | 22.4 | 0.7 | 26.0 | 8 | 2 | 90 |
| | 0.7 | 48.9 | 23.0 | 0.7 | 26.3 | 4 | 2 | 93 |
| | 1.9 | 49.4 | 23.1 | 0.8 | 24.5 | 12 | 3 | 85 |
| | 1.2 | 48.9 | 22.5 | 0.7 | 26.0 | 7 | 2 | 90 |
| | 1.5 | 49.2 | 22.4 | 0.8 | 25.3 | 9 | 3 | 88 |
| | 2.3 | 50.1 | 23.5 | 1.1 | 23.1 | 14 | 4 | 82 |
| | 1.4 | 49.0 | 22.4 | 0.7 | 25.6 | 8 | 3 | 89 |
| | 1.0 | 48.9 | 23.1 | 0.5 | 26.1 | 6 | 2 | 92 |
| | 2.3 | 49.7 | 23.8 | 1.2 | 23.0 | 14 | 4 | 81 |
| | 1.7 | 49.5 | 23.3 | 0.9 | 24.4 | 11 | 3 | 86 |
| | 2.2 | 49.9 | 23.5 | 0.8 | 23.6 | 14 | 3 | 83 |
| | 1.0 | 48.9 | 22.8 | 0.8 | 25.5 | 6 | 3 | 91 |
| | 1.5 | 49.2 | 22.9 | 0.7 | 25.2 | 10 | 2 | 88 |

| | | | | | | | | |
|---|---|---|---|---|---|---|---|---|
| | 1.5 | 49.6 | 23.3 | 0.7 | 24.6 | 10 | 2 | 88 |
| | 1.4 | 49.0 | 22.8 | 0.7 | 25.3 | 8 | 3 | 89 |
| | 1.2 | 48.9 | 22.4 | 1.0 | 25.6 | 7 | 4 | 89 |
| | 1.4 | 48.8 | 22.6 | 0.8 | 25.6 | 9 | 3 | 89 |
| | 1.3 | 49.5 | 22.9 | 1.2 | 25.0 | 8 | 4 | 88 |
| | 1.2 | 48.8 | 22.4 | 0.7 | 26.0 | 7 | 2 | 90 |
| 66 | 0.4 | 49.3 | 23.4 | 0.9 | 26.1 | 3 | 3 | 94 |
| | 1.1 | 49.6 | 23.4 | 1.0 | 25.1 | 7 | 3 | 90 |
| | 1.2 | 49.4 | 23.3 | 0.8 | 25.0 | 8 | 3 | 89 |
| | 4.5 | 51.2 | 24.7 | 0.7 | 19.0 | 29 | 3 | 69 |
| | 0.0 | 49.2 | 23.4 | 1.5 | 25.9 | 0 | 6 | 94 |
| | 0.5 | 49.1 | 23.3 | 0.8 | 25.9 | 3 | 3 | 94 |
| | 0.3 | 49.1 | 23.2 | 1.1 | 26.3 | 2 | 4 | 94 |
| | 1.1 | 49.7 | 23.4 | 0.9 | 24.8 | 7 | 3 | 89 |
| | 0.2 | 48.7 | 23.1 | 1.6 | 25.8 | 1 | 6 | 93 |
| | 1.3 | 49.5 | 23.1 | 1.0 | 24.7 | 8 | 4 | 88 |
| | 0.1 | 49.2 | 22.6 | 1.5 | 25.6 | 1 | 6 | 94 |
| | 1.0 | 49.3 | 23.3 | 0.8 | 25.3 | 6 | 3 | 91 |
| | 0.1 | 48.8 | 23.2 | 2.3 | 25.5 | 0 | 8 | 91 |
| | 0.2 | 48.8 | 23.2 | 2.0 | 25.3 | 1 | 7 | 92 |
| | 1.2 | 49.5 | 23.3 | 0.9 | 24.9 | 7 | 3 | 89 |
| | 0.1 | 48.8 | 23.3 | 2.0 | 25.6 | 0 | 7 | 92 |
| | 2.6 | 50.2 | 23.8 | 0.7 | 22.7 | 17 | 2 | 81 |
| | 1.3 | 49.5 | 23.4 | 0.8 | 24.8 | 8 | 3 | 89 |
| | 0.1 | 48.8 | 23.3 | 3.3 | 24.5 | 1 | 12 | 88 |
| | 1.0 | 49.4 | 23.6 | 1.1 | 24.9 | 7 | 4 | 90 |
| | 4.6 | 51.0 | 24.3 | 0.8 | 19.3 | 29 | 3 | 68 |
| | 0.1 | 48.8 | 23.1 | 2.1 | 25.8 | 1 | 7 | 92 |
| | 0.0 | 48.9 | 23.3 | 1.7 | 25.8 | 0 | 6 | 94 |
| | 0.0 | 49.1 | 23.4 | 3.2 | 24.3 | 0 | 12 | 88 |
| | 1.2 | 49.4 | 23.3 | 0.8 | 25.1 | 7 | 3 | 90 |
| | 4.1 | 50.8 | 24.1 | 0.5 | 20.5 | 26 | 2 | 72 |
| | 0.1 | 49.0 | 23.2 | 2.1 | 25.6 | 1 | 7 | 92 |
| | 1.0 | 49.3 | 23.2 | 0.7 | 25.4 | 7 | 3 | 91 |
| | 0.1 | 48.9 | 23.2 | 2.3 | 25.0 | 1 | 8 | 91 |
| | 0.4 | 49.2 | 23.5 | 0.8 | 26.1 | 3 | 3 | 94 |
| 205 | 4.14 | 50.34 | 23.75 | 1.67 | 19.24 | 26 | 6 | 68 |
| | 3.91 | 50.42 | 23.65 | 1.55 | 19.7 | 25 | 6 | 70 |
| | 5.65 | 51.31 | 24.09 | 1.61 | 16.62 | 36 | 6 | 59 |
| | 8.65 | 52.3 | 25.27 | 0.74 | 12.47 | 54 | 3 | 44 |
| | 4.91 | 51.01 | 24.04 | 1.43 | 17.78 | 31 | 5 | 64 |
| | 7.91 | 52.29 | 24.81 | 0.73 | 13.78 | 49 | 3 | 48 |
| | 11.07 | 53.46 | 25.7 | 1.04 | 8.13 | 68 | 4 | 28 |

| | | | | | | | | |
|---|---|---|---|---|---|---|---|---|
| | 4.28 | 50.82 | 23.97 | 1.61 | 18.74 | 27 | 6 | 67 |
| | 9.79 | 52.82 | 25.28 | 0.44 | 11.03 | 60 | 2 | 38 |
| | 10.11 | 52.59 | 25.58 | 1.04 | 9.73 | 63 | 4 | 34 |
| | 7.95 | 52.13 | 24.74 | 0.88 | 13.87 | 49 | 3 | 48 |
| | 9.4 | 52.8 | 25.26 | 0.42 | 11.15 | 59 | 2 | 39 |
| | 4.57 | 50.79 | 23.89 | 1.94 | 18.01 | 29 | 7 | 64 |
| | 9.1 | 52.74 | 25.19 | 0.73 | 11.87 | 56 | 3 | 41 |
| | 9.48 | 52.43 | 25.38 | 0.38 | 11.23 | 60 | 1 | 40 |
| | 5.59 | 51.41 | 24.54 | 0.94 | 17.34 | 35 | 3 | 61 |
| | 6.18 | 51.71 | 24.54 | 0.72 | 16.84 | 39 | 3 | 59 |
| | 8.83 | 52.57 | 25.04 | 0.48 | 12.37 | 55 | 2 | 43 |
| | 4.07 | 50.51 | 23.64 | 1.36 | 19.36 | 26 | 5 | 69 |
| | 10.77 | 53.3 | 25.32 | 1.01 | 8.92 | 66 | 3 | 31 |
| | 9.93 | 52.48 | 25.54 | 0.63 | 10.07 | 62 | 2 | 35 |
| | 10.15 | 52.89 | 25.85 | 0.64 | 9.66 | 64 | 2 | 34 |
| | 4.9 | 50.86 | 24.1 | 1.08 | 18.11 | 31 | 4 | 65 |
| | 9.97 | 52.31 | 25.31 | 0.65 | 10.32 | 62 | 2 | 36 |
| | 11.95 | 53.85 | 25.51 | 0.59 | 7.62 | 72 | 2 | 26 |
| | 6.28 | 46.9 | 29.36 | 1.48 | 14.82 | 41 | 5 | 54 |
| | 9.47 | 52.74 | 25.78 | 0.75 | 10.58 | 60 | 3 | 37 |
| | 9.54 | 53.31 | 25.21 | 1.04 | 10.9 | 59 | 4 | 38 |
| 64 | 4.43 | 50.96 | 23.35 | 0.36 | 20.68 | 27 | 1 | 71 |
| | 3.12 | 50.39 | 23.32 | 0.42 | 22.44 | 20 | 1 | 79 |
| | 4.27 | 51.15 | 23.7 | 0.5 | 20.39 | 27 | 2 | 72 |
| | 5.62 | 51.53 | 23.62 | 0.71 | 18.27 | 35 | 3 | 63 |
| | 4.86 | 51.49 | 23.9 | 0.61 | 19.15 | 30 | 2 | 67 |
| | 5.87 | 51.86 | 24.47 | 1.48 | 16.32 | 37 | 5 | 58 |
| | 4.93 | 51.12 | 23.67 | 0.76 | 19.06 | 31 | 3 | 67 |
| | 7.84 | 52.64 | 24.64 | 0.73 | 14.14 | 48 | 3 | 49 |
| | 5.67 | 55.41 | 22.48 | 0.48 | 15.21 | 39 | 2 | 59 |
| | 4.21 | 50.9 | 23.56 | 0.41 | 20.82 | 26 | 1 | 72 |
| | 6.45 | 52.01 | 24.48 | 0.8 | 16.26 | 40 | 3 | 57 |
| | 4.5 | 51.03 | 24.22 | 0.74 | 19.35 | 28 | 3 | 69 |
| | 4.13 | 50.8 | 23.59 | 0.36 | 20.81 | 26 | 1 | 73 |
| | 6.23 | 51.82 | 24.57 | 1.05 | 16.33 | 39 | 4 | 57 |
| | 4.45 | 51.06 | 23.5 | 0.38 | 20.19 | 28 | 1 | 71 |
| | 3.23 | 50.43 | 23.44 | 0.55 | 21.72 | 21 | 2 | 77 |
| | 4.13 | 50.73 | 23.42 | 0.36 | 20.89 | 26 | 1 | 73 |
| | 4.32 | 50.99 | 23.66 | 0.77 | 19.83 | 27 | 3 | 70 |
| | 2.94 | 50.12 | 23.26 | 0.77 | 22.03 | 19 | 3 | 78 |
| | 4.42 | 50.97 | 23.3 | 0.5 | 20.23 | 27 | 2 | 71 |
| | 4.29 | 51.26 | 24.08 | 0.73 | 19.63 | 27 | 3 | 70 |
| | 2.73 | 50.14 | 23.4 | 0.65 | 22.59 | 17 | 2 | 80 |

| | | | | | | | | |
|---|---|---|---|---|---|---|---|---|
| | 4.72 | 51.17 | 23.3 | 0.67 | 19.82 | 29 | 2 | 69 |
| | 3.21 | 50.05 | 23.19 | 0.61 | 22.22 | 20 | 2 | 78 |
| | 3.94 | 50.6 | 23.43 | 0.66 | 21.08 | 24 | 2 | 73 |
| | 4.12 | 50.36 | 23.76 | 0.73 | 20.54 | 26 | 3 | 72 |
| | 4.62 | 50.84 | 23.72 | 0.59 | 19.71 | 29 | 2 | 69 |
| | 4.16 | 50.48 | 23.48 | 0.72 | 20.51 | 26 | 3 | 72 |
| | 4.26 | 50.69 | 23.03 | 0.68 | 20.41 | 26 | 2 | 71 |
| | 4.31 | 50.85 | 23.41 | 0.58 | 20.33 | 27 | 2 | 71 |
| | 4.63 | 51.28 | 24.05 | 0.81 | 19.08 | 29 | 3 | 68 |
| 73 | 4.36 | 51.13 | 24.39 | 0.59 | 19.53 | 28 | 2 | 70 |
| | 5.07 | 51.16 | 24.3 | 0.6 | 18.88 | 32 | 2 | 66 |
| | 4.32 | 50.94 | 24.28 | 0.44 | 20.02 | 27 | 2 | 71 |
| | 3.58 | 50.75 | 23.93 | 0.75 | 21 | 23 | 3 | 75 |
| | 3.95 | 50.59 | 23.78 | 0.65 | 20.96 | 25 | 2 | 73 |
| | 4.3 | 50.89 | 24.09 | 0.66 | 20.06 | 27 | 2 | 71 |
| | 4.15 | 50.79 | 23.85 | 0.54 | 20.67 | 26 | 2 | 72 |
| | 4.24 | 50.84 | 24.14 | 0.7 | 20.01 | 27 | 2 | 71 |
| | 4.17 | 51 | 23.87 | 0.5 | 20.33 | 26 | 2 | 72 |
| | 4.1 | 50.85 | 24.16 | 0.61 | 20.29 | 26 | 2 | 72 |
| | 4.2 | 50.86 | 24.11 | 0.62 | 20.21 | 26 | 2 | 71 |
| | 3.1 | 50.68 | 23.62 | 0.65 | 21.95 | 20 | 2 | 78 |
| | 4.13 | 50.99 | 23.75 | 0.46 | 20.67 | 26 | 2 | 73 |
| | 5.12 | 51.22 | 24.14 | 0.57 | 18.95 | 32 | 2 | 66 |
| | 4.85 | 51.09 | 24.11 | 0.49 | 19.46 | 30 | 2 | 68 |
| | 4.74 | 50.93 | 24.59 | 0.58 | 19.15 | 30 | 2 | 68 |
| | 3.72 | 50.85 | 24.06 | 0.6 | 20.77 | 24 | 2 | 74 |
| | 4.41 | 51.05 | 24.13 | 0.58 | 19.82 | 28 | 2 | 70 |
| | 4.1 | 50.87 | 24.41 | 0.5 | 20.12 | 26 | 2 | 72 |
| | 4.31 | 50.95 | 24.28 | 0.72 | 19.74 | 27 | 3 | 70 |
| 56 | 2.7 | 50.44 | 23.51 | 0.51 | 22.65 | 17 | 2 | 81 |
| | 2.36 | 50.14 | 23.89 | 0.74 | 22.77 | 15 | 3 | 82 |
| | 1.17 | 49.15 | 23.02 | 0.7 | 25.16 | 7 | 3 | 90 |
| | 2.51 | 50.53 | 23.5 | 0.53 | 22.93 | 16 | 2 | 82 |
| | 3.44 | 50.57 | 23.57 | 0.72 | 21.52 | 22 | 3 | 76 |
| | 2.88 | 50.61 | 23.6 | 0.74 | 22.17 | 18 | 3 | 79 |
| | 3.5 | 51.05 | 23.61 | 0.6 | 21.24 | 22 | 2 | 76 |
| | 1.33 | 49.27 | 23.19 | 0.91 | 24.71 | 9 | 3 | 88 |
| | 2.01 | 50.23 | 23.34 | 0.7 | 23.71 | 13 | 3 | 85 |
| | 3.03 | 50.48 | 23.7 | 0.62 | 22.17 | 19 | 2 | 79 |
| | 2.4 | 50.1 | 23.51 | 0.74 | 23.03 | 15 | 3 | 82 |
| | 3.13 | 50.21 | 23.54 | 0.61 | 22.27 | 20 | 2 | 78 |
| | 1.44 | 49.68 | 23.48 | 0.84 | 24.16 | 9 | 3 | 88 |
| | 3.04 | 50.83 | 23.85 | 0.43 | 21.72 | 20 | 2 | 79 |

| | | | | | | | |
|---|---|---|---|---|---|---|---|
| 2.87 | 50.29 | 23.74 | 0.6 | 22.31 | 18 | 2 | 80 |
| 3.06 | 50.48 | 23.5 | 0.56 | 22.24 | 19 | 2 | 79 |
| 4.2 | 52.17 | 19.05 | 0.34 | 24.24 | 23 | 1 | 76 |
| 2.51 | 50.46 | 23.54 | 0.67 | 22.82 | 16 | 2 | 82 |
| 2.46 | 50.31 | 23.6 | 0.57 | 23.06 | 16 | 2 | 82 |
| 0.17 | 50.19 | 23.73 | 0.51 | 22.5 | 18 | 2 | 80 |
| 2.9 | 50.51 | 23.46 | 0.56 | 22.57 | 18 | 2 | 80 |
| 3.1 | 50.5 | 23.47 | 0.63 | 22.08 | 20 | 2 | 78 |
| 3.1 | 50.5 | 23.47 | 0.63 | 22.08 | 20 | 2 | 78 |
| 3.22 | 50.17 | 23.74 | 0.63 | 22.25 | 20 | 2 | 78 |
| 1.48 | 49.78 | 23.15 | 0.68 | 24.7 | 9 | 2 | 88 |

# Appendix 4: Geochronology Figures and Tables

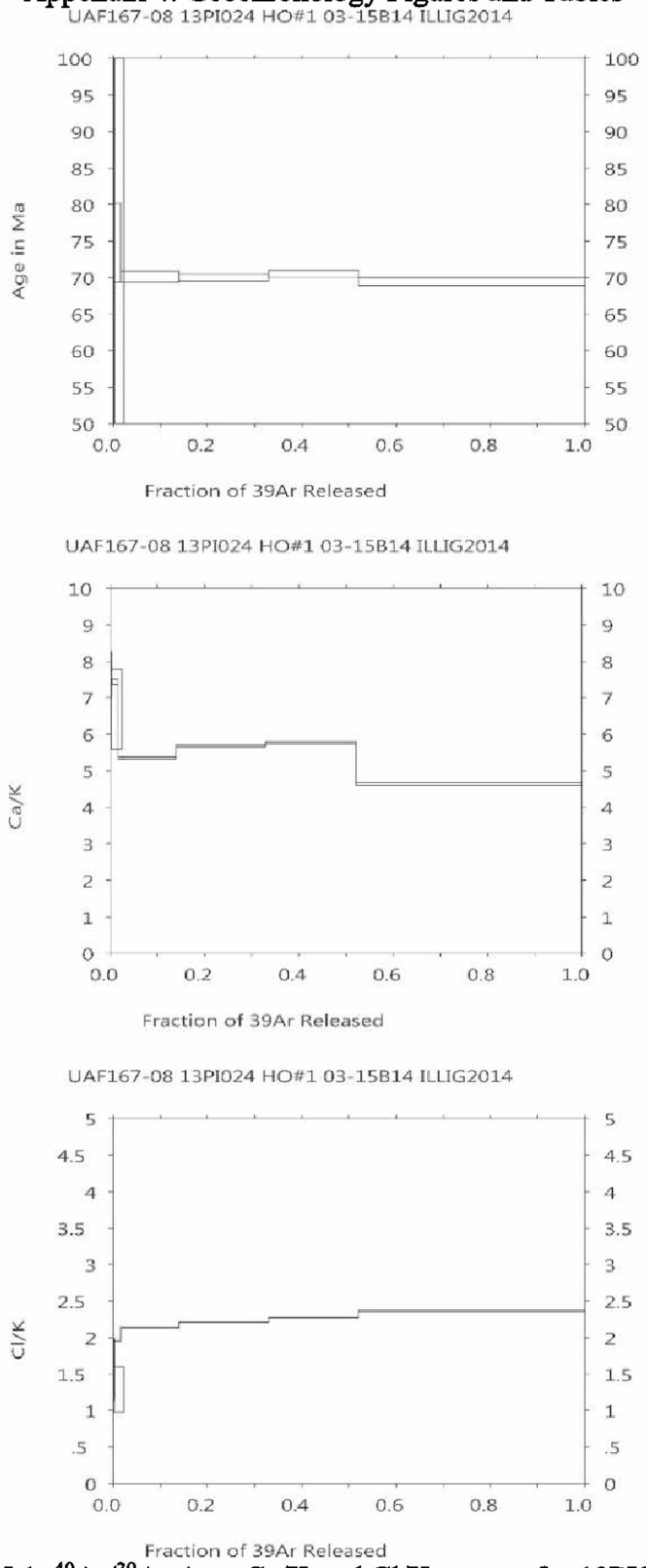


Figure A5.1: $^{40}Ar/^{39}Ar$ Age, Ca/K and Cl/K spectra for 13PI024 HO#1

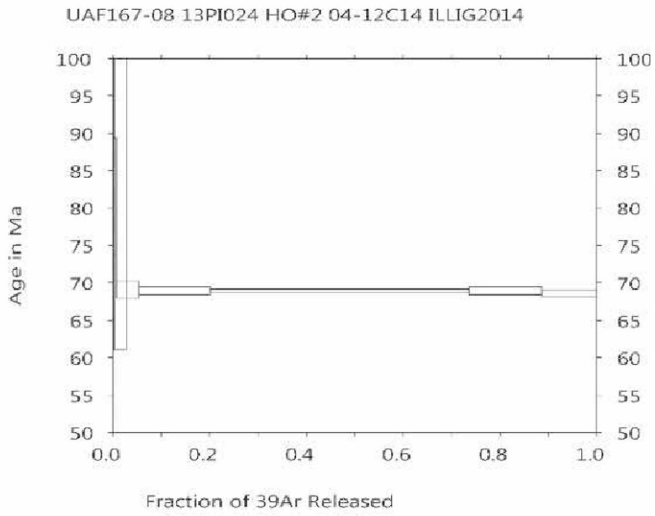


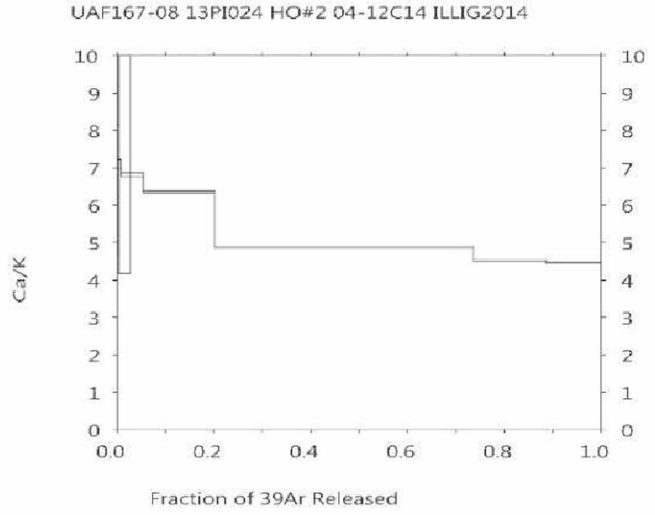


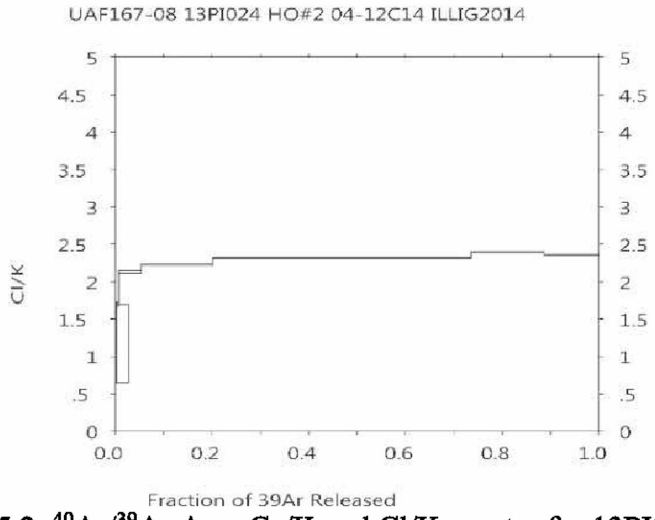


Figure A5.2: $^{40}Ar/^{39}Ar$ Age, Ca/K and Cl/K spectra for 13PI024 HO#2

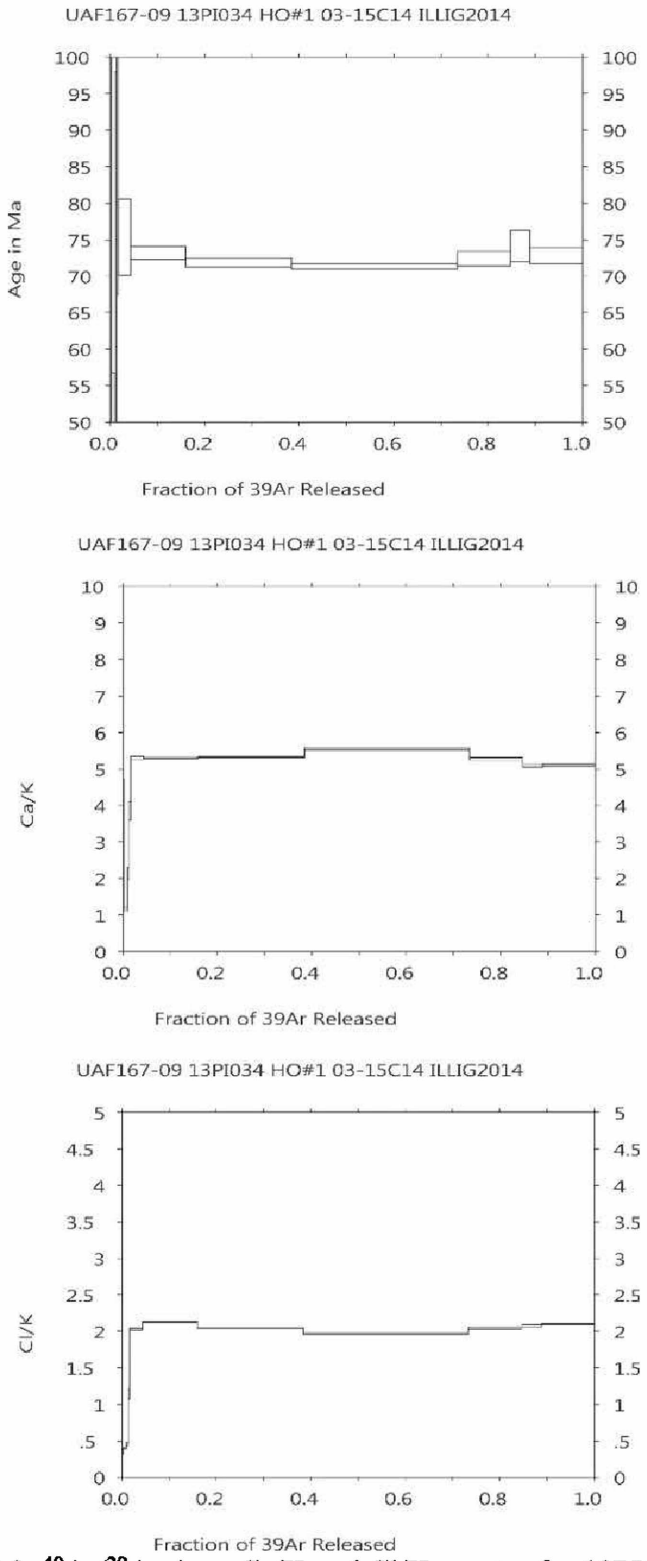


Figure A5.3: $^{40}Ar/^{39}Ar$ Age, Ca/K and Cl/K spectra for 13PI034 HO#1

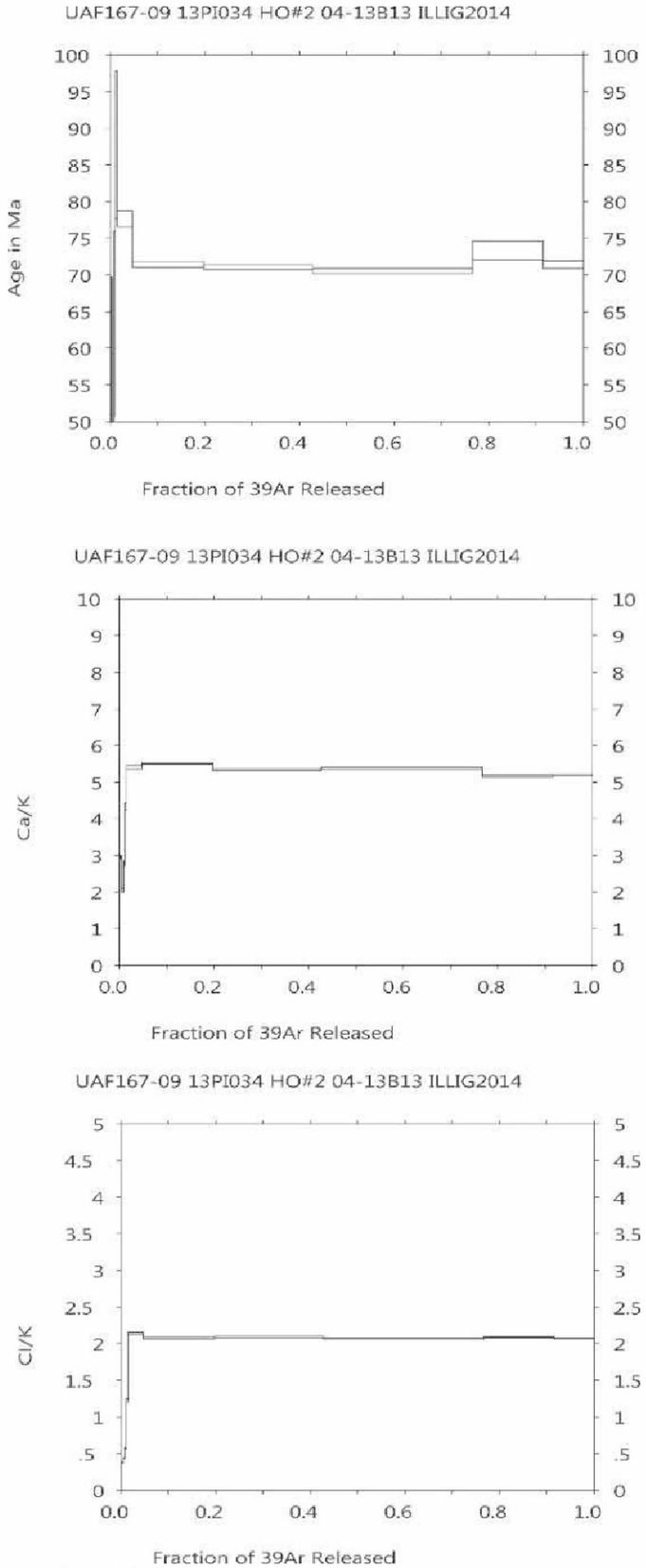


Figure A5.4: $^{40}Ar/^{39}Ar$ Age, Ca/K and Cl/K spectra for 13PI034 HO#2

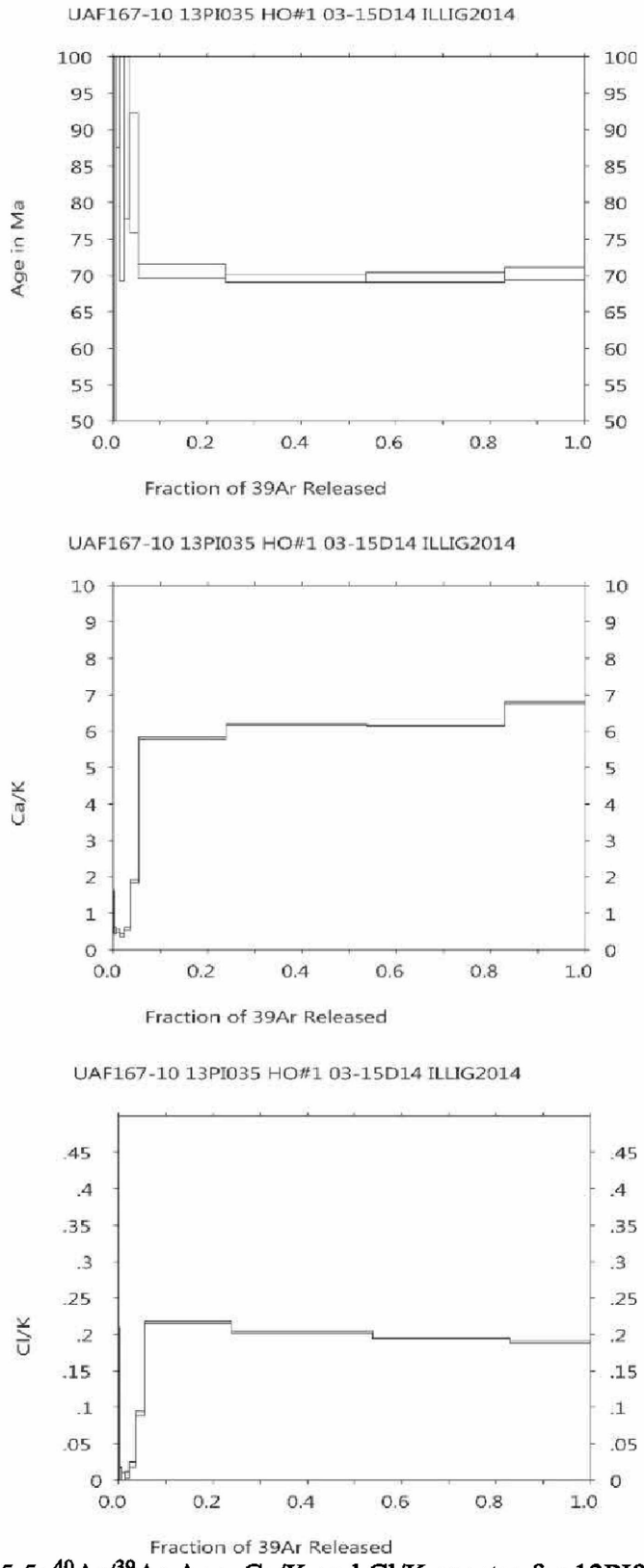


Figure A5.5: $^{40}Ar/^{39}Ar$ Age, Ca/K and Cl/K spectra for 13PI035 HO#1

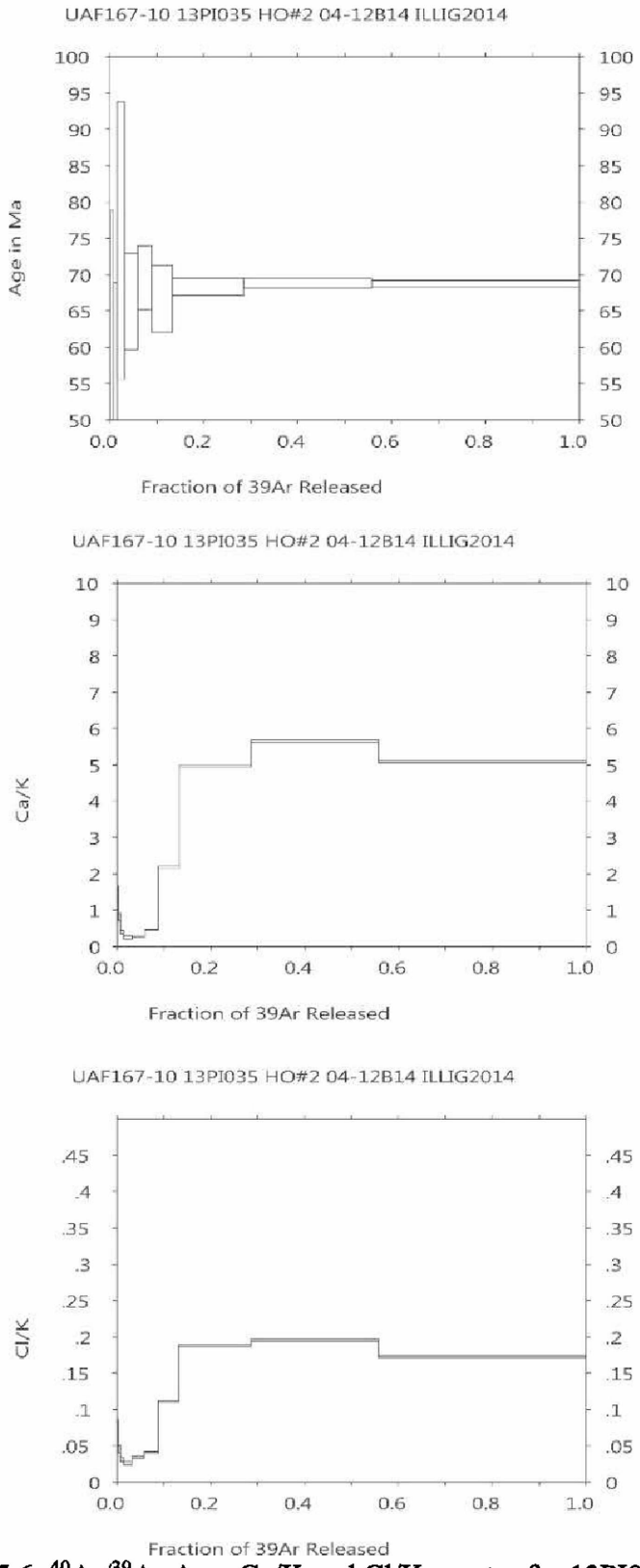


Figure A5.6: $^{40}Ar/^{39}Ar$ Age, Ca/K and Cl/K spectra for 13PI035 HO#2

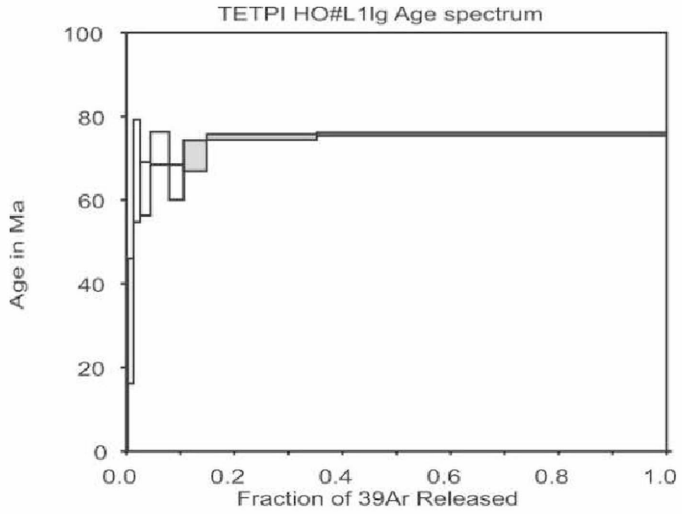


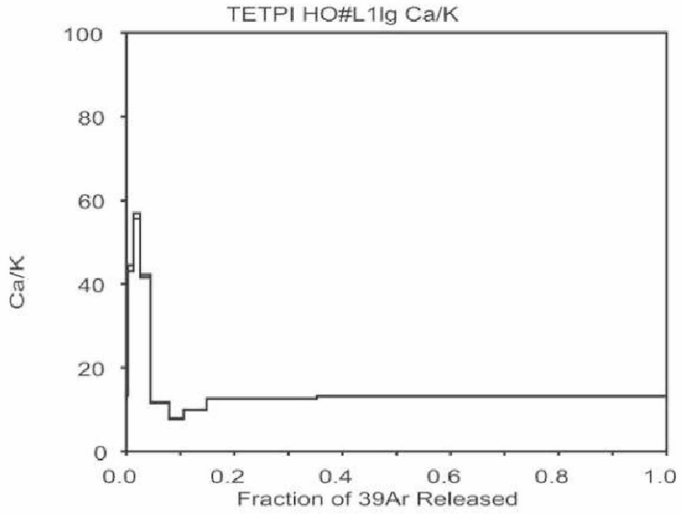


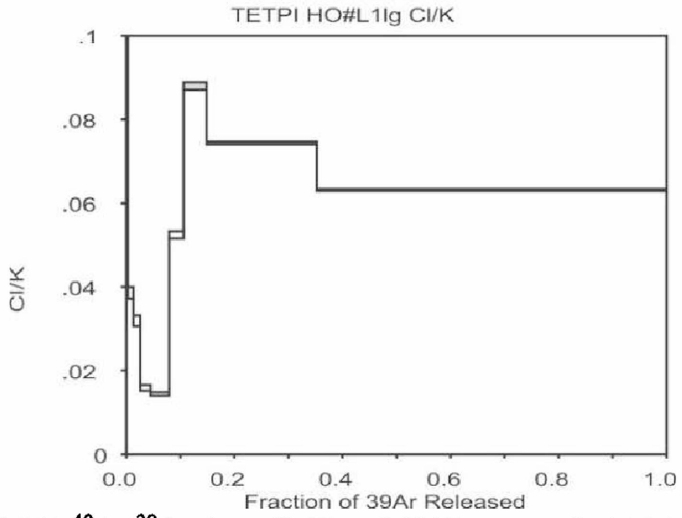


Figure A5.7: $^{40}Ar/^{39}Ar$ Age, Ca/K and Cl/K spectra for TETPI HO#1

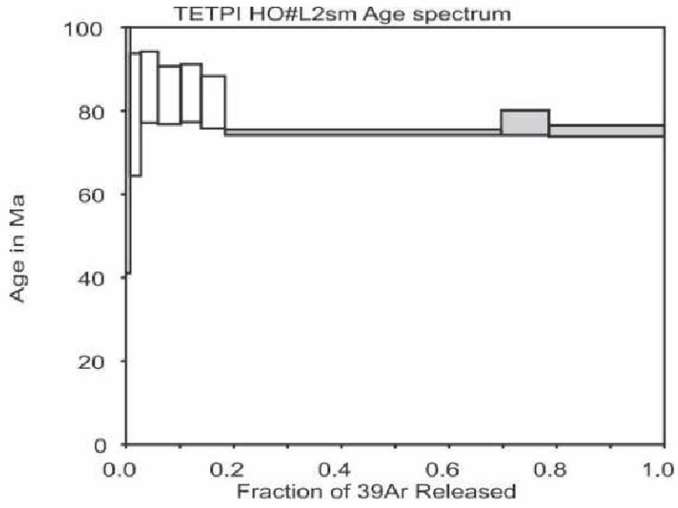


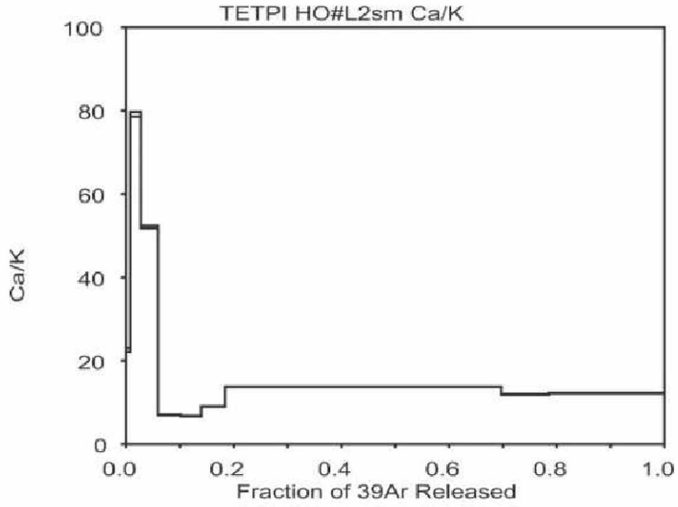


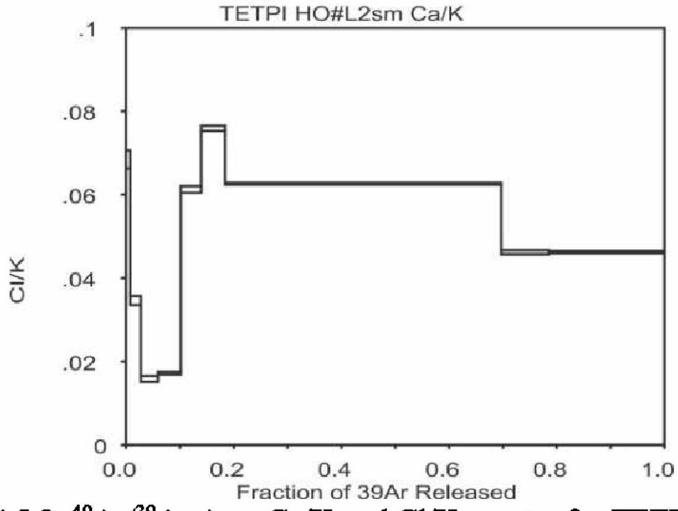


Figure A5.8: $^{40}Ar/^{39}Ar$ Age, Ca/K and Cl/K spectra for TETPI HO#2

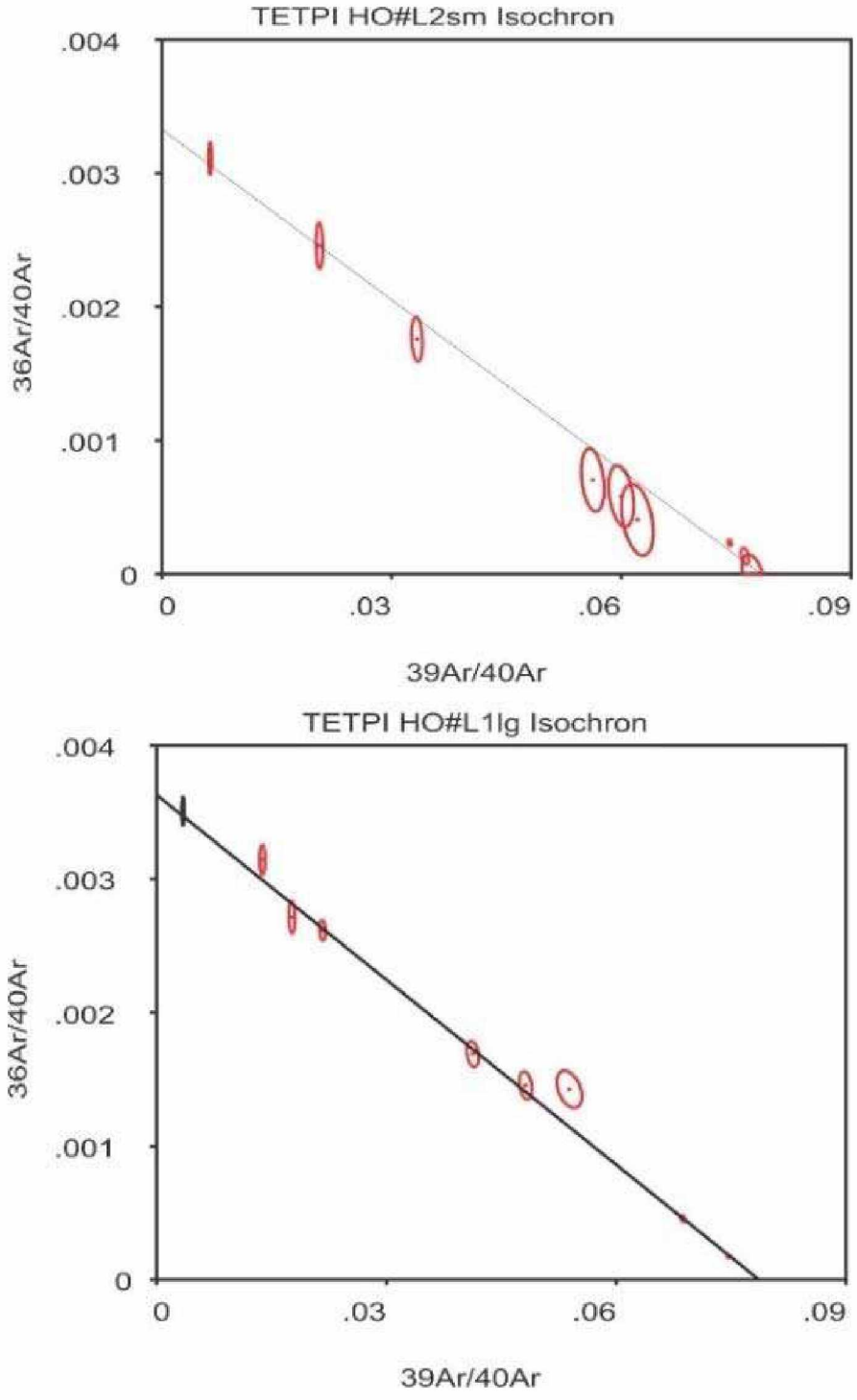


Figure A5.9: Isochron plots for TETPI HO#1

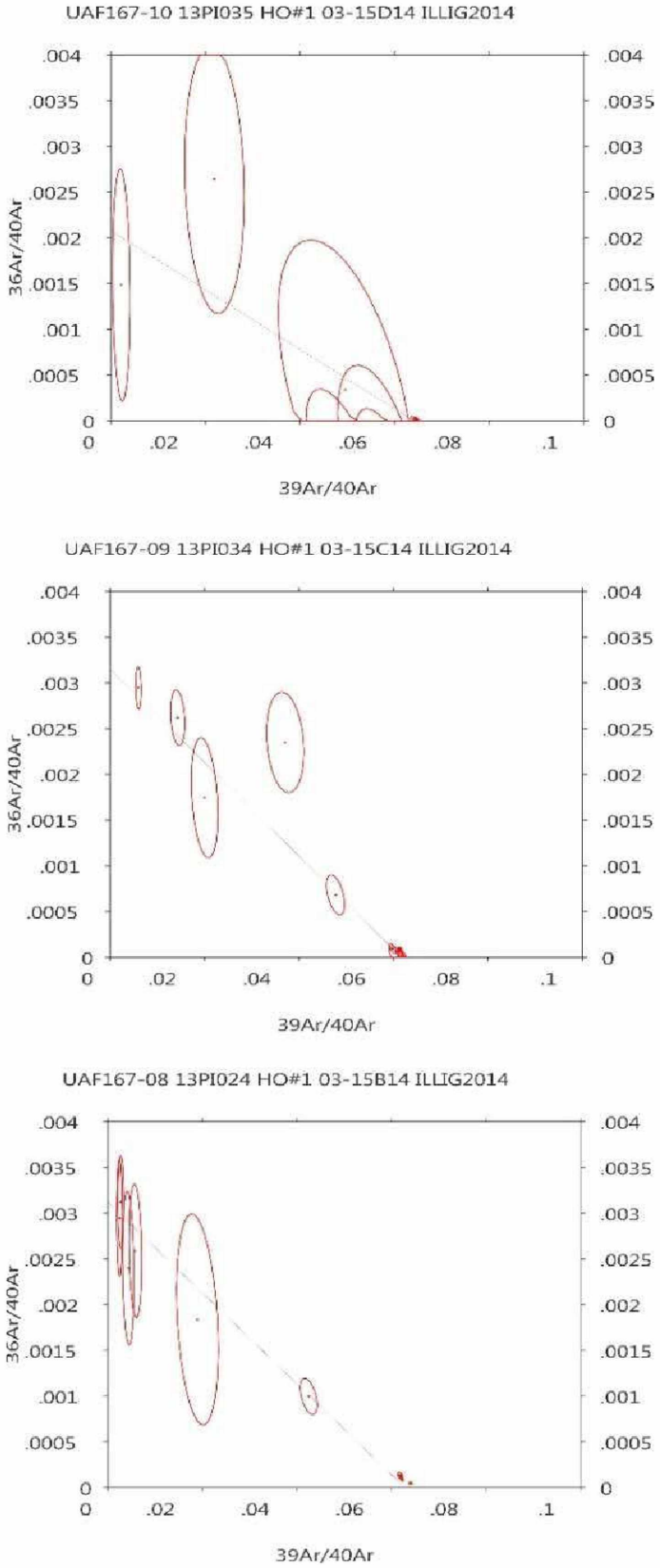


Figure A5.10: Isochron plots for 13PI035, 13PI034 and 13PI024

# Table A5.1: 40Ar/39Ar step heat analysis data for13PI024 HO#1 and 13PI024 HO#2

**UAF167-08 13PI024 HO#1 03-15B14 ILLIG2014**
Weighted average of J from standards = 2.552e-03 1.290e-05

| Laser Power (mW) | Cumulative 39Ar | 40Ar/39Ar meas. | +/- | 37Ar/39Ar meas. | +/- | 36Ar/39Ar meas. | +/- | % Atm. 40Ar | +/- | Ca/K | +/- | Cl/K | +/- | 40*/39K | +/- | Age (Ma) | +/- (Ma) |
|---|---|---|---|---|---|---|---|---|---|---|---|---|---|---|---|---|---|
| 400 | 0.0002 | 409.5136 | 80.35209 | 3.46047 | 0.77077 | 1.20759 | 0.35237 | 87.07479 | 18.83291 | 6.36505 | 1.4212 | 1.32696 | 0.26766 | 53.05633 | 78.01583 | 228.84 | 316.01 |
| 800 | 0.0005 | 371.4338 | 75.07966 | 2.67259 | 0.64091 | 1.16166 | 0.30029 | 92.3657 | 14.90785 | 4.91311 | 1.18043 | 1.07663 | 0.22367 | 28.40773 | 55.77584 | 126.13 | 239.18 |
| 1200 | 0.0008 | 234.1614 | 47.31827 | 2.91778 | 0.69598 | 0.56357 | 0.22287 | 71.02593 | 24.20775 | 5.36478 | 1.28231 | 1.02572 | 0.21852 | 67.97758 | 58.4671 | 288.29 | 229.14 |
| 1600 | 0.0012 | 172.296 | 23.91234 | 3.64261 | 0.59877 | 0.44752 | 0.13813 | 76.59185 | 21.18104 | 6.70092 | 1.10433 | 1.14378 | 0.16365 | 40.42837 | 37.02107 | 176.95 | 154.34 |
| 2000 | 0.0023 | 52.81405 | 4.18904 | 4.15567 | 0.33752 | 0.09823 | 0.05875 | 54.33989 | 32.61108 | 7.64752 | 0.62295 | 1.24242 | 0.10059 | 24.17237 | 17.37581 | 107.88 | 75.27 |
| 2500 | 0.016 | 23.5234 | 0.22924 | 4.04422 | 0.04305 | 0.02461 | 0.00406 | 29.53842 | 5.10264 | 7.44184 | 0.07945 | 1.96908 | 0.02033 | 16.60151 | 1.21356 | 74.78 | 5.35 |
| 3000 | 0.1393 | 16.18798 | 0.0923 | 2.91391 | 0.01664 | 0.00298 | 0.00045 | 3.96451 | 0.81731 | 5.35765 | 0.03066 | 2.13931 | 0.01186 | 15.54974 | 0.16008 | 70.13 | 0.71 |
| 4000 | 0.3289 | 16.1448 | 0.07292 | 3.09029 | 0.01457 | 0.00298 | 0.00027 | 3.88079 | 0.48942 | 5.68265 | 0.02686 | 2.21357 | 0.01009 | 15.52364 | 0.10653 | 70.02 | 0.47 |
| 5000 | 0.521 | 16.08445 | 0.078 | 3.13665 | 0.01581 | 0.00241 | 0.00026 | 2.81615 | 0.48685 | 5.7681 | 0.02915 | 2.27124 | 0.0116 | 15.63733 | 0.10961 | 70.52 | 0.48 |
| 9000 | 1 | 15.6306 | 0.10564 | 2.52432 | 0.02101 | 0.00147 | 0.00016 | 1.45616 | 0.30615 | 4.64006 | 0.03869 | 2.36634 | 0.01617 | 15.40124 | 0.11534 | 69.47 | 0.51 |
| Integrated | | 16.35693 | 0.05736 | 2.82076 | 0.01147 | 0.00352 | 0.00018 | 4.93933 | 0.33274 | 5.18604 | 0.02114 | 2.28293 | 0.00828 | 15.55181 | 0.07781 | 70.14 | 0.49 |

**UAF167-08 13PI024 HO#2 04-12C14 ILLIG2014**
Weighted average of J from standards = 2.552e-03 1.290e-05

| Laser Power (mW) | Cumulative 39Ar | 40Ar/39Ar meas. | +/- | 37Ar/39Ar meas. | +/- | 36Ar/39Ar meas. | +/- | % Atm. 40Ar | +/- | Ca/K | +/- | Cl/K | +/- | 40*/39K | +/- | Age (Ma) | +/- (Ma) |
|---|---|---|---|---|---|---|---|---|---|---|---|---|---|---|---|---|---|
| 500 | 0.0003 | 284.2396 | 41.65421 | 5.98164 | 0.9221 | 1.03388 | 0.21059 | 107.3216 | 15.28219 | 11.02205 | 1.70632 | 1.48282 | 0.21882 | -20.897 | 43.71124 | -98.76 | 212.36 |
| 750 | 0.0006 | 160.513 | 25.29597 | 2.47293 | 0.44735 | 0.53432 | 0.14424 | 98.25865 | 21.6794 | 4.54543 | 0.8237 | 0.89602 | 0.14175 | 2.79947 | 34.85888 | 12.83 | 159.18 |
| 1000 | 0.001 | 86.3971 | 12.15558 | 1.95567 | 0.35057 | 0.33081 | 0.07375 | 112.9987 | 19.9025 | 3.59336 | 0.64503 | 0.58619 | 0.08458 | -11.2422 | 17.25297 | -52.46 | 81.69 |
| 1500 | 0.0021 | 52.04911 | 2.50198 | 2.40247 | 0.13311 | 0.10375 | 0.02773 | 58.55553 | 15.54111 | 4.4157 | 0.24506 | 0.68 | 0.03324 | 21.59583 | 8.18221 | 96.68 | 35.66 |
| 2000 | 0.0071 | 26.80743 | 0.38387 | 3.86585 | 0.05989 | 0.03047 | 0.00595 | 32.43911 | 6.55478 | 7.11272 | 0.1105 | 1.69847 | 0.02525 | 18.14086 | 1.78201 | 81.56 | 7.83 |
| 2500 | 0.0543 | 17.2914 | 0.12074 | 3.7041 | 0.02813 | 0.00777 | 0.00083 | 11.52937 | 1.41822 | 6.81435 | 0.05188 | 2.12877 | 0.01486 | 15.31166 | 0.26917 | 69.08 | 1.19 |
| 3000 | 0.2008 | 16.13588 | 0.07927 | 3.45564 | 0.01606 | 0.00388 | 0.00028 | 5.34201 | 0.50632 | 6.35614 | 0.02962 | 2.22385 | 0.0105 | 15.28315 | 0.11263 | 68.95 | 0.5 |
| 4000 | 0.7351 | 15.82307 | 0.05196 | 2.66036 | 0.00849 | 0.00262 | 0.00006 | 3.51679 | 0.10685 | 4.89059 | 0.01565 | 2.31428 | 0.00759 | 15.26669 | 0.05408 | 68.88 | 0.24 |
| 5000 | 0.8869 | 15.7913 | 0.05665 | 2.46576 | 0.00933 | 0.00242 | 0.00036 | 3.23856 | 0.67952 | 4.53222 | 0.01717 | 2.38722 | 0.00907 | 15.27781 | 0.12105 | 68.93 | 0.54 |
| 9000 | 1 | 15.81639 | 0.06494 | 2.42042 | 0.01018 | 0.00272 | 0.00027 | 3.83088 | 0.4964 | 4.44875 | 0.01874 | 2.36684 | 0.01075 | 15.20796 | 0.10107 | 68.62 | 0.45 |
| Integrated | | 16.1721 | 0.03296 | 2.77591 | 0.00557 | 0.00385 | 0.00011 | 5.63008 | 0.21027 | 5.10342 | 0.01026 | 2.30309 | 0.00477 | 15.26355 | 0.04685 | 68.87 | 0.4 |

# Table A5.2: 40Ar/39Ar step heat analysis data for13PI034 HO#1 and 13PI034 HO#2

**UAF167-09 13PI034 HO#1 03-15C14 ILLIG2014**
Weighted average of J from standards = 2.552e-03 1.290e-05

| Laser Power (mW) | Cumulative 39Ar | 40Ar/39Ar meas. | +/- | 37Ar/39Ar meas. | +/- | 36Ar/39Ar meas. | +/- | % Atm. 40Ar | +/- | Ca/K | +/- | Cl/K | +/- | 40*/39K | +/- | Age (Ma) | +/- (Ma) |
|---|---|---|---|---|---|---|---|---|---|---|---|---|---|---|---|---|---|
| 400 | 0.002 | 164.4693 | 10.68286 | 2.40114 | 0.1761 | 0.48523 | 0.04933 | 87.07543 | 6.83247 | 4.41324 | 0.32422 | 0.34679 | 0.029 | 21.28921 | 11.34291 | 95.34 | 49.48 |
| 800 | 0.0099 | 26.96554 | 0.70519 | 0.62598 | 0.02452 | 0.06349 | 0.01462 | 69.45625 | 15.9365 | 1.1491 | 0.04502 | 0.4022 | 0.01204 | 8.23086 | 4.30077 | 37.46 | 19.37 |
| 1200 | 0.0132 | 69.60972 | 2.72836 | 1.16673 | 0.09045 | 0.18258 | 0.02171 | 77.40388 | 8.7294 | 2.14255 | 0.16624 | 0.45552 | 0.02125 | 15.73536 | 6.11501 | 70.95 | 27.04 |
| 1600 | 0.0167 | 49.84656 | 2.96763 | 2.09935 | 0.13626 | 0.08751 | 0.03153 | 51.56125 | 18.45061 | 3.85775 | 0.25076 | 1.13663 | 0.06879 | 24.16651 | 9.32052 | 107.85 | 40.38 |
| 2000 | 0.0433 | 20.9282 | 0.13596 | 2.88655 | 0.02067 | 0.01505 | 0.00398 | 20.13681 | 5.6262 | 5.30725 | 0.03809 | 2.03038 | 0.01361 | 16.72435 | 1.18367 | 75.32 | 5.22 |
| 2500 | 0.1594 | 16.71124 | 0.06088 | 2.88604 | 0.01229 | 0.00241 | 0.00065 | 2.84018 | 1.14577 | 5.30629 | 0.02265 | 2.12565 | 0.00753 | 16.24092 | 0.20074 | 73.19 | 0.89 |
| 3000 | 0.3836 | 16.31746 | 0.05506 | 2.90146 | 0.01152 | 0.00207 | 0.00042 | 2.28393 | 0.76828 | 5.3347 | 0.02122 | 2.04726 | 0.00683 | 15.94849 | 0.13672 | 71.89 | 0.6 |
| 4000 | 0.7342 | 16.2786 | 0.06982 | 3.01538 | 0.01305 | 0.0024 | 0.00019 | 2.83192 | 0.35312 | 5.54462 | 0.02405 | 1.97169 | 0.00799 | 15.8225 | 0.08954 | 71.34 | 0.4 |
| 5000 | 0.8467 | 16.17685 | 0.0959 | 2.86913 | 0.0187 | 0.0012 | 0.0007 | 0.73563 | 1.28041 | 5.27514 | 0.03445 | 2.04306 | 0.01277 | 16.06097 | 0.22818 | 72.39 | 1.01 |
| 6000 | 0.8886 | 16.36612 | 0.09933 | 2.76561 | 0.02054 | 0.00046 | 0.00158 | -0.55637 | 2.85461 | 5.08444 | 0.03784 | 2.08181 | 0.01327 | 16.45952 | 0.47787 | 74.15 | 2.11 |
| 9000 | 1 | 16.24526 | 0.07551 | 2.77575 | 0.0134 | 0.00109 | 0.00077 | 0.58363 | 1.39851 | 5.10313 | 0.02469 | 2.09961 | 0.01004 | 16.15264 | 0.23942 | 72.8 | 1.06 |
| Integrated | | 17.12048 | 0.03365 | 2.88837 | 0.00612 | 0.00463 | 0.00029 | 6.6132 | 0.50018 | 5.3106 | 0.01127 | 2.0114 | 0.0039 | 15.99322 | 0.09148 | 72.09 | 0.54 |

**UAF167-09 13PI034 HO#2 04-13B13 ILLIG2014**
Weighted average of J from standards = 2.552e-03 1.290e-05

| Laser Power (mW) | Cumulative 39Ar | 40Ar/39Ar meas. | +/- | 37Ar/39Ar meas. | +/- | 36Ar/39Ar meas. | +/- | % Atm. 40Ar | +/- | Ca/K | +/- | Cl/K | +/- | 40*/39K | +/- | Age (Ma) | +/- (Ma) |
|---|---|---|---|---|---|---|---|---|---|---|---|---|---|---|---|---|---|
| 500 | 0.0045 | 59.04671 | 0.76616 | 1.60715 | 0.02909 | 0.15582 | 0.00812 | 77.79717 | 3.93964 | 2.95225 | 0.05349 | 0.37536 | 0.00541 | 13.11835 | 2.33448 | 59.34 | 10.39 |
| 750 | 0.0085 | 24.6673 | 0.30525 | 1.11239 | 0.03464 | 0.06586 | 0.00634 | 78.62513 | 7.54791 | 2.04268 | 0.06366 | 0.44105 | 0.00586 | 5.2704 | 1.86309 | 24.08 | 8.45 |
| 1000 | 0.0111 | 34.8503 | 0.55289 | 1.51656 | 0.03796 | 0.07087 | 0.00961 | 59.78437 | 8.10273 | 2.78566 | 0.0698 | 0.56908 | 0.00999 | 14.01835 | 2.83386 | 63.34 | 12.58 |
| 1500 | 0.0146 | 34.84801 | 0.71706 | 2.36137 | 0.05097 | 0.05242 | 0.00769 | 43.92677 | 6.46274 | 4.34002 | 0.09384 | 1.2207 | 0.02535 | 19.55639 | 2.29115 | 87.77 | 10.04 |
| 2000 | 0.0472 | 18.59589 | 0.14975 | 2.94408 | 0.02591 | 0.00536 | 0.00068 | 7.22849 | 1.07262 | 5.41323 | 0.04774 | 2.13607 | 0.01793 | 17.26007 | 0.2441 | 77.68 | 1.08 |
| 2500 | 0.1976 | 16.51283 | 0.07344 | 3.00128 | 0.01251 | 0.00311 | 0.00021 | 4.0735 | 0.37675 | 5.51864 | 0.02305 | 2.07792 | 0.00971 | 15.84534 | 0.09524 | 71.44 | 0.42 |
| 3000 | 0.4273 | 16.3667 | 0.06658 | 2.90439 | 0.01427 | 0.00285 | 0.00014 | 3.69088 | 0.25294 | 5.3401 | 0.02629 | 2.09318 | 0.00922 | 15.76642 | 0.07719 | 71.09 | 0.34 |
| 4000 | 0.7667 | 16.25688 | 0.06787 | 2.93069 | 0.01412 | 0.00289 | 0.00012 | 3.77366 | 0.22476 | 5.38857 | 0.02602 | 2.06713 | 0.00973 | 15.64727 | 0.07574 | 70.56 | 0.33 |
| 5000 | 0.9154 | 16.36101 | 0.07131 | 2.81434 | 0.01263 | 0.00107 | 0.00097 | 0.52136 | 1.76001 | 5.17421 | 0.02328 | 2.08853 | 0.00928 | 16.27857 | 0.29671 | 73.35 | 1.31 |
| 9000 | 1 | 16.53351 | 0.07797 | 2.82245 | 0.01424 | 0.00316 | 0.00031 | 4.24439 | 0.55136 | 5.18915 | 0.02623 | 2.06825 | 0.00974 | 15.83494 | 0.11874 | 71.39 | 0.52 |
| Integrated | | 16.77375 | 0.03322 | 2.89038 | 0.00653 | 0.00403 | 0.00017 | 5.69305 | 0.30076 | 5.3143 | 0.01204 | 2.05932 | 0.00451 | 15.82316 | 0.05979 | 71.34 | 0.44 |

# Table A5.3: 40Ar/39Ar step heat analysis data for13PI035 HO#1 and 13PI035 HO#2

**UAF167-10 13PI035 HO#1 03-15D14 ILLIG2014**
Weighted average of J from standards = 2.552e-03 1.290e-05

| Laser Power (mW) | Cumulative 39Ar | 40Ar/39Ar meas. | +/- | 37Ar/39Ar meas. | | 36Ar/39Ar meas. | +/- | % Atm. 40Ar | +/- | Ca/K | +/- | Cl/K | +/- | 40*/39K | +/- | Age (Ma) | +/- (Ma) |
|---|---|---|---|---|---|---|---|---|---|---|---|---|---|---|---|---|---|
| 400 | 0.0002 | 470.1204 | 387.3715 | 1.25879 | 1.51028 | 0.69898 | 0.79586 | 43.91594 | 34.53958 | 2.31177 | 2.7761 | 0.09155 | 0.24552 | 263.8805 | 271.6768 | 927.86 | 746.63 |
| 800 | 0.0023 | 45.84307 | 4.50367 | 1.03744 | 0.14935 | 0.1214 | 0.0678 | 78.1169 | 43.08005 | 1.90496 | 0.27444 | 0.24189 | 0.03153 | 10.03274 | 19.77928 | 45.56 | 88.7 |
| 1200 | 0.0068 | 20.23444 | 0.86968 | 0.29316 | 0.0502 | 0.00694 | 0.02827 | 10.02589 | 41.34486 | 0.53802 | 0.09216 | 0.0082 | 0.00939 | 18.1828 | 8.39342 | 81.74 | 36.89 |
| 1600 | 0.0138 | 19.79122 | 0.55307 | 0.28012 | 0.03029 | -0.01445 | 0.01531 | -21.7249 | 22.88918 | 0.51408 | 0.0556 | 0.00376 | 0.00655 | 24.05945 | 4.57175 | 107.39 | 19.81 |
| 2000 | 0.0232 | 17.61295 | 0.53201 | 0.21776 | 0.02674 | -0.00911 | 0.01676 | -15.4069 | 28.16173 | 0.39962 | 0.04909 | 0.00688 | 0.00448 | 20.2954 | 4.9893 | 91 | 21.82 |
| 2500 | 0.0361 | 17.1625 | 0.31508 | 0.31302 | 0.01843 | -0.00982 | 0.00932 | -17.0953 | 16.06762 | 0.57448 | 0.03384 | 0.02139 | 0.00321 | 20.06614 | 2.7774 | 90 | 12.15 |
| 3000 | 0.0547 | 16.32056 | 0.19596 | 1.02131 | 0.0195 | -0.00786 | 0.00629 | -14.7808 | 11.40088 | 1.87531 | 0.03582 | 0.09138 | 0.00321 | 18.7123 | 1.87181 | 84.07 | 8.22 |
| 4000 | 0.2391 | 15.63902 | 0.08399 | 3.16167 | 0.01475 | 0.00083 | 0.00066 | -0.10199 | 1.25867 | 5.81421 | 0.02718 | 0.21652 | 0.00137 | 15.66027 | 0.21422 | 70.62 | 0.95 |
| 5000 | 0.5374 | 15.49646 | 0.05745 | 3.35817 | 0.01288 | 0.00117 | 0.00036 | 0.44769 | 0.67878 | 6.17644 | 0.02374 | 0.20283 | 0.00095 | 15.43419 | 0.11992 | 69.62 | 0.53 |
| 6000 | 0.83 | 15.46009 | 0.04812 | 3.34223 | 0.00853 | 0.00097 | 0.00049 | 0.06328 | 0.93485 | 6.14705 | 0.01572 | 0.19473 | 0.00061 | 15.45719 | 0.15244 | 69.72 | 0.67 |
| 9000 | 1 | 15.49201 | 0.0555 | 3.68774 | 0.01713 | 0.00081 | 0.00064 | -0.42554 | 1.21641 | 6.78417 | 0.0316 | 0.18925 | 0.00118 | 15.56873 | 0.19669 | 70.22 | 0.87 |
| Integrated | | 15.77491 | 0.03044 | 3.2207 | 0.00622 | 0.00089 | 0.00041 | -0.02249 | 0.77423 | 5.92302 | 0.01147 | 0.1922 | 0.00048 | 15.78472 | 0.12595 | 71.17 | 0.66 |

**UAF167-10 13PI035 HO#2 04-12B14 ILLIG2014**
Weighted average of J from standards = 2.552e-03 1.290e-05

| Laser Power (mW) | Cumulative 39Ar | 40Ar/39Ar meas. | +/- | 37Ar/39Ar meas. | +/- | 36Ar/39Ar meas. | +/- | % Atm. 40Ar | +/- | Ca/K | +/- | Cl/K | +/- | 40*/39K | +/- | Age (Ma) | +/- (Ma) |
|---|---|---|---|---|---|---|---|---|---|---|---|---|---|---|---|---|---|
| 500 | 0.0023 | 60.85097 | 5.55091 | 0.7866 | 0.12237 | 0.26778 | 0.06845 | 129.9941 | 31.25362 | 1.4441 | 0.22478 | 0.07246 | 0.01443 | -18.253 | 19.06604 | -85.96 | 91.97 |
| 750 | 0.0069 | 19.49131 | 1.08132 | 0.44538 | 0.06136 | 0.03828 | 0.03125 | 57.92797 | 47.39757 | 0.81746 | 0.11265 | 0.04509 | 0.00537 | 8.19047 | 9.24685 | 37.28 | 41.66 |
| 1000 | 0.0143 | 15.95826 | 0.57069 | 0.21521 | 0.02851 | 0.02007 | 0.01759 | 37.13037 | 32.62056 | 0.39493 | 0.05233 | 0.03119 | 0.00253 | 10.01575 | 5.21519 | 45.48 | 23.39 |
| 1500 | 0.0318 | 15.52055 | 0.21899 | 0.13503 | 0.02887 | -0.00366 | 0.01464 | -7.04923 | 27.92876 | 0.24779 | 0.05299 | 0.02657 | 0.00232 | 16.58442 | 4.33268 | 74.7 | 19.12 |
| 2000 | 0.059 | 15.2888 | 0.21153 | 0.15417 | 0.01343 | 0.00196 | 0.00501 | 3.72104 | 9.69929 | 0.28291 | 0.02465 | 0.03427 | 0.00118 | 14.6929 | 1.49433 | 66.34 | 6.62 |
| 2500 | 0.0881 | 15.41255 | 0.1928 | 0.24449 | 0.01014 | -0.0001 | 0.0033 | -0.3224 | 6.34153 | 0.44869 | 0.01861 | 0.04066 | 0.00112 | 15.43512 | 0.99466 | 69.62 | 4.4 |
| 3000 | 0.1324 | 15.74638 | 0.0976 | 1.18953 | 0.0167 | 0.00358 | 0.00355 | 6.1004 | 6.6698 | 2.18446 | 0.0307 | 0.11102 | 0.00121 | 14.77033 | 1.05334 | 66.68 | 4.67 |
| 4000 | 0.2851 | 15.84173 | 0.10277 | 2.70903 | 0.01651 | 0.00313 | 0.00084 | 4.43274 | 1.56519 | 4.98023 | 0.0304 | 0.18816 | 0.00141 | 15.14014 | 0.26725 | 68.32 | 1.18 |
| 5000 | 0.5572 | 15.48105 | 0.07194 | 3.07985 | 0.01633 | 0.00159 | 0.00045 | 1.40425 | 0.86653 | 5.66343 | 0.03009 | 0.19511 | 0.00114 | 15.26765 | 0.15212 | 68.88 | 0.67 |
| 9000 | 1 | 15.50908 | 0.08089 | 2.76147 | 0.01429 | 0.00171 | 0.00022 | 1.80256 | 0.42124 | 5.07682 | 0.02633 | 0.17271 | 0.00125 | 15.23011 | 0.10354 | 68.72 | 0.46 |
| Integrated | | 15.6782 | 0.04563 | 2.54666 | 0.00797 | 0.00275 | 0.00047 | 3.84242 | 0.88106 | 4.68119 | 0.01468 | 0.1664 | 0.00067 | 15.07438 | 0.14518 | 68.03 | 0.73 |

# Table A5.4: 40Ar/39Ar step heat analysis data for TETPI HO#1 and TETPIHO#2

**TETPI HO#L1lg**

Weighted average of J from standards = 3.377e-03 +/- 8.438e-06

| Laser Power (mW) | Cumulative 39Ar | 40Ar/39Ar meas. | +/- | 37Ar/39Ar meas. | +/- | 36Ar/39Ar meas. | +/- | % Atm. 40Ar | +/- | Ca/K | +/- | Cl/K | +/- | 40*/39K | +/- | Age (Ma) | +/- (Ma) |
|---|---|---|---|---|---|---|---|---|---|---|---|---|---|---|---|---|---|
| 500 | 0.0028 | 290.9883 | 12.06508 | 7.58397 | 0.33172 | 1.02277 | 0.05386 | 103.6582 | 3.37779 | 13.99047 | 0.61522 | 0.10627 | 0.00672 | -10.7013 | 9.89027 | -66.33 | 62.45 |
| 1000 | 0.013 | 71.29857 | 1.09598 | 23.4594 | 0.36543 | 0.23058 | 0.00903 | 92.88988 | 3.45176 | 43.76993 | 0.6933 | 0.03856 | 0.00143 | 5.1527 | 2.50313 | 31.09 | 14.97 |
| 1500 | 0.0254 | 55.44892 | 0.58377 | 30.0191 | 0.3189 | 0.15877 | 0.00709 | 80.19363 | 3.68015 | 56.27393 | 0.61076 | 0.03192 | 0.00129 | 11.2144 | 2.08791 | 66.99 | 12.24 |
| 2000 | 0.045 | 45.46931 | 0.38553 | 22.47699 | 0.19005 | 0.12516 | 0.00374 | 77.31241 | 2.33789 | 41.9074 | 0.36006 | 0.0159 | 0.00068 | 10.47554 | 1.08422 | 62.65 | 6.37 |
| 2500 | 0.0793 | 24.15207 | 0.1954 | 6.33125 | 0.05216 | 0.04255 | 0.00226 | 49.95725 | 2.73523 | 11.66915 | 0.09658 | 0.01442 | 0.00045 | 12.12578 | 0.67094 | 72.32 | 3.92 |
| 3000 | 0.1059 | 18.533 | 0.16776 | 4.22574 | 0.04104 | 0.02756 | 0.00238 | 42.12973 | 3.77716 | 7.77685 | 0.07576 | 0.05242 | 0.00087 | 10.74001 | 0.7081 | 64.2 | 4.16 |
| 4000 | 0.1488 | 20.70815 | 0.09746 | 5.38203 | 0.02786 | 0.03159 | 0.00212 | 43.00424 | 3.01914 | 9.91297 | 0.05152 | 0.08799 | 0.00091 | 11.83087 | 0.62977 | 70.6 | 3.69 |
| 5000 | 0.3527 | 14.51313 | 0.03459 | 6.83615 | 0.01724 | 0.00853 | 0.00036 | 13.51799 | 0.73382 | 12.60424 | 0.03195 | 0.07432 | 0.00033 | 12.58645 | 0.11141 | 75.02 | 0.65 |
| 9000 | 1 | 13.35072 | 0.04068 | 7.15904 | 0.01823 | 0.00431 | 0.00017 | 5.13212 | 0.37423 | 13.20261 | 0.0338 | 0.06316 | 0.00022 | 12.70172 | 0.06402 | 75.69 | 0.37 |
| Integrated | | 16.95007 | 0.03268 | 7.67248 | 0.01366 | 0.01779 | 0.00025 | 27.32335 | 0.4422 | 14.15464 | 0.02534 | 0.0631 | 0.00017 | 12.36427 | 0.07983 | 73.72 | 0.5 |

**TETPI HO#L2sm**

Weighted average of J from standards = 3.377e-03 +/- 8.438e-06

| Laser Power (mW) | Cumulative 39Ar | 40Ar/39Ar meas. | +/- | 37Ar/39Ar meas. | +/- | 36Ar/39Ar meas. | +/- | % Atm. 40Ar | +/- | Ca/K | +/- | Cl/K | +/- | 40*/39K | +/- | Age (Ma) | +/- (Ma) |
|---|---|---|---|---|---|---|---|---|---|---|---|---|---|---|---|---|---|
| 500 | 0.0076 | 156.9067 | 3.29516 | 12.15669 | 0.25834 | 0.49152 | 0.02248 | 91.94585 | 3.77309 | 22.499 | 0.48227 | 0.06847 | 0.00217 | 12.74454 | 5.97795 | 75.94 | 34.88 |
| 1000 | 0.0273 | 47.15833 | 0.28636 | 41.8625 | 0.28366 | 0.12751 | 0.00831 | 72.62426 | 5.18663 | 79.15196 | 0.55268 | 0.03462 | 0.00106 | 13.29511 | 2.52062 | 79.15 | 14.68 |
| 1500 | 0.0588 | 29.43937 | 0.18513 | 27.81943 | 0.18715 | 0.05946 | 0.00489 | 51.94476 | 4.90181 | 52.06778 | 0.35729 | 0.01582 | 0.00073 | 14.4164 | 1.47375 | 85.67 | 8.55 |
| 2000 | 0.102 | 17.75514 | 0.1187 | 3.80429 | 0.03201 | 0.01353 | 0.00402 | 20.78686 | 6.70619 | 6.99915 | 0.05904 | 0.01727 | 0.00033 | 14.07877 | 1.19589 | 83.71 | 6.95 |
| 2500 | 0.1396 | 16.08799 | 0.11374 | 3.6637 | 0.02873 | 0.00754 | 0.00403 | 12.00177 | 7.41017 | 6.73983 | 0.05299 | 0.06128 | 0.00079 | 14.16774 | 1.19738 | 84.22 | 6.95 |
| 3000 | 0.1839 | 16.64244 | 0.08175 | 4.89285 | 0.02718 | 0.01105 | 0.00364 | 17.23576 | 6.48291 | 9.00884 | 0.05021 | 0.07595 | 0.00061 | 13.79717 | 1.083 | 82.07 | 6.3 |
| 5000 | 0.6967 | 13.44349 | 0.0267 | 7.43842 | 0.01365 | 0.00519 | 0.00035 | 6.86451 | 0.76599 | 13.72055 | 0.02531 | 0.06262 | 0.00023 | 12.55912 | 0.10656 | 74.86 | 0.62 |
| 6000 | 0.7853 | 12.93254 | 0.06272 | 6.49338 | 0.04148 | 0.00184 | 0.0017 | 0.05989 | 3.89914 | 11.96935 | 0.07682 | 0.04621 | 0.00055 | 12.95466 | 0.50937 | 77.16 | 2.97 |
| 9000 | 1 | 13.10229 | 0.02431 | 6.61922 | 0.01456 | 0.00358 | 0.00078 | 3.92973 | 1.75804 | 12.2024 | 0.02697 | 0.04622 | 0.00027 | 12.61799 | 0.23213 | 75.2 | 1.36 |
| Integrated | | 16.03775 | 0.01952 | 8.15136 | 0.01074 | 0.01317 | 0.00049 | 20.11548 | 0.8977 | 15.04321 | 0.01993 | 0.05425 | 0.00015 | 12.86213 | 0.14556 | 76.62 | 0.87 |

Table A5.5: U-Pb radiometric age analysis data for TET11006-68m

| Analysis Name | Preferred Age (Ma) | 2 sigma | 207Pb/235Uc Ratio | 2 sigma | 206Pb/238U Ratio | 2 sigma | Error Correlation |
|---|---|---|---|---|---|---|---|
| 111AZ1_1 | 69.48 | 1.77 | 0.07229 | 0.00670 | 0.01084 | 0.00028 | 0.04 |
| 111AZ1_2 | 287.43 | 7.52 | 0.33305 | 0.01222 | 0.04560 | 0.00122 | 0.40 |
| 111AZ1_3 | 0.00 | 0.00 | 0.00000 | 0.00000 | 0.00000 | 0.00000 | 0.00 |
| 111AZ1_4 | 71.75 | 2.77 | 0.07539 | 0.00525 | 0.01119 | 0.00043 | 0.27 |
| 111AZ1_5 | 0.00 | 0.00 | 0.00000 | 0.00000 | 0.00000 | 0.00000 | 0.00 |
| 111AZ1_6 | 74.89 | 1.62 | 0.07847 | 0.00450 | 0.01168 | 0.00025 | 0.10 |
| 111AZ1_7 | 68.35 | 1.73 | 0.07271 | 0.00719 | 0.01066 | 0.00027 | 0.05 |
| 111AZ1_8 | 71.05 | 1.79 | 0.07546 | 0.00491 | 0.01108 | 0.00028 | 0.12 |
| 111AZ1_9 | 70.07 | 1.92 | 0.07523 | 0.00778 | 0.01093 | 0.00030 | 0.05 |
| 111AZ1_10 | 70.22 | 1.97 | 0.07574 | 0.00941 | 0.01095 | 0.00031 | 0.05 |
| 111AZ1_11 | 68.27 | 2.40 | 0.07189 | 0.00583 | 0.01065 | 0.00038 | 0.20 |
| 111AZ1_12 | 69.03 | 4.60 | 0.07322 | 0.00681 | 0.01077 | 0.00072 | 0.38 |
| 111AZ1_13 | 69.01 | 5.04 | 0.07544 | 0.00875 | 0.01076 | 0.00079 | 0.30 |
| 111AZ1_14 | 69.64 | 1.48 | 0.07235 | 0.00597 | 0.01086 | 0.00023 | 0.07 |
| 111AZ1_15 | 71.48 | 1.81 | 0.07510 | 0.00670 | 0.01115 | 0.00028 | 0.05 |
| 111AZ1_16 | 69.23 | 1.49 | 0.07036 | 0.00472 | 0.01080 | 0.00023 | 0.09 |
| 111AZ1_17 | 69.15 | 1.73 | 0.07120 | 0.00375 | 0.01079 | 0.00027 | 0.21 |
| 111AZ1_18 | 68.93 | 1.61 | 0.07138 | 0.00319 | 0.01075 | 0.00025 | 0.32 |
| 111AZ1_19 | 82.84 | 2.19 | 0.08777 | 0.00873 | 0.01293 | 0.00034 | 0.04 |
| 111AZ1_20 | 75.28 | 2.05 | 0.08016 | 0.00739 | 0.01175 | 0.00032 | 0.10 |
| 111AZ1_21 | 70.53 | 2.12 | 0.07584 | 0.00783 | 0.01100 | 0.00033 | 0.05 |
| 111AZ1_22 | 70.29 | 2.02 | 0.07768 | 0.00992 | 0.01096 | 0.00032 | 0.04 |
| 111AZ1_23 | 69.20 | 2.51 | 0.07562 | 0.00948 | 0.01079 | 0.00039 | 0.04 |
| 111AZ1_24 | 70.75 | 2.60 | 0.07622 | 0.01041 | 0.01104 | 0.00041 | 0.06 |
| 111AZ1_25 | 68.15 | 2.34 | 0.07224 | 0.01107 | 0.01063 | 0.00037 | 0.04 |
| 111AZ1_26 | 70.01 | 3.54 | 0.07630 | 0.01143 | 0.01092 | 0.00056 | 0.11 |
| 111AZ1_27 | 70.41 | 4.96 | 0.07565 | 0.00795 | 0.01098 | 0.00078 | 0.36 |
| 111AZ1_28 | 69.48 | 1.66 | 0.07424 | 0.00597 | 0.01084 | 0.00026 | 0.05 |
| 111AZ1_29 | 69.21 | 1.76 | 0.07155 | 0.00675 | 0.01079 | 0.00028 | 0.05 |
| 111AZ1_30 | 71.20 | 2.45 | 0.07574 | 0.00795 | 0.01111 | 0.00038 | 0.07 |